# RADAR DETECTION OF ULTRA HIGH ENERGY COSMIC RAYS

by

Isaac J. Myers

A dissertation submitted to the faculty of
The University of Utah
in partial fulfillment of the requirements for the degree of

Doctor of Philosophy

in

Physics

Department of Physics and Astronomy

The University of Utah

August 2015

# The University of Utah Graduate School

## STATEMENT OF DISSERTATION APPROVAL

The dissertation of **Isaac J. Myers**

has been approved by the following supervisory committee members:

| | | |
|---|---|---|
| **John Belz** | , Chair | **May 6, 2015**<br>Date Approved |
| **Douglas Bergman** | , Member | **May 6, 2015**<br>Date Approved |
| **Behrouz Farhang** | , Member | **May 5, 2015**<br>Date Approved |
| **Mikhail Raikh** | , Member | **May 1, 2015**<br>Date Approved |
| **Gordon Thomson** | , Member | **May 14, 2015**<br>Date Approved |

and by **Carleton Detar** , Chair/Dean of

the Department/College/School of **Physics and Astronomy**

and by David B. Kieda, Dean of The Graduate School.

# ABSTRACT

TARA (Telescope Array Radar) is a cosmic ray radar detection experiment co-located with Telescope Array, the conventional surface scintillation detector (SD) and fluorescence telescope detector (FD) near Delta, UT. The TARA detector combines a 40 kW transmitter and high gain transmitting antenna which broadcasts the radar carrier over the SD array and in the FD field of view to a 250 MS/s DAQ receiver. Data collection began in August, 2013. TARA stands apart from other cosmic ray radar experiments in that radar data is directly compared with conventional cosmic ray detector events. The transmitter is also directly controlled by TARA researchers.

Waveforms from the FD-triggered data stream are time-matched with TA events and searched for signal using a novel signal search technique in which the expected (simulated) radar echo of a particular air shower is used as a matched filter template and compared to radio waveforms. This technique is used to calculate the radar cross-section (RCS) upper-limit on all triggers that correspond to well-reconstructed TA FD monocular events. Our lowest cosmic ray RCS upper-limit is 42 $\mathrm{cm}^2$ for an 11 EeV event.

An introduction to cosmic rays is presented with the evolution of detection and the necessity of new detection techniques, of which radar detection is a candidate. The software simulation of radar scattering from cosmic rays follows. The TARA detector, including transmitter and receiver systems, are discussed in detail. Our search algorithm and methodology for calculating RCS is presented for the purpose of being repeatable. Search results are explained in context of the usefulness and future of cosmic ray radar detection.

# CONTENTS

**CHAPTERS**

# LIST OF FIGURES

# ACKNOWLEDGMENTS

Planning and building of the TARA detector spanned nearly five years, followed by two years of data collection. During this period many people took part in advancing our experiment, and helped me in a personal way to meet the challenges of science research. Several people stand out in my mind as having made outstanding contributions. I have had many invaluable discussions with Helio Takai, a co-founder of the MARIACHI experiment, about radar echo simulation and air shower physics. Ben Stokes, Gordon Thomson, Stan Thomas, Jeremy Smith, and Dmitri Ivanov provided assistance on numerous occasions. Tom Stroman deserves special thanks for providing fluorescence detector events for comparison with TARA data. All of my friends in TA and TARA have offered a helping hand at some point, whether through physics or programming discussions or career advice and encouragement.

Dave Barr, Gary McDonough, Stanton Thomas, and Patrick Wright assisted in numerous hardware and facilities tasks that kept our experiment functioning. Support from Frank Misak has been indispensable in keeping TARA affairs in order. John Matthews has offered his knowledge about the fine details of operating a large experiment, including navigating the University of Utah bureaucracy and working with private contractors.

Bill Ramsey not only helped procure the television transmitters used in the experiment, but assisted several times in the field to prepare the transmitters for operation. For the last several years Bill Gillman has been our to go-to guy for his transmitter expertise and broad electronics knowledge. He directed us in commissioning our final high power transmitter system in Hinckley, UT and he serviced the transmitters while we pushed them beyond the commercial specification.

Most importantly, I would like to thank my advisor John Belz for many physics and research discussions and his constant availability and willingness to help me understand and learn new things. TARA is a group effort, but the analysis presented in this dissertation is primarily the work of John and me. Without John's assistance and experience in experimental physics, I wouldn't have been able to produce such a clear and appropriate methodology. Finally, I want to express my appreciation to my family for their support, both financial and moral.

Early TARA funding was a seed grant from VP for Research Tom Parks. U.S. National Science Foundation grants NSF/PHY-0969865 and NSF/MRI-1126353 and a special grant from the W.M. Keck Foundation carried our experiment for its duration. On a personal level, these grants supported my research assistantship which allowed me to spend my time doing research. I would also like to acknowledge the generous donation of analog television transmitter equipment by Salt Lake City KUTV Channel 2 and ABC Channel 4, and the general cooperation of the Telescope Array collaboration.

# CHAPTER 1

# INTRODUCTION TO COSMIC RAY PHYSICS

The title “cosmic ray” is misleading because cosmic rays are single highly energetic *particles* that propagate through space both within and outside of our galaxy. Gamma rays and electrons are sometimes included in the definition. In this text the term will primarily denote hadronic particles, from single protons to atomic nuclei as heavy as iron and higher.

In 1912 Victor Hess conducted research[19] that showed evidence of cosmic origins of previously observed charged particles in the atmosphere, work about which he later wrote a book[20] (translated to English) and won the Nobel prize. From measurements taken with an electroscope while aboard a balloon, Hess showed that the rate of discharge in an electroscope increases with altitude. An electroscope is a device that shows a net charge by the separation between charged foils. Energetic charged particles bombarding the instrument create trails of ionization electrons that allow leakage current from the charged foil, allowing discharge which decreases deflection. Prior to Hess’s discovery, the radiation that discharged electroscopes was thought to originate in the earth.

Pierre Auger is credited with the discovery of atmospheric particle cascades called air showers, which are initiated by a single cosmic ray primary particle.[21] Interest grew from the realization that energetic secondary particles indicate a highly energetic primary. With a basic understanding of the atmospheric phenomenology of cosmic rays, the scientific community turned its attention to the question of their origin. The answer to this question is still being pursued today. Theoretical frameworks for acceleration sources are abundant, but arrival direction and possible astronomical objects haven’t been correlated with high probability.

Cosmic Ray (CR) research has led to the discovery of new fundamental particles such as the positron[22] ($e^+$), muon[23] ($\mu^-$) and pion[24] ($\pi^\pm$, $\pi^0$), which opened the door to particle physics. In the decades since the early discoveries, the range of detected cosmic ray energies has increased by over eleven orders of magnitude, from $10^9$ to $10^{20}$ eV. Ultra high energy cosmic rays (UHECR) are classified as those that have energies greater than $10^{18}$ eV (Exa-eV, EeV) and exceed the most powerful particle accelerators in single-particle energy made by humankind by a factor of roughly 100,000 (1 EeV cosmic ray primary proton compared to 7 TeV LHC proton beam[25]).

The primary question of CR physics still remains. There is no strong evidence of correlations between CR and known astronomical structures. Galactic and extragalactic magnetic fields smear CR arrival directions. UHECRs are the best candidates for source correlation because the Larmor radius is proportional to energy, so the random component of the arrival direction is minimized.

Unfortunately, the UHECR flux is very low. Section 1.1 contains an explanation of the measured energy spectrum (Figure 1.1) which indicates, e.g., that one can expect a single $10^{20}$ eV cosmic ray particle per square kilometer per century. Therefore, detectors are large; Pierre Auger Observatory (PAO, southern hemisphere) surface detector covers over $3000\,\mathrm{km}^2$ and Telescope Array (TA, northern hemisphere) covers nearly $700\,\mathrm{km}^2$. Large detectors are expensive to build and maintain, and funding agencies have been hesitant to fund substantial expansions of the current large detectors.

Investigation of alternate detection methods is driven by the desire for better statistics. The CR energy spectrum dictates that UHECR event rates are low. Any new technique that measures energy, composition and geometry in a large fiducial volume at lesser cost will be successful. Cherenkov,[26] molecular bremsstrahlung,[27] and geomagnetic synchrotron[28] are passive detection methods currently being investigated. Radar detection of cosmic rays[29] is the only active technique being pursued. CR physics needs new tools and detection methods which will allow better statistics at the highest energies. Radar detection of cosmic rays is one possible solution that would allow remote detection at 100% duty cycle.

What follows in this chapter is a brief description of the CR spectrum, possible

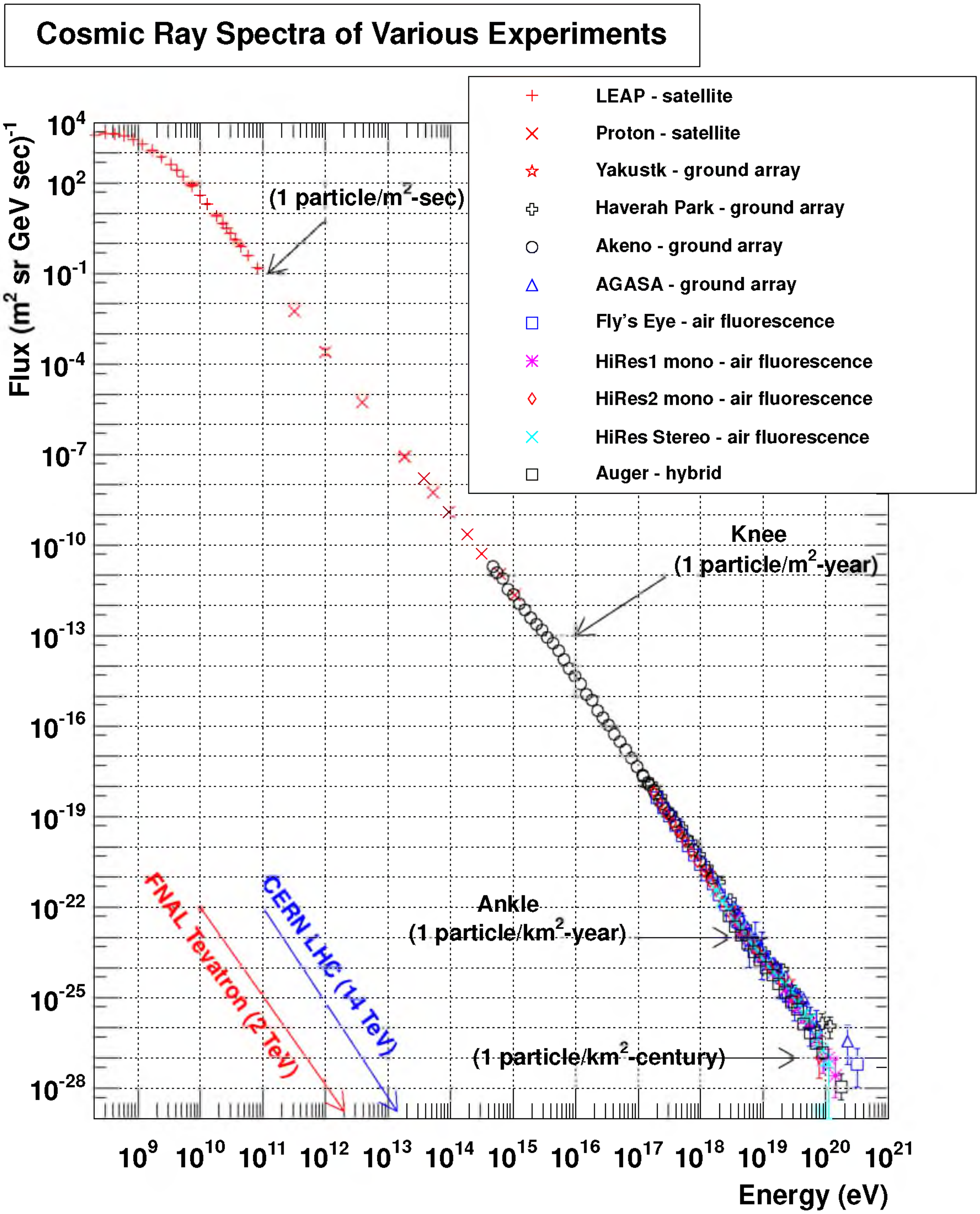

**Figure 1.1**: The cosmic ray energy spectrum for all particles as seen from a several experiments.[1] Reprinted figure with permission from E. Barcikowski, copyright 2011.

source acceleration mechanisms, and primary particle composition and propagation. Air shower footprint and novel radio emission detection techniques are introduced. Cosmic ray radar detection is proposed as a method of detection which may have advantages over other channels.

Chapter 2 gives an explanation of air showers including the cascade processes of electromagnetic and hadronic components, and the longitudinal profile and lateral distribution of particles. Plasma physics and scattering models relevant to radar echo simulation is discussed in Section 2.3. Chapter 3 gives a complete description of the Telescope Array Radar (TARA) detector, including transmitter, receiver antennas and DAQ, and performance estimates. Chapter 4 introduces the data, experimental challenges, and processing techniques. Chapter 5 describes the analysis procedure in which I search waveforms for evidence of radar echoes and calculate the radar cross-section (RCS). Analysis results and conclusion follow in Chapters 6 and 7.

## 1.1 Energy Spectrum

An energy spectrum plot (flux vs. energy) is shown in Figure 1.1. Notice the nearly constant $E^{-3}$ power law and the large range of detected energies. The low and high energy ends of the spectrum require dramatically different detection and measurement techniques because of orders of magnitude difference in flux. For example, above $10^{18.9}$ eV the TA detector has an aperture of $890\,\mathrm{km}^2\,\mathrm{sr}$.[30] Using the figure, the rate of $10^{19}$ eV primaries detected by TA is calculated to be slightly less than one per day. Note that TA is the world's second largest UHECR detector, covering approximately $680\,\mathrm{km}^2$.[30]

At the other end of the spectrum, consider a $100\,\mathrm{cm}^2$, $2\pi$ steradian detector flown on a high-altitude balloon or satellite. Its count rate would reasonably be greater than $50\,\mathrm{s}^{-1}$ for 10 GeV particles.

A spectral index of $-3$ indicates a nonthermal acceleration source because the spectrum is not peaked as in, e.g., Planck's Law. Spectral features can be seen more readily if the featureless Figure 1.1 ordinate is multiplied by $E^3$. Figure 1.2 shows this modification.

Three prominent spectral features at $\sim 10^{15}$ eV, $\sim 4 \times 10^{17}$ eV and $\sim 4 \times 10^{18}$ eV are known as the knee, second knee and ankle. Above $\sim 6 \times 10^{19}$ eV the spectrum

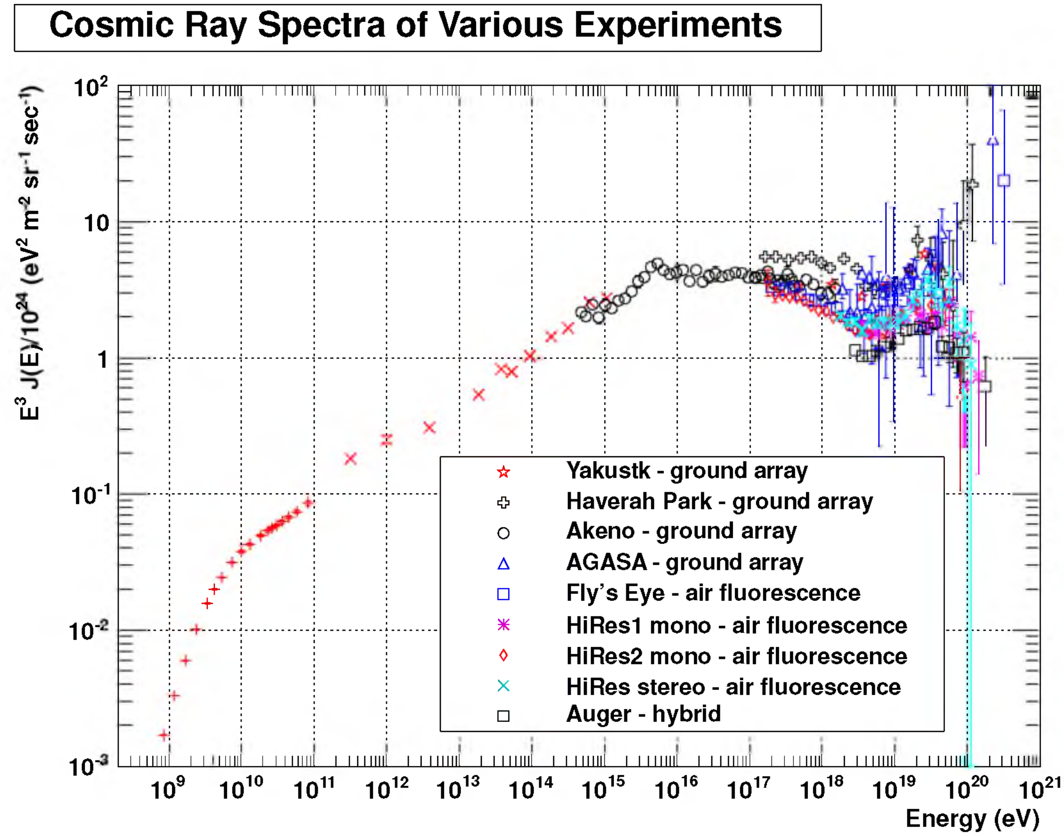

**Figure 1.2**: The cosmic ray energy spectrum for all particles multiplied by $E^3$ to expose spectral features.[1] Reprinted figure with permission from E. Barcikowski, copyright 2011.

falls rapidly due to the Greisen-Zatsepin-Kuzmin (GZK) cut-off.[31] Figure 1.2 best shows the knee. A third spectrum plot, shown in Figure 1.3, is a scaled version of Figure 1.2 that best shows the ankle and second knee. These features are evidence of specific source mechanisms and propagation models (Section 1.2). The spectral index changes from $-2.7$ to $-3.1$ after the knee, a softening of the spectrum. After the second knee the spectrum steepens again and finally becomes less steep at the ankle.

## 1.2 Sources and Propagation

The knee is often associated with the upper limit of galactic acceleration sources. It is near the maximum energy that can be obtained by protons accelerated at supernova shock fronts (see the following paragraph) and below the critical energy $E_c$ at which the galactic magnetic field ($B \sim 3\,\mu\text{G}^{32}$) domain correlation length

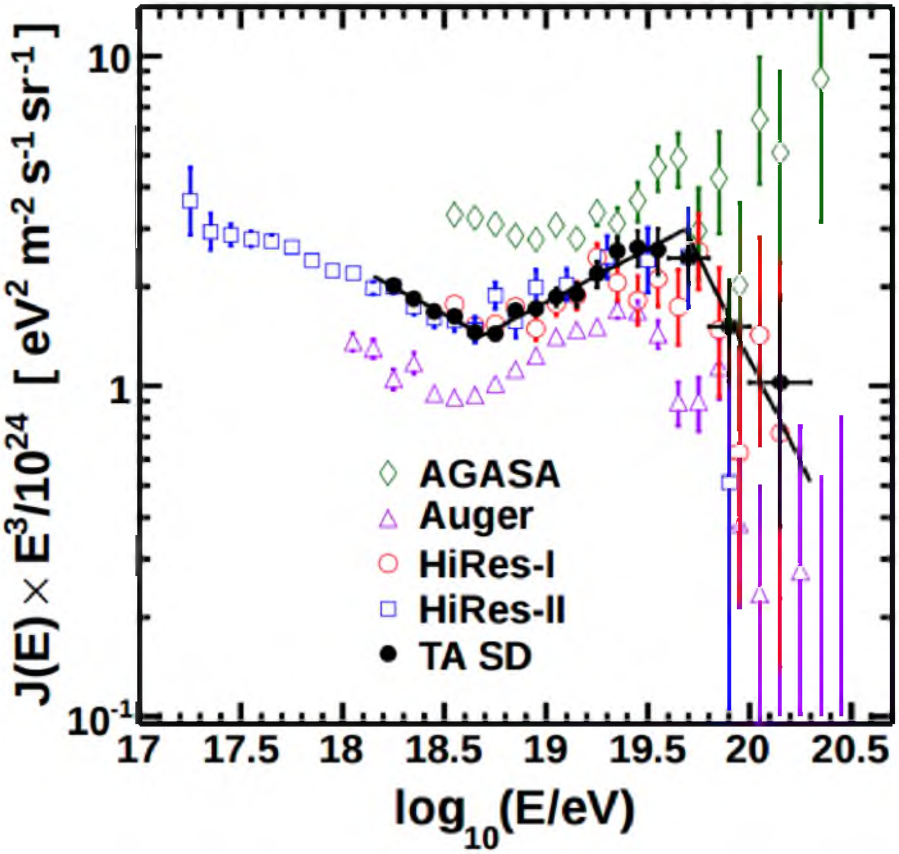

**Figure 1.3**: The TA SD cosmic ray energy spectrum[2] for all particles multiplied by $E^3$ to expose spectral features. A broken power line has been fit to the data. © AAS. Reproduced with permission.

$l \sim 0.1$ kpc[33] is comparable to the Larmor radius

$$r_L = 1.08\,\mathrm{pc}\,\frac{E\,[\mathrm{PeV}]}{ZB\,[\mu\mathrm{G}]}\,. \tag{1.1}$$

$Z$ is atomic number. CRs with energy less than the critical energy take a very long time to leave the galaxy, and thus are more likely to encounter the earth. Substituting $l$ for $r_L$ and solving, $E_c \simeq 3 \times 10^{17}$ eV for protons, two orders of magnitude greater than the energy of the knee. Therefore, it is a natural assumption that the decreasing flux is related to acceleration limits of galactic sources. Furthermore, all experiments agree in a steepening of the spectrum above several times $10^{15}$ eV.[34,35]

One popular model for a galactic CR source is acceleration at supernova shock fronts associated with supernova remnants.[36,37] According to the Fermi theory,[38] CR acceleration is a diffusive process in which a particle gains energy by interacting with the supernova remnant's magnetic field each time the particle crosses the shock front. There is some probability that each crossing of the shock front by the particle can be its last. Additionally, shock acceleration predicts a power law spectrum, which has been shown to be supported by experimental data such as that in Figure 1.3. The maximum kinetic energy achieved is $E_{\text{max}} = Ze\,\beta_s\,B\,T\,V_s$, where $\beta_s = V_s/c$ is the velocity of the shock in units of $c$, and $T$ is the time the particle remained in the shock front. For typical values, $E_{\text{max}} = Z \times 10^{14}$ eV,[39] much less than the knee energy, $\sim 10^{15}$ eV for protons.

Figure 1.4 is a Hillas plot[3] that shows magnetic the field and size of astrophysical objects. It demonstrates that certain species of astrophysical objects have the necessary size, magnetic field strength and live long enough to boost nuclei to large energies. Diagonal lines show the minimum product of field strength and size that can produce a $10^{20}$ eV proton primary.

The steepening of the slope above the knee can be explained by a combination of the maximum energy that can be obtained by specific nuclei and propagation losses. It has already been shown that $E_{\text{max}}$ is proportional to $Z$, which implies that the maximum energy obtained by a species with atomic number $Z$ is equal to $Z$ times the energy obtained by a proton, $E^Z = ZE^p$. As low-$Z$ nuclei reach their acceleration limits after the knee, higher $Z$ nuclei take over. Propagation losses cause spectrum steepening by leakage from the galaxy[40–42] or interaction with background photons or massive particles.[43,44]

The second knee is often related to a loss of the heaviest remaining galactic primaries. An extragalactic population of CR sources stiffens the spectrum above the ankle. The spectrum at energies greater than the ankle may be buoyed by an excess of proton primaries that originated with higher energies but suffered electron-pair production losses on cosmic microwave background (CMB) photons or result from an originally light source composition.[45] More protons are detected with energies lower than their original maximum energies which increases the spectral index over the region above the ankle.[5] The proton pair production process is

$$p + \gamma \rightarrow p + e^- + e^+ \,. \tag{1.2}$$

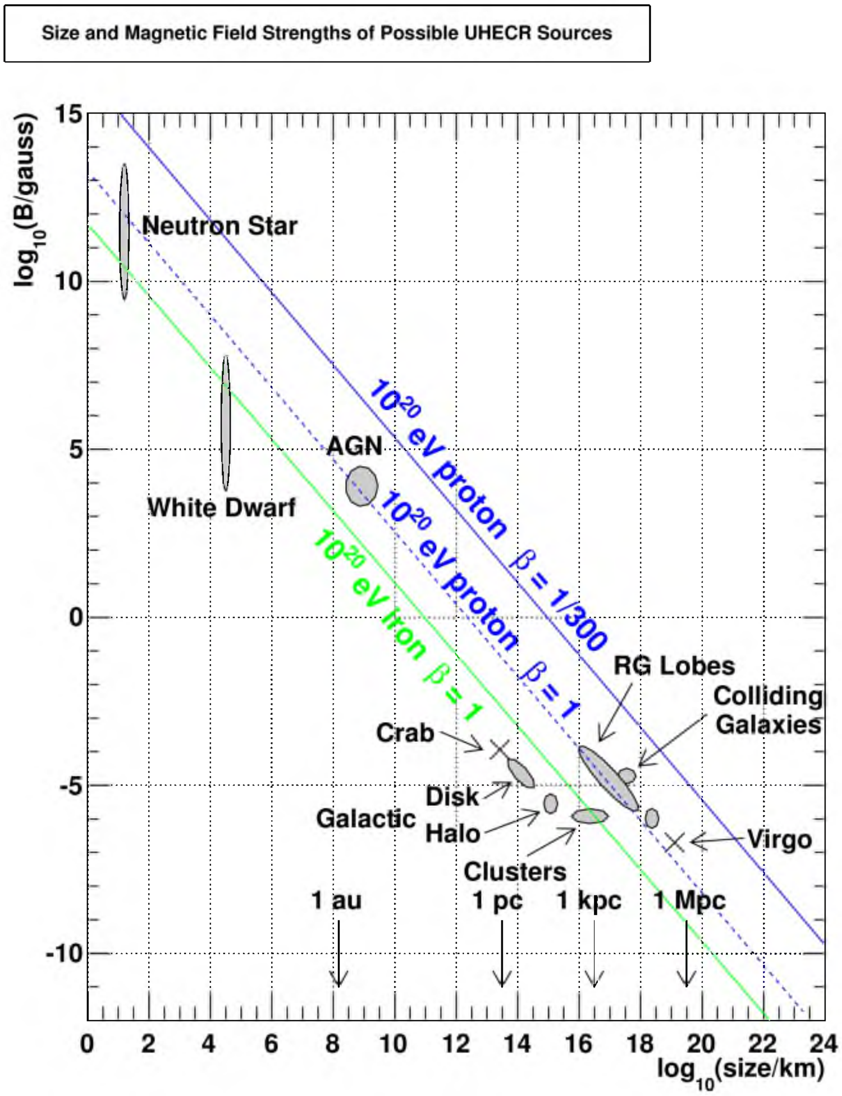

**Figure 1.4**: Hillas plot.[1,3] The product of an astrophysical object's size and typical magnetic field is a major factor in the Fermi shock acceleration model. Diagonal lines mark the minimum limit of that product necessary to accelerate protons to $10^{20}$ eV, under the assumption that $\beta_s = V_s/c$ is 1 and 1/300, respectively. $V_s$ is the shock front velocity. Reprinted figure with permission from E. Barcikowski, copyright 2011.

Opposing the bolstering effects are red-shift losses from Hubble expansion and ultimately the GZK cut-off (described below).

There are two categories of theories that seek to describe natural phenomena that result in extremely high-energy particles. The first category consists of so-called bottom-up models, which involve accelerating existing particles to highly relativistic energies. As can be inferred from the Hillas plot (Figure 1.4), either very large acceleration regions or very energetic shock fronts are necessary to accelerate particles above 1 EeV. Compact objects such as gamma ray bursts (GRB) have been favored recently because of analyses which suggest that the kinetic energy released in such events is sufficient to produce 100 EeV charged particles.[46] GRB sources would not be seen because the GRB would have occurred long before the arrival of the cosmic ray. Radio galaxies are another example of a bottom-up CR source.

The second category consists of top-down models which avoid the acceleration mechanism debate. Instead, they suggest currently unknown super-massive particles whose decay cascades produce relativistic protons and neutrons.[47] Other top-down sources include relics from the Big Bang[48] and dark matter that are outside the scope of this work.

Above 50 EeV most experiments observe a strong decrease in flux, with the exception of the Akeno Giant Air Shower Array (AGASA)[49] which observes an increase. This suppression was predicted in 1966 by Greisen,[50] and independently Zatsepin and Kuzmin[31] in the same year. Although predicted independently, the energy loss mechanism uses all three names, thus GZK. It represents the interaction of CR hadrons with the cosmic microwave background (CMB) 2.7 K photons. Proton interactions with the CMB form a $\Delta^+(1232)$ resonance (center of mass) which quickly decays:

$$p + \gamma \rightarrow \Delta^+ \rightarrow \begin{cases} \pi^0 + p \\ \pi^+ + n \end{cases} . \tag{1.3}$$

A $2.7\,\mathrm{K} = 7 \times 10^{-4}\,\mathrm{eV}$ CMB photon interacting with a CR proton achieves this center of mass energy if the proton has energy $\sim 10^{20}$ eV. However, the position of the cut-off can be detected at lower energies because of the interaction of protons with higher energy photons, i.e., those in the tail of the distribution. The cut-off was first observed with $5.1\sigma$ significance by the HiRes collaboration[51] and later observed with $5.5\sigma$ significance by Telescope Array.[2]

Spectral features above GZK could help narrow possible sources. The hope is that UHECRs, detected with good statistics and minimal magnetic field blurring, will point at their sources. The Telescope Array collaboration has published encouraging evidence of a an arrival direction "hot spot" with a statistical maximum significance of $5.1\sigma$ in a 20° radius circle for CR with energies above 57 EeV.[4] The significance of such a cluster occurring on an isotropic sky (modified for detector acceptance) is $3.6\sigma$. Figure 1.5 shows plots of the significance on a skymap in equatorial coordinates. Definitive source discovery requires that the next generation of CR detectors have much larger apertures.

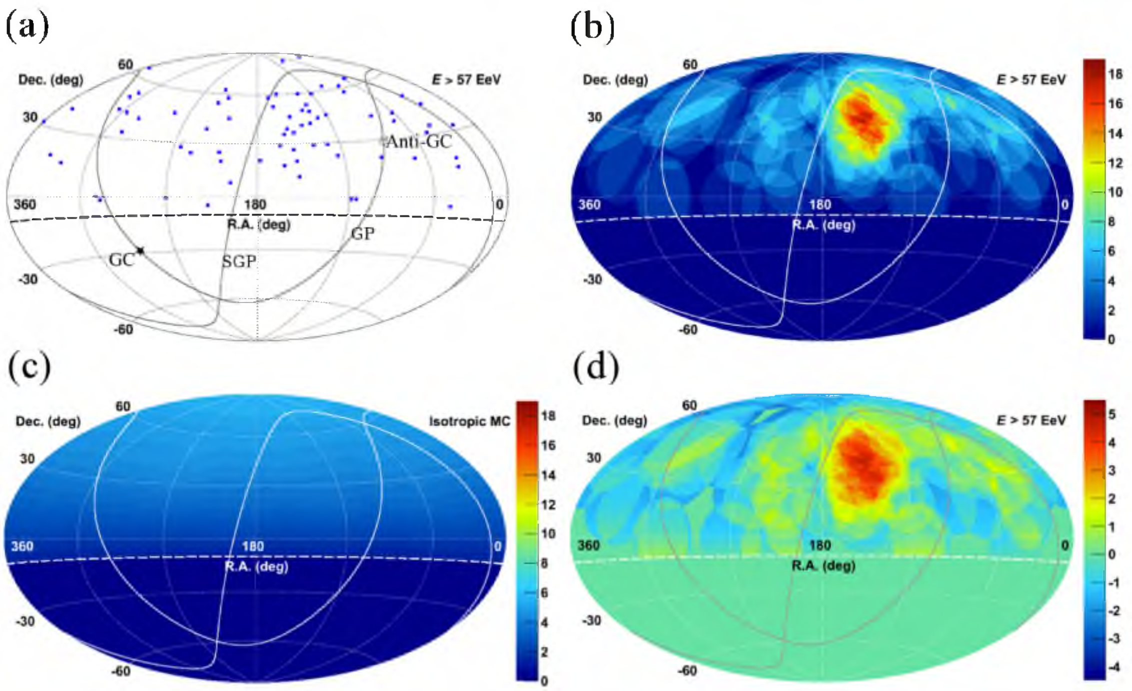

**Figure 1.5**: Significance skymaps[4] in equatorial coordinates of Telescope Array event clustering, known as the "hotspot." Seventy-two events were detected with $E_0 >$ 57 EeV (a). The maximum number of events that occurred in a 20° radius circle is 19 (b), with $5.1\sigma$ statistical significance. Background expectation from geometrical exposure to an isotropic sky in the same circle size (c) and a significance map (d) of events (b) occurring in the simulated sky are shown. © AAS. Reproduced with permission.

## 1.3 Composition

The chemical composition of cosmic rays combined with spectrum information allows for the most accurate construction of source and propagation models. Techniques have been developed to measure composition directly for low energy primaries and statistically for high energy primaries that are detected by their extensive air shower initiated in the atmosphere. At the highest energies, HiRes and PAO disagree about the trend toward heavier mass composition (see[5] and[7]).

At low energies, typically below the knee, CR mass and charge (and thus composition) can be measured directly. At the knee and higher, surface detector arrays determine composition by observing the electron to muon ratio near $X_{\mathrm{max}}$, which is proportional to $\ln A$,[32, 52] the log of the mass number. $X_{\mathrm{max}}$ is depth in the atmosphere in units of $\mathrm{g/cm^2}$ where the shower reaches its maximum. After $X_{\mathrm{max}}$ the shower decreases in size. The relative abundance of CR particles to that found in the solar system is high for low atomic number nuclei. Figure 1.6 shows both CR and solar system abundances (each relative to Si). Elements lighter than carbon and several elements lighter than iron show a large discrepancy with the solar system counterpart. This is consistent with spallation from CMB photons as CR propagate through the galaxy.

The High Resolution Fly's Eye experiment (HiRes) found a trend in CR composition with energy using FD telescopes which shows that cosmic rays become more protonic as primary energy increases above $10^{18}$ eV.[5,8] Figure 1.7 shows mean $X_{\mathrm{max}}$ as a function of $E_0$ for CORSIKA[6] Monte Carlo shower simulations using several different hadronic interaction models. Also shown are the HiRes data points. These data indicate protonic composition above 1 EeV.

Contrasting the HiRes result is the PAO UHECR composition,[7] Figure 1.8. Unlike HiRes, PAO data suggest an increasingly heavy composition at the highest energies. TA has recently published a five-year hybrid (SD and FD) composition result[9] (see Figure 1.9). With systematic uncertainty, this result is consistent with protons at the highest energies. There is speculation that the disparity is evidence of a northern-southern hemisphere source or propagation asymmetry. TA/PAO working groups are trying to resolve this discrepancy.[53]

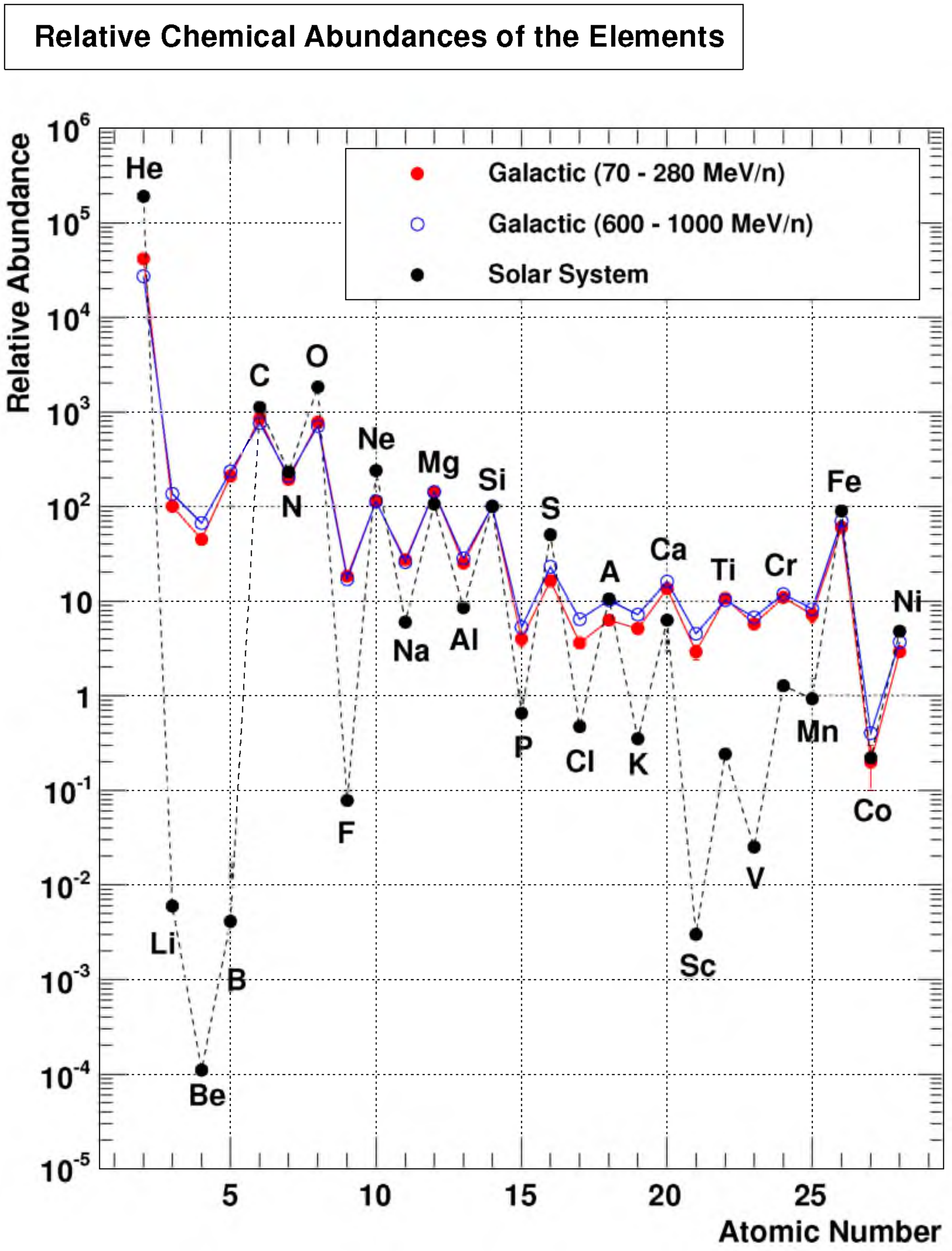

**Figure 1.6**: Element abundances of cosmic rays and the solar system,[1] both relative to Si. Nuclei lighter than C are and some nuclei lighter than Fe are over-abundant in the cosmic ray flux. Reprinted figure with permission from E. Barcikowski, copyright 2011.

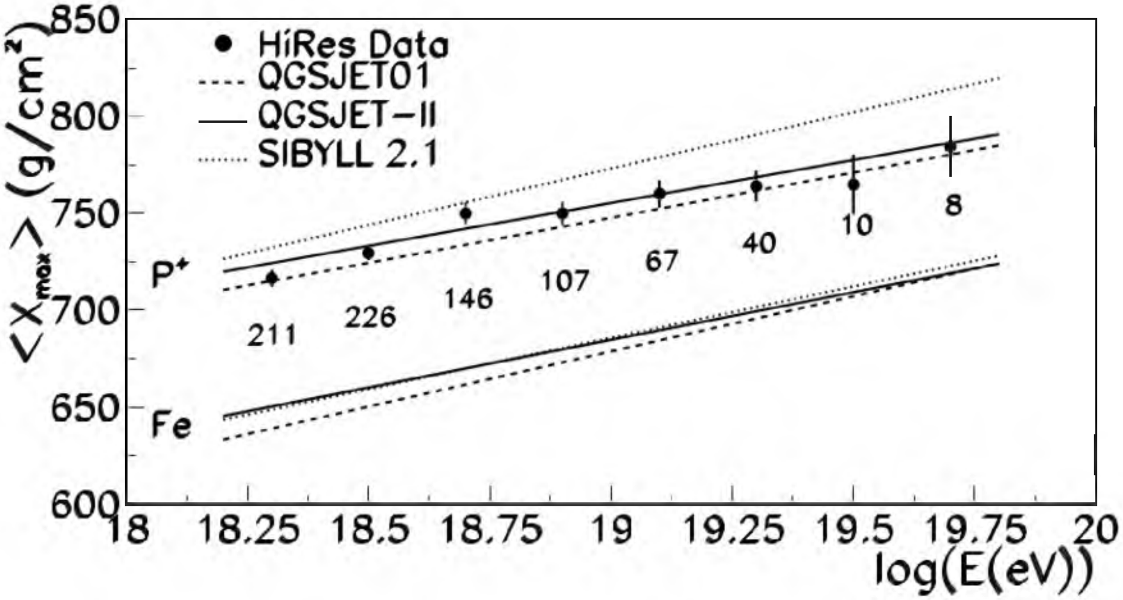

**Figure 1.7**: High Resolution Fly's Eye (HiRes) composition for $E_0 > 10^{18}$ eV.[5] The lines are the result of CORSIKA[6] air shower simulations using the different hadronic interaction models. Data are shown with the points and clearly indicate a light composition at high energies. Reprinted figure with permission from R. Abbasi, et al., Phys. Rev. Lett. **104**, 161101 (2010). http://dx.doi.org/10.1103/PhysRevLett.104.161101. Copyright 2010 by the American Physical Society.

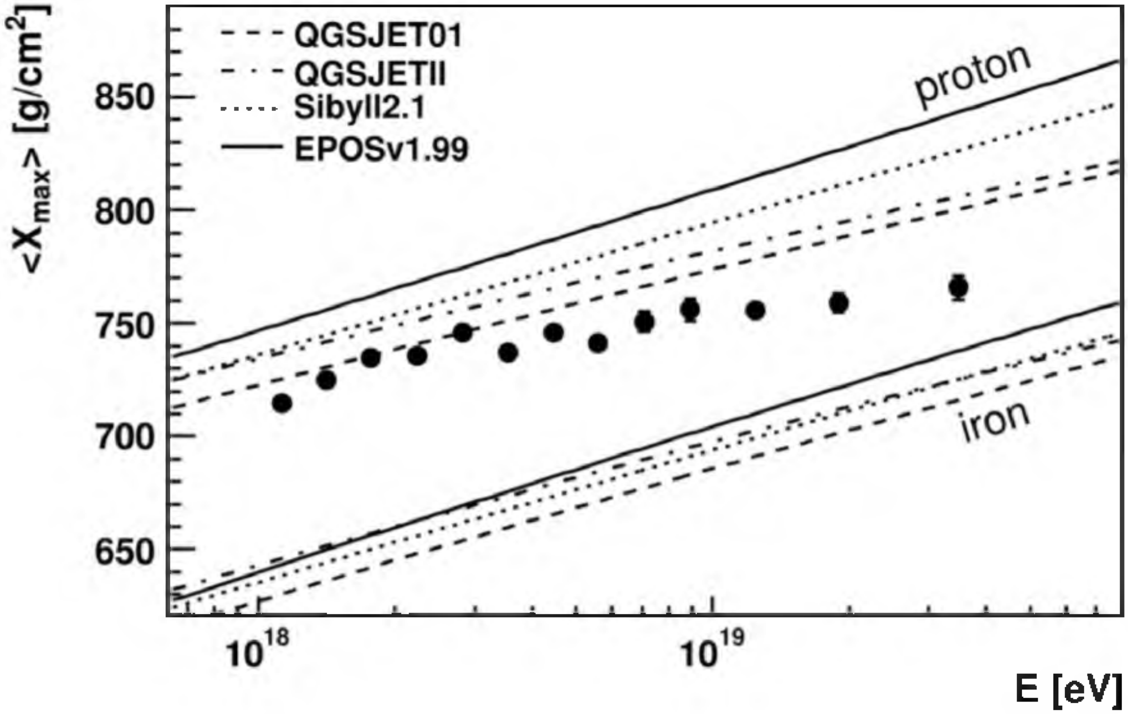

**Figure 1.8**: Pierre Auger Observatory (PAO) composition result.[7] The lines are the result of CORSIKA[6] Monte Carlo shower simulation studies using different hadronic models. The points are data. Note the error bars. These data indicate that the composition is increasingly protonic before $E_0 = 10^{18.25}$ eV, and increasingly heavier beyond. This result in in stark contrast to the earlier HiRes result[8] (Figure 1.7) which showed a protonic composition up to the highest energies. Reprinted figure with permission from J. Abraham, et al., Phys. Rev. Lett. **104**, 091101 (2010). `http://dx.doi.org/10.1103/PhysRevLett.104.091101`. Copyright 2010 by the American Physical Society.

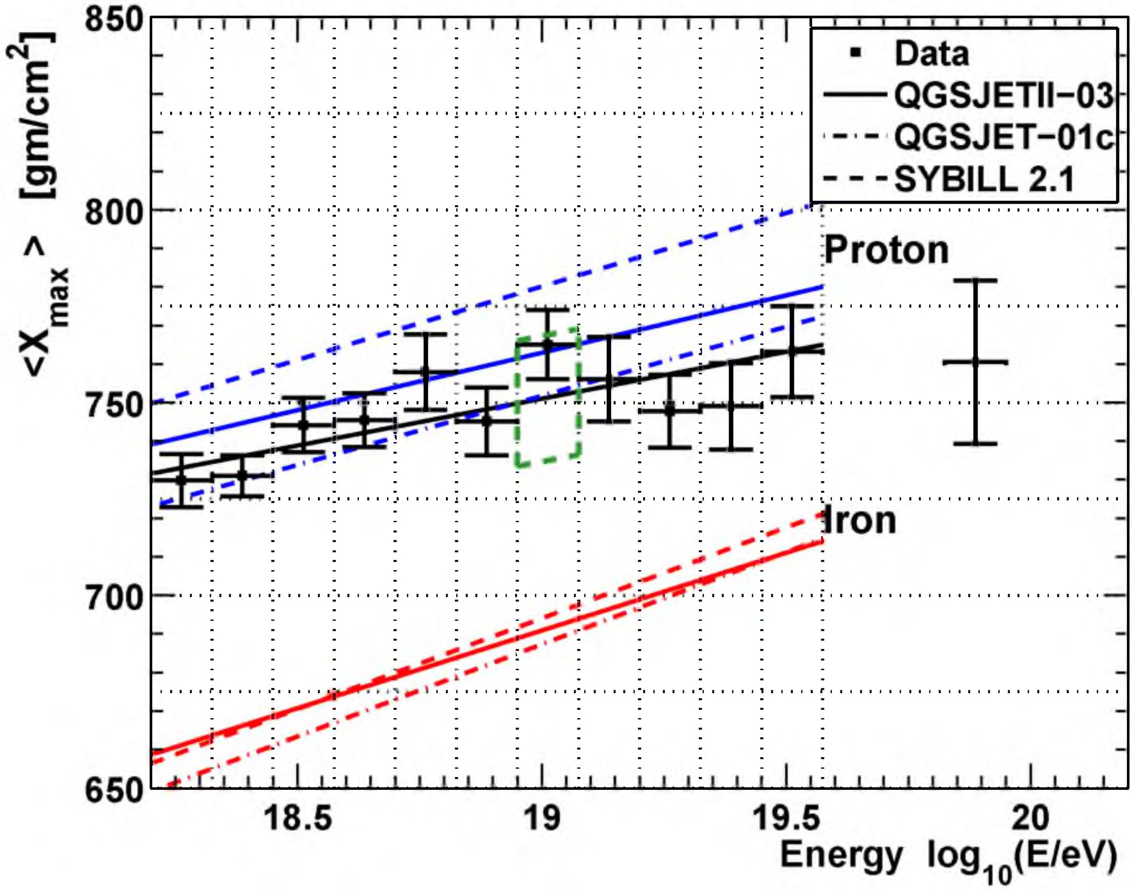

**Figure 1.9**: Telescope Array hybrid five-year composition result.[9] The red and blue lines represent different hadronic models used in simulating proton (blue) and iron (red) extensive air showers. Reprinted from Astroparticle Physics, 64, R.U. Abbasi, et al., Study of Ultra-High Energy Cosmic Ray Composition Using Telescope Array's Middle Drum Detector and Surface Array in Hybrid Mode, 49–62, Copyright (2015), with permission from Elsevier.

## 1.4 Detection Methods

Surface detection (SD) and fluorescence detection (FD) techniques currently dominate cosmic ray physics experiments. There are drawbacks to each technique, high cost being common to both. Experiments that host both SD and FD apparatus can record hybrid measurements in an approach that exploits the best qualities of each technique. FD data precisely determine energy scale and shower evolution and SD data constrain core location and timing.[54]

There are several emerging detection methods, one of which is radar detection, which may allow low-cost CR detection or increased detection ability over large areas.

Cherenkov, geo-magnetic synchrotron, and molecular bremsstrahlung emission offer three types of potential passive detection channels which involve radio emission from air showers. Section 1.4.3 briefly introduces shower radio emission detection methods.

In contract, radar is an active detection method. Radar detection of cosmic rays has the possibility of being remote sensing with 100% duty cycle. Depending on the magnitude of scattering by extensive air showers (EAS), radar detection could allow extremely large apertures by using broad antenna beamwidths that detect CR showers tens or hundreds of kilometers away, such as in meteor detection by radar.[55] Section 1.4.4 includes a brief history of radar detection of cosmic rays and an overview of TARA.

### 1.4.1 Surface Detector

An array of surface detectors (SD) allows multipoint sampling of shower products at one plane in shower longitudinal development. Shower reconstruction relies on model-dependent Monte Carlo simulations and $X_{\mathrm{max}}$ is not observed directly. The duty cycle of surface detector arrays is 100%, good for extremely low flux UHECR, but the cost of instrumenting and maintaining an array covering hundreds of square kilometers is high. Figure 1.10 shows a TA scintillator-type SD with solar panel and radio communications tower.

SDs measure several quantities that are used to calculate $X_{\mathrm{max}}$. Shower front curvature will be less for those that evolve earlier in the atmosphere (low $X_{\mathrm{max}}$), and the time distribution of particle arrival, often called width, will be less if the shower occurs lower in the atmosphere (large $X_{\mathrm{max}}$). Also, the logarithm of the electron-to-muon ratio at the ground level is a function of $\ln A$,[32,52] where $A$ is the primary particle atomic mass number. The ratio can be measured to give information about composition and thus $X_{\mathrm{max}}$.

### 1.4.2 Fluorescence Detector

Fluorescence telescopes detect air showers remotely via fluorescence light emitted by atmospheric $N_2$ molecules that have been excited by collisions with passing shower products. TA fluorescence telescopes (Figure 1.11) have a range of about 40 km at the highest energies. Unlike surface detector measurements the fluorescence technique

**Figure 1.10**: Picture of a single Telescope Array surface detector (SD), composed of a communications tower, solar panel for providing power to electronics and plastic scintillator enclosed in sheet metal.

captures the longitudinal and lateral development of the shower with mirrors that focus the light on cameras with photomultiplier tube pixels. Atmospheric calorimetry also gives an absolute energy scale. Because the intensity of UV fluorescence light is low relative to sky noise backgrounds, the fluorescence method only works on clear, moonless nights. The average duty cycle for the TA FD is ~ 10%.[56]

FDs offer the best measurement of $X_{\mathrm{max}}$ because the brightest part of the shower can be seen directly, but lack the exposure of SDs because of a 10% duty cycle. The fluorescence method is viable on cloudless, moonless nights when faint UV signal can pass through the atmosphere without attenuation and light pollution is minimal.

### 1.4.3 Air Shower Radio Emission

Charge excess in co-moving secondary particles (20-30% negative charge excess[57]) near the shower front can produce Cherenkov radiation known as the Askaryan effect.[58] Askaryan radiation is expected to be coherent, polarized and in the microwave band. Low cost light cones on the ground and in the path of the shower will collect Cherenkov radiation in a direct measurement of $X_{\mathrm{max}}$ a composition dependent parameter[59] (see Section 1.3). Primary geometry can be determined from timing

**Figure 1.11**: Picture of Black Rock Mesa (BRM) FD building with the telescope doors open showing the segmented focusing mirrors.

and energy can also be calculated by comparison to Monte Carlo studies.

Geo-magnetic synchrotron emission is another type of radiation produced as air showers propagate through the atmosphere. Shower electrons interact with the Earth's magnetic field to form relativistically forward beamed low VHF signals.[28] Shower front thickness is comparable to the emission wavelength so the benefit of coherent signals are expected.

Ionization electrons in the shower path may emit bremsstrahlung radiation during rapid thermalization by interactions with neutral molecules. Molecular bremsstrahlung radiation (MBR) is incoherent and unpolarized.[27] Just as in fluorescence light emission, MBR is proportional to the number of shower products and therefore directly sensitive to primary energy. Recent measurements of the total microwave emission of air showers indicate polarized waves, which discredits an explanation in terms of molecular bremsstrahlung emission.[60]

### 1.4.4 Cosmic Ray Radar

The idea of radar detection of cosmic rays was first mentioned in the literature in 1941.[29] Anomalous radar events seen by T.L. Eckersley[61] were the impetus for the investigation. This was the first time radar was suggested as a high energy CR detection technique. Blackett and Lovell later used pulsed military radar mounted in air planes (see Ref.[12]). Although they were ultimately unsuccessful proving the technique, their efforts spurred nearly 70 years of similar attempts. Their subsequent ground based radar investigations at Jodrell Bank evolved into the Jodrell Bank radio astronomy observatory.

In 1962 K. Suga proposed[13] searches for ultra-high energy cosmic rays (UHECR) using the radar echo method. This suggestion directly followed his statement that the observable range of CR particles should extend above $10^{20}$ eV. He determined that a scintillator array that could detect such high energies with a reasonable count rate would have to cover an area of 1000 km$^2$, a prescient observation given the size of TA and PAO observatories' large ground arrays. He concluded, "the method of density sampling by large plastic scintillators is basically unsuitable for observing these large events and that essentially different methods must be used for this purpose."

In 2003 a radar experiment was proposed to search for radar echoes alongside the Large Area Air Shower (LAAS) array (see[62]). Unfortunately, no results were reported. The Jicamarca Radio Observatory used pulsed radar in an attempt to detect CR air showers.[63] Regarding detected radar signals, they said, "it has not been possible to conclude that they are caused by ultra high energy cosmic rays." In Shigaraki, Japan, the atmospheric MU-Radar[64] data were searched for short-duration echoes. No convincing evidence has been produced.

Each of these experiments used traditional military pulsed radar, which is a poor choice for detecting rare, random CR events. Additionally, early and recent experiments (with the exception of radar experiments at LAAS) had no means of confirming that features in the data correspond to actual CR events. It is clear that an investigation into CR radar detection needs a continuous wave (CW) (or otherwise constant) carrier and conventional CR detector in close proximity with which data can be correlated.

P. Gorham authored a theoretical paper[65] about the prospect of radar detection. He categorized the scattering properties of EAS relative to carrier frequency and offered some practical analysis about EAS parameters that may be measurable using the radar technique. As I'll demonstrate in Chapter 2, Gorham neglected to consider the unique time-frequency signature expected in the received signal and significantly overestimated the scattering magnitude.

MARIACHI[66,67] investigated bi-static radar scattering of VHF signals from EAS, making parasitic use of commercial television transmissions in Long Island, New York. They found a correlation between receiver antenna waveform and co-located scintillator detector impulses. Unfortunately, further investigation into MARIACHI results is limited because the carrier source is not known (there are many television and radio transmitter stations in the area) and the amount of data collected during the short MARIACHI operational period is very small.

Telescope Array Radar (TARA)[68,69] is the culmination of decades of CR radar detection experiments. We have further developed the bi-static technique by using a dedicated high power, constant wave (CW), low-VHF transmitter in a radio-quiet area, co-located with Telescope Array, the largest conventional cosmic ray observatory in the Northern Hemisphere.

The TARA detector can potentially detect events in coincidence with TA. Positive correlation of radar events with TA data will allow confirmation of the scattering ability of EAS. Nondetection presumably allows only the calculation of upper limits on the scattering magnitude.

In August 2012, TARA broke ground on a transmitter facility located just outside the TA surface detector array. High gain transmitting antennas focus the radar signal over the SD array to receiver antennas located at the Long Ridge FD station. Two 20 kW analog TV transmitters operating in CW mode broadcast a 54.1 MHz radar signal. Experimental radio station WF2XZZ went live in March 2013 with initial 25 kW power output.

In the following chapters I give a complete description of the challenge of CR radar detection and the solutions (both hardware and software) we have engineered to make the first measurement of the upper limit of the CR radar cross-section. First, I cover EAS evolution and plasma physics pertinent to formulation of the problem, including a description of the CR radar echo simulation I have created. In the next chapter I describe the TARA detector that emphasizes co-location with Telescope Array, high gain antennas, continuous wave high power transmitter directly under our control and high sample rate data acquisition (DAQ). Following that, I describe the data and analysis chain. In the last chapter I discuss results in comparison with other experiments and both our brief theoretical expectation and that of others. Finally, I offer my perspective on the prospect of future CR radar detection.

# CHAPTER 2

# EAS RADAR ECHOES

In this chapter I address issues related to the TARA expected received signal. First, I discuss relevant signal fundamentals and the unique challenges radar echo detection presents. Then I discuss reflection mechanisms in the context of atmospheric gases ionized by CR showers and present results from my chirp simulation. The simulation incorporates shower evolution, detector parameters and radar cross-section models from literature. Full detail CORSIKA[6] simulations are shown to agree with the shower evolution models used in the simulation. I then show distributions of simulation results assuming TARA detector parameters.

## 2.1 Bi-static Radar

The bi-static radar equation

$$P_R = \frac{P_T G_T}{4\pi R_T^2}\,\sigma\,\frac{G_R}{4\pi R_R^2}\frac{\lambda^2}{4\pi}\,, \tag{2.1}$$

is the foundation of all radar scattering calculations. $P_R$ is received power, $P_T$ is transmitter power, $G_R$ and $G_T$ are the receiver and transmitter station antenna gains, respectively, $\lambda$ is the radar wavelength, $R_T$ is distance between transmitter and target, $R_R$ is distance between target and receiver, and $\sigma$ is the RCS. Depending on target symmetry, the RCS can be a constant or a function of several parameters.

The RCS is defined as

$$\lim_{r\to\infty} 4\pi r^2\,\frac{S_s}{S_i}\,, \tag{2.2}$$

where $r$ is distance from target to receiver (RX), $S_s$ is the scattered power density and $S_i$ is the incident power density from the transmitter (TX). A limit is included in Equation 2.2 to ensure only the far-field pattern is tested. The RCS is an effective target area whose magnitude depends on the orientation of the target relative to the receiver, target composition and relative size of the target to interrogating signal wavelength. As I will show, the primary difficulty in determining the feasibility of radar detection is in quantifying the RCS for CR air showers.

## 2.2 Properties of EAS-Induced Ionization Columns

Radar detection of cosmic rays depends on charged particle production in the atmosphere. A cascade of interactions composed primarily of electrons and muons occurs when the primary cosmic ray particle collides with molecules in the atmosphere. This is called an Extensive Air Shower (EAS). For a detailed discussion of EAS see, e.g., Heitler[70] or Sokolsky.[71]

### 2.2.1 Air Shower Properties

Some common EAS parameters are primary particle energy $E_0$ (eV), depth $X_{\max}$ (g/cm$^2$) in the atmosphere where the maximum number of particles $N_{\max}$ is reached, and the depth of first interaction $X_0$ (g/cm$^2$). The critical energy $E_c$ (eV) is the energy below which the dominant energy loss mechanism is bremsstrahlung radiation rather than pair production. In air $E_c$ is 81 MeV.[72] When the average particle energy decreases below $E_c$, particle production ceases and the EAS starts to decrease in size. Typically, UHECR are considered to be those with $E_0 > 10^{18}$ eV. We may expect the cosmic ray RCS to depend on $E_0$ because $N_{\max}$ is proportional to $E_0$. Therefore, the received power is related to primary energy.

Gaisser-Hillas[73]

$$N(X) = N_{\max}\left(\frac{X - X_0}{X_{\max} - X_0}\right)^{\frac{X_{\max}-X_0}{\lambda}} \exp\left[\frac{X_{\max} - X}{\lambda}\right] \tag{2.3}$$

is a parameterization of the average shower longitudinal profile, the number of charged shower products as a function of depth $X$ in the atmosphere, where $\lambda$ is interaction length in air. $N_{\max}$, $X_0$, $X_{\max}$ and $\lambda$ only loosely represent their physical counterparts and are typically determined from Monte Carlo simulations using hadronic interaction models. The majority of particles $N(X)$ are free electrons that do not include ionization electrons.

The radial dimension of EAS electrons is given by the Nishimura-Kamata-Greisen (NKG)[74] equation:

$$\rho(r) = \frac{N(X)}{r_1^2}\, f\left(s, \frac{r}{r_1}\right) , \tag{2.4}$$

which gives the number area density as a function of radius, at a specific shower age $s$. Shower age[71] is defined as

$$s = \frac{3}{1 + 2\ln(E_0/E_c)/X/\lambda}\,. \tag{2.5}$$

Also, $r_1$ is the Moliere multiple scattering unit[71,75] and the function $f$ in Equation 2.4 is[76]

$$f\left(s, \frac{r}{r_1}\right) = \left(\frac{r}{r_1}\right)^{s-2} \left(1 + \frac{r}{r_1}\right)^{s-4.5} \frac{\Gamma(4.5 - s)}{2\pi\,\Gamma(s)\,\Gamma(4.5 - 2s)}\,. \tag{2.6}$$

With NKG and the Gaisser-Hillas parameterization one can determine free electron density in three dimensions as the shower evolves.

### 2.2.2 Ionization in EAS

Atmosphere ionization by energetic shower particles is the primary plasma production mechanism. Ionization electrons are quantified by calculating the number of free electrons produced in EAS as a function of shower progress and radius, then using energy deposition models to determine the ionization yield.

An electron produced by the shower will ionize atmospheric molecules until its energy is below the mean ionization energy, $I = 33.8$ eV.[77] The number of ionization electrons $N_{\text{tot}}$ produced over some track length $\ell$ is dependent on the number of particles created by the shower $N(X)$, the mean ionization energy of the atmosphere $I$, atmospheric density $\rho(X)$, and the minimum-ionizing energy loss factor $\frac{dE}{dX}(X)$, all a function of depth $X$ (g/cm$^2$, typically):

$$N_{\text{tot}}(X) = N(X)\,\frac{dE}{dX}(X)\,\rho(X)\,\ell\,I^{-1}\,. \tag{2.7}$$

Energy deposition in the atmosphere $\frac{dE}{dX}(X)$ is obtained from Nerling's parameterization,[78] shown in Equation 2.8, where $\alpha_{\text{eff}}(X)\,N(X) = \frac{dE}{dX}(X)$. Together with coefficients (Table 2.1), $\alpha_{\text{eff}}$ is given as a function of shower age $s$:

$$\alpha_{\text{eff}}(s) = \frac{c_1}{(c_2 + s)^{c_3}} + c_4 + c_5 \cdot s\,. \tag{2.8}$$

Atmosphere ionization occurs more rapidly in regions where the charged shower products' density is high. Therefore, the distribution of ionization electrons created by shower products should follow the lateral distribution (NKG).

**Table 2.1**: Constants in the Nerling parameterization[78] (Equation 2.8) of EAS energy deposit in the atmosphere.

| | |
|---|---|
| $c_1$ | 3.90883 |
| $c_2$ | 1.05301 |
| $c_3$ | 9.91717 |
| $c_4$ | 2.41715 |
| $c_5$ | 0.13180 |

To verify NKG at $X_{\text{max}}$, we have generated an unthinned CORSIKA[6] with QGSJETII[79] hadronic interaction model shower at $10^{19}$ eV. The ionization electron density is calculated by summing the number of ionization electrons in a given radial bin $N_r$ produced by shower-generated charged particles, which consist primarily of energetic electrons. Each electron has simulated energy and radial distance from the shower axis, which defines an area determined by the radial bin size. This energy/area $E_\rho$ is multiplied by the ratio of atmospheric density at ground level (roughly the location of $X_{\text{max}}$ for TA for a $10^{19}$ eV shower) to the radiation length in air $\rho_{\text{air}}/l$ ($l$ is in units of g/cm$^2$), which is the inverse of the distance a particle will travel that results in an energy reduction of all but $1/e$. Resulting energy density is divided by the mean ionization energy per electron pair $I$ and multiplied by $1 - e^{-1}$ to account for the radiation length loss per unit of distance travelled. At $X_{\text{max}}$, ionization loss per radiation length is equal to the electron energy.[77]

The summation algorithm, with explicit units, that produces the total ionization electrons in a radial bin $r$ is

$$\rho_{\text{ion,r}}\left[\text{cm}^{-3}\right] = \sum_{i=0}^{N_r-1}\left(E_{\rho,i}\left[\frac{\text{eV}}{\text{cm}^2}\right]\right)\cdot\frac{\rho_{\text{air}}\left[\frac{\text{g}}{\text{cm}^3}\right]}{l\left[\frac{\text{g}}{\text{cm}^2}\right]}\cdot(1-e^{-1})/I\,[\text{eV}]\;. \tag{2.9}$$

It is assumed that a radial distance from shower core and area represented by the radius can be computed from simulation output for each charged particle. A comparison plot showing good agreement between free electron density as predicted by CORSIKA and GH/NKG is shown in Figure 2.1. Ionization electron density can be obtained by substituting the NKG density (Equation 2.4) for $N(X)$ in Equation 2.7. In the remaining sections, electron quantity and lateral distribution are calculated exclusively with GH and NKG.

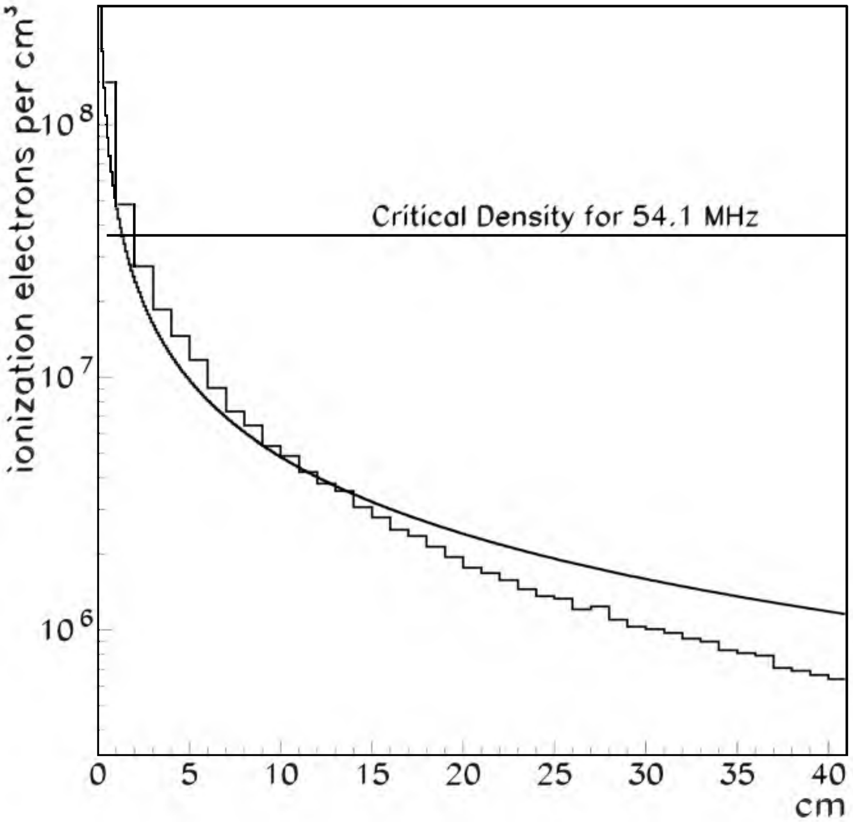

**Figure 2.1**: A CORSIKA (histogram) vs. Gaisser-Hillas and NKG (curve) comparison of ionization electron density as a function of radius near $X_{\max}$ for a $10^{19}$ eV vertical shower. Agreement is good near the core where electron density is highest.

## 2.3 Plasma Physics

### 2.3.1 Neglecting Electron-neutral Collisions

Natural longitudinal oscillations occur in ionized gases because of Coulomb interactions between free electrons. The free electron plasma frequency can be calculated using first principles. Consider a macroscopically neutral plasma whose density is low such that collisions are ignored. An incident electromagnetic field with frequency $\omega_r$ will cause the electrons to oscillate according to the equation of motion

$$e\mathbf{E} - m\frac{\partial^2 \mathbf{r}}{\partial t^2}, \tag{2.10}$$

where $\mathbf{r}$ is the electron displacement vector giving the position caused by the incident field relative to where the electron would be in the absence of a disturbance. Both $\mathbf{E}$

and $\mathbf{r}$ have the harmonic component $\exp(-i\omega_r t)$. The product of plasma density $N$, displacement $\mathbf{r}$, and the electron charge $e$ is the polarizability $\mathbf{P}$, which is proportional to permittivity of the medium[80]

$$\epsilon\mathbf{E} = \epsilon_0\mathbf{E} + \mathbf{P}\,. \tag{2.11}$$

Using $Ne\mathbf{r} = \mathbf{P}$ and multiplying both sides of Equation 2.10 by $Ne$, we have

$$N\mathbf{E}e^2 = -\omega_r^2 m\mathbf{P}\,. \tag{2.12}$$

The index of refraction $n$ is the ratio of speed of light in free space to that in the medium $\sqrt{\epsilon/\epsilon_0} = \sqrt{1 + \mathbf{P}/(\mathbf{E}\epsilon_0)}$. Substituting the previous expression solved for $\mathbf{P}$ in Equation 2.12,

$$n^2 = 1 - \frac{Ne^2}{\omega_r^2\epsilon_0 m} = 1 - \frac{\omega_e^2}{\omega_r^2}. \tag{2.13}$$

Neglecting geomagnetic or collisional effects, the plasma frequency is

$$\omega_e \equiv \sqrt{\frac{Ne^2}{\epsilon_0 m}} \quad [\mathrm{rad/s}]\,. \tag{2.14}$$

The index of refraction in this case is either real or imaginary, but not complex. If the plasma frequency is greater than the wave frequency, $n$ is real. Refraction angle is determined via Snell's law.

Plasma frequency greater than the incident wave frequency results in a purely imaginary index of refraction, meaning that beyond a certain skin depth the waves cannot penetrate—the electric field is reflected. Such a plasma is called overdense. If the sounding wave frequency is larger, the index of refraction is real so the transmitted wave is refracted in the underdense regime.

Maxwell's equations can be manipulated to form the wave equation. For example,

$$\frac{d^2E_{\mathrm{x}}}{dx^2} + k^2n^2E_{\mathrm{x}} = 0 \tag{2.15}$$

represents a plane wave travelling in the z direction, with $k = \omega/c$[a]. The solution is $E_{\mathrm{x}} = E_0\exp[i(\omega_r t - knx)]$. When $\omega_r < \omega_e$, $n^2 < 0$, the wave $E_{\mathrm{x}} =$

---

[a] The constant in the second term is originally $\omega^2\,\epsilon\mu$, but the assumption can be made for most materials that $\mu = \mu_0$. Permittivity $\epsilon$ can be written $\epsilon_0\,n^2$ which gives the constant $n^2\,\omega^2\epsilon_0\mu_0$. The speed of light in vacuo $c = 1/\sqrt{\epsilon_0\mu_0}$. Therefore, the constant can be written $k^2n^2$ where $k$ is the wave number in free space.

$E_0 \exp(i\omega_r t) \exp(-k|n|x)$ is attenuated in the plasma and reflected. Otherwise $n^2 > 0$ so the wave can penetrate the ionized gas region in which there may be secondary scattering mechanisms that can reflect the signal. This splits the classification of the scattering center into two regimes, underdense and overdense. A plasma is overdense when incident waves are reflected and the index of refraction is purely imaginary. Waves in an underdense plasma are refracted when the index of refraction is real or complex.

In the underdense regime, Thomson scattering is a coherent scattering mechanism that may interfere constructively or deconstructively at the receiver, depending on the size of the scattering volume relative to the radar wavelength. Radar waves penetrate the CR shower and scatter off free electrons by exciting them with the electric field component of the wave. The Thomson scattering cross-section for an electron is[80]

$$\sigma_T = \frac{8\pi}{3}\left(\frac{e^2}{4\pi\epsilon_0 m_e c^2}\right)^2 . \tag{2.16}$$

UHECR air shower particles exist up to several kilometers from the core, though at very low density following the trend in Figure 2.1. Therefore, Thomson scattering is negligible from large radius parts of the shower. Approximately 80% of shower particles are contained within a 100 m radius,[14] where scattering from a 5.5 m wavelength (54.1 MHz, TARA radar frequency) will interfere, possibly destructively.

Above a few centimeters radius from the shower axis $\omega_r > \omega_e$ (see Figure 2.2). Charged particle density near the shower core is accurately described by NKG. This has been measured directly for PeV-level showers.[81] The plasma is overdense only at small radii ($\sim 1$ cm).

### 2.3.2 Including Electron-neutral Collisions

As free electrons are jostled by thermal motion of neutral molecules, they are prevented from radiating coherently. Interactions with ions are not considered because of the relatively few ionization electrons and corresponding parent ions compared to neutral molecules. Very near the core, ionization electron density reaches $10^8\ \text{cm}^{-3}$ (see Figure 2.2), whereas atmospheric density at 4.5 km above sea level and 300 K is $N/V = P/kT = 10^{17}\ \text{cm}^{-3}$, which gives a neutral molecule to electron ratio of $10^9$.

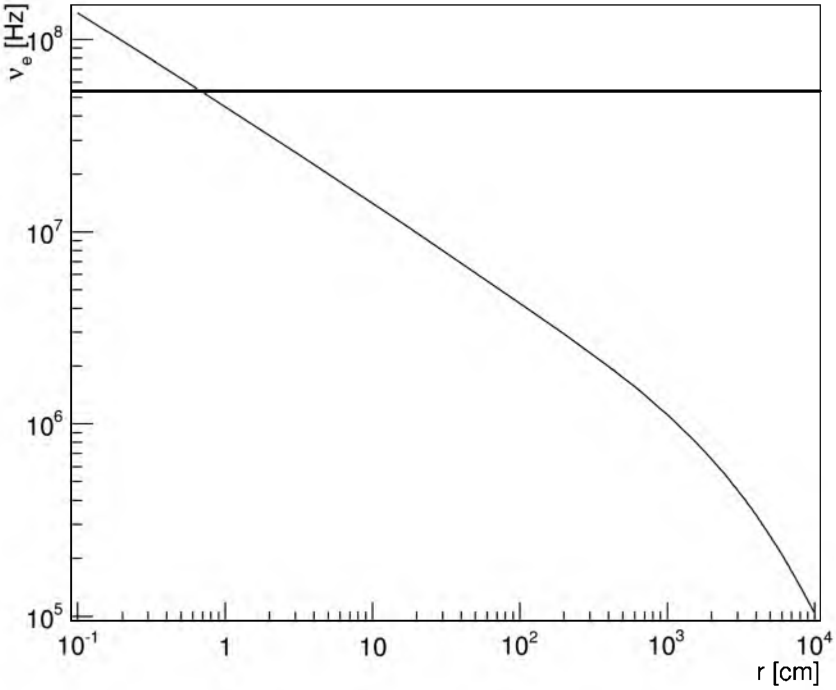

**Figure 2.2**: Plasma frequency as a function of radius at $X_{\text{max}}$ for a $10^{19}$ eV shower calculated using Gaisser-Hillas and NKG parameterizations. Gaisser-Hillas parameters were averages of values obtained by CORSIKA simulations. The horizontal black line corresponds to the TARA radar carrier frequency at 54.1 MHz.

Coherent scattering decreases as the effective collision frequency climbs relative to the radar frequency because interactions with neutral particles occur many times each cycle. If one includes collisional effects and assumes that all of an electron's excess momentum gained from interaction with the radar wave is lost with each collision with a molecule, the equation of motion is written

$$e\mathbf{E} = m\frac{\partial^2 \mathbf{r}}{\partial t^2} - m\nu\frac{\partial \mathbf{r}}{\partial t}\,. \tag{2.17}$$

Following the same procedure as before, the equation for the index of refraction becomes

$$n^2 = 1 - \frac{\omega_e^2}{\omega_r^2(1 - i\nu/\omega_r)}\,. \tag{2.18}$$

When the effect of electron-neutral collisions is included, the index of refraction is complex. In general $n \equiv \mu - i\chi$. The absorption coefficient $\chi$ characterizes exponential plane wave amplitude decay as a function of distance. $\mu$ is the index of refraction. Let $A = (\omega_e/\omega_r)^2$ and $B = \nu/\omega_r$, then

$$n^2 = 1 - \frac{A}{1+B^2} - i\frac{AB}{1+B^2} = a + ib\,. \tag{2.19}$$

By the square root formula for complex numbers[82] the real and imaginary components of $n$ are

$$\mu = \sqrt{\frac{(a^2+b^2)^{1/2}+a}{2}}\,, \quad \chi = -\sqrt{\frac{(a^2+b^2)^{1/2}-a}{2}}\,. \tag{2.20}$$

In the case of CR shower plasmas, the free electron density is low compared to neutral molecules, and therefore the collision rate $\nu$ between electrons and neutral particles is high relative to the radar frequency. Electron scattering is damped by collisions with neutral particles. Collisional damping has often been neglected in the CR radar literature. As will be shown, this effect is large and greatly impacts the viability of CR radar.

When collision frequency is large compared to the wave frequency, very little energy is extracted from the wave. From the perspective of the incident field, rapid collisions effectively "pin" free electrons in place, preventing work from being done.[83] Partial scattering is only expected for high plasma frequencies, or when the sounding frequency is the same order of magnitude as the collision frequency. Even near the core, when the plasma frequency exceeds the sounding wave frequency (see Figure 2.2), scattering is highly attenuated.

Figure 2.3 shows collision frequency in air at varying altitudes as calculated by several different authors. It also includes a simple mean free path estimate that agrees fairly well with the other results. All collision frequency values beside the mean free path result were calculated using a standard form of the collision frequency which is a function of the momentum transfer cross-sections and electron velocity:[84]

$$\nu(v) = v\left(N_{\mathrm{N}_2} Q_m^{\mathrm{N}_2}(v) + N_{\mathrm{O}_2} Q_m^{\mathrm{O}_2}(v)\right) \tag{2.21}$$

where $Q_m(v)$ is the momentum transfer cross-section as a function of velocity and $N$ is the mass density.

Vidmar's values[10] come from a simulation which includes experimental values of air density and temperature as a function of altitude, momentum transfer collision

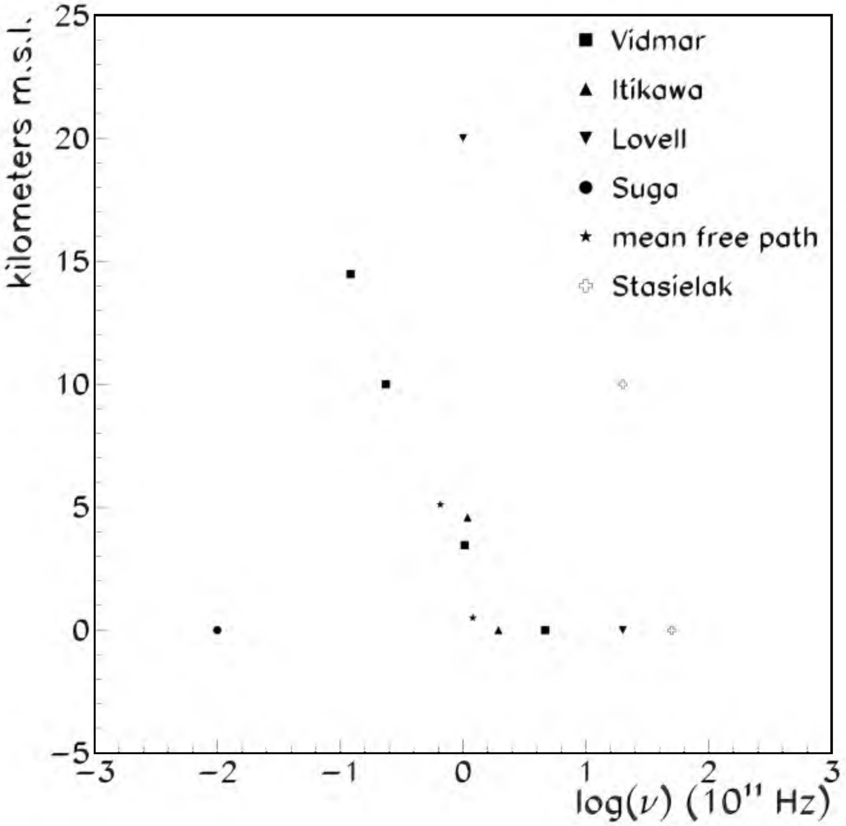

**Figure 2.3**: Survey of estimates of electron-neutral collision frequency as a function of altitude. Data points are from Vidmar,[10] Itikawa,[11] Lovell,[12] Suga,[13] Stasielak et al.,[14] and the mean free path points are calculated by dividing mean electron speed by the mean free path.

rates as a function of altitude, and recombination/attachment rates. Collision rates are reported for electrons with temperatures $T_e = 300, 400, 500$ K. Itikawa[11] calculates the collision frequency from experimental values of the momentum transfer cross-section for electron temperatures up to 5000 K. The Lovell values[12] are given without justification, and are included mainly for historical significance. Suga's value[13] is also given without justification. Stasielak et al.[14] take a different approach that approximates the ionization electron energy distribution as Maxwellian with $T_e = 1.5 \times 10^5$ K (13 eV), then calculates the average collision frequency over the velocity distribution. At similar altitudes the collision frequencies vary over one order of magnitude.

At $X_{\max}$ the average shower particle energy is $E_c = 81$ MeV. The average energy of ionization electrons increases with the energy of the incident particle.[85] In the limit where the secondary electron distribution has a substantial portion of relativistic energies, the collision frequency may decrease with energy due to decreasing momentum transfer cross-section.

$Q_m^{\mathrm{N}_2}$ decreases nearly two orders of magnitude for each decade increase in electron energy above 1,000 eV.[85] High energy momentum transfer data do not exist in the literature. Assuming this trend continues, the product $vQ_m$ decreases as the relativistic regime is approached. In this case, we overestimate the collision frequency by assuming a near thermal secondary electron energy distribution.

Without high energy cross-section data, we estimate the damping magnitude by assuming the electron-neutral collision rate in air is $\sim 10^{11}$ Hz, large compared to our 54.1 MHz radar wave (see Chapter 3). Plasma frequency is also small compared to $\nu$, so we expect significant damping at all shower radii. The large discrepancy in frequencies also justifies the neglect of geomagnetic effects which have been ignored because the cyclotron frequency $\omega_B = e|B|/m \simeq 5 \times 10^6$ Hz $\ll \nu = 10^{11}$ Hz.

A quick comparison between Equations 2.10 and 2.17 elucidates the extreme level of damping caused by such a large discrepancy in radar frequency and effective collision frequency. After substituting terms and taking derivatives the right hand side of the equations become $-m\omega_r^2\mathbf{r}$ and $-m\omega_r^2\mathbf{r}\left(1 - i\frac{\nu}{\omega_r}\right)$. We define an effective mass in the second expression $m_{\text{eff}} = m\left(1 - i\frac{\nu}{\omega_r}\right)$. Scattering power is proportional to $\mathbf{a} = \partial^2\mathbf{r}/\partial t^2$ and $\mathbf{a} \propto 1/m$, so reduction in scattering power from collisional damping is

$$\left|\frac{m}{m_{\text{eff}}}\right|^2 = \frac{1}{1 + \left(\frac{\nu}{\omega_r}\right)^2} \simeq \left(\frac{\omega_r}{\nu}\right)^2 . \tag{2.22}$$

For relevant values $\omega_r = 10^8$ Hz and $\nu = 10^{11}$ Hz, damping in power is of order $10^{-6}$.

Our result is not consistent with P. Gorham's paper on the subject.[65] There are two fundamental differences between Gorham's assumptions and ours that give disparate results. First, the effect of collisional damping is ignored in Gorham. The second difference is the large electron lifetime used in his calculations. It is stated that $\tau \gtrsim 10\,\mu$s and greater at higher altitudes and possibly as long as 20 ms at 10 km, which is larger—by a factor of one million—to values found in.[10,86,87] His RCS estimate is therefore very large, $\sigma_{\rm EAS} = 10^4$ m$^2$ for a 100 EeV shower perpendicular to a 10 m wavelength radar wave.

Including collisions, the plasma is never truly overdense, where the index of refraction is purely imaginary. Rather, both refraction and attenuation in plasma will occur. Portions of the shower only approach the overdense regime when $\omega_r \sim \nu$ and $\omega_r > \omega_e$. Given TARA transmitter frequency and collision frequency in air ($\omega_r \ll \nu$ and $\omega_r > \omega_e$ only at small radii), CR showers will never appear overdense. In this case Thomson scattering is the primary scattering mechanism, though it will be strongly damped by collisions.

Figure 2.4 shows $\mu$ and $\chi$ plotted using $10^{11}$ Hz collision frequency for three different plasma frequencies $\omega_e = (10^{-3},\ 10^{-2},\ 10^{-1})\,\nu$ over a sounding frequency range relevant to our 54.1 MHz radar. The complex index of refraction $n$ shows that the real part of $n$, the part that affects refraction, never deviates from unity at TARA radar frequency 54.1 MHz and plasma frequency $\omega_e$ equal to $10^{-3}\,\nu$. The imaginary part of $n$, proportional to absorption in the medium, is only about 1/1000. Scattering is very small even when the plasma frequency meets and exceeds the radar frequency ($\omega_e \simeq 10^{-3}\ \nu$).

The plots in Figure 2.4 contain all the information necessary to conclude that EAS scattering is very small—the real part of the index of refraction never appreciably moves away from unity and the imaginary part is very small so absorption is also negligible. Stasielak et al. first consider absorption from the perspective of electrical conductivity of the plasma medium, from which they derive the refractive index and subsequently determine the absorption coefficient $\alpha_{\rm abs}$ from the imaginary part. Using $E_0 = 100$ EeV and reasonable values for $\omega_p$ and $\nu_c$, plasma frequency and collision frequency (their notation), they estimate $\alpha_{\rm abs} < 3$ dB/km near the shower core ($\sim$ cm diameter) and less than 0.3 dB/km for larger radii. Given the high density radius is small and remaining shower plasma density decreases above that, absorption is ignored. We have also ignored the effect of absorption in the RCS model proposed in Section 2.5.2.

Stasielak et al. continue with a calculation of reflected power using the Fresnel

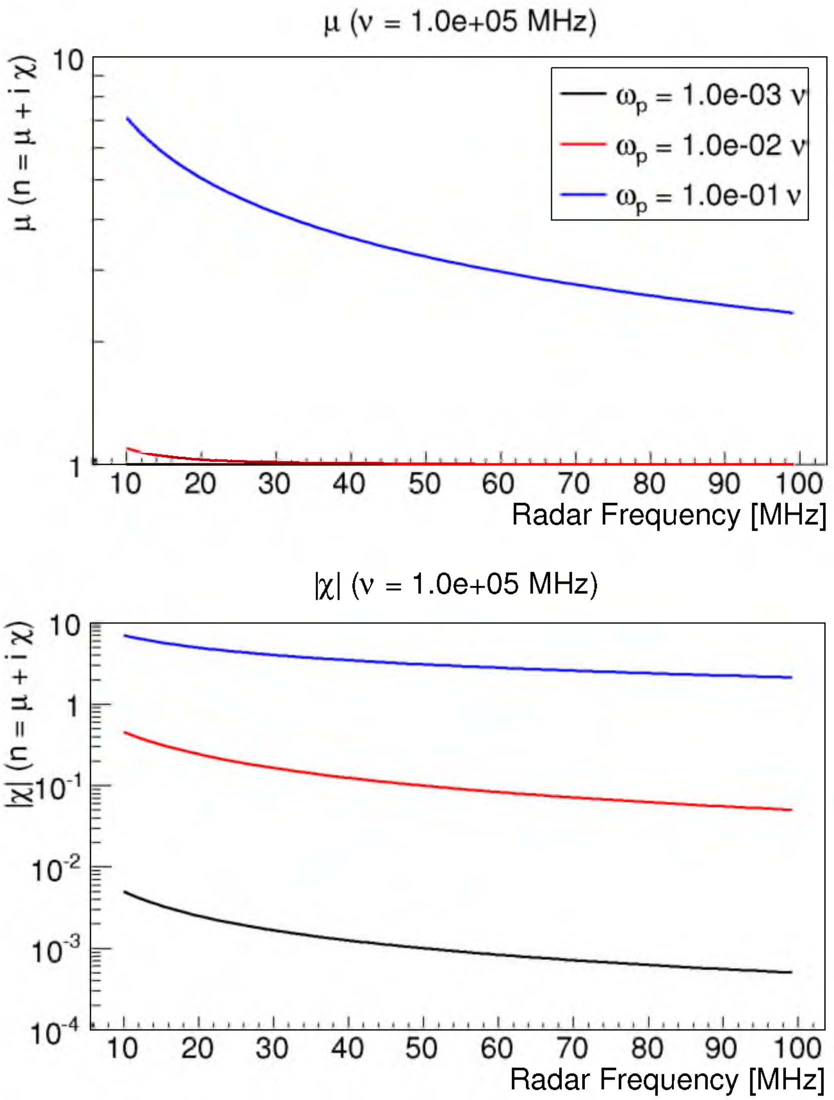

**Figure 2.4**: Real and imaginary parts of the index of refraction ($n = \mu - i\,\chi$) with $10^{11}$ Hz collision frequency each with $\omega_e = (10^{-3},\ 10^{-2},\ 10^{-1})\,\nu$. The TARA radar frequency is 54.1 MHz. Note that the red and black curves in the top plot are very close to one.

formula,

$$R_p = \left| \frac{n - n_p}{n + n_p} \right|^2 . \tag{2.23}$$

$R_p$ for two cases is considered. The first case assumes $\nu_c = 2$ THz, $\nu = 1$ MHz (radar frequency), $\nu_p = 100$ MHz, distance from the shower axis $r_L$ is of order a few centimeters and $E_0 = 100$ EeV, for which Equation 2.23 gives $R_p = 6 \times 10^{-5}$. In the second case all parameters are the same except $\nu_p$, which is much less, and $r_L = 1$ m;

$R_p$ drops to $10^{-11}$. Collisions between electrons and molecules reduce reflection to one part in 10,000 even in the case where $\nu_p/\nu = 100$.

Scattering is simulated by Stasielak et al. with the Thomson scattering cross section $\sigma_T$ modified by the reduction in power, proportional to particle acceleration, derived from the equation of motion. Their procedure is the same as that in Section 2.3. I arrive at a damping factor in Equation 2.22 which is equal to the damping factor in their result for the reduction in RCS

$$\sigma_{sc} = \left(\frac{\omega}{\nu_c}\right)^2 \sigma_T \, . \tag{2.24}$$

Finally, they give RCS versus time for a 1 EeV shower perpendicular to the direction of a $\nu = 1$ MHz radar wave is plotted for several different integration limits. Collision frequency is $\nu_c = 4.5$ THz, much greater than the value we use (see Figure 2.3), typically 0.1 THz. In the maximum case, all parts of the shower are integrated from very near the shower core to the radius wherein 95% of plasma electrons are located. Only a very small longitudinal portion of the shower is considered, where the plasma density is greatest. At the maximum of the 95% curve, $\sigma_{\mathrm{EAS}} = 4 \times 10^{-10}$ cm$^2$, 174 dB below Gorham's result.

## 2.4 Forward Enhancement

Depending on radar frequency and the scattering model, bi-static radar may have a forward scattering enhancement relative to the mono-static case. When $a/\lambda \ll 1$, no forward scattering benefit is obtained. A conductive thin wire with radius of order one centimeter (the collision-less overdense region radius) is much smaller than the wavelength of VHF radar waves (54.1 MHz inclusive), so no appreciable forward scattering enhancement is expected. Figure 2.5 shows a comparison of metallic cylinder forward scattering radiation patterns as a function of the angle from the forward direction for several different cylinder radii expressed as fractions of the radar wavelength. The diffraction peak vanishes when $a/\lambda$ is below 0.1.

Thomson scattering in a region where the majority of shower electrons lie ($\sim$ 100 m) would also not be expected to have a scattering enhancement. Forward enhancement is only expected when the characteristic size of the target is the order of the radar wavelength.

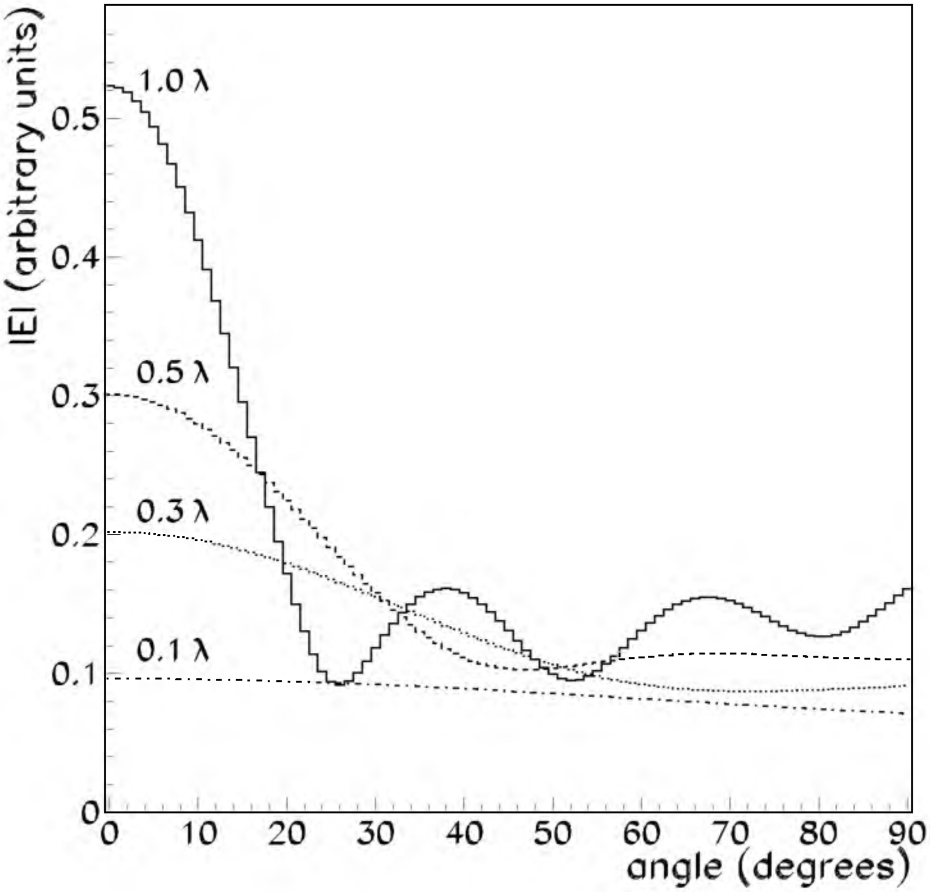

**Figure 2.5**: Relative scattered electric field[15] magnitude for several different cylinder radii, expressed as fractions of the incident wavelength, as a function of angular deviation from the forward scattering direction.

## 2.5 Simulation

### 2.5.1 Frequency Modulation

A simple plasma physics model has been discussed which includes collisional effects. In the frequency space under consideration, the model predicts that CR air showers are weak scattering targets. Section 2.3.2 gives a calculation of the order of magnitude of damping based on the radar wave frequency and collision rate in air. Section 2.5 describes the model-independent frequency dynamics of received EAS radar echoes and Section 2.5.2 introduces a RCS model used for simulating the collision-less overdense region.

Energetic shower particles travel in a disk coaxial with the EAS direction of propagation. Less energetic products are quickly thermalized. From the perspective of a radar system, an EAS is a disk moving through the atmosphere at the speed of light, leaving a quickly fading plasma trail. I have created a simulation that uses the bi-static radar equation, TARA detector geometry and known EAS dynamics to calculate the received signal based on a scattering model, which will be discussed shortly. From the simulation perspective, the superposition principle indicates that multiple scattering path lengths from different points along the shower track (see Figure 2.6) result in summation of scattered rays of the same frequency but with different phase.[88]

Continuing with the simulation perspective, during a given time step $\delta t$ at time $t_i$, the bi-static radar equation is applied to each longitudinal shower segment (each with length $c\,\delta t$) from which light could have reached the receiver. Both the shower particles and radar echo move at the speed of light, so a segment $j$ is included if the shower progress $\mathcal{P}_i$, the distance the shower has travelled since first interaction, is greater than the distance from segment $j$ to the receiver $R_{R,j}$ minus the progress of the shower at segment $j$, $\mathcal{P}_j$. The plasma state of segment $j$, and thus RCS properties, are that of the segment at retarded time $t'_{i,j} = (\mathcal{P}_i - R_{R,j} - \mathcal{P}_j)/c$. Notice the retarded time is not $(\mathcal{P}_i - R_{R,j})/c$, which gives the time when scattered light from segment $j$ left the segment, but does not give its age. Segment age must be tracked properly to include plasma dissipation.

Consider the EAS to be a chain of longitudinal segments. Each segment has magnitude and phase determined by the segment's total path length, radar wavelength, RCS at the current point in the shower, shower geometry relative to the TX and RX and geometrical antenna factors. The integrated contribution of all segments $j$ is the received signal at time $t_i$. Complex phase factors are included in the sum.

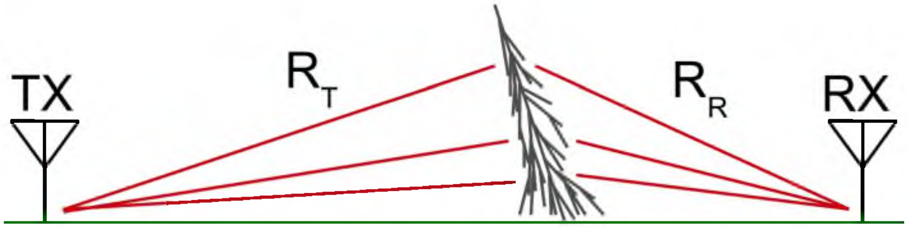

**Figure 2.6**: Contributions from paths of varying lengths (red), TX → target → RX, summed at the receiver result in a chirp signal (bi-static configuration).

The dynamical received signal will be a chirp signal,[88] which has time-dependent frequency. Furthermore, signal components scattered early in shower evolution when the RCS is small and path length is large will have low amplitude, while signals scattered near $X_{\mathrm{max}}$ (typically 3-5 km from ground level at the location of the detector) will be from portions with larger RCS and shorter path lengths so the expected received signal later in the shower is large. Section 2.5.2 is devoted to a discussion of the received power.

Some of the expected radar echo chirp properties can be understood using geometrical arguments. Let $L$ be the total path length $R_T + R_R$ and $L' = dL/dt$ the instantaneous rate of change of path length. The magnitude of $L'$ is proportional to chirp rate. If $L' > 0$ the received frequency is less than the radar frequency and if $L' < 0$ the received frequency is greater than the radar frequency. Time-dependent frequency is analogous to Doppler shifted light or sound waves, though not identical because the wavelength of scattered radar carrier is fixed at the receiver—only combined phase changes.

Typical CR air showers, which start far away and move toward the Earth's surface, albeit with occasionally large incidence angles, produce a down chirp (decreasing frequency) as long as the core location is between TX and RX. One can imagine geometries in which $L'$ approaches zero, then becomes positive as the shower crosses the line connecting TX and RX. In this case, the chirp frequency will first match, then descend below the radar frequency. Neutrino air showers originating close to the earth's surface or low in the atmosphere could produce down chirps that start below the radar frequency and descend to lower frequencies as the shower evolves.

Just as signal amplitude gives information about the primary, the chirp signature contains information about the air shower geometry. With the exception of lateral symmetry about a plane perpendicular to the ground and containing the TX and RX points, and a rotational symmetry about a line connecting the transmitter and receiver, chirp signals are unique.

Figure 2.7 shows three canonical chirps with different TX → RX baselines. Canonical chirps are simulated radar echoes from small zenith angle air showers located midway between transmitter and receiver. Unless otherwise stated, the primary

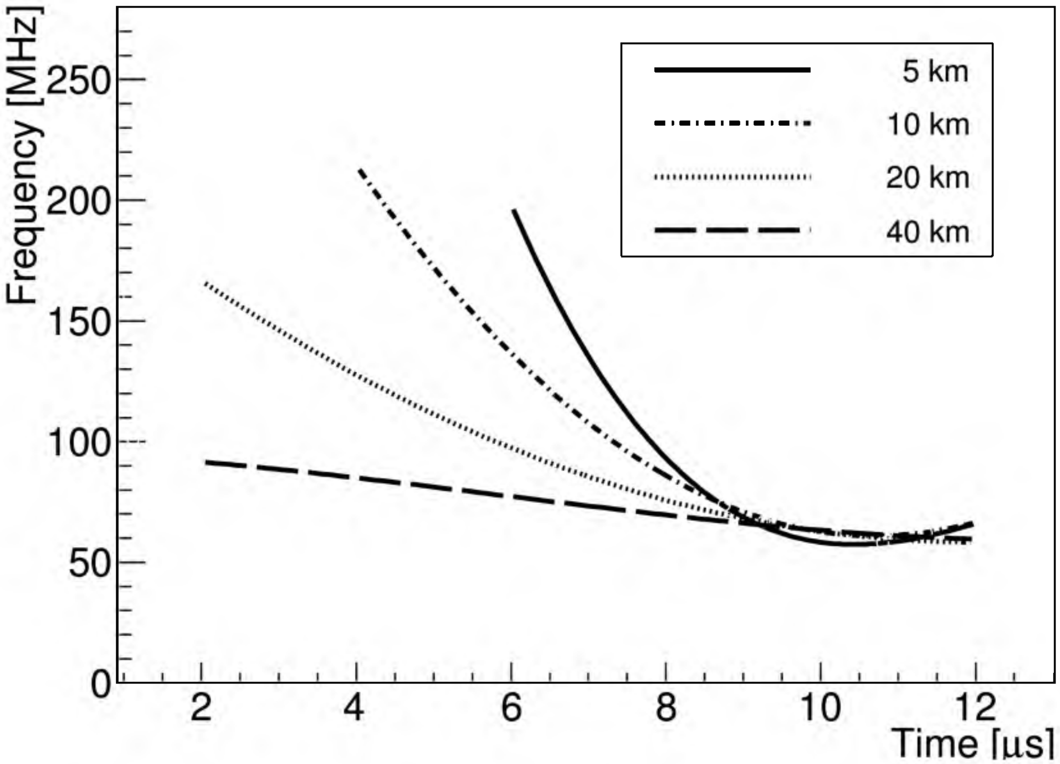

**Figure 2.7**: Simulated chirp spectra fits to highest amplitude frequency component for four different geometries. Each simulation represents a vertical, 10 EeV CR shower located midway between transmitter and receiver. TX → RX separation distances are shown on the legend. Both the time offsets and absolute frequency ranges have been justified for direct chirp rate comparison.

energy is 10 EeV. The lines are fits to the highest amplitude frequency component in each time bin. Amplitude is neglected on the plot, so the length of the fit line is not proportional to duration. However, I define duration to be the time that received power is within 10 dB of maximum. Likewise, bandwidth is defined as the frequency difference between the above and below maximum 10 dB power points. Duration for the four simulations are 4.7 $\mu s$, 7.1 $\mu s$, 12.4 $\mu s$ and 21.7 $\mu s$ for the 5 km, 10 km, 20 km and 40 km separation distances, respectively. Their bandwidths are 63 MHz, 59 MHz, 63 MHz and 62 MHz. Bandwidths are similar because the steepness of the chirp slope compensates for short duration. In practice, short-baseline chirps would be difficult to detect because their high frequencies imply correspondingly high bandwidths.

A very basic echo simulation that only tracks the phase of a point (determined by total path length $L$) with speed $c$ will correctly yield the primary component of the chirp signature, frequency as a function of time. As an example, I have generated three different radar echoes using the simulation code with different electron lifetimes and antenna gains. Figure 2.8 show spectrograms of the simulated waveforms. Spectrograms are three-dimensional: time in $\mu$s on the horizontal axis, frequency in MHz on the vertical axis and Power Spectral Density (PSD) in dBm/Hz on the $z$ or color axis. PSD is the received power in dBm (dB relative to mW) divided by the Fourier transform band used to calculate the spectrogram. It is useful in comparing received power in an absolute way between different measurements and Fourier transform window sizes. Simulated waveforms used in each of the figures have been superimposed on Gaussian noise to hide features caused by aliasing.

The first two simulations use constant value cross-section; the third uses a thin-wire approximation model for the RCS (see Section 2.5.2 for more detail) in combination with shower evolution models. The top plot in Figure 2.8 shows a spectrogram for a very short free electron lifetime, which means there is only one scattering path length per time step. It can be thought of as a very small metallic (re: scattering) target that moves at the speed of light. In the second simulation (Figure 2.8, middle plot) a very long lifetime is used such that the shower can be thought of as a thin metallic cylinder that starts high in the sky and grows toward the ground at the speed of light, its scattering properties remaining intact for the duration of the simulation. The last spectrogram (Figure 2.8, bottom plot) is from the full radar echo simulation, which uses antenna radiation pattern, shower evolution models and the thin-wire approximation as the radar cross-section. The frequency at maximum amplitude $F_{\mathrm{max}}$ vs. time is the same in all three plots. Absolute power varies widely, as expected from different targets. Figure 2.9 shows $F_{\mathrm{max}}$ vs. time for each of the three simulation results on the same plot. One concludes that the chirp frequency signature is not dependent on RCS model.

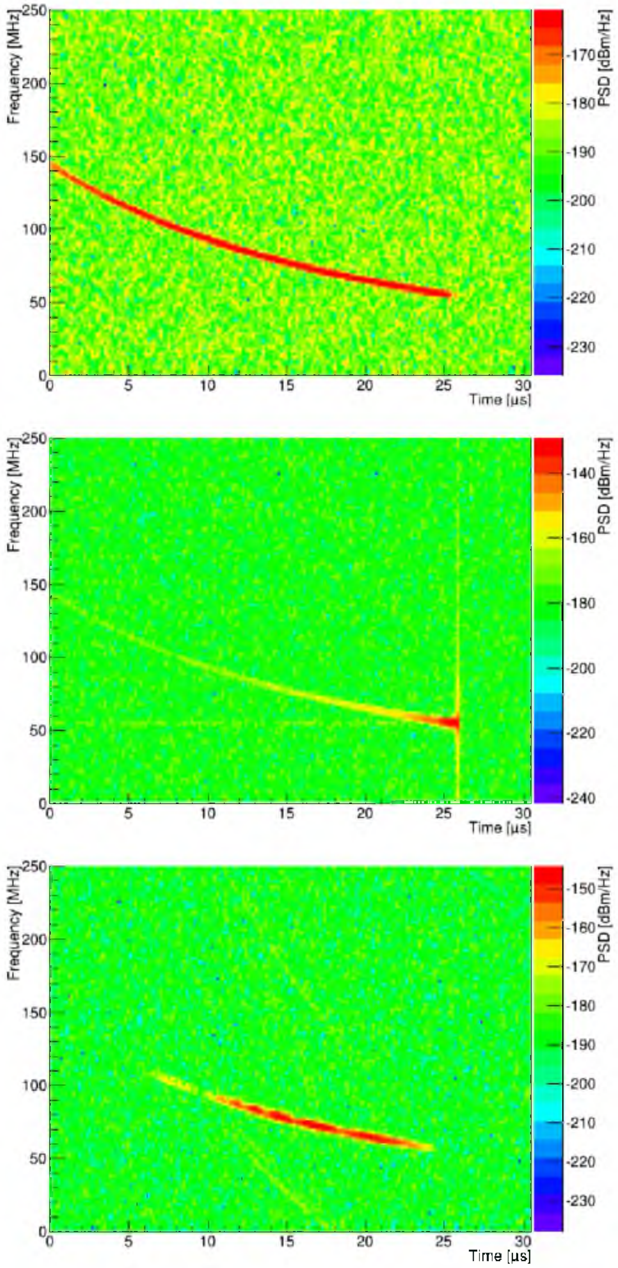

**Figure 2.8**: Spectrograms showing simulated radar echoes for a shower midway between transmitter and receiver and inclined 30° out of the TX/RX plane. Top: Electron lifetime is fixed at 1 ns and antenna gain is held constant. This configuration simulates a small scattering object travelling at the speed of light toward the ground. Middle: Electron lifetime is fixed at 100,000 ns and antenna gain is held constant. This configuration simulates a scattering rod beginning high in the atmosphere and growing toward the ground at the speed of light. Bottom: Electron lifetime is determined from empirical models and RCS comes from the thin-wire approximation (Section 2.5.2) and shower evolution models. Antenna gain is determined from lookup tables generated by NEC.[16] This configuration simulates a cosmic ray radar echo.

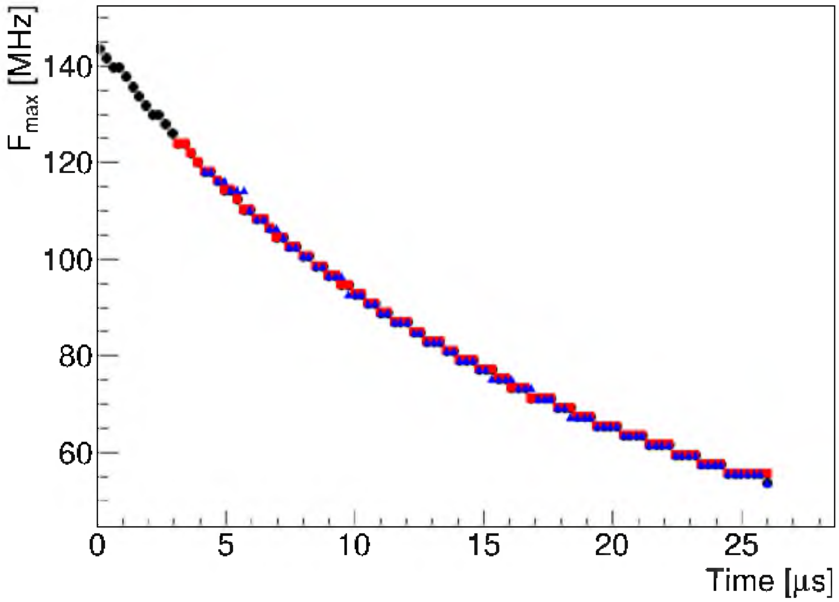

**Figure 2.9**: Plot showing $F_{\max}$ vs. time for the three simulated echo waveforms shown in Figure 2.8. Black points represent $F_{\max}$ for the short lifetime waveform. Red and blue points represent $F_{\max}$ for the long lifetime and full simulation waveforms, respectively.

### 2.5.2 Received Power

The principal component of the echo simulation is the bi-static radar equation 2.1, which gives the received power as a function of detector/target geometry, transmitter/receiver antenna parameters, transmitter power and sounding wavelength. A simulation time step $\delta t$ is chosen such that $c\delta t \ll \lambda$, then the shower is considered to be a string of longitudinal segments of length $c\,\delta t$ as described in the previous section. At time $t_i$, the amplitude of each longitudinal segment (including phase) is included in the sum

$$V_{R,i} = \sum_j \sqrt{P_j(t_i')\,Z}\;. \tag{2.25}$$

$P_j(t_i')$ is the received power from the bi-static radar equation 2.1 calculated at the retarded time and $Z$ is the impedance of the receiving antenna. $V_{R,i}$ is the received voltage at time $t_i$. According to the superposition principle, it is correct to sum the *voltage amplitude* at the receiver, not the received power.

As described, the echo simulation is quite simple. The challenge lies in choosing realistic scattering, shower evolution and plasma description models. Several effects are included to make the simulation more accurate. Gaisser-Hillas parameters are coded as functions of primary energy $E_0$ using CORSIKA Monte Carlo data (Zech[89]). The NKG function combined with Nerling's parameterization[78] of $\alpha$ (see Equation 2.8) give the ionization lateral distribution. Atmospheric density as a function of altitude is obtained from the 1976 Standard Atmosphere.[90] Electron lifetime as a function of altitude comes from Vidmar.[10] The collision-less overdense radius is determined from the lateral distribution, which is used in the thin-wire approximation to give the segment cross-section. Transmitter and receiver radiation patterns have been simulated[16] and confirmed observationally (see Chapter 3).

Shower products recombine or attach quickly in the atmosphere. The electron recombination/attachment lifetime for near-thermal electrons (500 K) $\tau \simeq 10$ ns.[10,86] Ionization electrons will have a range of energies, the mean of which will be much greater than thermal energy. At $X_{\max}$ the mean particle energy is the critical energy $E_c = 81$ MeV—the typical particle is highly relativistic. As the ionizing particle energy increases, the mean energy of secondary particles increases.[85] Those with energies above the mean require additional collisions with neutral particles to reach equilibrium before attachment can occur, so the attachment lifetime is greater than that of thermal electrons.

The lower limit signal duration is the time it takes for the EAS to reach the ground. A typical CR proton first interaction depth is 40 g/cm$^2$,[7] or about 12 km above sea level. Assuming the EAS propagates at the speed of light, radar echoes are expected to be 30 $\mu$s in duration. High energy ionization electrons may prolong the plasma lifetime. Even assuming Gorham's high $\tau = 10\,\mu$s, the duration is only increased by 30%.

To estimate received power from EAS-scattered radar waves, it is necessary to make assumptions about the RCS of air shower plasmas. Certain types of atmospheric radar[91] rely on scattering either by local irregularities in the index of refraction or coherent strata with gradients in the refractive index in the direction parallel to propagation. Air shower free electron density changes rapidly as radius decreases over hundreds of meters. However, the magnitude of electron density is not sufficient to modify the index of refraction in a significant way, even near the high-density core (see Section 2.3.2). Scattering due to plasma irregularities or rapidly changing density is negligible.

The overdense region in the collision-less case resembles a thin conducting wire. Though there is no expectation of spectral reflection at this region when collisions are included, it represents a natural boundary where plasma frequency is greatest because electron density is highest near the core. Including collisions, the region where scattering is maximized due to the steep shower density profile is narrow relative to $\sim$ km shower size, likely similar to a $\sim$ 100 m radius cylinder.[14] All forms of scattering from this region will be highly attenuated (see Section 2.3.2).

We use the collision-less overdense region in simulation and proceed as if collisions do not occur. This region is treated as a short-lived, conductive thin wire. The model overestimates the RCS because collisions are neglected, but does not affect frequency vs. time as described in Section 2.5.1. In Chapter 5 and, briefly, in this section a strategy is proposed to account for the over-estimated echo power that arises from neglecting collisional damping.

The RCS of a perfectly conducting thin wire $\sigma_{\mathrm{TW}}$ many wavelengths long but only a fraction of a wavelength in diameter is given by,[92]

$$\sigma_{\mathrm{TW}} = \frac{\pi L^2 \sin^2\theta \left[\frac{\sin\eta}{\eta}\right]^2}{\left(\frac{\pi}{2}\right)^2 + \left(\ln\frac{\lambda}{\gamma\pi a \sin\theta}\right)^2} \cos^4\phi \,,\; \eta = \frac{2\pi L}{\lambda}\cos\theta \,. \tag{2.26}$$

$L$ is the wire length, $\theta$ is the angle between the wire and the direction of incidence, $\phi$ is the angle between the incident wave polarization and the wire axis, $a$ is the radius, $\lambda$ is the wavelength and $\gamma$ is 1.78, $e$ raised to the power of Euler's constant 0.577. Equation 2.26 is prescribed for the case $L \gg \lambda$, but the reader will see that $\sigma_{\mathrm{TW}}$ is not strongly dependent on $L$.

In simulation the thin-wire radius $a$ is dependent on shower lateral distribution, itself a function of shower geometry, primary energy, etc., and the state of the plasma at retarded time $t'$. Segment $j$ at time step $i$ is described by NKG with $N = N_{0,j}\exp(-t'_{i,j}/\tau)$, where $N_{0,j}$ is the initial number of ionization electrons in segment $j$ and $\tau$ is electron lifetime. The maximum radius where NKG multiplied by segment length $c\,\delta t$ has a free electron density that exceeds the density corresponding to a 54.1 MHz plasma frequency is the thin-wire radius $a$.

I make a few observations about the the thin-wire model and Equation 2.26:

- Polarization dependence goes as $\cos^4\phi$, peaked for polarization parallel to wire axis and zero for polarization perpendicular to wire axis. To maximize received signal, **E**-field polarization should be parallel to the air shower trajectory.
- All dependence on wire radius $a$ is in the denominator where it enters logarithmically.
- Unlike scattering in the $a \approx \lambda$ regime, scattered radiation will not be enhanced in the forward direction (Figure 2.5). Rather, we can treat the short-thin-wire radiation as dipole emission.
- A change of $\sim 30°$ in aspect $\theta$ will cause significant oscillations because of amplification in the $(\sin\eta/\eta)^2$ term.

Known shortcomings of the model:

- High electron density air shower core ionization will likely be an imperfect conductor, due again to the high rate of collisions with neutral molecules. We expect significant damping of RCS due to this effect.
- Even absent collisional effects, plasmas have an associated "skin depth" given by $\delta = c/\omega_p$. If the radius of the wire $a \ll \delta$ only a small part of the incident radiation may be absorbed and re-radiated by the wire.
- Radius $a$ is itself linearly dependent on $E_0$ meaning the RCS is only logarithmically dependent on primary energy.

These first two factors will have the effect of reducing the intensity of scattered radiation by an unknown amount, but will not change the geometrical dependence of RCS. This suggests a (somewhat model dependent) way of quantifying the observed RCS of extensive air showers, or placing limits on RCS in the case of nonobservation.

We assume $\sigma$ is proportional to $\sigma_{\mathrm{TW}}$, and therefore that each segment of the shower has a radar cross section given by

$$\sigma = \Gamma\, \sigma_{\mathrm{TW}} \tag{2.27}$$

where $\Gamma$ is a constant representing the effects of imperfect conductivity and collisional damping. Received power is proportional to the RCS and therefore also to $\Gamma$. The observation of echoes at some power level would thus be a measure of $\Gamma$, and nonobservation will allow calculation of an upper limit on $\Gamma$. Analysis details regarding this proposition will be discussed in Chapter 5.

In the following section, I apply the thin-wire approximation for a particular transmitter/receiver configuration and use transmitter power $P_T$ and gain values $G_T$, $G_R$ specific to the TARA radar detector currently in operation near Delta, UT (Section 2.6).

## 2.6 Case Study: TARA

The TARA detector consists of a VHF transmitter, custom transmitting and receiving antennas, and an intelligent DAQ (described in detail in Chapter 3). The transmitter is a reconfigured analog television transmitter which broadcasts a 54.1 MHz CW radar signal under the FCC's experimental licensing system. It is located near Delta, UT and directs its radar beam south-west across the TA surface detector array toward receiving antennas at the Long Ridge fluorescence detector. Transmitter total power output is 40 kW, typically 25–30 kW. Construction on the transmitter station and antennas began in August, 2012. The complete TARA detector (transmitter site and receiver antennas/DAQ) went online in August, 2013.

Figure 2.10 shows the spectrogram of a canonical shower for TARA geometry. Properties relevant to detection are chirp slope, $F_{\max}$ and chirp duration. I have used simulation results to determine optimal TARA transmitting antenna radiation patterns and in data acquisition system design.

### 2.6.1 Detector Design

TARA's primary goal is to achieve coincidences with Telescope Array. The bistatic radar detector transmits its radar beam over TA fiducial volume. TX → RX

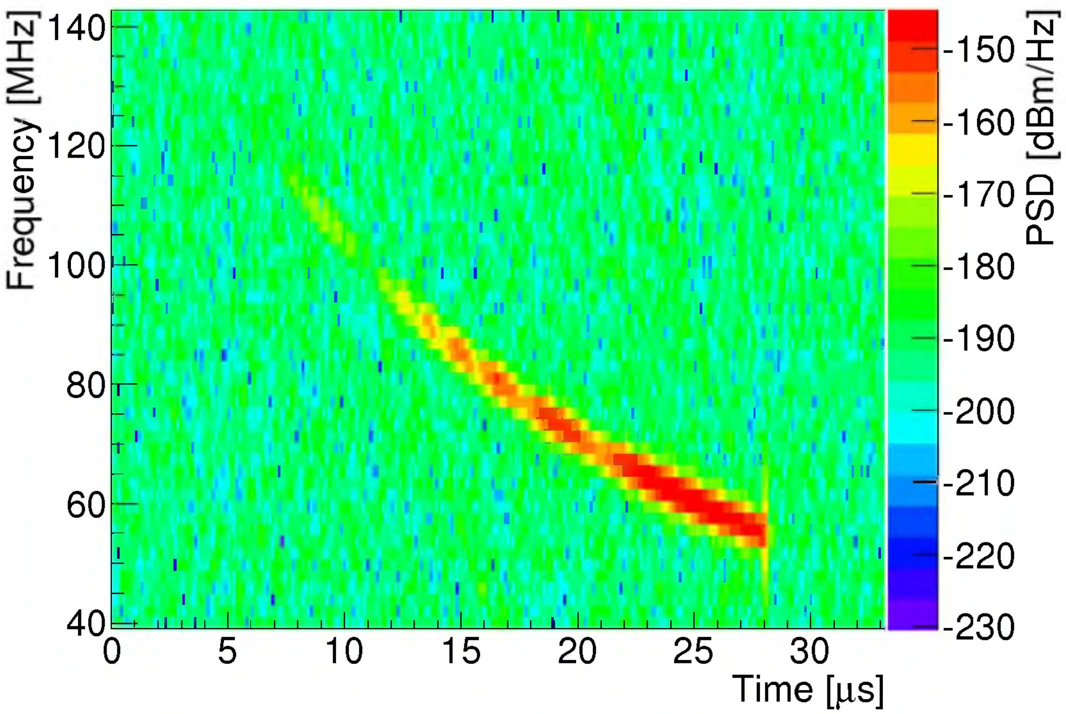

**Figure 2.10**: Radar echo spectrogram from a $10^{19}$ eV shower located midway between transmitter and receiver inclined 30° out of the plane connecting the two. TX → RX separation is 39.5 km, the TARA separation distance.

spacing is critical because it strongly influences received signal characteristics. As the separation distance decreases, $L'$ increases so the chirp rate and frequency, relative to transmitted frequency, also increase. Correspondingly, chirp duration decreases.

Echoes typically exhibit frequency *shifts* of order $\omega_r$ (Figure 2.10). This implies that even a low-VHF signal (such as TARA's 54.1 MHz) requires a broadband receiver. Higher frequency radar requires larger bandwidth. A DAQ detection frequency range from 50 MHz to 100 MHz requires a 200 MS/s baseband receiver or 50 MS/s passband receiver by the Nyquist sampling theorem.[93]

Large bandwidths are unusual in radar applications, which rarely exceed hundreds of Hz. Noise power $P_N$ is proportional to bandwidth $P_N = kTB$ [W], where $k$ is Boltzmann's constant and $B$ is the bandwidth in Hz. Therefore, large bandwidth receivers have high noise floors compared to traditional narrow-band radar. In all radar systems the noise floor is limited by sky and thermal noise. At 54.1 MHz, receiver noise is dominated by galactic synchrotron emission which is greater than thermal noise[17] (see Section 3.5).

### 2.6.2 Chirp Characteristics

To understand radar echo characteristics in the TARA detector, I have generated 10,000 simulated events. TA has a large CORSIKA Monte Carlo (MC) set that emulates the distribution of real events seen by the TA surface detector which are used for MC/data comparisons. From the subset of well-reconstructed MC events, I chose 10,000 events randomly from which I use geometry and energy for the radar echo simulation. The majority of TARA triggers will be recorded in self-triggered mode, during which the TA surface detector will also be recording CR events. Results from the radar echo simulation of MC events have guided antenna and trigger design.

During its first year of operation the TARA transmitting antenna was horizontally polarized. The thin-wire approximation predicts the largest cross-section when **E**-field polarization is aligned with the shower axis. Because of atmospheric attenuation, TA acceptance decreases as the zenith angle approaches the horizon. Well-reconstructed TA events will align better on average with a vertically polarized radar signal and therefore bias radar echo signal-to-noise ratio (SNR) against a horizontally polarized antenna. However, practically zero events will align within a few degrees of horizontal because of atmospheric attenuation. A vertically polarized transmitting antenna has a better chance of aligning very closely with a small of number of EAS. All of the data considered in this dissertation were recorded with a horizontally polarized transmitter antenna. In Nov. 2014 transmitting antenna polarization was changed to vertical.

SNR is defined as

$$\mathrm{SNR} = \frac{P_\mathrm{c}}{\sigma^2_\mathrm{noise}}\,, \tag{2.28}$$

where $P_\mathrm{c}$ is the chirp signal power and $\sigma_\mathrm{noise}$ is the standard deviation of the background noise. A second definition is necessary for signals with time-varying amplitude like those predicted by the EAS radar echo simulation. For such signals we use the amplitude signal-to-noise ratio (ASNR)

$$\mathrm{ASNR} = \frac{\bar{V}^2_\mathrm{max,\ c}}{\sigma^2_\mathrm{noise}}\,. \tag{2.29}$$

$\bar{V}_\mathrm{max,\ c}$ is the maximum chirp amplitude.

Simulated received power for an ideal EAS geometry is compared with background noise which has been integrated over the TARA DAQ passband in Figure 2.11. The same curve is shown multiplied by the damping factor $10^{-6}$. Even with a large bandwidth receiver, some radar echoes are expected with positive SNR under the assumptions given in previous sections.

Distributions of chirp slope, duration and $F_{\text{max}}$ are shown in Figures 2.12, 2.13 and 2.14. Chirp slope is calculated from a weighted fit (by power) to the echo spectrogram. Duration is defined as the time difference between the –10 dB points above and below the time when maximum power is received. $F_{\text{max}}$ is the frequency bin that corresponds to the highest received power in an echo spectrogram.

The echo slope distribution was useful in DAQ design. Our self-trigger scheme is optimized to detect chirp signals in the range [-1,-3] MHz/$\mu$s, which includes the majority of radar echoes in the simulated set. Similarly, the duration and $F_{\text{max}}$ distributions were used to determine the band size and frequency. Section 3.6 in Chapter 3 describes DAQ trigger logic in detail.

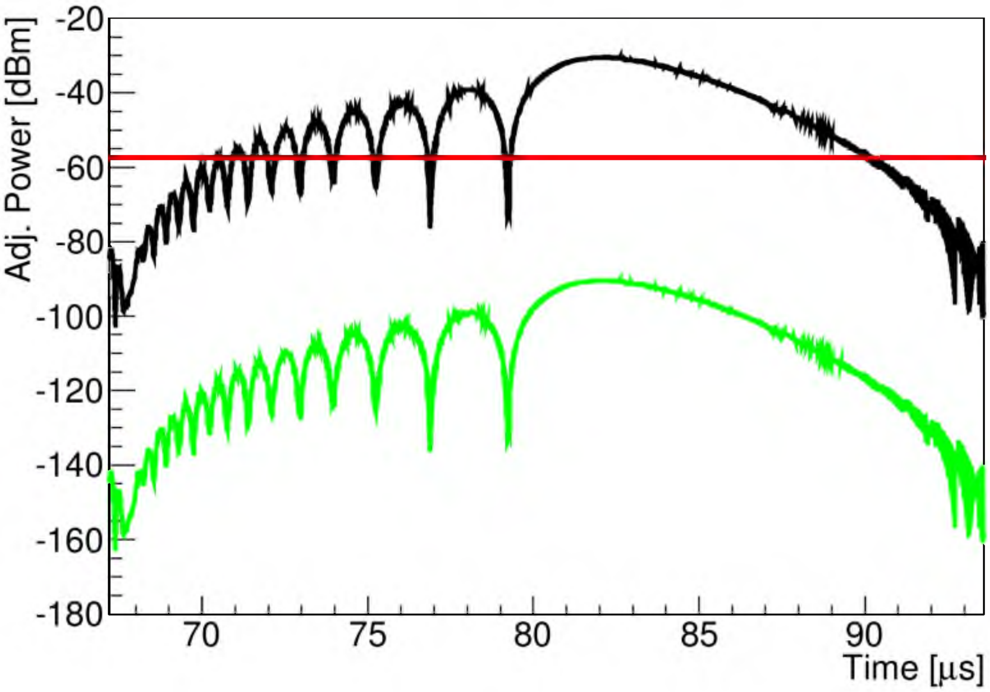

**Figure 2.11**: Received power vs. time for a simulated radar echo assuming a geometry that maximizes signal (black). The same received power curve is shown multiplied by a damping factor of $10^{-6}$ (green) to account for collisional damping. Note that the damping factor is calculated assuming a collision frequency of $10^{11}$ Hz, which is likely overestimated due to the assumption of near-thermal ionization electron energies (see Section 2.3.2). The red line is integrated background noise power in the TARA passband (see Chapters 3 and 4). Simulated received power has been adjusted by +30 dB to account for front end amplifiers, through which background noise has passed.

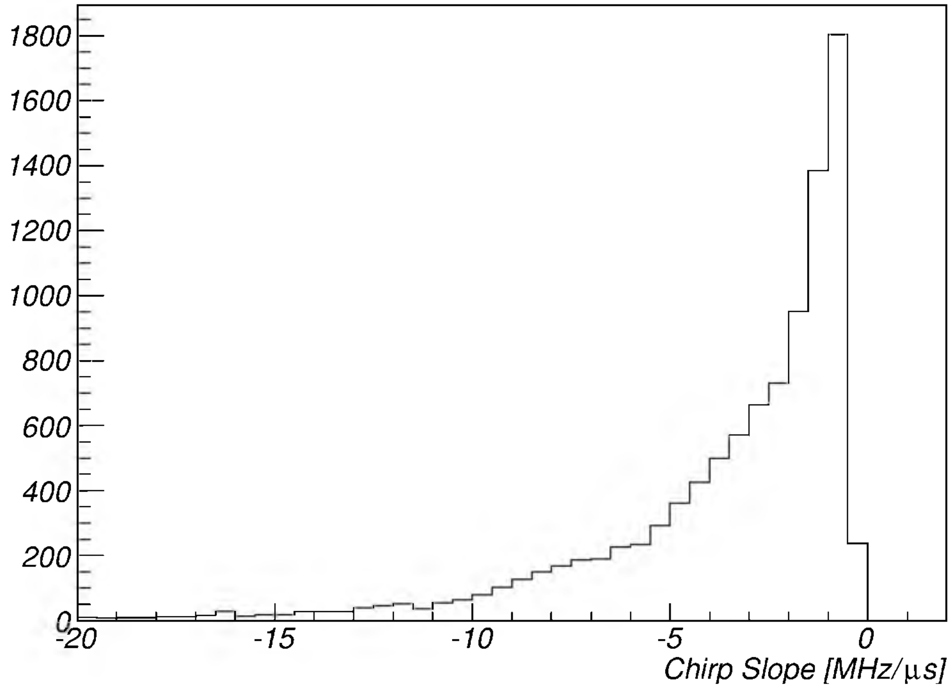

**Figure 2.12**: Radar echo chirp slope distribution for 10,000 simulated radar echoes. Chirp slope is determined by a linear fit to an $F_{\mathrm{max}}$ vs. time plot with each point weighted by its Fourier amplitude. The sounding wave polarization does not affect the slope. Near $F_{\mathrm{max}}$ the chirp rate is actually slightly concave. Linear chirp rates are used for easy comparison.

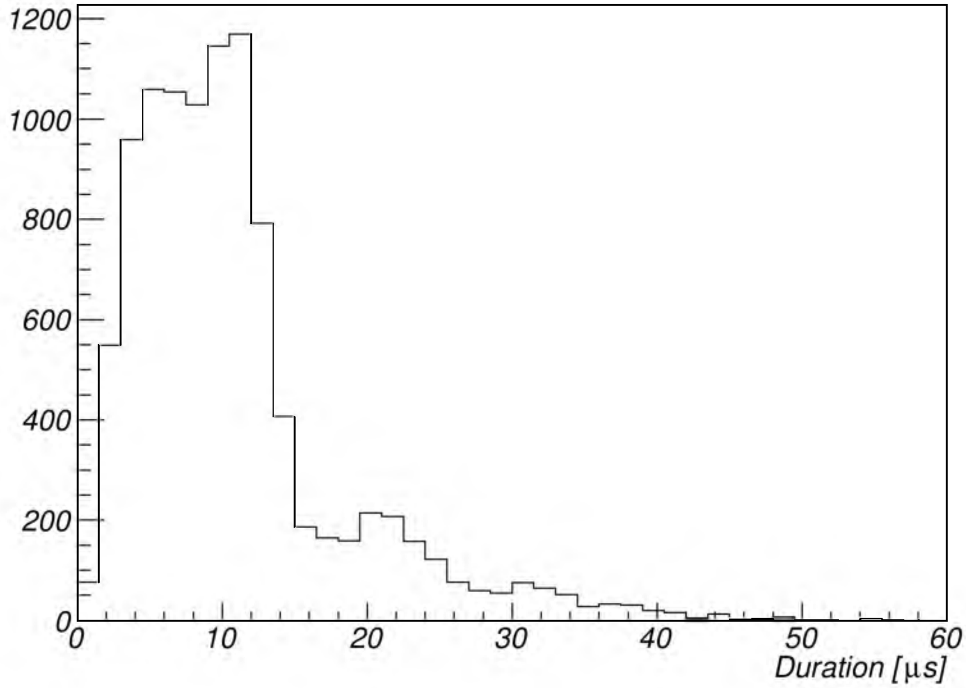

**Figure 2.13**: Radar echo duration distribution from 10,000 simulated echoes. Echo duration is defined as the time difference between the $P_{\text{max}} - 10$ dB points.

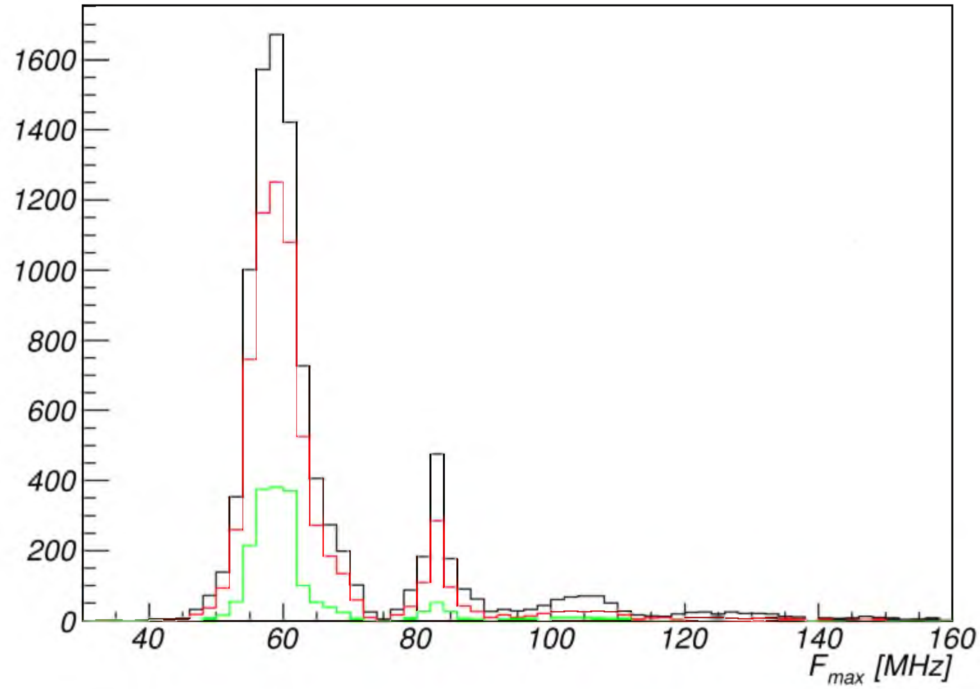

**Figure 2.14**: $F_{\text{max}}$ distribution for 10,000 simulated radar echoes. The different histograms are for no cuts (black), $P_{\text{max}} > -100$ dBm (red) and $P_{\text{max}} > -80$ dBm (green). $F_{\text{max}}$ is the frequency component that occurs with the highest power. Peaks in $F_{\text{max}}$ correspond to fluctuations in $\sigma_{\text{TW}}$, which can be seen in Figure 2.10, and which were discussed in Section 2.5.2.

# CHAPTER 3

# TARA DETECTOR[a]

The possibility of radar observation of cosmic rays dates to the 1940s, when Blackett and Lovell[29] proposed cosmic rays as an explanation of anomalies observed in atmospheric radar data. At that time, a radar facility was built at Jodrell Bank to detect cosmic rays, but no results were ever reported. Recent experimental efforts utilizing atmospheric radar systems were conducted at Jicamarca[63] and at the MU-Radar.[64] Both observed a few signals of short duration indicating a relativistic target. However in neither case were the measurements made synchronously with a conventional cosmic ray detector.

A new approach, first attempted by the MARIACHI[66,67] project, is to utilize *bi-static* or two-station radar in conjunction with a conventional set of cosmic ray detectors. Air shower particles move very close to the speed of light, so the Doppler shift is large compared with air planes or meteors. The bi-static configuration in which the sounding (interrogating) wave Poynting vector is generally perpendicular to shower velocity (as shown in Figure 2.6) minimizes the large Doppler shift in frequency expected of the reflected signal (see,[88,95] and Section 2.5.) This scenario is unlike that explored in[95] in which the two vectors are roughly antiparallel. In the latter case, the relativistic frequency shift is maximized. Also, depending on the size of the radar cross section relative to the square of the sounding wavelength, scattering in the forward direction might be enhanced relative to back scatter,[96] thus providing an advantage in detecting the faintest echoes in comparison to mono-static radar (ranging radar).

---

[a] This chapter is taken from the author's previously published article.[94] Permission to include partial or complete published articles in a thesis or dissertation is among the rights retained by Elsevier authors (`http://www.elsevier.com/journal-authors/author-rights-and-responsibilities`).

Co-location with a conventional detector allows for definitive coincidence studies to be performed. If coincidences are detected, the conventional detector's information on the shower geometry will allow direct comparison of echo signals with the predictions of air shower Radio Frequency (RF) scattering models.

The Telescope Array Radar (TARA) project is the next logical step in the development of the bi-static radar technique. Whereas MARIACHanangleI made parasitic use of commercial television carriers as a source of sounding radiation (now impossible due to the transition to digital broadcasts), TARA employs a single transmitter in a vacant VHF band which is under the experimentalists' control. The TARA receiver consists of broadband log-periodic antennas, which are read out using a 250 MS/s digitizer. TARA is co-located with the Telescope Array (TA), a state-of-the-art "conventional" cosmic ray detector, which happens to be located in a low-noise environment. The layout of the TA and TARA detection facilities are shown in Figure 3.1.

As will be described Section 3.6, TARA relies on the TA fluorescence detector as a trigger source. The ability to compare radar waveforms with TA reconstructed events is a major advantage of TARA compared to other experiments. Chapter 4 describes the FD data, and its use in TARA data analysis is described in Chapter 5. Details of the TA SD and FD are given in Section 3.1.

## 3.1 Telescope Array Detectors

Telescope Array (TA) is located near Delta, Utah, USA. It is home to the world's second largest surface detector array, which operates both independently and in hybrid mode with each of three fluorescence detectors. Both SD and FD data will be used for comparison with the radar data stream, although the analysis I explain in future chapters only uses FD data (as described in Chapter 4). Figure 3.2 shows the grid of SDs and the three FDs that are positioned to allow hybrid event detection.

### 3.1.1 Surface Detector

The SD has recently been described in the literature.[97] Telescope Array hosts 507 surface scintillator detectors positioned on a 1.2 km grid that covers approximately 700 $\text{km}^2$. Figure 1.10 is a picture of a single SD in the Utah desert near Delta. Each

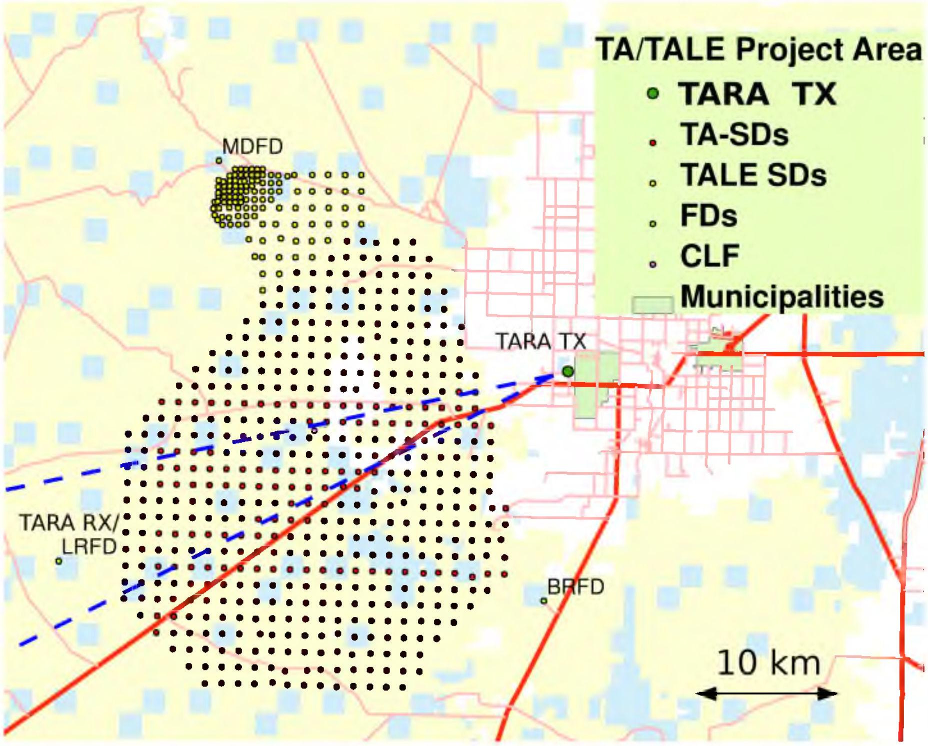

**Figure 3.1**: Map of TARA Observatory sites (transmitter and receiver) along with the Telescope Array (TA) detector facilities. The transmitter broadcasts as station WF2XZZ near Hinckley, Utah, towards a receiver site located at the TA Long Ridge Fluorescence Detector (FD). The sounding radiation illuminates the air over the central portion of the TA Surface Detector array, shown with dashed blue lines that indicate the beamwidth 3 dB below the peak gain.

detector consists of a steel-enclosed 3 m$^2$ plastic scintillator, separate stainless steel electronics box, 1 m$^2$ (125 W) solar panel and 3-m high communication tower. A deep cycle battery powers the charge controller, FPGA-based DAQ, wireless modem, GPS receiver and photo multiplier tube (PMT) bases.

Each SD has two layers of plastic scintillator (see Figure 3.3 for a schematic) divided by a 1 mm stainless steel plate. Each layer is divided into four slabs with grooves in the plastic separated by 2 cm which accept an optical fiber that collects scintillation light. Both ends of the optical fiber join those from other grooves to form a bundle that terminates in a PMT, one for each layer of plastic.

PMT output is sampled by a 50 MHz FADC. Signals are scaled to units of minimum ionizing particles (MIP), which are calculated once per 10 minutes by a histogram of pulse heights from Level-0 triggers. Level-0 triggers (greater than 0.3

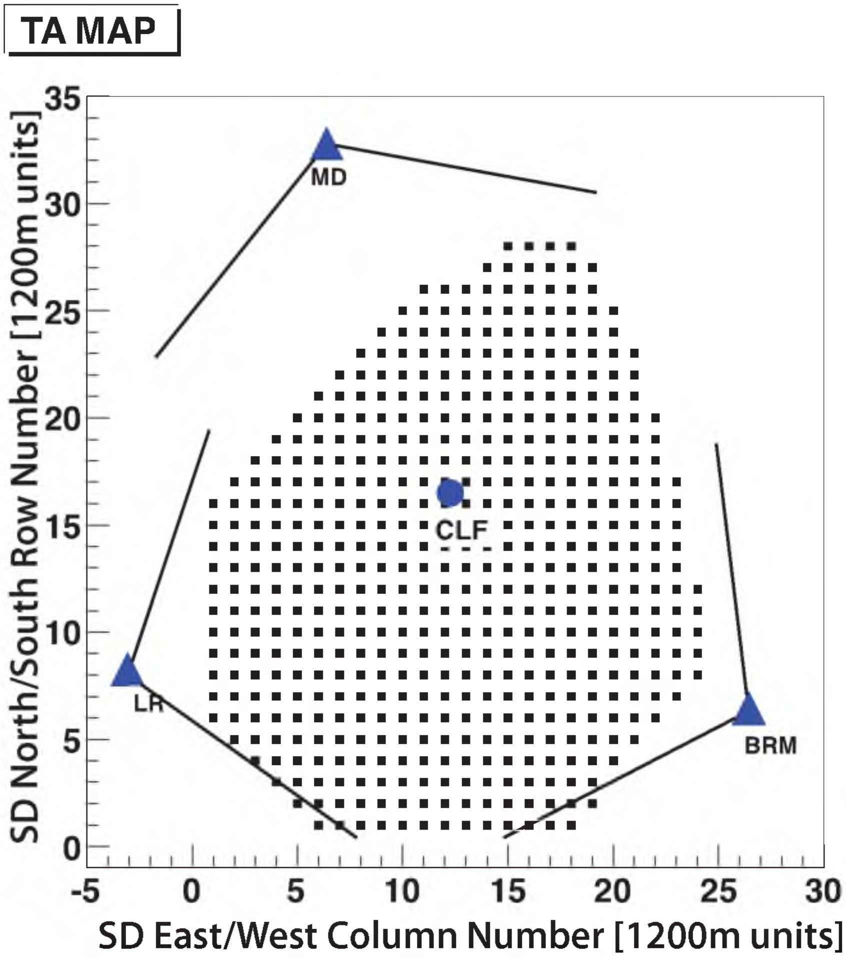

**Figure 3.2**: Map of Telescope Array[9] showing fluorescence detectors (FD) as blue triangles, with their approximate detection angle, overlooking surface detectors (SD) represented by small black squares. Reprinted from Astroparticle Physics, 64, R.U. Abbasi, et al., Study of Ultra-High Energy Cosmic Ray Composition Using Telescope Array's Middle Drum Detector and Surface Array in Hybrid Mode, 49–62, Copyright (2015), with permission from Elsevier.

MIP) are stored in the local SD only. If the signal is a Level-1 trigger (exceeds 3.0 MIP), information is sent to a central communication tower.

Three subarrays divide Telescope Array to permit reliable communication between SDs and their communication tower. Each tower requests all Level-1 triggers from its subarray once per second. If three adjacent SDs register Level-1 triggers within 8 $\mu$s, a Level-2 trigger is recorded and all waveforms within a 32 $\mu$s window of the trigger are requested from all SDs within the subarray. TA SD efficiency is 97% for $E_0 > 10^{19}$ eV.

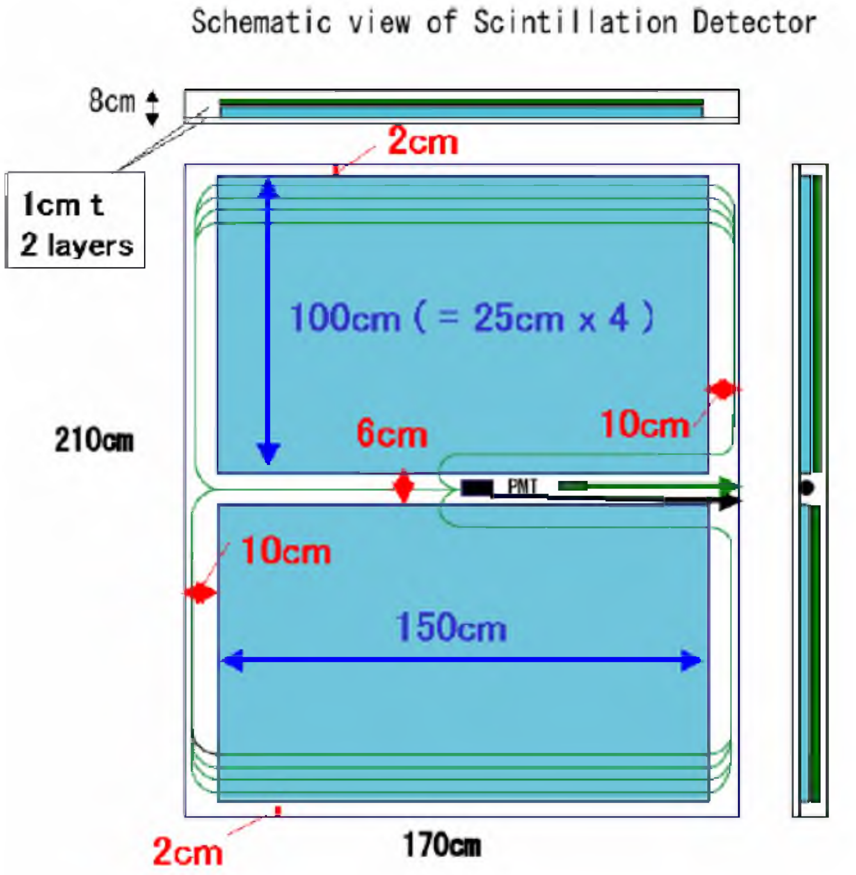

**Figure 3.3**: Schematic of surface detector plastic scintillator.

Triggered events record three pieces of information from each SD in the subarray: Integrated particle count in units of vertical equivalent muon (VEM, 2.05 MeV deposited in each scintillator layer[98]), shower arrival time and SD coordinates. Event reconstruction utilizes the modified Linsley shower shape function[99] to determine arrival direction and core position, and the AGASA method[100] to determine primary energy. Reconstructed event information includes primary energy ($E_0$), core location, and pointing direction (zenith and azimuth).

### 3.1.2 Fluorescence Detector

TA employs two different types of FD detector stations.[101] The northern middle drum (MD) detector utilizes refurbished High Resolution Fly's Eye sample-and-hold electronics[51] in which each PMT reports a single value and the time of occurrence.

Two southern stations have been custom built using FADC-electronics.[101] Long Ridge (LR) station is east of the array and Black Rock Mesa (BRM) station is west of the array. Figure 3.2 shows the positions of FD stations near the SD array. Figure 1.11 shows the latter FD building with the telescope doors open.

BRM and LR FDs each have 12 telescopes. A single telescope views 3° to 33° in elevation using a 3.3 m diameter segmented mirror, which focuses light on a cluster of 256 hexagonal PMTs. Each PMT feeds 14 bit dynamic range FADC electronics sampling at 10 MHz. Mean and variance of each PMT is calculated in five sliding time windows that range from 0.8 to 12.8 $\mu$s. When the instantaneous signal exceeds $6.0\sigma$ in any time window, the low-level trigger criterion is met. A 51.2 $\mu$s waveform (25.6 $\mu$s frame plus 12.8 $\mu$s buffer on both ends) is written out for all 3072 PMTs when five or more adjacent PMTs within a 25.6 $\mu$s frame are triggered.

A hardware-level Nuclear Instrumentation Module logic pulse (NIM, true for $-0.8$ V at 50 $\Omega$) is generated each time low-level trigger criteria is met. As I describe in Sections 3.6.3 and 4.1, this low-level trigger output feeds the radar DAQ in FD-trigger mode. The typical secondary trigger rate (five adjacent PMTs) is 2 Hz.

After a secondary trigger, the DAQ electronics impose a "dead time" which prevents triggering for a short period. Long Ridge dead time is 8.7% of the total on-time after removing bad weather days and other poor data periods. TA FDs operate on only moonless nights which results in a duty cycle of about 10%.

## 3.2 Transmitter

### 3.2.1 Hardware

TARA operates a high power, Continuous Wave (CW), low frequency radar transmitter built from repurposed analog TV transmitter equipment with FCC call sign WF2XZZ, an experimental license. The transmitter site (39° 20′ 19.82400″ N, 112° 42′ 3.24000″ W) is just outside Hinckley, UT city limits where human exposure to RF fields is of little concern. A high gain Yagi array (Section 3.3) focuses the radar wave toward the receiver station (Section 3.4) located 40 km away. Figure 3.1 shows the transmitter location near Hinckley and relative to the TA SD array.[97] The geometry was chosen to maximize the possibility of coincident SD and radar echo events.

Figure 3.4 shows a schematic of the transmitter hardware configuration. A Tektronix arbitrary function generator (AFG 3101; Tektronix, Inc.) provides the primary sine wave, which is amplified over nine orders of magnitude before reaching the antenna. 54.1 MHz was chosen as the sounding frequency because of the lack of interference in the vacated analog channel two TV band and the 100 kHz buffer between it and the amateur radio band which ends at 54.0 MHz.

Two 20 kW analog channel 2 TV transmitters have a combined 40 kW power output. The primary signal from the function generator is split to feed both transmitters (Harris Platinum HT20LS, p/n 994-9236-001; Harris Broadcast) with the same level of gain. Each transmitter includes a control cabinet and two cabinets of power amplifier modules. RF power from each cabinet is combined in a passive RF combiner (620-2620-002; Myat, Inc.) that routes any out-of-phase signal to a 50 Ω load. The combined output of each transmitter is sent to a 90° hybrid combiner (RCHC-332-6LVF; Jampro, Inc.) that sums the total output of each transmitter.

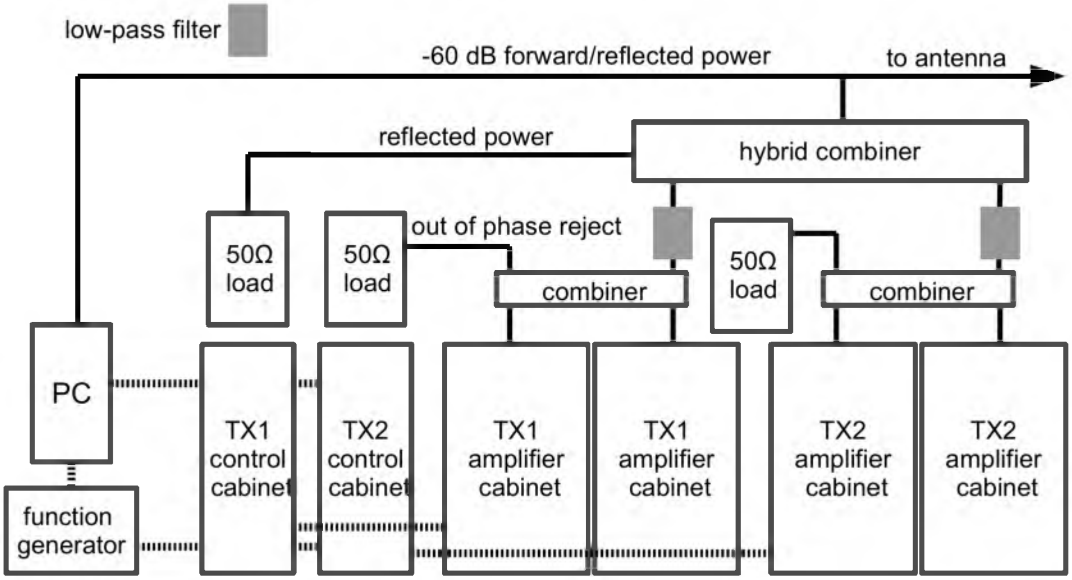

**Figure 3.4**: Schematic of the transmitter hardware configuration. A computer connected to RF sensor equipment, an arbitrary function generator and transmitter control electronics orchestrates the two distinct transmitters and provides remote control and logging. RF power from each transmitter's two amplifier cabinets is combined with out of phase power rejected into a 50 Ω load. A hybrid combiner sums the combined output of each transmitter and sends that power to the antenna. Power reflected back into the hybrid combiner is directed to a third RF load.

Between the final combined input and each transmitters' combined output there is an in-line analog channel 2 low pass filter (visual low-pass filter, 3 1/8"; Myat, Inc.) to minimize harmonics. RF power leaves the building through 53 m of semiflexible 3 1/8" circular air-dielectric wave guide (HJ8-50B; Andrew, Inc.).

Modifications were made to the transmitters to bypass interlocks that detect the presence of aural and visual inputs and video sync pulses necessary for standard TV transmission. Control cabinet electronics were calibrated to measure the correct forward and reflected power of the 54.1 MHz tone instead of the RF envelope during the sync pulse. Currently, total power output is limited to 25 kW because of limitations that arise from amplifying a single tone versus the full 6 MHz TV band.

Air conditioning and ventilation are critical to high power transmitter performance. Currently, transmitter efficiency is slightly better than 30%, which implies that nearly 75 kW of heat must be removed from the building. The environment at the site is very dry and dusty, so all of the air brought into the building is filtered and positive gauge pressure is maintained. A single 25 ton AC unit filters and pumps cool air into the building. An economizer will shut down the compressor if the outside air temperature drops below 15.6° C (60° F). However, if the room is not cooling quickly with low outside ambient temperature, the compressor will be turned back on. Hot air near the ceiling is vented as necessary to maintain a slight positive pressure.

Future improvements to the transmitter will include biasing the power amplifiers for class B operation, in which amplification is applied to only half the 54.1 MHz cycle. Resonance in the transmitter and antenna allow the second half of the wave to complete the cycle. Efficiency will nearly double compared with the current configuration.

### 3.2.2 Remote Monitoring and Control

Remote monitoring and control of the transmitter is important for two reasons. First, Federal Communications Commission (FCC) regulations require that non-staffed transmitter facilities be remotely controlled and several key parameters monitored. Second, forward power and other parameters must be logged for receiver data analysis.

A computer interfaces with digital I/O and analog input devices that, in turn, are connected to the transmitters' built-in digital I/O and analog output interface. RF power sensors (PWR-4GHS; Mini-Circuits) measure the final forward and reflected power via strongly attenuating sample ports on the wave guide near the building exit port. The sum of the two control cabinets' forward and reflected power measurements can be compared with the separate RF final forward and reflected power measurements.

The host computer monitors transmitter digital status, analog outputs and RF power sensors and controls the function generator. Logs are updated every five minutes with forward and reflected power for each transmitter, *final* (re: antenna) forward and reflected power, room temperature and various transmitter status and error states. Warning and error thresholds can trigger emails to the operators and initiate automatic shut down. The program also provides a simple interface that allows the operator to remotely turn the transmitter on and off, increase or decrease forward power, and add a text log entry.

### 3.2.3 Performance

TV transmitters are designed for 100% duty cycle operation. Similarly, the TARA transmitter is intended for continuous operation to maximize the probability of detection of UHECRs. With fixed gain and input signal, power is strongly correlated with transmitter room ambient temperature. Large temperature fluctuations in April 2013 resulted in a $\sim 3$ kW spread in output power (Figure 3.5).

Transmitter forward power is more stable if room temperature is kept lower than 300 K (80° F). Figure 3.6 shows forward power fluctuations in August 2013 are much smaller than April. Built-in automatic gain control was increased during this period as well. The average power in December is higher than the average power in April because a slightly higher power input signal was used in later months. Reflected power is typically $\sim 100$ W, which is very low for such a high power system. This can be attributed to very good impedance matching with the extremely narrow-band Yagi antenna array.

Figure 3.7 shows the total forward and reflected power in red and blue, respectively, referenced to the right vertical axis and the integrated on-time in black, referenced to the left vertical axis, since its commissioning in late March, 2013.

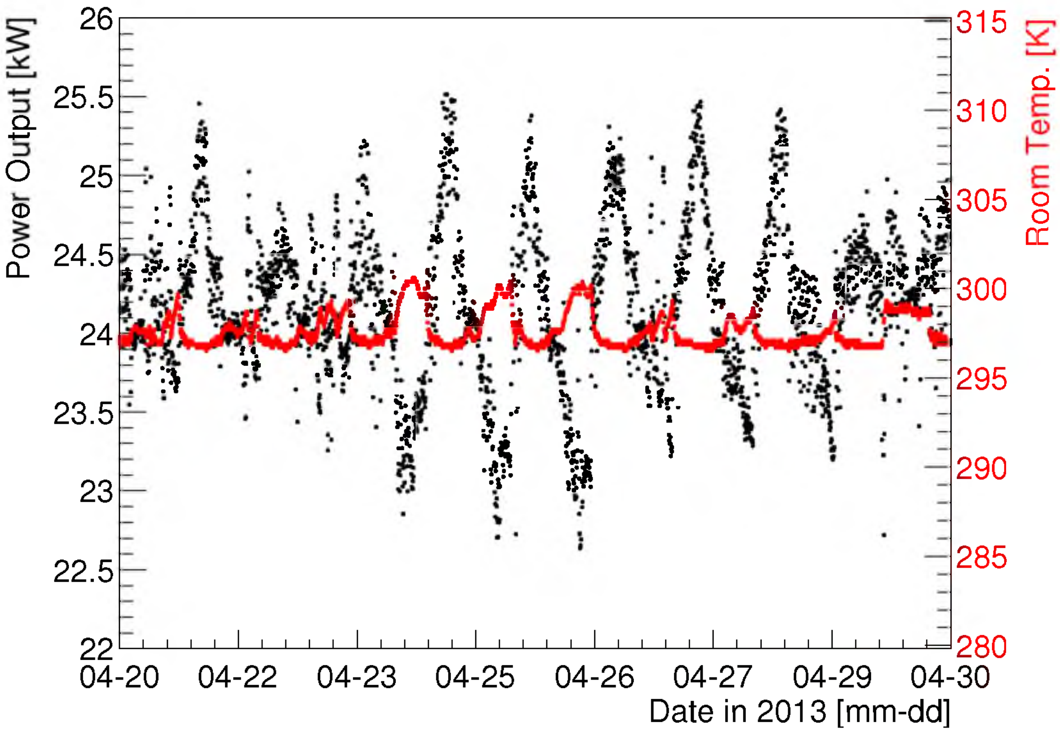

**Figure 3.5**: Transmitter forward power (black) and room temperature (red) during April 2013. Poor air conditioning calibration resulted in daily temperature fluctuations which caused large output power modulation.

The transmitter has been turned off several times for maintenance and testing and during periods when our receiver equipment was removed from the field for upgrades. Although forward power is not continuous and fluctuations were large in the past, we consider 200 days of operation in the first year to bode well for future data collection.

Harmonics have been measured to confirm compliance with FCC regulations and to avoid interfering with other stations. With total forward output at 25 kW, the fundamental and several harmonic frequencies were measured from a low power RF sample port. The first five harmonics are about 60 dB below the fundamental (see Table 3.1). Harmonics will be further attenuated by about 30 dB by the intrinsic bandpass of the antenna.

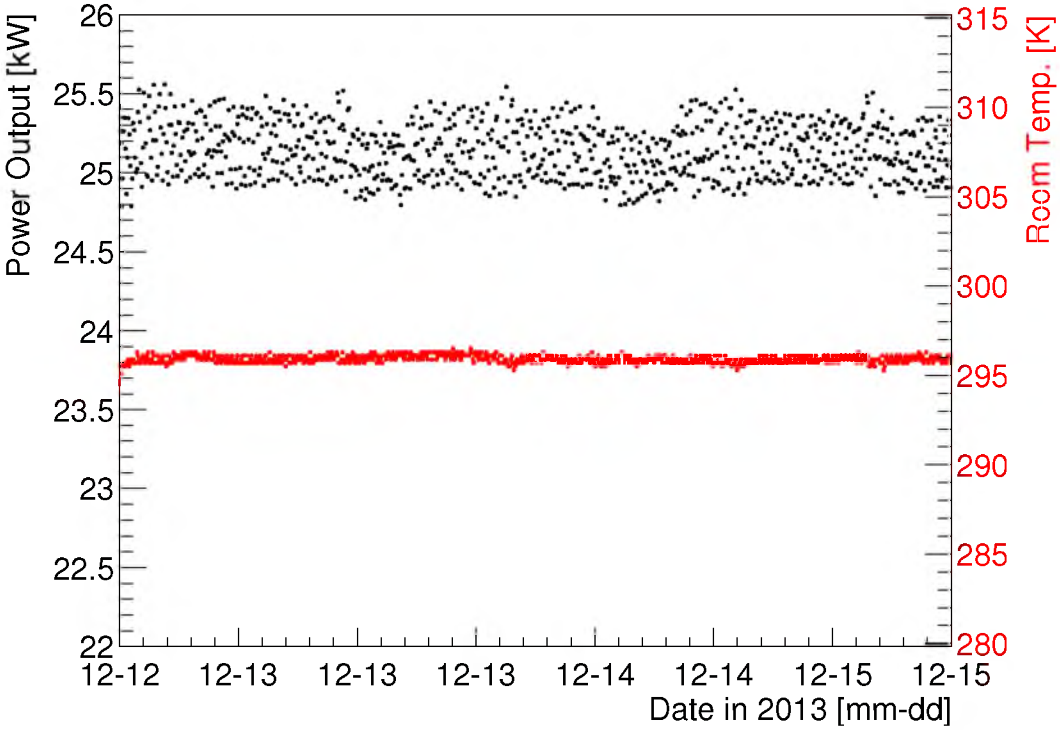

**Figure 3.6**: Transmitter forward power (black) and room temperature (red) during December 2013. A well-calibrated air conditioning system keeps room temperature stable and increased automatic gain control minimizes forward power fluctuations.

## 3.3 Transmitting Antenna

### 3.3.1 Physical Design

As the bi-static radar equation (Equation 2.1) shows, the received power is the product of the scattering cross section, transmitted power, transmitter antenna gain, receiver antenna gain and receiver aperture. Because the physics of the radar scattering cross section is not well understood, an antenna with high gain and directivity was chosen to maximize received power.

The TARA transmitting antenna is composed of 8 narrow band Yagi antennas designed and manufactured by M2 Antenna Systems, Inc. Each Yagi is constructed of aluminum and capable of handling 10 kW of continuous RF power. The specifications for each Yagi are a frequency range of 53.9 - 54.3 MHz, 12 dBi free space gain, front to back ratio of 18 dB, and beamwidths (defined as the angle in the plane under consideration over which the radiated power is within three dB of the maximum) of

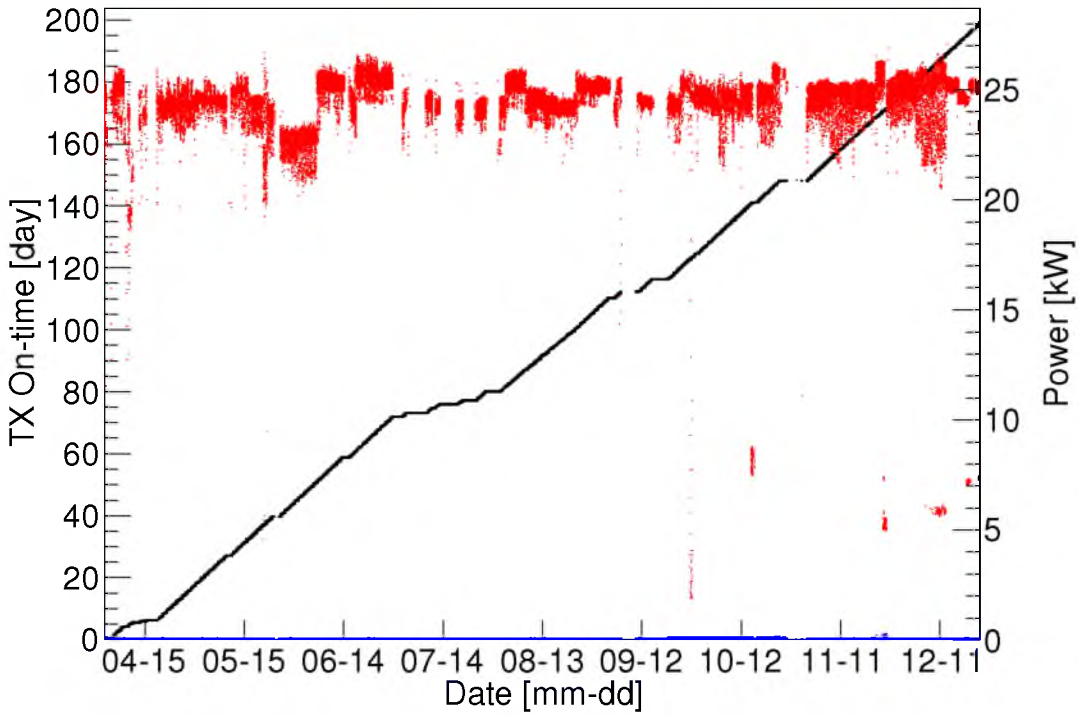

**Figure 3.7**: Transmitter on-time in days (black, left vertical axis) and forward and reflected power in units of kW (red and blue, right vertical axis) during 2013. Total duty cycle during this period is 83%.

27° and 23° in the vertical and horizontal planes, respectively.

Each Yagi antenna is composed of five elements: a reflector, driven element, and three directors, and are mounted on a 21.6 ft long, 2″ diameter boom. A balanced t-match is fed from a 4:1 coaxial balun which transforms the unbalanced 50 Ω input to the balanced 200 Ω used to drive the antenna. A 50 Ω 7/8″ coaxial waveguide connects the balun to the four-port power dividers. Table 3.2 describes the lengths and positions of the antenna elements on the boom. All elements are constructed of aluminum tubing of 3/4″ outer diameter. Each element, except for the driven element, is constructed of two equal sections that are joined at the boom via 7/8″ outer diameter sleeve elements. The weight is 35 lbs when completely assembled.

Transmitter output power is delivered to the antenna array via approximately 100 feet of CommScope HJ8-50B 3 1/8″ Heliax air dielectric coaxial wave guide. The Heliax then connects to a two-port power divider located at the base of the

**Table 3.1**: Power of fundamental frequency and first 10 harmonics for the 54.1 MHz radar sounding wave. These measurements were taken from a highly attenuated final forward power RF sample port. Total transmitted power was approximately 25 kW. FM and TV stations are required by the FCC to limit the first 10 harmonics to at least 60 dB below their approved total transmitted power. Experimental station WF2XZZ is exempt from this requirement although it readily meets it. (*fluctuating value, ±5 dB)

| Frequency (MHz) | Power (dBm) |
|---|---|
| 54.1 | 8.5 |
| 108.2 | -66.0 |
| 162.3 | -68.3 |
| 216.4 | -84.4 |
| 270.5 | -89* |
| 324.6 | -77* |
| 378.7 | -94* |
| 432.8 | -87* |
| 486.9 | -98* |
| 541.0 | -91* |

**Table 3.2**: Length and relative boom position of antenna elements of the TARA Yagi antennas. All elements have a diameter of 0.75″.

| Element | Length (in) | Position (in) |
|---|---|---|
| Reflector | 107.625 | -44.375 |
| Driven Element | 100.500 | 0.000 |
| Director 1 | 99.500 | 51.125 |
| Director 2 | 97.250 | 131.625 |
| Director 3 | 97.000 | 193.625 |

antenna array. Each output port of the power divider feeds equal length 1 5/8″ coaxial cables, which in turn feed a four-port power divider. Each four-port power divider then delivers power to the individual Yagi antennas via equal length 7/8″ coaxial cables. All components in the transmission line chain are impedance matched to 50 Ω.

The antennas are mounted on four wooden telephone poles, two stacked vertically on each pole. The bottom and top antennas on each pole are located 10 ft and 30 ft above the ground, respectively. Currently, the antennas are mounted in a configuration that provides a horizontally polarized signal. Wooden poles were used to allow a change of polarization. The poles, separated by 20 ft, are aligned in a plane perpendicular to the line pointing toward the receiver site located at the Long Ridge fluorescence detector 39 km to the southwest. Figure 3.8 shows the antenna array configuration.

### 3.3.2 Theoretical Performance

The eight Yagi antennas are operated as a phased array to take advantage of pattern multiplication to improve gain and directivity relative to the individual antennas. The design philosophy of the antenna array is to deliver a large amount of power in the forward direction in a very narrow beam to maximize the power density over the TA surface detector. High power density is equivalent to a large $P_T G_T$ factor in the bi-static radar equation, which is needed to increase the chance of detection of a cosmic ray air shower via radar echo given the uncertainty in the radar scattering cross section $\sigma_{EAS}$. Before construction, modeling of the array was performed using version two of NEC,[16] an antenna modeling and optimization software package.

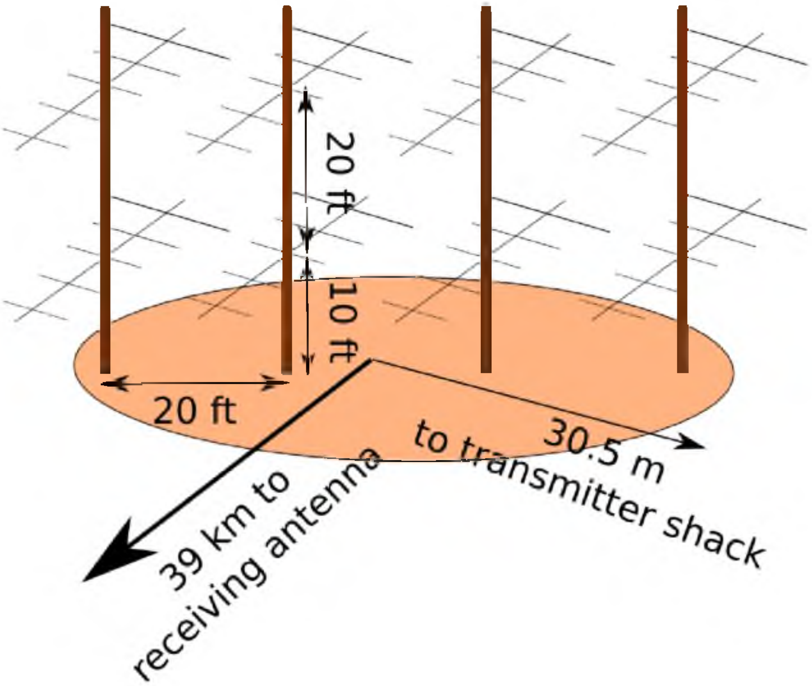

**Figure 3.8**: Configuration of the eight Yagi antennas and mounting poles which comprise the TARA transmitting antenna array.

Figure 3.9 shows the radiation pattern of the full eight-Yagi array when configured as shown in Figure 3.8. Forward gain is 22.6 dBi, horizontal beamwidth is 12°, vertical beamwidth is 10°, the front-to-back (F/B) ratio is 11.8 dB and the elevation angle of the main lobe is 9°.

Simulations were performed to find the best spacing between the mounting poles, vertical separation of antennas and height above ground to shape and direct the main lobe in a preferred direction. Antenna pole spacing influences the main lobe beamwidth. A narrower beamwidth can be obtained at the expense of transferring power to the side lobes which do not direct RF energy over the TA surface detector. Elevation angle is manipulated by antenna height above ground. Changing this parameter does little else to the main lobe. Elevation angle and beamwidth were selected to increase the probability that air shower $X_{\text{max}}$ would fall in the path of the main lobe where the charged particle density is the greatest. The 9° main lobe elevation angle is chosen such that the sounding wave illuminates the mean $X_{\text{max}}$ midway between transmitter and receiver for a distribution of showers (varying zenith angle) of order $10^{19}$ EeV.[5]

### 3.3.3 Measured Performance

The ability of an antenna to transmit energy is best characterized by the reflection coefficient $S_{11}$ (also called return loss when expressed in dB). It is a measure of the ratio of the voltage reflected from a transmission line relative to input. Large reflection coefficient implies significant energy is reflected back into the transmitter building which can interfere with other electronics, elevate ambient temperature and even damage the transmitter. Figure 3.10 shows the reflection coefficient for the Yagi array. It shows a return loss of -37.25 dB at the sounding frequency, which is excellent. $S_{11}$ of -20 dB or less is considered good.

To verify that the transmitting antenna is operating as designed, an RF power meter or similar device can be used to measure the power as a function of position relative to the antenna. This measurement is challenging because it must be performed in the far field of the antenna (typically $r \gg \lambda$). To fully probe the radiation pattern of the TARA transmitting antenna, power measurements must be made high above the ground since the main lobe is inclined 9° relative to horizontal.

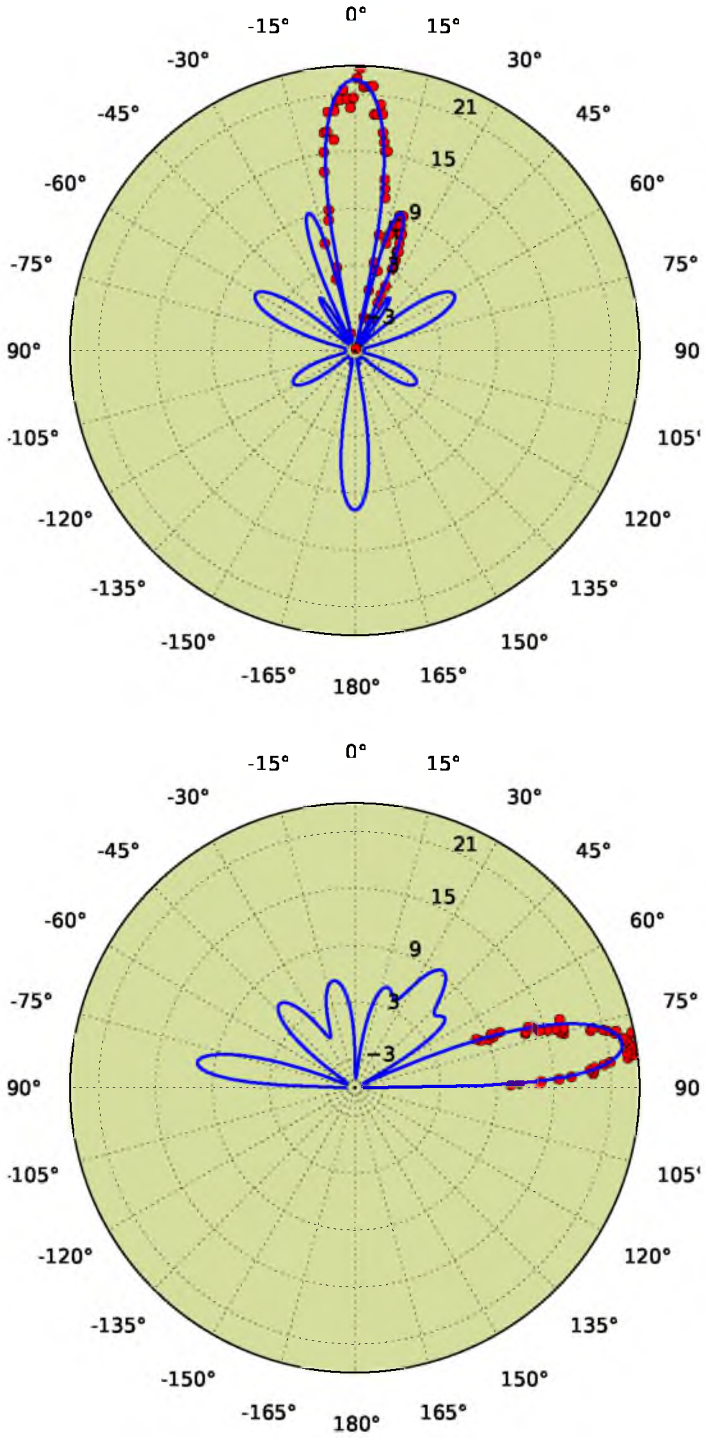

**Figure 3.9**: Simulated horizontal (top) and vertical (bottom) radiation patterns of the eight-Yagi TARA antenna array shown in blue. Red points are measured data that have been uniformly scaled to best fit the model. Forward gain is 22.6 dBi, beamwidth is 12° horizontal, 10° vertical, and the F/B ratio is 11.8 dB.

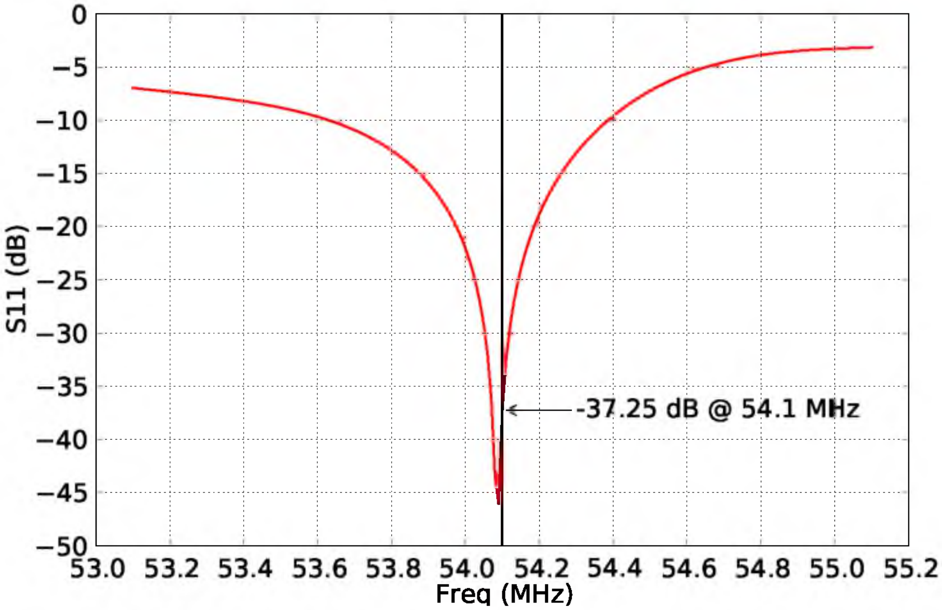

**Figure 3.10**: Reflection coefficient ($S_{11}$) for the eight-Yagi array.

Vertical radiation pattern measurements were taken by using antenna transmitting/receiving symmetry. A tethered weather balloon was floated with a custom battery powered 54.1 MHz signal generator that fed a dipole antenna. Over a range of discrete heights, received power was recorded at the output (normally the input) of the Yagi array.

The horizontal (azimuthal) radiation pattern was measured using a spectrum analyzer on the ground to determine the pointing direction and shape of the main lobe. Measurements of transmitted RF power were taken at distances between 650 and 1000 m radially from the center of the array. Power was measured along a road that does not run perpendicular to the pointing direction of the transmitter so a $1/r^2$ correction was made. Figure 3.9 shows the measured points for the horizontal and vertical patterns overlayed on the models. These measurements are all relative, not absolute, so a uniform scale factor was determined by minimizing $\chi^2$ between the model and data. The measured pattern agrees very well with the model in pointing direction and shape.

## 3.4 Receiver Antenna

The TARA receiver antenna site is located at the Telescope Array Long Ridge Fluorescence Detector (39° 12′ 27.75420″ N, 113° 7′ 15.56760″ W). Receiver antennas are dual-polarized log periodic dipole antennas (LPDA) designed to match the expected $< 100$ MHz signal frequency characteristics. Due to noise below 30 MHz and the FM band above 88 MHz, the effective band is reduced to 40 to 80 MHz. Each antenna channel is comprised of a series of six $\lambda/2$ dipoles. The ratio of successive dipole lengths is equal to the horizontal spacing between two dipoles (the defining characteristic of LPDA units), with the longest elements farthest from the feed-point to mitigate large group delay across the passband. Table 3.3 gives the lengths and positions of the antenna elements on the boom from the front edge to the back. All elements are constructed of aluminum tubing of 1/4″ outer diameter. Figure 3.11 shows a schematic of the receiver LPDA.

The impedance of the antenna against a 50 Ω transmission line was measured in an anechoic chamber at the University of Kansas. The standing wave ratio (SWR), the magnitude of the complex reflection coefficient ($S_{11}$), is shown as a function of frequency in Figure 3.12. An SWR of 3.0 implies greater than 75% signal power is transmitted from the antenna to the receiver at a given frequency.

The complex $S_{11}$ measurement also quantifies the *effective height* of the LPDA. The effective height translates the incident electric field strength in V/m to a voltage at the antenna terminals. It is given as $\mathbf{E_{inc}} \cdot \mathbf{h_{eff}} = |E_{inc}||h_{eff}|\cos(\theta) = V$, where $\theta$ is the polarization angle and the antenna is assumed to be horizontally polarized. The boresight effective height can be expressed[102] as

**Table 3.3**: Length and relative boom position of antenna elements of the TARA Log Periodic Dipole Antennas. All elements have a diameter of 0.25″.

| Element | Length (in) | Position (in) |
|---|---:|---:|
| 1 | 21.875 | 3.625 |
| 2 | 26.625 | 18.0625 |
| 3 | 32.5 | 35.625 |
| 4 | 39.625 | 57.0 |
| 5 | 48.3125 | 83.125 |
| 6 | 58.3125 | 115.0 |

**Figure 3.11**: Dual polarized TARA Log Periodic Dipole Antenna (LPDA).

$$h(\nu) = 2 * \sqrt{\frac{Gc^2|Z_{in}|}{4\pi\nu^2 Z_0}}. \tag{3.1}$$

In the effective height expression, $G$ is the measured gain of 12.6 dBi (see Figure 3.13), $c$ is the speed of light, $Z_{in}$ is the complex antenna impedance, $\nu$ is the frequency, and $Z_0 = 120\pi$ is the impedance of free space. In terms of the measured complex reflection coefficient $S_{11}$, the impedance is given by $|Z_{in}| = \left|\frac{1+S_{11}}{1-S_{11}}\right| 50\,\Omega$. The frequency-dependent magnitude of the effective height is plotted in Figure 3.14.

Receiver antenna gain is a factor in the bi-static radar equation that affects detection threshold. NEC was used in simulating the radiation pattern of the antenna to confirm directionality (see Figure 3.13). Simulated forward gain is 12.6 dBi and the vertical beamwidth is 23° at the carrier frequency, 54.1 MHz. Figure 3.15 displays measured beamwidth in the band of interest.

## 3.5 Receiver Front-end

There are three dual-polarization antennas at the receiver site, two of which are currently connected to the DAQ (Section 3.6). RF signal from the antennas pass through a bank of filters and amplifiers. The components include an RF limiter (VLM-33-S+; Mini-Circuits), broad band amplifier, low pass filter (NLP - 100+; Mini-

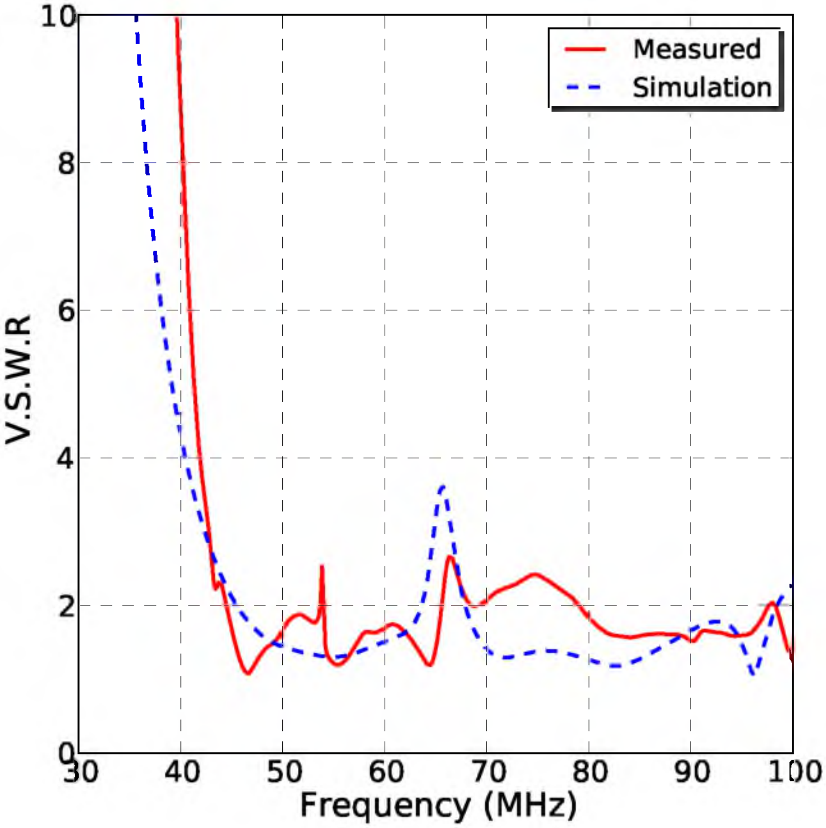

**Figure 3.12**: SWR of a horizontally polarized TARA LPDA as measured in an anechoic chamber.

Circuits), high pass filter and an FM band stop filter (NSBP-108+; Mini-Circuits). Both polarizations from one antenna are filtered (37 MHz cutoff frequency high pass filter, SHP-50+; Mini-Circuits) and amplified (40 dB, ZKL-1R5+; Mini-Circuits) at the antenna, where a bias tee (ZFBT-4R2G+; Mini-Circuits) is used to bring DC power from the control room. The second antenna's channels are filtered (25 MHz high pass filter, NHP-25+; Mini-Circuits) and amplified (30 dB, ZKL-2R5+; Mini-Circuits) inside the control room. The lightning arrester (LSS0001; Inscape Data) minimizes damage to sensitive amplifiers by electric potentials that accrue during thunderstorms. The RF limiter prevents damage by transient high amplitude pulses (see Section 3.6.2).

Signal conditioning in the amplifier/filter banks is characterized by the transmission coefficient (Figure 3.16) $S_{21}$. It is a measure of the ratio of the voltage at the end

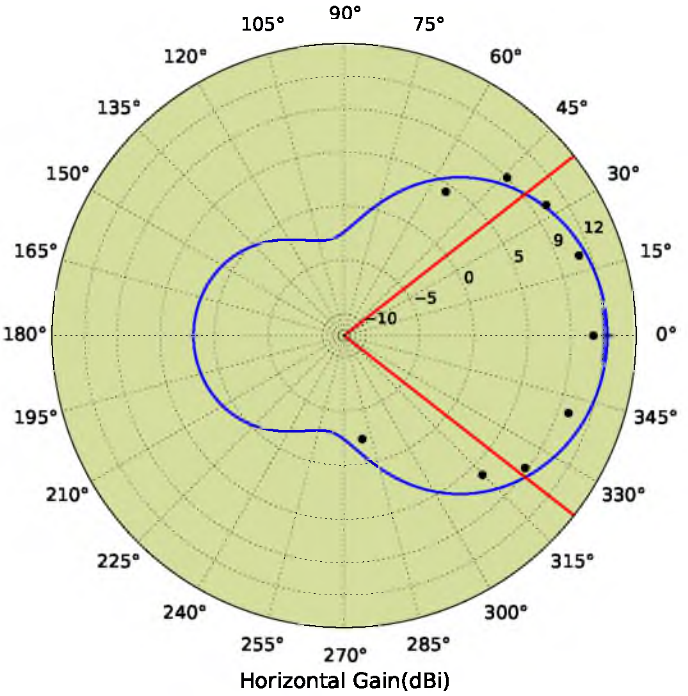

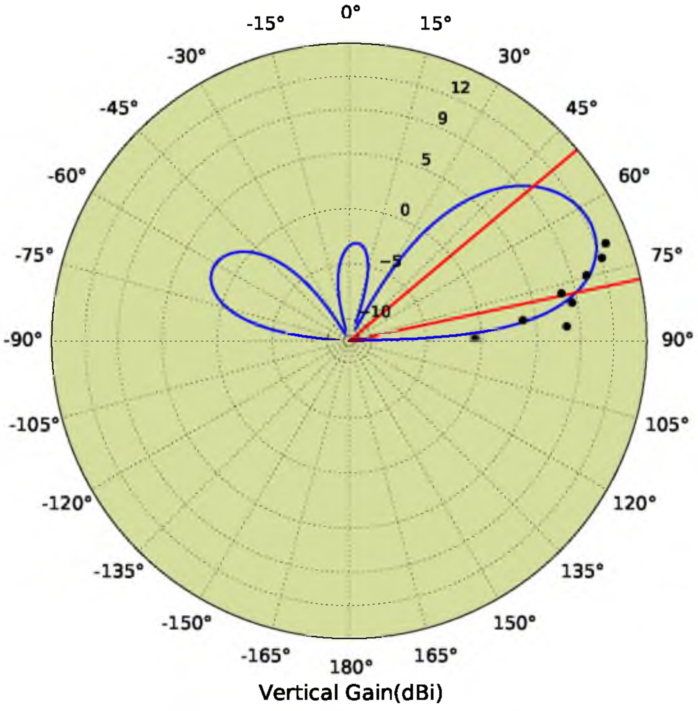

**Figure 3.13**: Simulated horizontal (top) and vertical (bottom) radiation pattern of a horizontally polarized TARA LPDA at the transmitter sounding frequency of 54.1 MHz. Beamwidths (−3 dB below peak gain) are shown with red lines. Peak gain is 12.6 dBi.

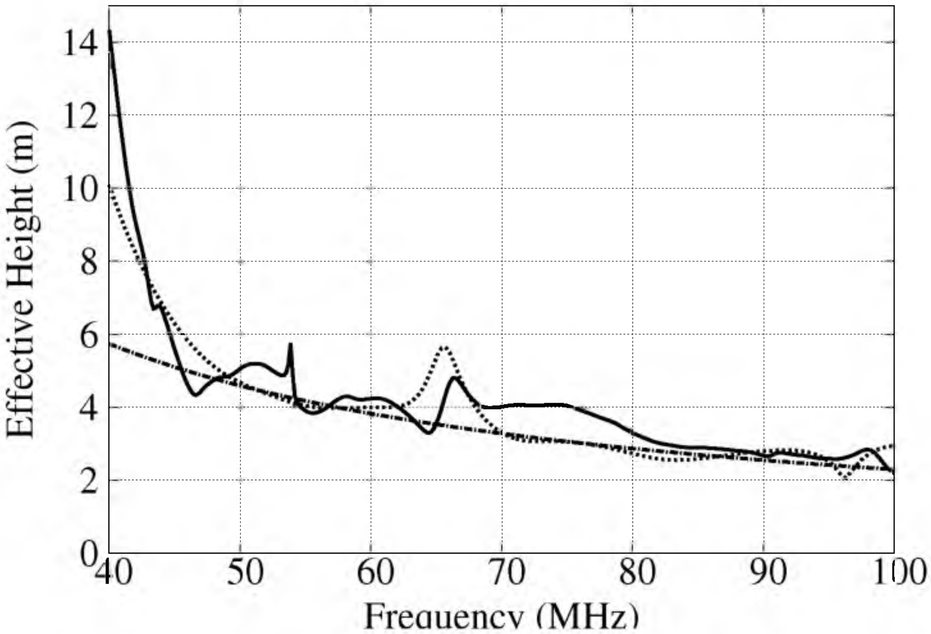

**Figure 3.14**: Effective height in meters vs. frequency in MHz of the TARA receiver LPDA. The $S_{11}$ parameter and gain of the receiver antenna are inserted into Equation 3.1 and plotted vs. frequency using the anechoic chamber data (solid line), simulated data from NEC (fine dashed), and simulated data with the 54.1 MHz values of $S_{11}$ and gain held constant (dot-dashed line).

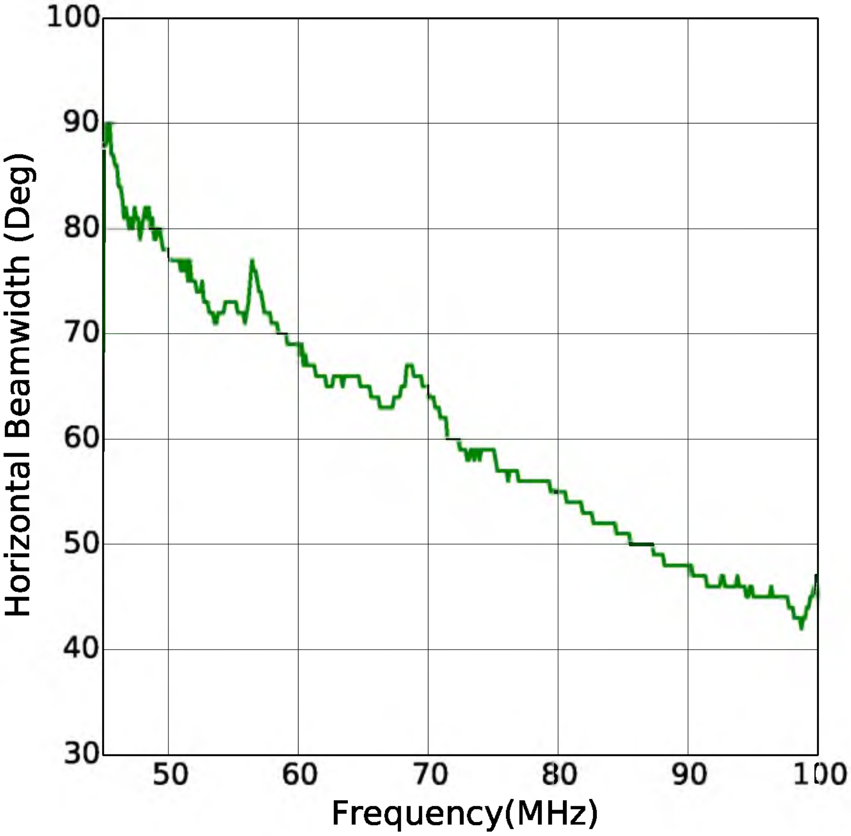

**Figure 3.15**: Beamwidth of a single channel LPDA as measured in an anechoic chamber at the University of Kansas.

of a transmission line relative to the input. Impedance mismatch relative to a 50 Ω transmission line, insertion loss for the various devices and gain from the amplifiers are combined in $S_{21}$ data. Of note in Figure 3.16 is the flat, high-gain (30 dB), broadband ($\simeq$ 40 MHz) passband necessary for Doppler-shifted radar echoes.

In any RF receiver system, sensitivity is limited by the combination of external noise entering through the antenna and internal noise from various sources like low noise amplifiers and other resistive losses from filters, cables and couplers. Noise entering the antenna is generated by the sky, earth and antenna resistive loss. Diffuse radio noise from the galactic plane is nonpolarized and is the dominant noise source in the TARA frequency band. Figure 3.17 shows diurnal variation in the snapshot (forced trigger, 1 $\text{min}^{-1}$) spectrum that remains consistent in data taken six months apart. Each plot shows the Power Spectral Density (PSD, units of dBm/Hz) averaged over eight days versus Local Mean Sidereal Time (LMST). Horizontal and vertical error bars are bin width and std. dev. of the mean, respectively. The effects of amplifiers and cable losses have been removed such that absolute received power is shown. Data taken in December, 2013 are shown in the top plot, with those recorded

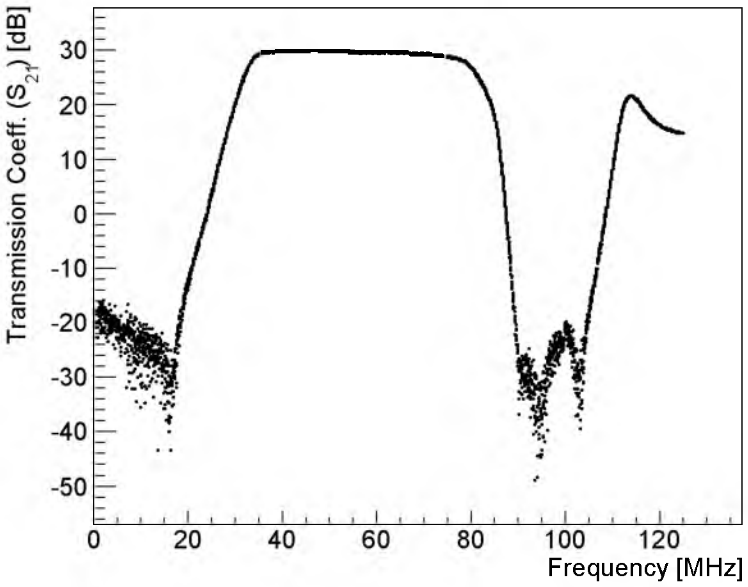

**Figure 3.16**: $S_{21}$ (transmission coefficient) of the filter and amplifier bank connected to the triggering channel of the DAQ.

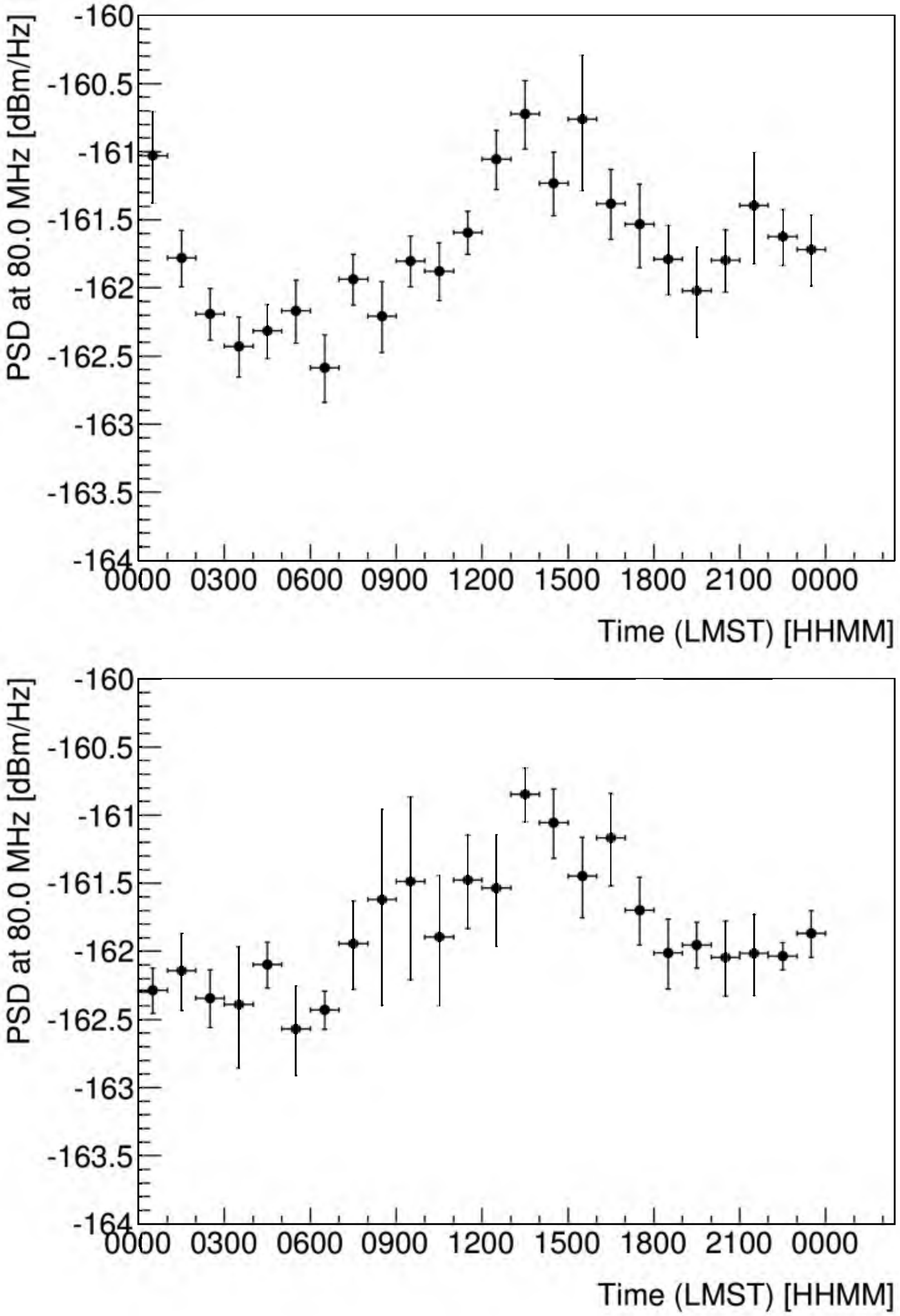

**Figure 3.17**: Snapshot (forced trigger) Power Spectral Density (PSD) at 80.0 MHz averaged over eight days versus Local Mean Sidereal Time (LMST). Top: Data taken in December, 2013. Bottom: Data taken in May, 2014. There is strong correlation in peak PSD and sidereal time which indicates the signal is galactic in origin. Horizontal error bars show bin width. Vertical error bars are std. dev. in the mean.

in May, 2014 shown in the bottom plot. We observe that the peak occurs at the same time and power in each plot. Our conclusion is diurnal fluctuations are caused by changing perspective on the galactic center.

By accounting for amplifier and instrumental gains and losses, the observed noise background can be compared with the irreducible galactic noise background[103] across the passband. Our average measured system noise is calibrated by removing the effects of individual components in the receiver RF chain from average snapshot spectra to determine the absolute received power. Without any other scaling, our corrected received power compares nicely with the galactic noise standard[17] (Figure 3.18). Important components for which adjustments were made include filters and amplifiers via the measured transmission coefficient $S_{21}$ and LMR-400 transmission line with attenuation data. Anthropogenic noise sources are transient and stationary noise is absent within our measurement band due to the receiver site's remote location. In this frequency region, galactic noise dominates thermal and other noise sources.

## 3.6 Receiver DAQ

### 3.6.1 DAQ Structure

The National Instruments FlexRIO system provides an integrated hardware and software solution for a custom software defined radio DAQ. It is composed of three basic parts: adapter module, FPGA module and host controller (as shown in the lower box of Figure 3.19). A description of each of these subsystems follows.

The NI-5761 RF adapter module is a high-performance digitizer that defines the physical inputs and outputs of the DAQ system. It digitizes four analog input channels at a rate of 250 MS/s with 14-bit resolution. Eight TTL I/O lines are available for additional control, some of which are used in custom DAQ triggering schemes.

The NI-7965R FPGA module is based on the PXI express platform which uses a Xilinx Virtex-5 FPGA with 128 MB on board DRAM. FPGA design provides accurate timing and intelligent triggering. The PXI-express platform has a high-speed data link to the host controller, which is connected to the development machine, a Windows based computer, which uses the LabVIEW environment to design and compile FPGA code. A host controller application, also designed in LabVIEW, runs on the development machine.

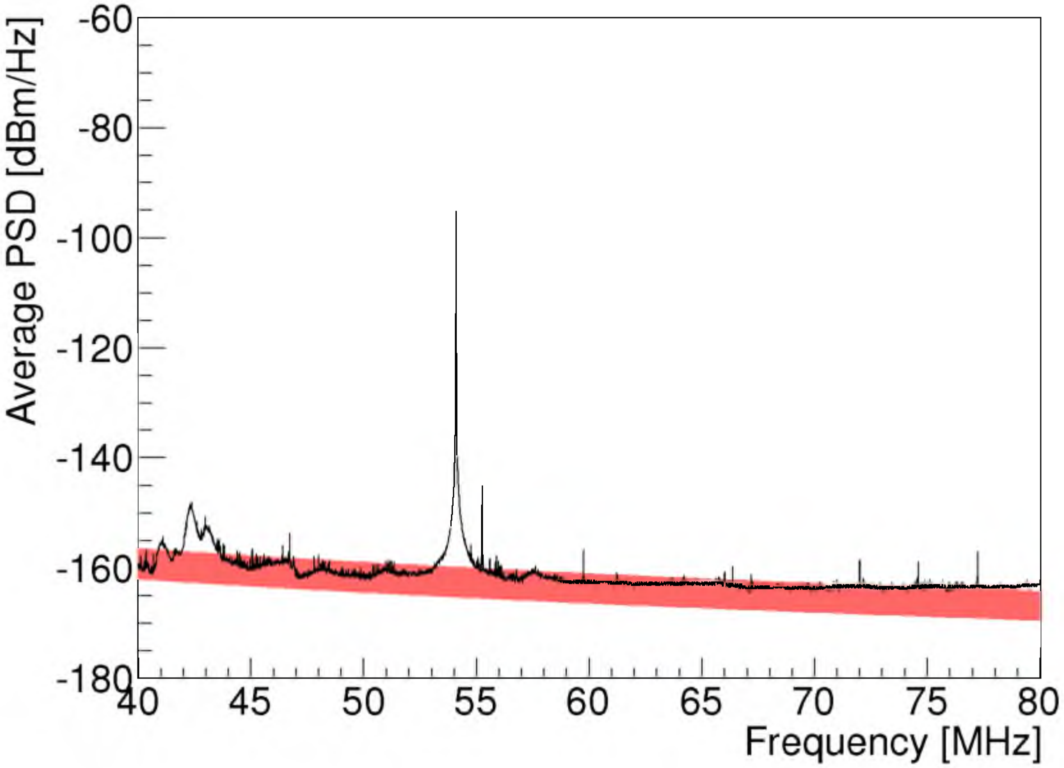

**Figure 3.18**: Average receiver system (black) Power Spectral Density (PSD) in dBm/Hz superimposed with a fit to measured galactic background noise and its associated error[17] (red band). System attenuation, filters and amplifiers were accounted for to determine absolute received power. No other calibration or scaling was applied to the receiver data.

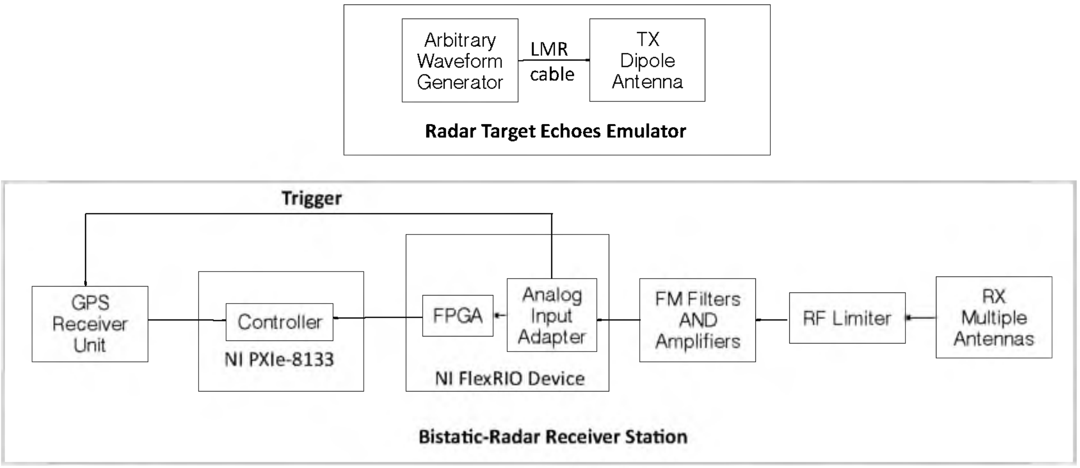

**Figure 3.19**: Elements of the radar receiver station.

### 3.6.2 Design Challenges

Based on the high velocity of the radar target, echoes are excepted to be characterized by a rapid phase modulation-induced frequency shift, covering tens of MHz in 10 $\mu$s. As the magnitude of the Doppler blue shift decreases as the shower develops in the atmosphere, these signals sweep (approximately) linearly from high to low frequency and are categorized as linear-downward chirp signals. Echo parameters are dependent on the physical parameters of the air showers. Thus, unlike existing chirp applications, we are interested in the detection of chirp echoes of variable amplitude, center frequency and frequency rates within a relatively wide band. In addition, the detection threshold must be minimized in order to increase the probability of detecting radar echoes with SNR less than one.

Furthermore, UHECR events are rare and random in time. TA receives only several $> 10^{19}$ eV events per week, so background noise and spurious RF activity dominate.

Figure 3.20 shows a spectrogram of data acquired in the field using the complete receiver and test system (Figure 3.19), where FM radio and noise below $\sim$ 30 MHz are filtered out. The time-frequency representation shows that the background noise of our radar environment is rich with multiple undesirable components including stationary tones outside the 40-80 MHz effective band located at 28.5 MHz and, inside the band, the carrier at 54.1 MHz as well as broadband transients. Sudden amplitude modulation of stationary sources and powerful, short-duration broadband noise can cause false alarms. A robust signal processing technique is needed to confront these challenges.[104]

### 3.6.3 DAQ Implementation

The DAQ is designed to detect chirp echoes and confront the problem of a variable noise environment. Two antennas feed the DAQ's four input channels. Each antenna is a dual-polarized LPDA (Section 3.4) with one output channel each for horizontal and vertical polarization. Data are collected simultaneously from each of the four analog channels with one horizontal channel considered the triggering channel, then sampled using a 250 MS/s ADC (Texas Instruments; ADS62P49). Analog to digital conversion is followed by fast digital memory storage on the FPGA chip, which stores

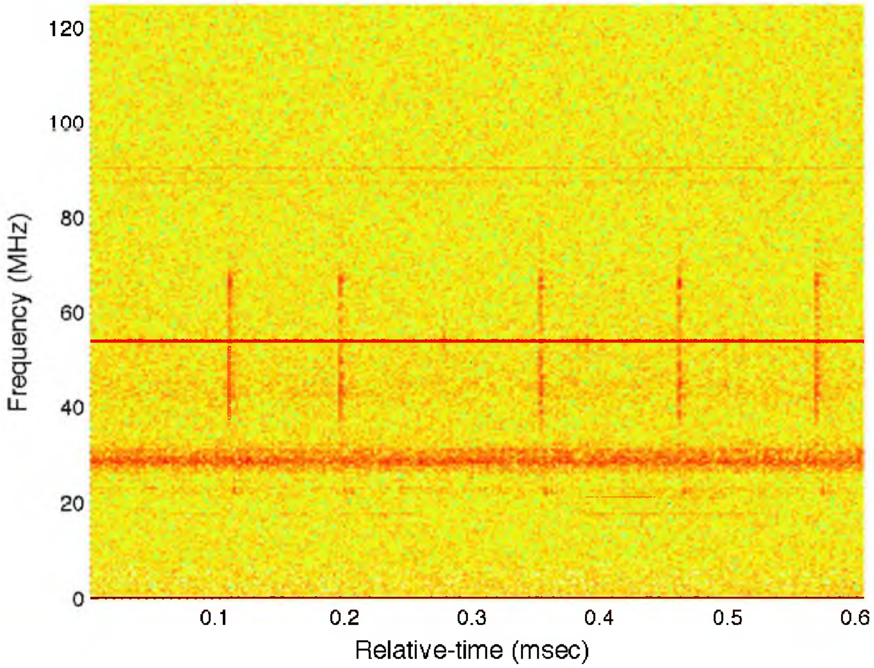

**Figure 3.20**: Spectrogram of background noise at the receiver site. Frequency and time are on the vertical and horizontal axes, respectively, with color representing the power in a particular frequency component. The carrier signal is represented by the horizontal line at 54.1 MHz. Broadband transients are the vertical lines and stationary noise sources are the horizontal band near 30 MHz.

the incoming samples from each channel sequentially, in a 131 $\mu$s (32744 sample) continuous circular buffer such that data in each buffer are continually overwritten. Three distinct trigger modes are implemented: "snapshot," "Fluorescence Detector (FD) external," and "matched-filter bank."

When a trigger occurs, the circular buffer information is sent to the host controller to be permanently stored on the computer's disk. A 320 $\mu$s dead-time is required to transfer data from a buffer to FPGA memory, during which the DAQ cannot accept triggers. Sustained maximum trigger rate is 50 Hz due to FPGA-to-host data transfer limitations. As depicted in Figure 3.21, *pre/post* trigger acquisition is set to 95 $\mu$s and 36 $\mu$s, respectively, to allow for delay and jitter in the FD trigger timing (33 $\mu$s delay, 1 $\mu$s jitter) and sufficient post-trigger data to see an entire echo wave form. A GPS time stamp is retrieved from a programmable hardware module[18] and recorded for each trigger with an absolute error of ±20 ns.

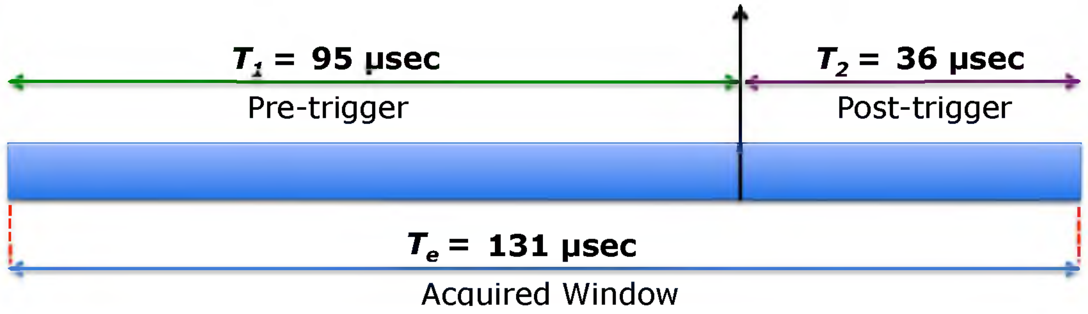

**Figure 3.21**: Position of the triggering pulse within the data window that is written to disk.

The snapshot trigger is an unbiased trigger scheme initiated once every minute that writes out an event to disk. These events will (likely) contain background noise only. Unbiased triggers are crucial for background noise estimation and analysis.

During active FD data acquisition periods, the Long Ridge FD (the location of the TARA receiver site) emits a NIM (Nuclear Instrumentation Module) pulse for each low level trigger with a typical rate of $\sim$ 3–5 Hz or much higher during FD calibration periods. The low level trigger is an OR of individual FD telescope mirror triggers. Dead time due to high FD-trigger rates are as high as several milliseconds during calibration periods. This does not reduce data acquisition time significantly because these periods occur only for several minutes and less than half a dozen times per FD data acquisition period. Further, FD operation only amounts to 10% duty cycle on average. The FlexRIO is forced to trigger by each pulse received from the FD. Each FD run will result in many thousands of triggers which can be narrowed to several events that coincide with real events found in reconstructed TA data.

The matched filter (MF) bank is a solution for the problem of detecting radar chirp echoes in a challenging noise background using signal processing techniques. The signal of interest is assumed to be a down-chirp signal that has duration $T_c$ seconds with a constant amplitude, start (high) frequency $f_{\mathrm{H}}$, center frequency $f_{\mathrm{C}}$, end (low) frequency $f_{\mathrm{L}}$ and chirp rate $\kappa$ Hz/sec. An example of the signal of interest is shown in Figure 3.22. Assuming that it is centered around time $t = 0$, such a chirp signal is written as

$$s(t) = \mathrm{rect}\left(\frac{t}{T_c}\right)\cos(2\pi f_{\mathrm{C}} t - \pi\kappa t^2)\,, \tag{3.2}$$

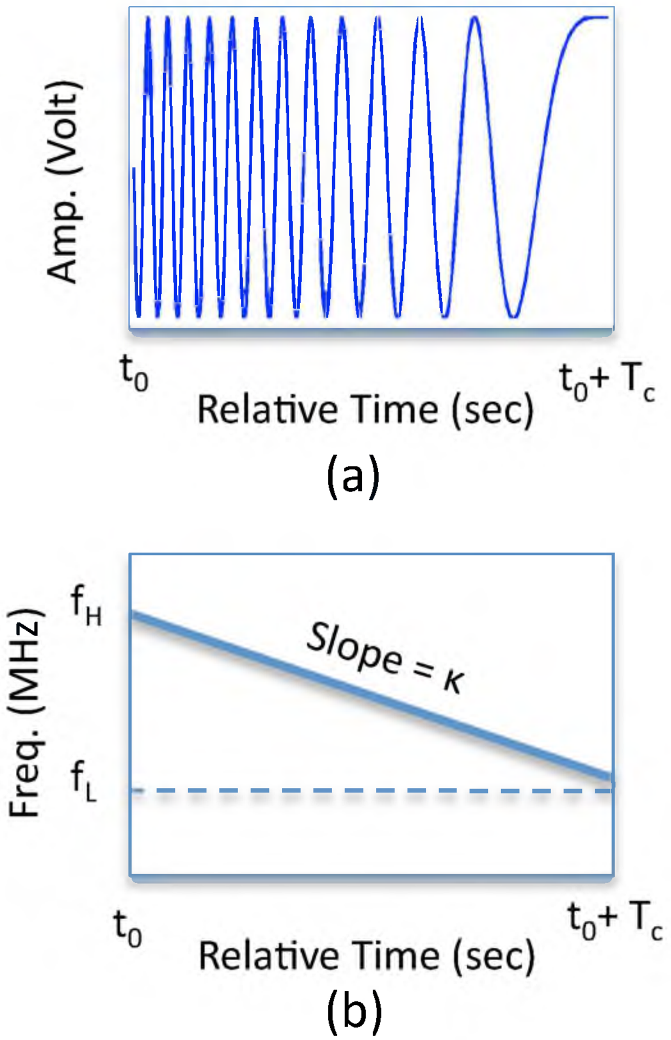

**Figure 3.22**: Linear down-chirp signal. (a) Signal in time-domain. (b) Signal in time-frequency domain.

where

$$\mathrm{rect}(x) = \begin{cases} 0 & \text{if } |x| > \frac{1}{2} \\ \frac{1}{2} & \text{if } |x| = \frac{1}{2} \\ 1 & \text{if } |x| < \frac{1}{2} \end{cases} \tag{3.3}$$

is the rectangle function and $t$ is the time in seconds.

We limit our interest to detecting the presence of $s(t)$ within a certain bandwidth, without prior knowledge of the chirp rate $\kappa$. Based on simulation of the physical target, reflected echoes are expected to have a peak amplitude within or near the range [60-65] MHz. Thus, we consider $f_{\mathrm{H}}$ to be 65 MHz and $f_{\mathrm{L}}$ to be 60 MHz.

Since the chirp rate varies, we use a bank of filters matched to a number of quantized chirp rates, $\kappa_1$, $\kappa_2$, $\cdots$, $\kappa_M$. A functional block diagram of the detection process is illustrated in Figure 3.23.

Let $\mathbf{y}_m$ denote the output samples of the $m$th matched filter and $\gamma_m$ the threshold at the filter output. As depicted in Figure 3.23, a trigger decision is made at the output of the matched-filter bank by comparing magnitudes of the elements of $\mathbf{y_1}, \mathbf{y_2}, \cdots, \mathbf{y_M}$, each, against the corresponding threshold levels $\gamma_1, \gamma_2, \cdots, \gamma_M$, respectively.

Threshold levels are defined as $n_\gamma$ units of the signal level (equivalently, noise standard deviation) at the output of each filter, denoted by $\sigma_m$ for the $m$th matched filter. Every time a trigger condition (the presence of a chirp) is met, an event is declared. Since the background noise level varies with time, $\sigma_m$ is measured every five seconds to maintain a constant data acquisition rate.

The most probable chirp-rate interval for a distribution of simulated radar echoes is $\mathcal{K} = [-3, -1]$ MHz/$\mu$s. We choose $M = 5$ and the chirp rates (in MHz/$\mu$s) as

$$\kappa_1 = -1.1161, \kappa_2 = -1.3904, \kappa_3 = -1.7321,$$

$$\kappa_4 = -2.1577, \kappa_5 = -2.6879\,.$$

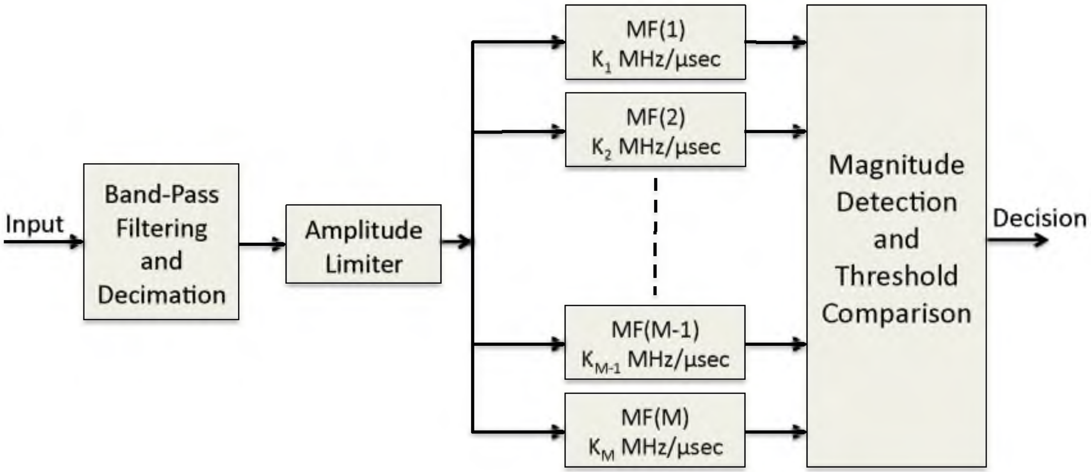

**Figure 3.23**: Block diagram of the matched-filter-type detector.

#### 3.6.3.1 Amplitude Limiter

Radio background at the remote receiver site is clear of stationary interference signals in the frequency band of interest, 40–80 MHz. Therefore, the broadband transients mentioned in Section 3.6.2 are the primary source of false alarms. Consequently, the threshold of the MF detector must be raised in order to maintain the desired false alarm rate. The result is high data rate in return for low trigger thresholds. A digital amplitude limiter applied immediately before the input to the MF detector helps to minimize false alarms while keeping the detection threshold as low as possible and without significantly degrading detection efficiency.

The amplitude limiter clips the amplitude of the received signal to a fraction $k$ of its RMS value before further analysis. Its mathematical expression is

$$\begin{cases} y = x, & |x| < k\sigma_s \\ y = k\sigma_s, & x > k\sigma_s \\ y = -k\sigma_s, & x < -k\sigma_s. \end{cases} \tag{3.4}$$

where $x$ is the raw input, $y$ is the amplitude limited output, and $\sigma_s$ is the RMS value of the signal before clipping. The result is a reduced relative power ratio of the spurious impulses to the nonperturbed background. Clipping also lowers the waveform RMS in proportion to the clipping level.

#### 3.6.3.2 Band-Pass Filtering

We observe considerable CW noise within the 40–80 MHz band, including the carrier signal. The carrier and other persistent tones can have large amplitudes and lead to high matched filter RMS output which can, as shown in the next section, prevent detection of low SNR chirp signals. Such tones, including the carrier, can be easily filtered out. Before the amplitude limiter, a narrow band-pass filter eliminates all frequencies outside a 60-65 MHz band with -80 dB stop band attenuation. Data stored in the ring buffer are not filtered this way.

### 3.6.4 Performance Evaluation

Detection performance of the MF detector has been evaluated under two test signal conditions: noise only or signal plus noise. For each test, the Boolean result of the threshold comparison with the MF outputs is recorded. The probability of signal plus noise exceeding MF thresholds is the efficiency and the average rate of erroneous detection decisions caused by filtered noise is false alarm rate.

The ability to detect a received chirp signal in background noise depends on the ratio of the signal power to the background noise power. Radar carrier power dominates the background so two quantities are used to describe the background noise. First, we define the ratio of the test chirp signal power to the radar carrier power as the signal-to-carrier ratio (SCR). Second, we use either the SNR (Equation 2.28) or ASNR (Equation 2.29), depending on the type of test chirp signal input to the matched-filter bank, after filtering out the powerful carrier signal.

Consider the following observations about performance analysis. First, it is clear that system performance depends on the chosen threshold level $n_\gamma$ (user defined, a multiple of $\sigma_m$ as defined previously) for each SNR value. False alarm rate is expected to decrease as the threshold level increases, at the expense of detection efficiency of low SNR chirp signals. Conversely, detection efficiency increases as the threshold decreases. Second, the false alarm rate is expected to decrease as the amplitude limiter level decreases because high amplitude transients are effectively removed. To this date, radar echoes from CR air showers have not been detected, so it's unlikely that the EAS cross section is large enough to produce such large amplitude impulses. Therefore such signals are dismissed *a priori*. Our strategy is to choose the threshold and amplitude limiter level that gives high detection efficiency for a given SNR and low false alarm rate.

Two tests are conducted to determine the ideal amplitude limiter level and the efficiency as a function of MF threshold. The goal of the first test is to measure the average false alarm rate of the non-Gaussian noise environment and evaluate the improvement that could be achieved by adding the amplitude limiter. Results are shown in Figure 3.24 for three different amplitude limiter levels, which clearly show that the limiter level has a significant effect on the false alarm rate. Efficiency curves for different amplitude limiter levels (described in the next paragraphs) show that the amplitude limiter does not *decrease* detection performance of chirp signals, although they are also clipped.

Consider the following interpretation of Figure 3.24. In order to achieve a 2 Hz

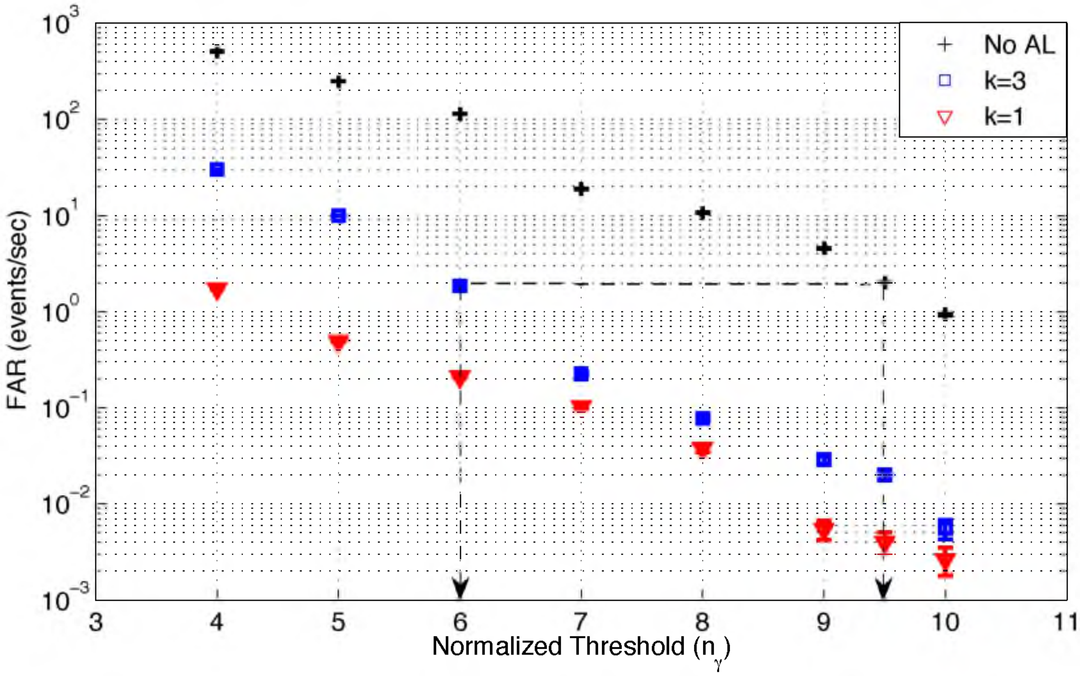

**Figure 3.24**: False alarm rate versus relative threshold ($n_\gamma$ units of the standard deviation at each filter output) for different amplitude limiter levels.

false alarm rate, $n_\gamma$ has a value of six for $k = 3$ and 9.5 for $k = 10$ (black dashed line). Thus, detection thresholds can be decreased which enhances positive detection of low SNR signals.

The second test applies a theoretical chirp signal with various chirp rates and SNR values that correspond to a reasonable false alarm rate. Based on data storage and postprocessing computational requirements, we have decided that a false alarm rate of $\sim$ 1 Hz is reasonable. Artificially generated chirp signals are transmitted *in situ* to the receiving antennas by an arbitrary waveform generator (AFG 3101; Tektronix, Inc.) and a dipole antenna. Both linear chirp signals and a simulated radar echo (see Section 2.5) are used in measuring detection performance.

#### 3.6.4.1 Linear Chirp Signal

A periodic, linear chirp with -1 MHz/$\mu$s rate is embedded in a real receiver site background wave form. Figure 3.25 shows the spectrogram of a chirp embedded with -10 dB SNR and -40 dB SCR value.

Figure 3.26 shows detection performance for a 2 Hz false alarm rate. Efficiency

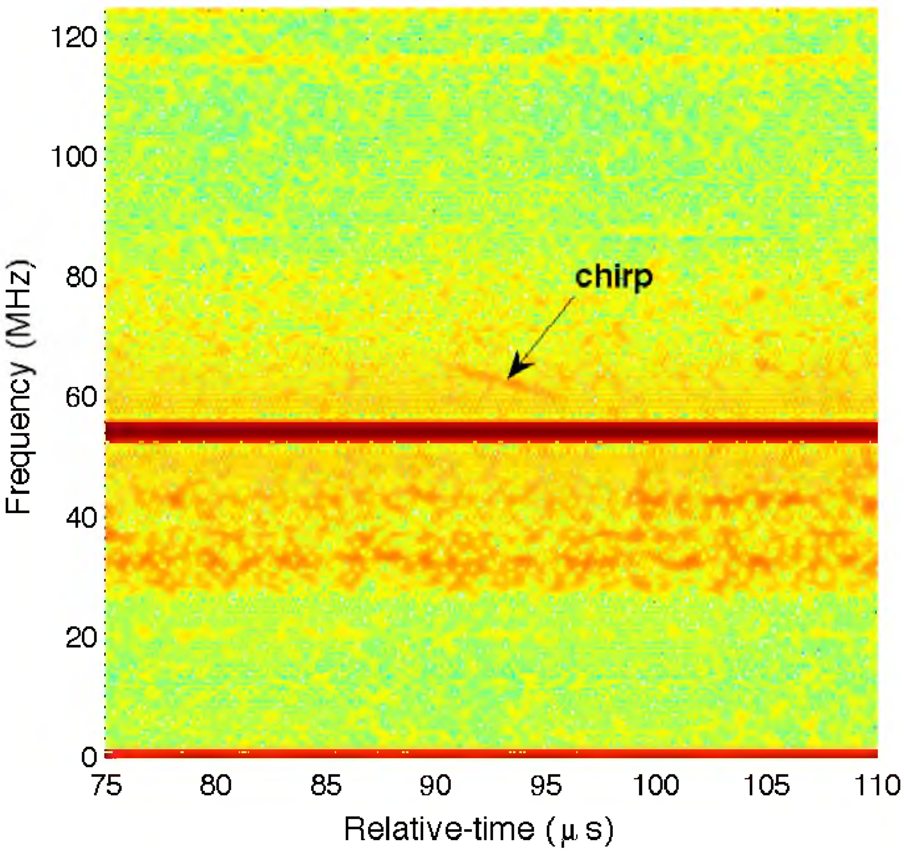

**Figure 3.25**: Time-frequency (spectrogram) representation of a linear, −1 MHz/$\mu$s, -10 dB SNR received chirp signal as recorded by the DAQ system.

is shown for cases where the amplitude limiter is removed and at two different levels that result in the same false alarm rate, each with different threshold levels. The minimum SNR for which complete detection is achieved is 5 dB when no amplitude limiter is applied, 0 dB for $k = 10$ (*soft clipping*), -6 dB for $k = 3$ (*hard clipping*). These results imply that by using the amplitude limiter, high detection performance can be achieved with low complexity. To maximize detection ability, the amplitude limiter is currently fixed at $k = 3$.

#### 3.6.4.2 Simulated Air Shower

In a more realistic test, a simulated radar echo from a 10 EeV air shower inclined 30° out of the $TX \rightarrow RX$ plane and located midway between the transmitter and receiver is scaled and transmitted to the receiving antennas using a function generator. Figure 3.27 shows a spectrogram of the received waveform with 5 dB ASNR and

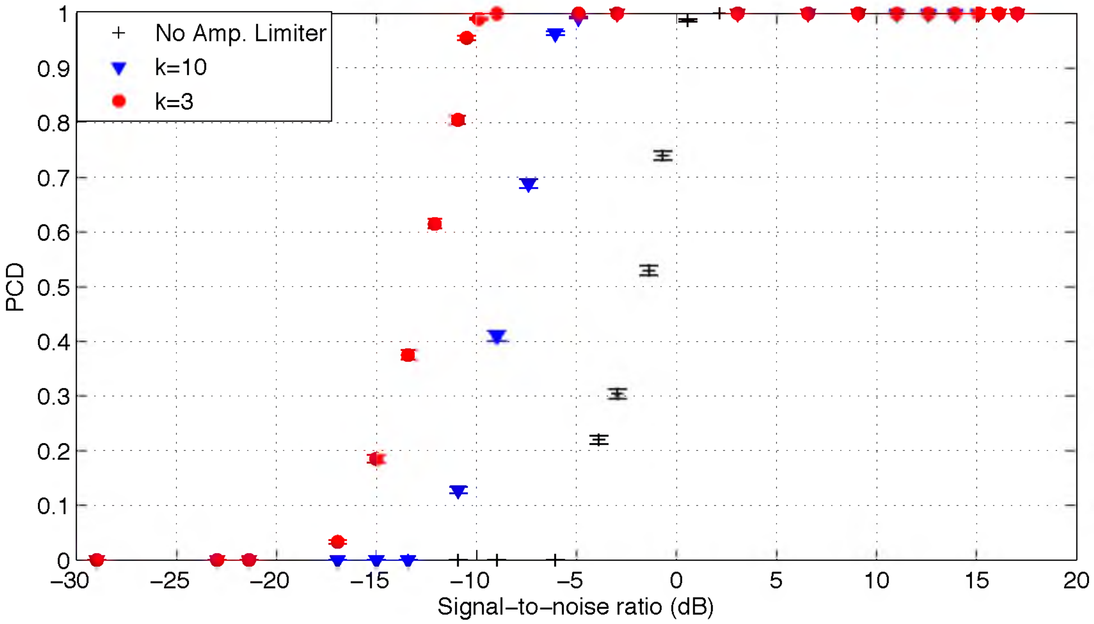

**Figure 3.26**: Probability of detection for the matched-filter-type detector with $n_\gamma = 6$.

-25 dB SCR. The echo is broadband (about 25 MHz) and short in duration (10 $\mu$s). Detection efficiency of the emulated chirp is shown in Figure 3.28. The minimum ASNR for which complete detection is achieved is -7 dB.

## 3.7 Conclusion

The TARA detector is designed to search for cosmic ray radar echoes with very small radar cross sections (RCS). Specifically, the following characteristics strongly reduce the minimum detectable RCS: high transmitter power (40 kW, Section 3.2), high-gain transmitter antenna (22.6 dBi, 182 linear, Figure 3.9), low noise RF environment consistent with galactic backgrounds (Figure 3.18, Section 3.4), innovative triggering scheme that permits detection of signals 7 dB below the noise (Section 3.6.4.2), and broadband receiver antenna (12.6 dBi gain, 18.2 linear, Figure 3.13).

Figure 3.29 shows a calculation of the minimum detectable TARA RCS for a cosmic ray Extensive Air Shower (EAS) located in several positions along a line perpendicular to the transmitter/receiver plane, midway between the transmitter and receiver. The bi-static radar equation (Equation 2.1) permits this simple calculation that assumes a constant power radar echo self-triggered in the DAQ 5 MHz

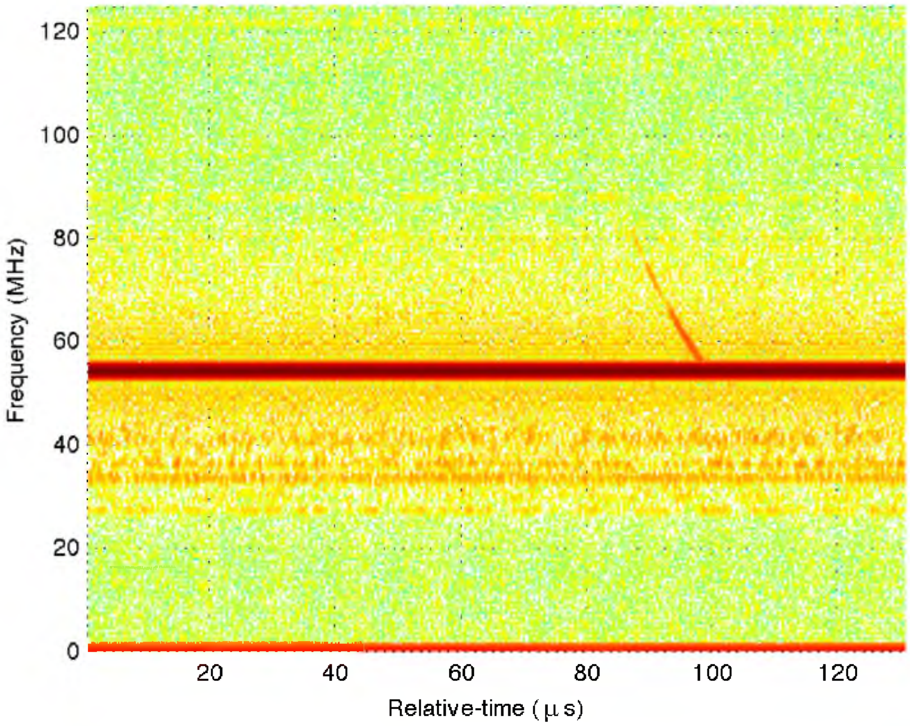

**Figure 3.27**: Spectrogram of simulated air shower radar echo with 5 dB ASNR. The radar echo is from a simulated shower inclined 30° out of the $TX \rightarrow RX$ plane and located midway between the transmitter and receiver.

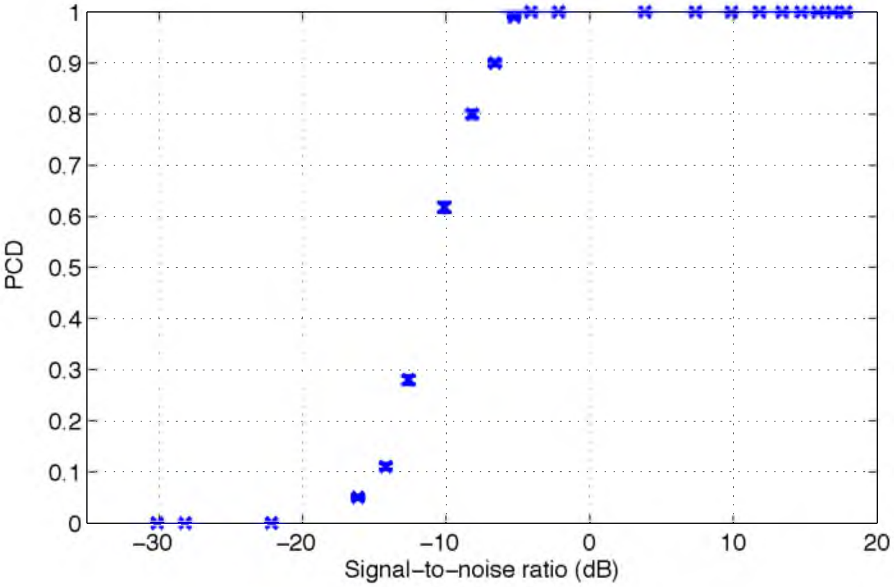

**Figure 3.28**: Probability of correct detection for the matched-filter detector using $n_\gamma = 6$ for a simulated air-shower echo that is scaled and emulated with a function generator.

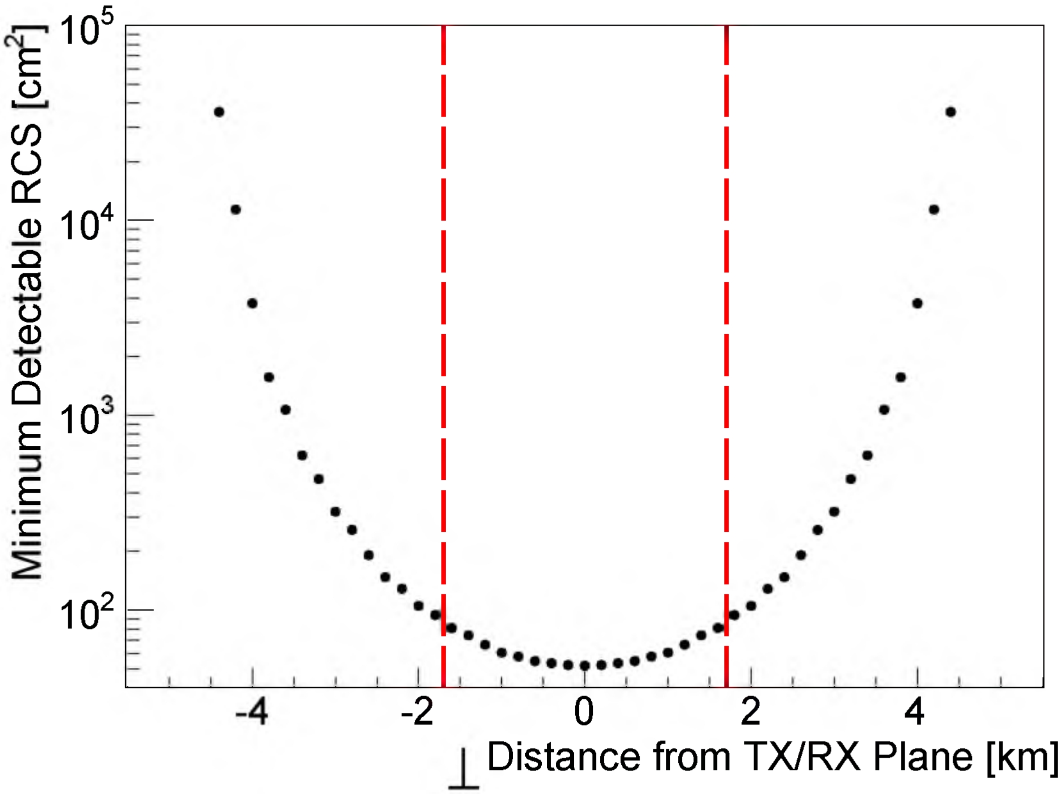

**Figure 3.29**: Minimum detectable radar cross section (RCS) as a function of distance perpendicular to the plane connecting the transmitter and receiver. The transmitter antenna main lobe points along this plane. For simplicity, the minimum RCS is calculated from the bi-static radar equation (Equation 2.1) for a cosmic ray air shower midway between transmitter and receiver with maximum transmitter and receiver gains. The 5 MHz FlexRIO passband trigger scheme (Section 3.6.3.2) was assumed to detect a constant amplitude radar echo with chirp rate in [-3,-1] MHz/$\mu$s (Section 3.6.3) and signal-to-noise (SNR) ratio 7 dB (Section 3.6.4.2) below background noise (Figure 3.18, Section 3.4), the empirical detection performance for the 5 MHz DAQ passband. Further assumptions are ground-level detection and constant wavelength $\lambda$. Vertical dashed red lines show the -3 dB beamwidth of the transmitter antenna.

band (Section 3.6.3.2) with chirp rate in [-3,-1] MHz/$\mu$s (Section 3.6.3). Maximum transmitter/receiver gains are used for each point, given the azimuthal position of the shower core location. Further, the signal is assumed to have constant wavelength and is Doppler-shifted into the DAQ [60,65] MHz band, for which the -7 dB noise floor correction is appropriate, and scattered near the ground (to simplify distance calculation).

The TARA project represents the most ambitious effort to date to detect the radar signature of cosmic ray induced atmospheric ionization. These signals will be characterized by their low power, large Doppler shift (several tens of MHz), and short duration ($\sim 10\ \mu$s). TARA combines a high-power transmitter with a state-of-the-art high sampling rate receiver in a low-noise environment in order to maximize the likelihood of cosmic ray echo detection. Importantly, TARA is co-located with the Telescope Array astro-particle observatory, which will allow for definitive confirmation that any echoes observed are the result of cosmic ray interactions in the atmosphere.

# CHAPTER 4

# DATA DESCRIPTION AND ANALYSIS TECHNIQUES

The DAQ records custom binary files that each contain 1,000 triggers. Each binary file has a meta-data header that describes the contents of the file. The resulting data are a series of individual trigger data comprised of a header and four waveforms. The header contains information about the type of trigger and triggering information like the current MF thresholds and the actual value of each of the five MFs at the triggering time. An ASCII file containing the time stamps of each trigger is simultaneously and asynchronously written to disk.

A GPSY[18] (referred to as "gypsy") GPS event logger is used to precisely record the time stamps of any DAQ triggers with an absolute error of ± 20 ns. Triggers that occur during a second are sent over the network at the beginning of the following second. During the first second, the DAQ was recording triggers, so the two data streams cannot be combined into the same file. In the data parsing step, all triggers that occur in a binary file are discarded if the quantity does not match the number of time stamps found in the time stamps file due to ambiguity in matching. The occurrence of mismatched time stamps is infrequent. Also note that the number of waveform triggers need not be 1,000. It is possible the DAQ is stopped before a file reaches 1,000: The only condition is that the quantity of triggers and time stamps match.

Binary and time stamps data are parsed into ROOT[105] files with the header information. The ROOT data analysis framework simplifies analysis by supplying many classes and functions to select, plot, and read and write data to disk. Once data are parsed, nothing more is done until the main analysis chain begins. At this level of data processing, all three types of triggers are ready for analysis.

All trigger modes record four waveforms 130.976 $\mu$s in duration, or 32,744 samples at 250 MS/s. As described in Section 3.6, two LPDA antennas feed the DAQ. Two polarizations, horizontal and vertical, from each antenna comprise the four inputs. We have chosen the horizontal polarization from the first antenna to be the triggering channel used in the self-triggered data stream. Data from this channel are used in the present analysis.

## 4.1 FD-triggered Data

The Long Ridge fluorescence detector only operates on good weather nights when the moon is below the horizon. Cloud cover must be very sparse or non-existent. FD data acquisition occurs roughly during two weeks per month. Unless the moon is below the horizon for at least three hours, the detector is not turned on. An "FD run" is the series of nights during the month when the detector is turned on and data are acquired. Naturally, the TARA FD-triggered data are sorted and analyzed in groups that correspond to FD runs.

The hardware level trigger from the FD to the TARA DAQ is a NIM (Nuclear Instrumentation Module) pulse. Each pulse forces time stamp and DAQ triggering, which writes an event to disk. NIM pulses represent low-level triggers from the FD DAQ (see Section 3.1.2), which include star light intensity fluctuations, passing air planes and self-calibration triggers. Data rate during standard FD acquisition is 3–5 Hz. Rates increase during occasional calibration periods up to $\sim$ 50 Hz (see Figure 4.1).

After FD data are reconstructed I obtain an ASCII file with key parameters: time stamp (precise to $\mu$s), primary energy (EeV), core location (km, TA coordinates), zenith/azimuth angle, $X_{\text{max}}$. The set of all FD-triggered TARA data are then time-matched to the list of reconstructed events. Reconstructed FD events are selected by quality cuts designed to remove those which are reconstructed poorly. Table 4.1 gives the list of cuts and their descriptions.

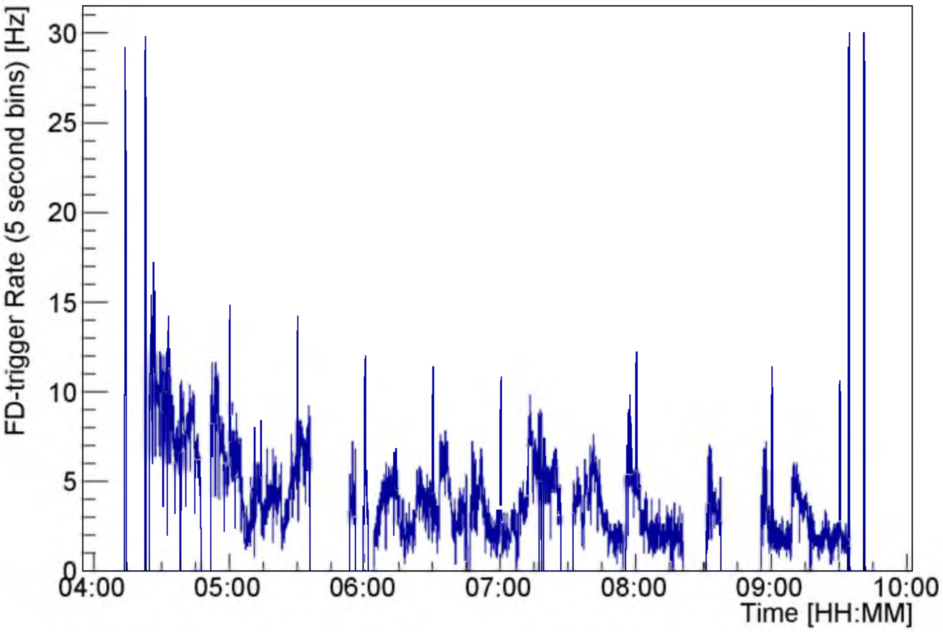

**Figure 4.1**: FD-triggered data rate on a night in August, 2013. The rate is averaged over 5 sec time bins. High rate periods occur primarily at the beginning and end of data acquisition and at several periods throughout the run when the detector is calibrated. Typical trigger rates over many runs are between 3 and 5 Hz.

**Table 4.1**: Long Ridge FD reconstructed events quality cuts. (NPE = number photo-electrons; SDP = shower detector plane).

| Cut Name | Criteria | Description |
|---|---|---|
| tube fraction | $\geq 3.5\%$ | data quality, noise reduction |
| good tubes | $\geq 6$ | data quality, noise reduction |
| NPE/degree | $\geq 25$ | data quality, sufficient signal |
| pseudo-distance | $\geq 1.5$ | geometry, shower resolution |
| SDP angle | $< 80°$ | geometry |
| $R_p$ | $R_p \geq 1$ km | geometry |
| $\Psi$ | $0° \leq \Psi < 150°$ | geometry |
| $\delta\Psi$ | $< 36°$ | fit reconstruction, $\Psi$ error |
| tangent fit | $\chi^2/\mathrm{DOF} < 10$ | fit reconstruction |
| zenith angle | $< 70°$ | geometry |
| $t_0$ | $t_0 < 25.6\,\mu\mathrm{s}$ | event occurs in trigger window |
| $R_p$ and $t_0$ | $!(R_p < 5\,\mathrm{km}\ \&\&\ t_0 < 3\,\mu\mathrm{s})$ | geometry |
| first tube depth | $150 < X_1 < 1200$ [g/cm$^2$] | geometry, first tube illuminated from reasonable depth |
| slant depth | $> 150$ g/cm$^2$ | geometry, minimum track length |
| $X_{\max}$ | $400 < X_{\max} < 1200$ [g/cm$^2$] | fit reconstruction |

## 4.2 Waveforms

Figure 4.2 shows an event display for a FD-triggered event chosen at random from the August FD run. The top plot in the display is the time domain–voltage vs. time. The bottom plot is a spectrogram with frequency vs. time and power spectral density (PSD) on the color scale. PSD is absolute power in dBm divided by the Fourier transform band in Hz. It is useful for comparing measurements using different equipment or window size. The spectrogram is created by successively performing Fourier transforms on the waveform in a 512 sample window, then sliding the window by 256 samples and repeating. The time domain of Figure 4.2 is shown on a smaller scale in Figure 4.3 so radar wave detail can be seen.

The radar carrier at 54.1 MHz is the strongest frequency component, dominating the time domain plot such that no other features can be seen. Two of the first analysis tools used to better present the data are digital notch[106] and high pass filters.[106] A digital notch filter is an adaptive filter that removes a range of frequencies in the stopband, which is characterized by the central notch frequency and the stopband width.

The high pass filter, often written HP filter, passes all frequencies above some cut-off frequency, which is typically the frequency at which the power is attenuated by 3 dB. Figure 4.4 shows the same event as Figure 4.2, but with both 54.1 MHz notch and 30 MHz HP filters applied. Near the beginning of the time and frequency domain plots the high amplitude 54.1 MHz frequency component can be seen. It diminishes as the notch filter adapts its phase and amplitude to cancel the carrier.

The event display in Figure 4.4 shows a waveform that has already passed through the receiver frontend 3.5. After the carrier and noise band at 30 MHz have been removed, the system passband can be seen between 40 and 80 MHz. For comparison, Figure 4.5 shows a snapshot event display also taken during the August FD run with the filters applied. Snapshot frequency characteristics and absolute power are very similar to the FD-triggered waveform shown in Figure 4.4.

The majority of FD triggers are random from the perspective of RF in the receiver because they arise from background fluctuations in the UV spectrum that are observed with the FD and they occur at a rate much higher than the rate of occurrence of

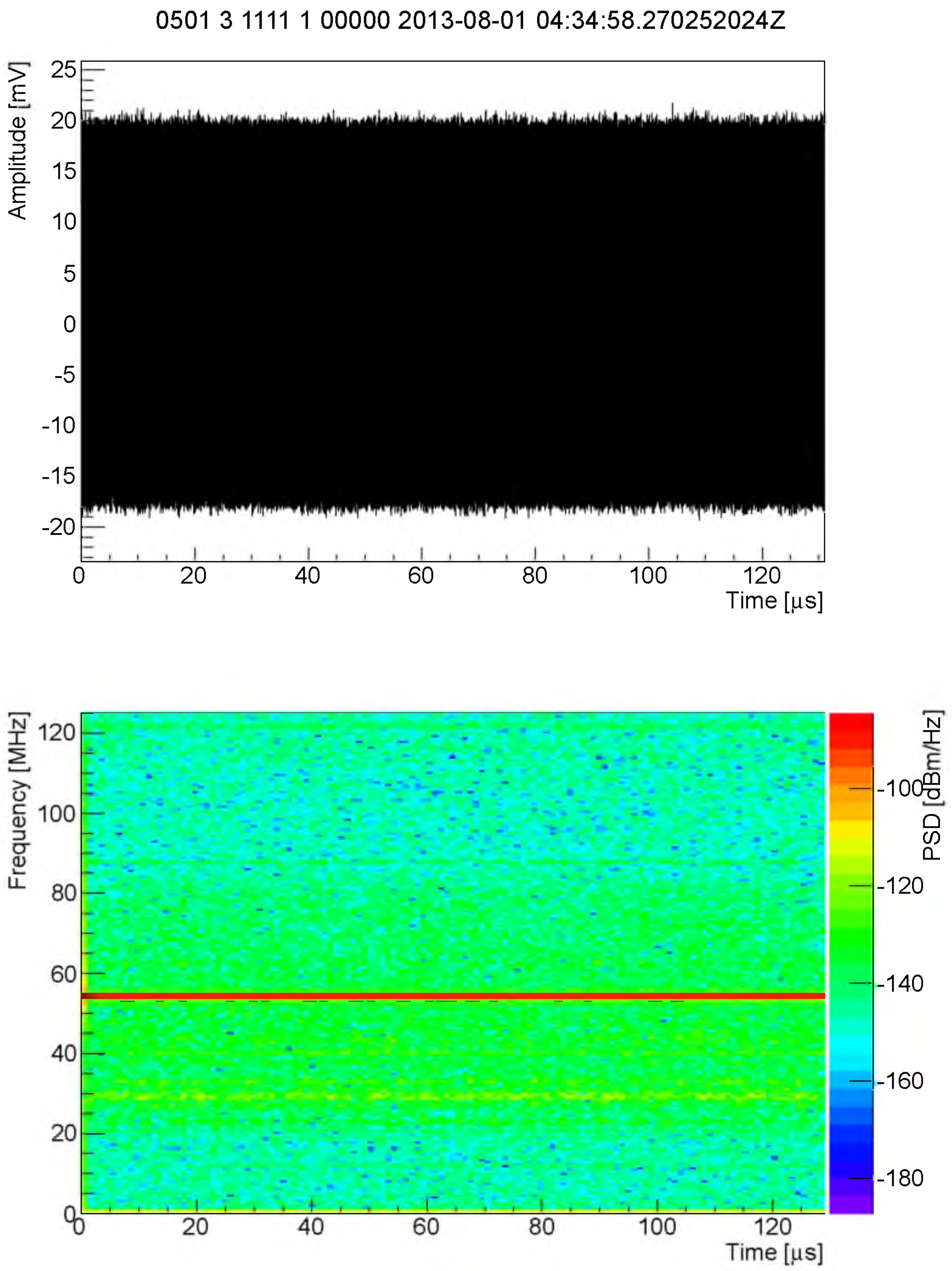

**Figure 4.2**: Event display for an FD-trigger chosen at random from the August, 2013 FD run. The top plot is the time domain waveform with voltage on the vertical axis and time on the horizontal axis. The bottom plot is a spectrogram of the waveform created using a 512 sample window size, and 256 sample overlap. Power spectral density (PSD) is shown on the z or color axis.

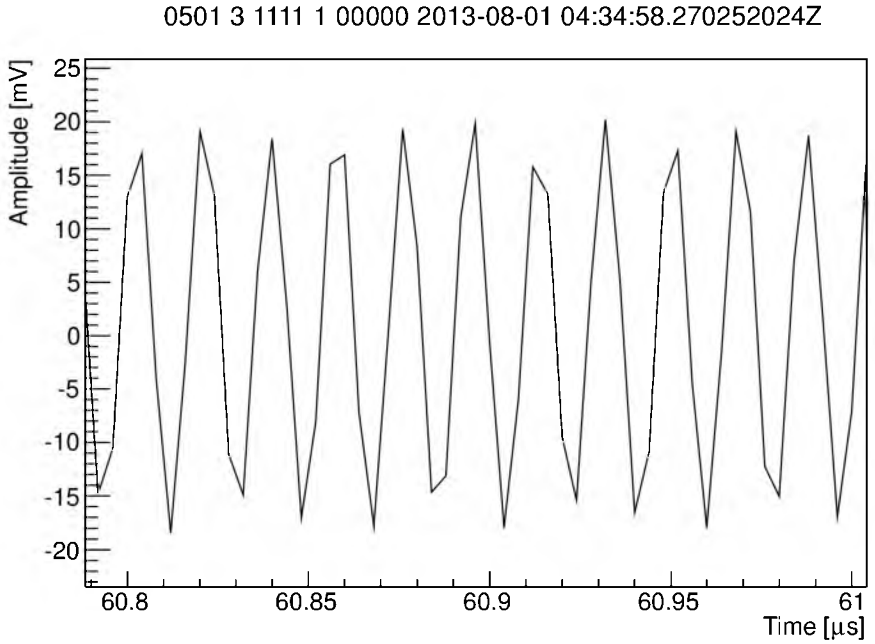

**Figure 4.3**: Time domain of Figure 4.2 on a smaller scale. The primary frequency component of the total waveform is the 54.1 MHz radar carrier.

high energy cosmic rays. Background estimation may be possible with nonmatched FD-triggered data. However, there is no way to ensure that any features in the data are not caused by the source that initiated the trigger.

Snapshot triggers occur once per minute and are not correlated to any external trigger. They offer a potential unbiased representation of the RF background. If there is trigger noise from the FD electronics or TARA DAQ, snapshots will not represent the RF background relevant to FD-triggered data.

A quantitative comparison of snapshot and FD triggers is shown via their notch and 30 MHz high pass filtered waveform sample voltage RMS values (VRMS) in Figure 4.6. The red histogram is the distribution of 249 total matched FD-trigger VRMS values that occurred during the August, 2013 FD run. The black histogram contains a distribution of the first 249 snapshots in the set selected for analysis, as described in Section 5.1.3. There is good agreement between distributions, indicating that snapshots can be used to represent FD-triggered data backgrounds.

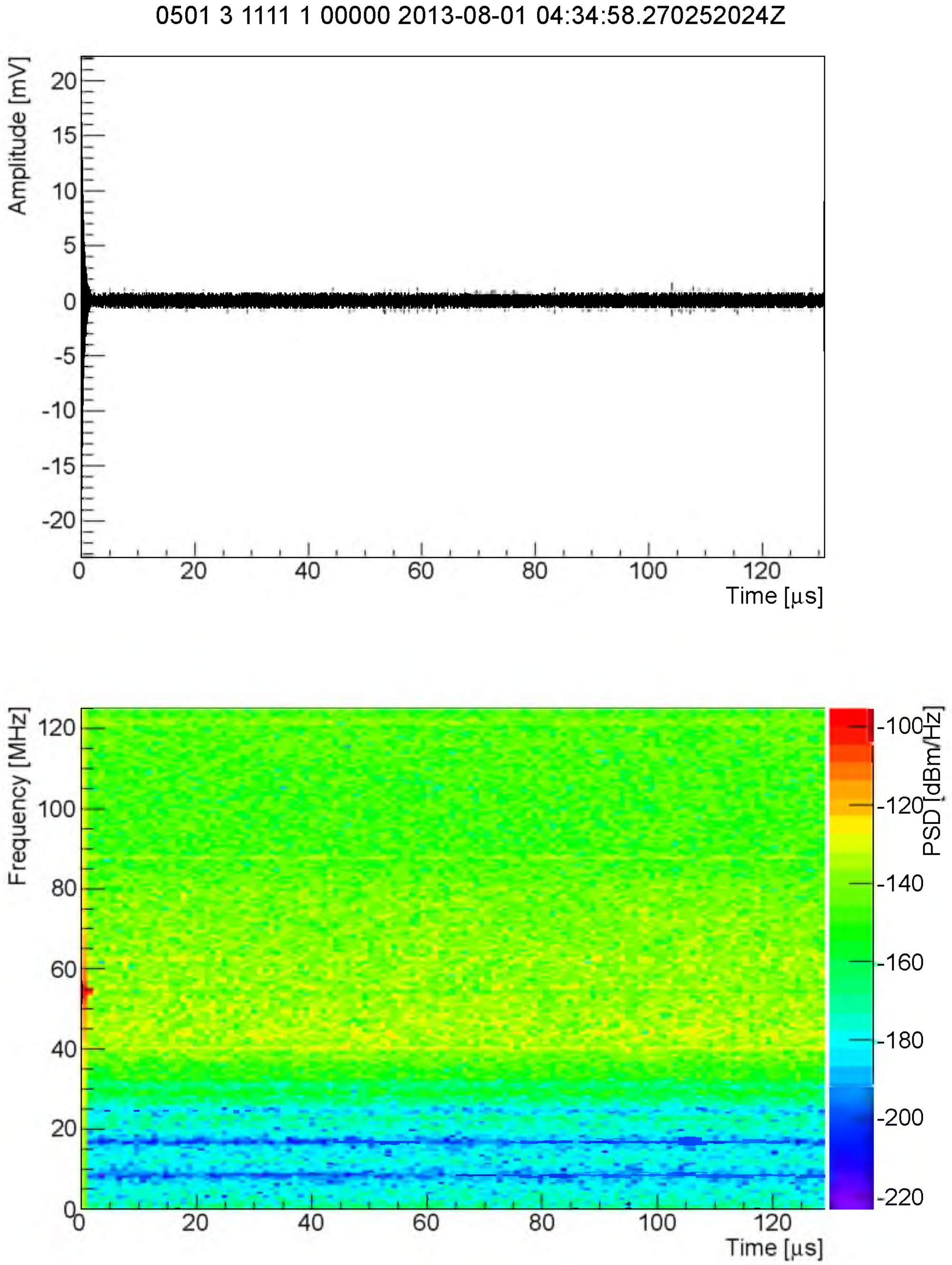

**Figure 4.4**: Event display for an FD-trigger chosen at random from the August, 2013 FD run. This plot is the same as that in Figure 4.2 but with 54.1 MHz notch and 30 MHz high pass digital filters applied.

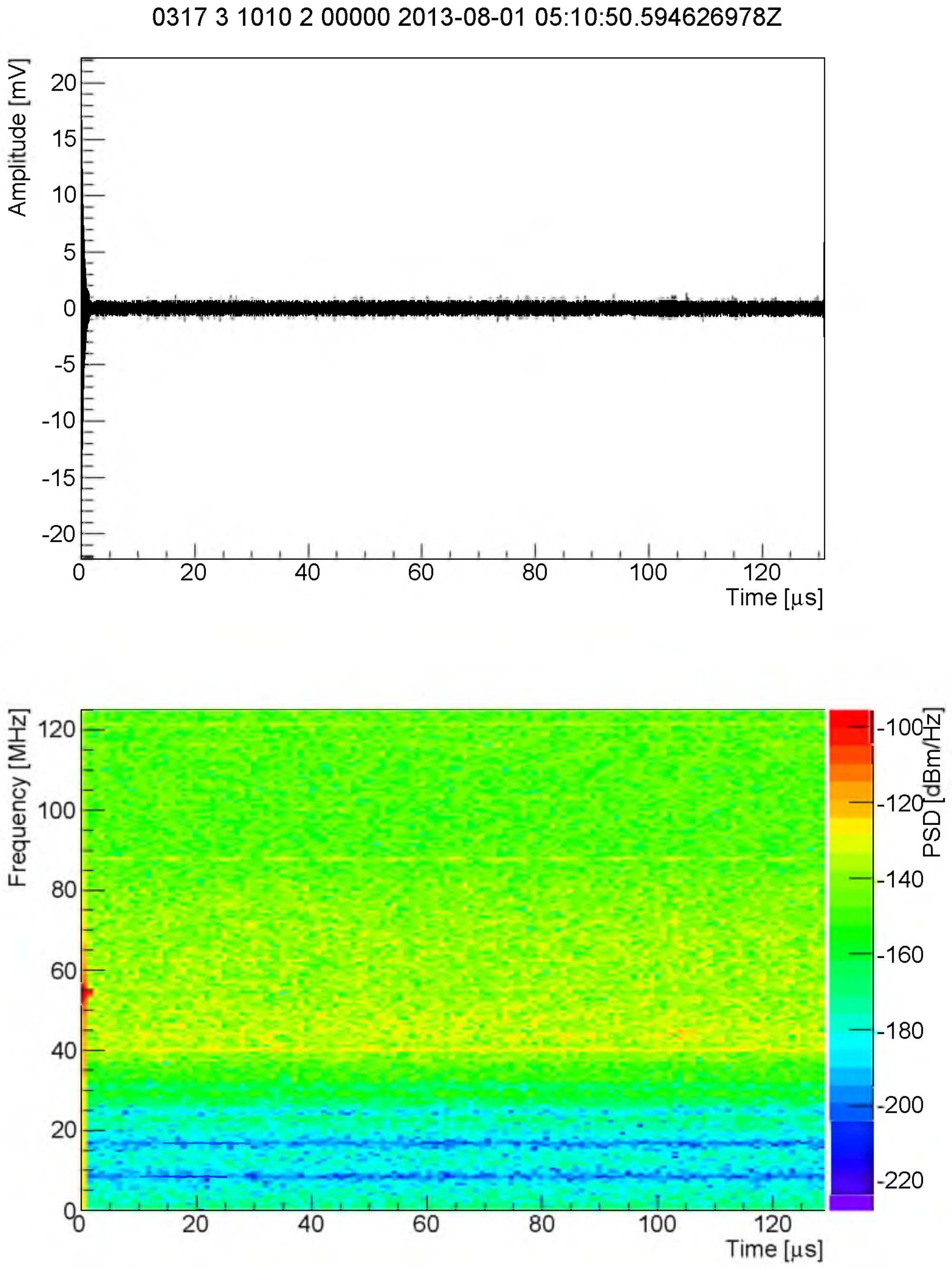

**Figure 4.5**: Event display for a snapshot chosen at random from the August, 2013 FD run with both 54.1 MHz notch and 30 MHz high pass digital filters applied. The waveform and spectrogram are very similar to the FD-triggered event display shown in Figure 4.4.

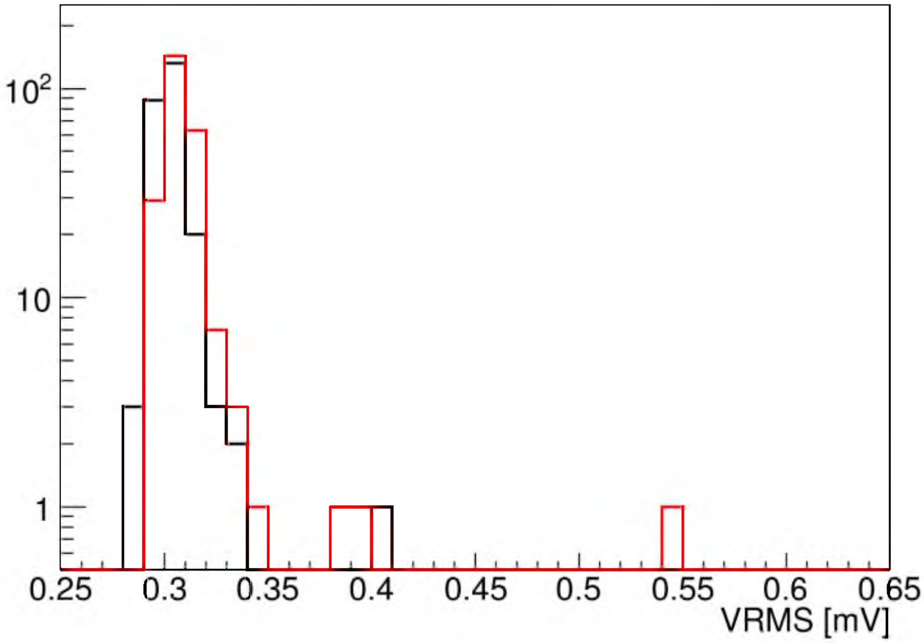

**Figure 4.6**: Voltage RMS distribution of 249 matched FD-triggered events in red overlayed with that of snapshots in black. All FD-triggered, matched events from the August, 2013 FD run are included in the red histogram. Only values from the first 249 snapshots from the set used for estimating backgrounds in August, 2013 data are included for comparison. FD-triggered data and snapshots have been filtered by a set of cuts described in Section 5.1.3.

## 4.3 Noise

Radio noise in the desert west of Delta, UT at the receiver is very low compared to more populated areas. However, our receiver system is more sensitive to noise than other receivers because of high sample rate (250 MHz) and broad passband (40–80 MHz). Static noise sources outside the passband are not problematic because they elevate the mean of the matched filter (MF) response distribution (similar to the DAQ implementation in Section 3.6.3 and discussed in detail in this chapter in Section 4.5), with the exception of rare cases in which a specific MF has a relatively good match with noise. There are no static noise sources in the passband. Intermittent noise can cause false positives by temporarily elevating the MF response.

There are four primary types of noise present in TARA data:

- spurious, low amplitude impulses (Figure 4.7)

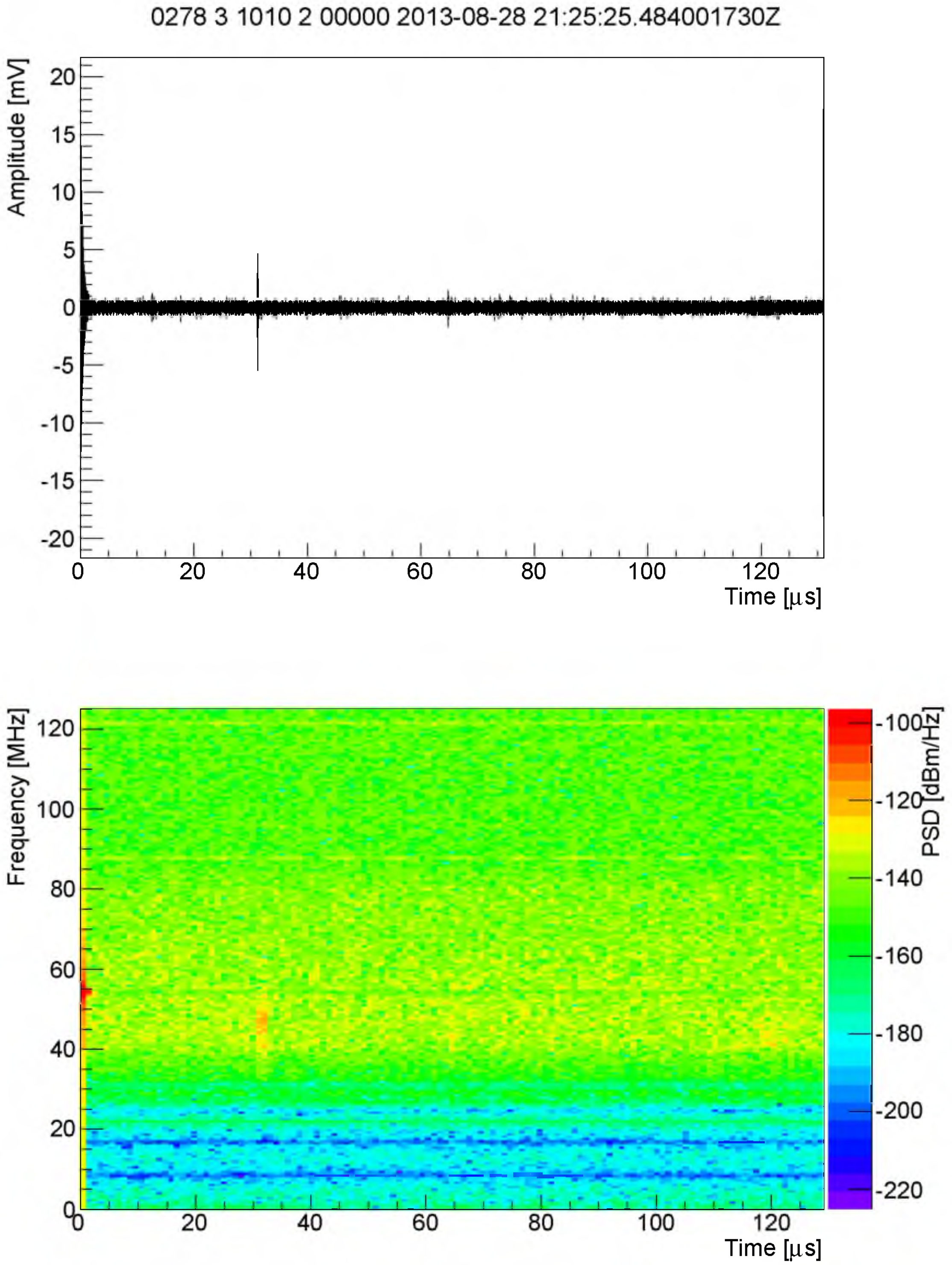

**Figure 4.7**: Event display for low amplitude, transient broadband noise. This type of noise can give high MF response.

- high VRMS noise (Figure 4.8)
- intermittent carrier signals (Figure 4.9)
- artificial phase shift (Figure 4.10)

The first three items are present in the radio environment and are most likely due to anthropogenic sources. Intermittent carriers are from communications systems and broadband impulsive noise is produced by electronic equipment, internal combustion engines, etc. All of these possible sources are present at the receiver site including a diesel generator that was in operation 24 hours per day at the time these data were collected, air conditioning units, personal computers, wi-fi and other sources.

The last item is caused by a bug in the DAQ which occasionally drops two samples. Adaptive notch filtering fails at the point of dropped samples, and must readapt to the amplitude and phase. This problem is never completely corrected. Later versions of the firmware (circa 2014) dramatically reduce the occurrence of dropped samples. Detection performance is greatly decreased if the dominating carrier signal is not removed before analysis. I have developed an algorithm based on the Fourier transform that detects a phase shift in an input waveform. All snapshots and FD triggers with phase shifts are removed from analysis.

Average passband PSD is shown to agree with the galactic prediction in terms of absolute power and diurnal fluctuation in Chapter 3, Section 3.5 (specifically in Figure 3.18). The challenge remains to remove or account for the three noise sources. Figure 4.11 shows the VRMS distribution of all snapshots (phase-shift waveforms removed) selected from the active August, 2013 FD run. High side tails are not representative of the true VRMS distribution because they are injected from anthropogenic sources, yet influence detection thresholds by increasing MF response. Low side lower limits are set by the background noise floor, either galactic noise (tenths of mV VRMS) or quantization noise (Figure 4.12, $< 0.1$ mV VRMS) in the case of dead amplifiers. In Section 5.3 I discuss the technique used to determine detection thresholds in a way that includes high VRMS triggers, which is critical to properly addressing anthropogenic sources.

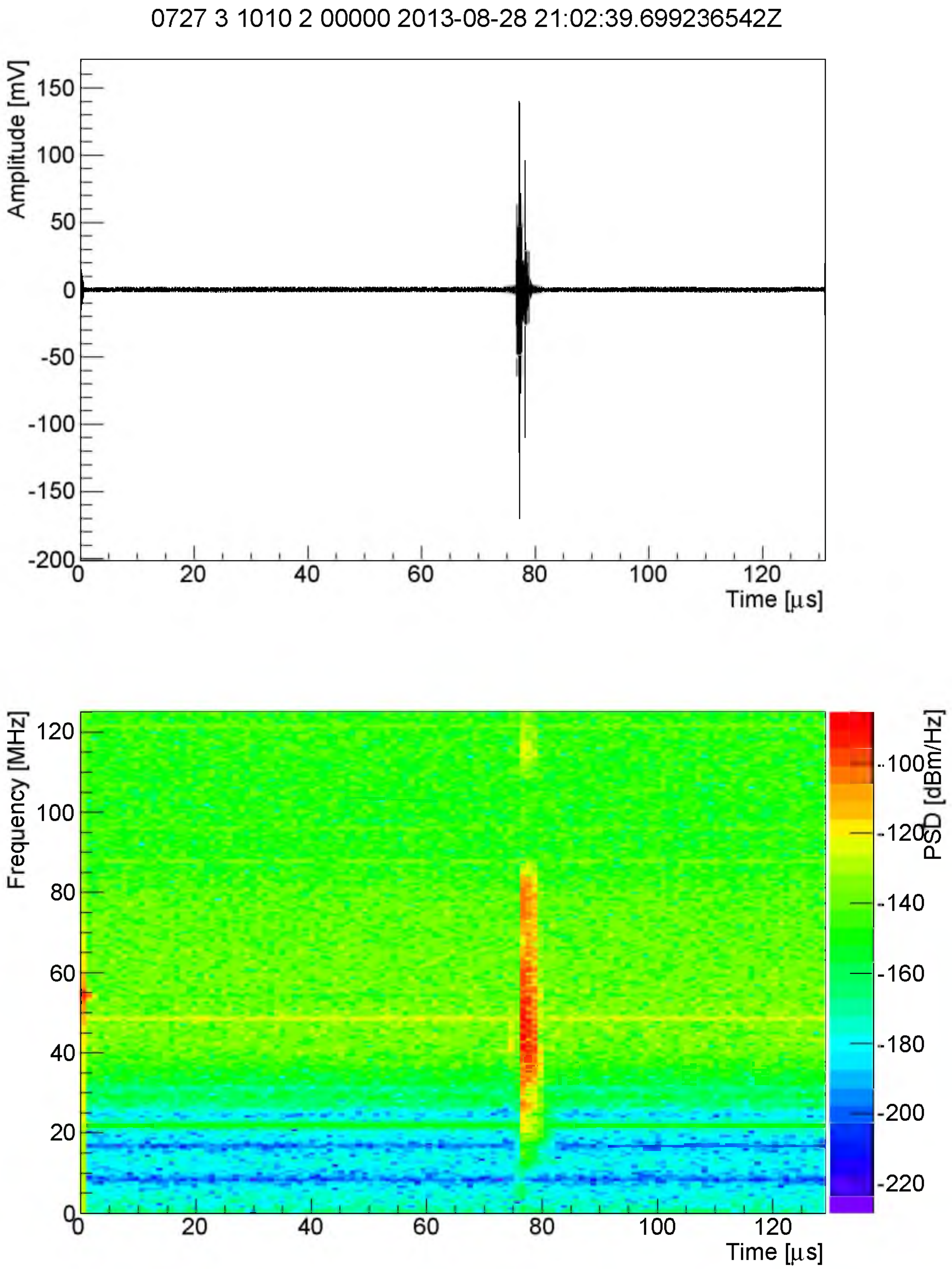

**Figure 4.8**: Event display for high VRMS, broadband transient noise. MF response is always high for any noise with large amplitude relative to the standard background.

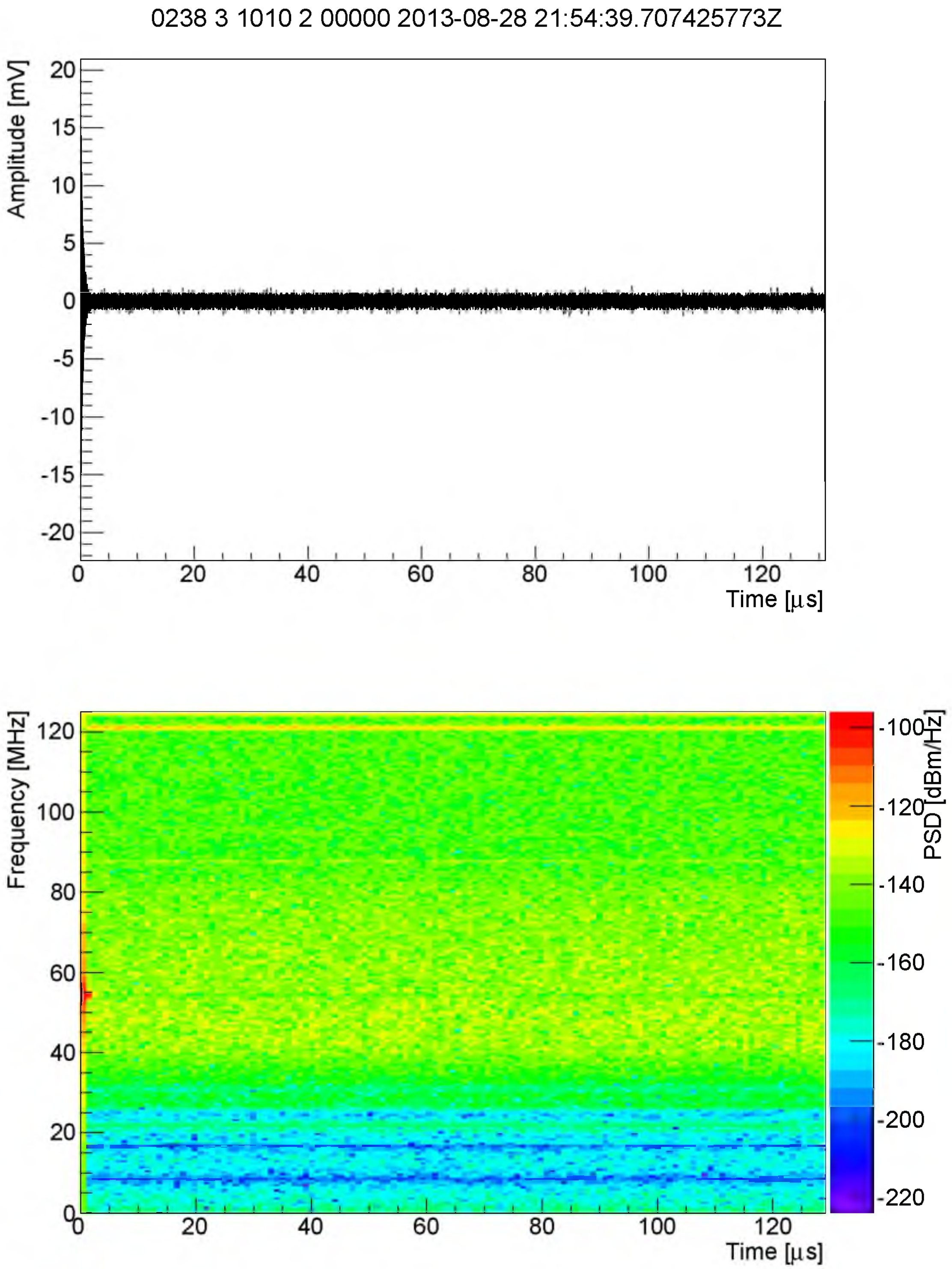

0238 3 1010 2 00000 2013-08-28 21:54:39.707425773Z

**Figure 4.9**: Event display showing an intermittent carrier at 120 MHz. Intermittent carriers are typically present in most spectra, but at much lower power. When carrier power increases spuriously, it can interfere with detection by raising the MF response.

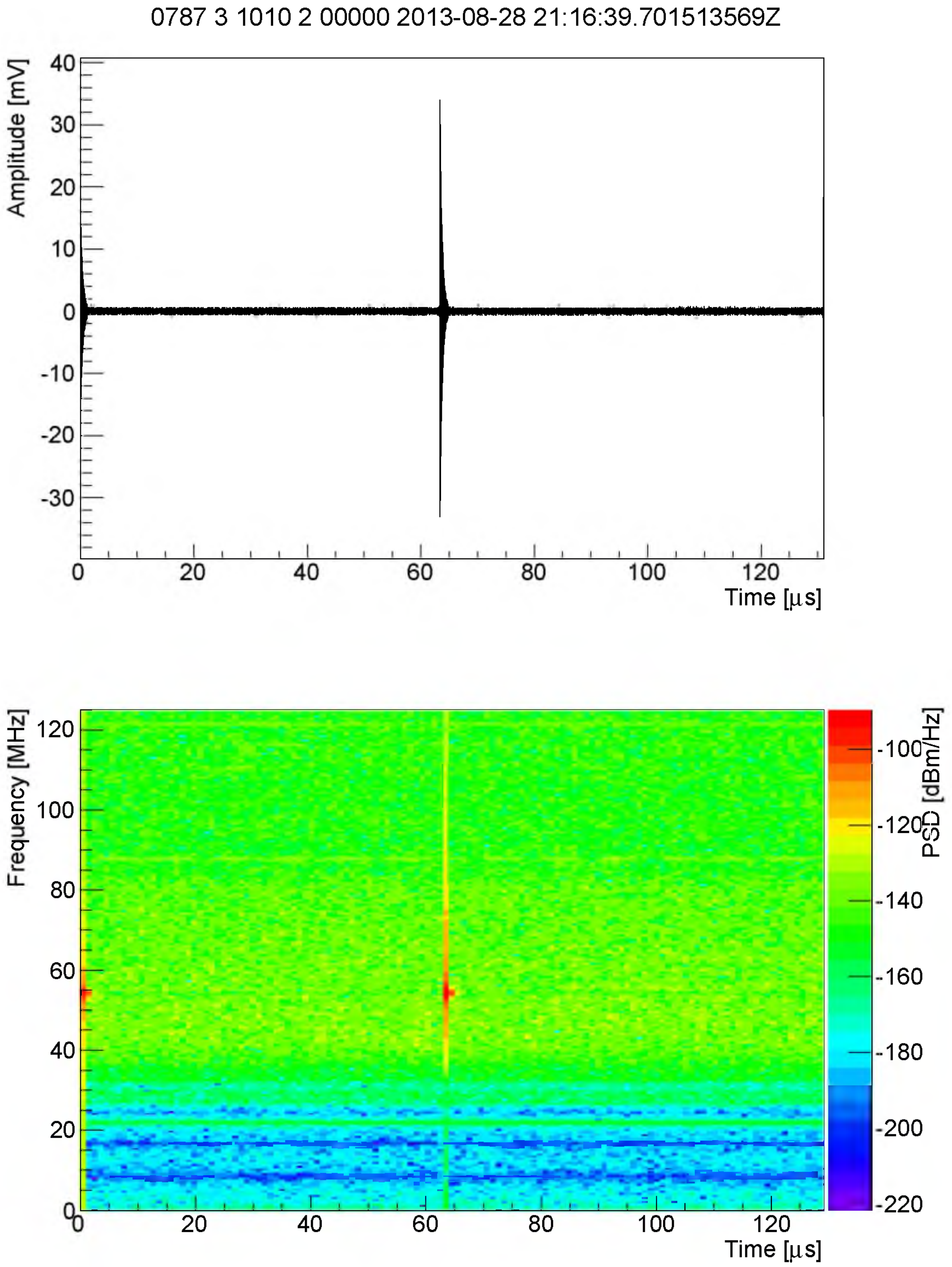

**Figure 4.10**: Event display showing an artificial high amplitude impulse caused by applying the notch filter to a waveform with dropped samples. A bug in the DAQ occasionally causes two dropped samples. When the notch filter, which is adapted to a specific phase and amplitude, passes over the region with dropped samples it briefly loses the ability to notch the frequency of interest before readapting.

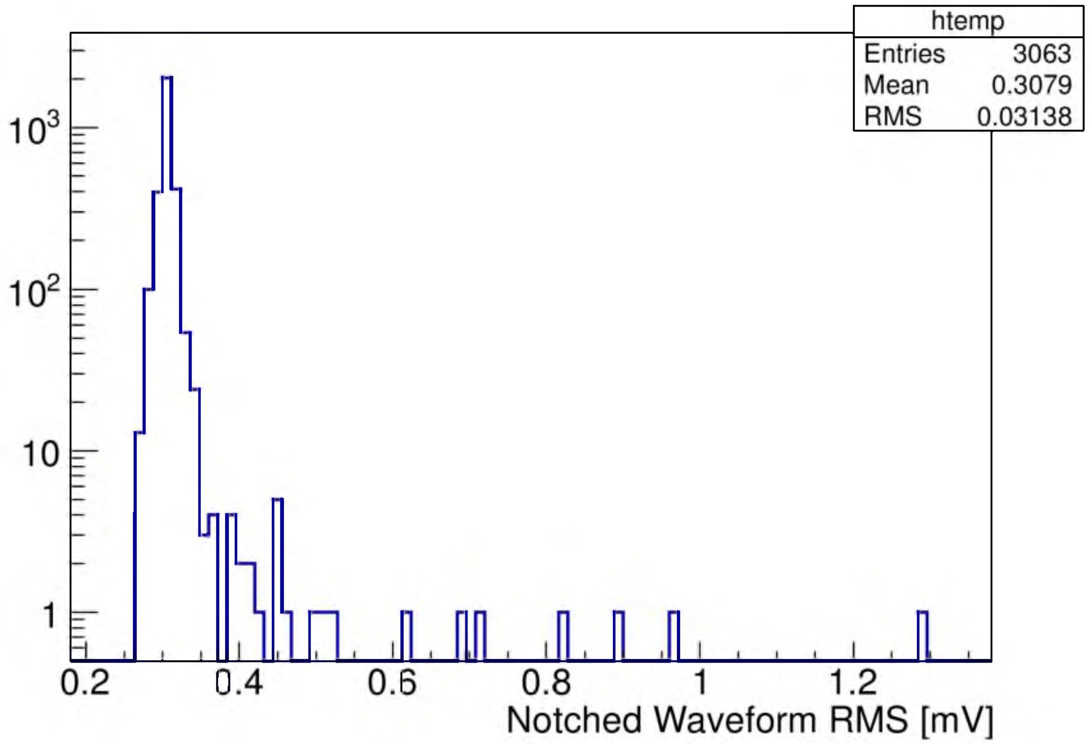

**Figure 4.11**: Notch filtered snapshot VRMS distribution for a selection of snapshots taken during the August, 2013 FD run.

Note that quantization noise is 20 dB lower than galactic noise. Figure 3.18 shows the average corrected PSD, which needs to be increased by about 30 dB to account for amplifier gain to be compared directly with quantization noise at the level where the two sources will be superimposed. After making the correction, galactic noise is 130 dBm/Hz, 20 dB above quantization noise (Figure 4.12) which can be neglected.

## 4.4 FIR Filter

Simulation of the receiver RF front-end in TARA is necessary to understand the response of the system to theoretical chirp signals and, ultimately, to estimate the cross-section upper limit of UHECR air showers. Both the LPDA antenna response and the filter/amplifier banks need to be mapped as a function of frequency. In the case of the antenna, there are geometrical factors that must be accounted for, which contributes an additional level of complexity. Here I introduce the theory and application of designing a filter (which is applied in the time domain) from a desired

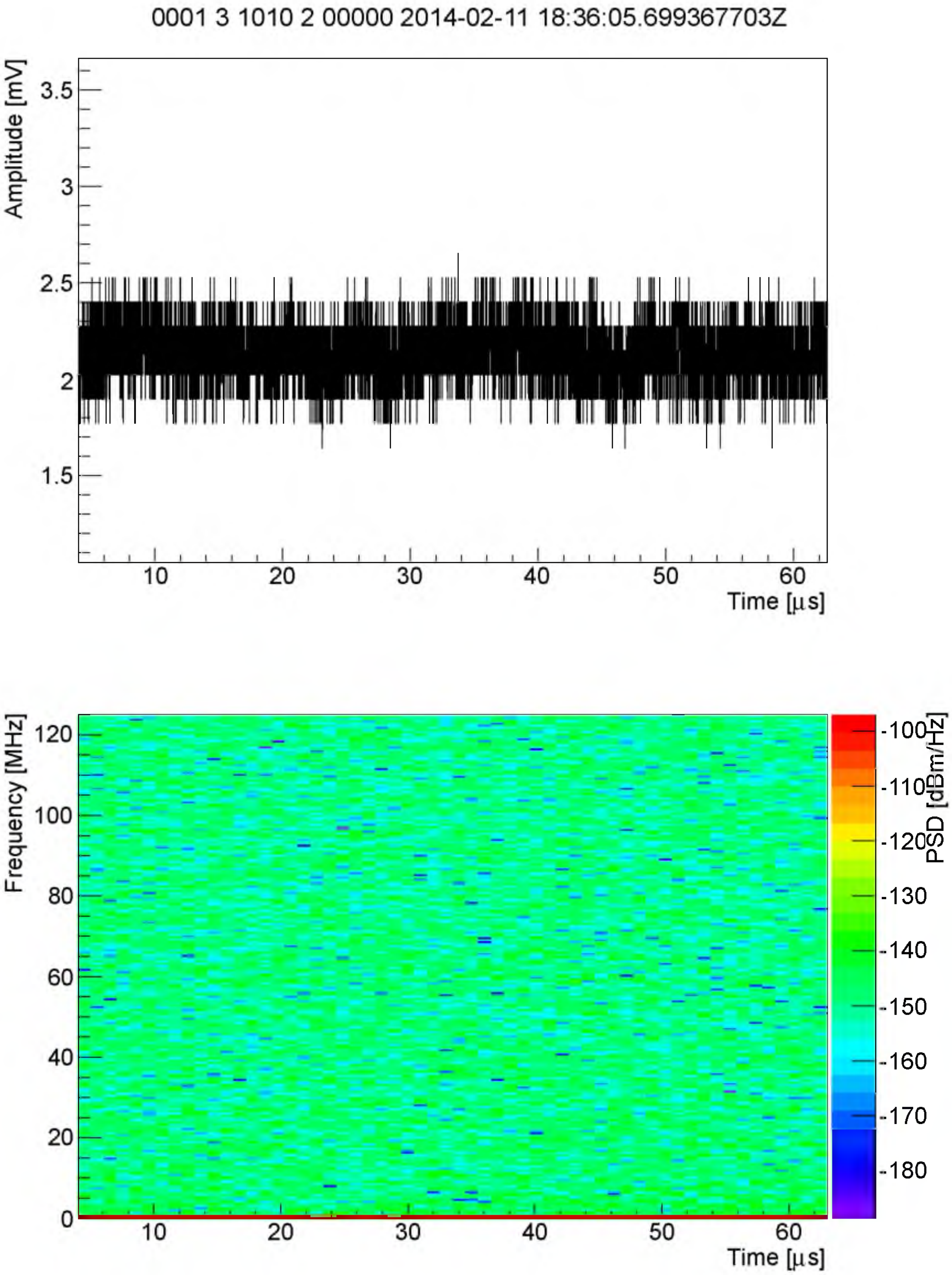

**Figure 4.12**: Event display showing the FlexRIO DAQ quantization noise. These data were taken with a 50 Ω terminator on the channel input. Quantization noise at $\simeq -150$ dBm/Hz is over two orders of magnitude higher than room temperature thermal noise at –174 dBm/Hz. Note that quantization noise cannot be compared directly to previous event displays because RF input for this plot has not passed through the frontend amplifiers and filters.

frequency response.

For the present analysis the specified frequency response comes from a measurement of the transmission coefficient $S_{21}$ of the filter/amplifier banks receive path. This is accomplished with a two-port vector network analyzer (VNA, sometimes referred to as just "network analyzer"). $S_{21}$ specifies the transmission coefficient measured at port 2, input from port 1. The RF frontend (Section 3.5), including RF limiter, amplifiers and filters, is detached from the antenna and transmission line. VNA port 1 is connected to the input or antenna side of the amplifier/filter bank and port 2 is connected the transmission line side. $S_{21}$ is measured at discrete points along a predetermined frequency range and written to flash memory. This measurement has been performed on all four banks, though only channel 3 information is used in the present analysis. Figure 3.16 shows $S_{21}$ for channel 3.

The majority of persons reading this dissertation will not be familiar with the construction of FIR filters. The following three sections give a brief overview of digital signal processing toward implementation of FIR filter design specific to the goals of the present analysis. Section 4.4.1 introduces properties of linear, time-invariant (LTI) signal processing systems. Fourier analysis properties useful in the construction of FIR filters is presented in Section 4.4.2 and implementation is discussed in Section 4.4.3.

### 4.4.1 LTI Systems

This discussion follows a distillation of content from.[106] DSP (Digital Signal Processing) techniques for communications and relevant signal analysis are typically described in the framework of LTI (Linear, Time Invariant) systems. LTI systems are used because there are many mathematical techniques that can be applied to such systems, and because most practical systems either are LTI systems or can be approximated as such.

Time invariant systems produce the same output given uniform input independent of time. A system which takes an input $x(n)$ and produces the output $y(n)$ when operated on by the system $H$ is time-invariant if the relationship $y(n,k) = H[x(n-k)] = y(n-k)$ holds for any value of $k$. Linear systems behave according to the principle of superposition. For example, suppose $y_1(n) = H[x_1(n)]$ and $y_2(n) = H[x_2(n)]$. A linear system $H$ would satisfy the following equality: $a_1y_1(n)+a_2y_2(n) =$

$H[a_1x_1(n) + a_2x_2(n)]$.

One common method of characterizing the response of LTI systems is accomplished by first decomposing the input signal into a weighted sum of unit impulses $\delta$

$$\delta(n) = \begin{cases} 1 & \text{for } n = 0 \\ 0 & \text{for } n \neq 0 \end{cases} . \tag{4.1}$$

The sum of unit impulses multiplied by amplitude

$$x(n) = \sum_{k=-\infty}^{\infty} x(k)\delta(n-k)\,, \tag{4.2}$$

can also be written as

$$x(n) = \sum_k c_k x_k(n)\,, \tag{4.3}$$

where $x_k(n) = \delta(n-k)$ and $c_k$ are the coefficients. System response for a single elementary impulse is written as $y_k(n) = H[x_k(n)]$. Total response from the decomposed signal looks like

$$y(n) = H\left[\sum_k c_k x_k(n)\right] = \sum_k c_k H[x_k(n)] = \sum_k c_k y_k(n)\,, \tag{4.4}$$

where the linearity property was used to factor $c_k$ out of the response function.

The impulse response $h(n,k)$ ($n$ is time index, $k$ is location parameter) is the system response to the unit impulse at $n = k$: $h(n,k) = y(n,k) = H[\delta(n-k)]$. Using the impulse response, the complete system response can be written as

$$\begin{aligned} y(n) &= H\left[\sum_{k=-\infty}^{\infty} x(k)\delta(n-k)\right] \\ &= \sum_{k=-\infty}^{\infty} x(k)H[\delta(n-k)] \\ &= \sum_{k=-\infty}^{\infty} x(k)h(n,k)\,. \end{aligned} \tag{4.5}$$

The result,

$$y(n) = \sum_{k=-\infty}^{\infty} x(k)h(n-k) \equiv x(n) * h(n)\,, \tag{4.6}$$

is simplified in practical systems (where limits on the sum become finite) and is called a convolution sum. The significance of the result is important, but subtle. It says that the system response at a specific time is given by a sum of products of the input signal and the impulse response. The system is characterized by its impulse response, which could be a filter or chain of signal conditioning components. Also, each output sample relies only on application of the filter impulse response and some number of samples, i.e., there is no feedback from previous outputs which makes this an FIR (*Finite* Impulse Response) filter.

FIR filters have other properties which make them useful for an array of signal processing applications. For the physics discussion the important criterion is that there is no feedback, which is in contrast to IIR (Infinite Impulse Response) filters which require feedback.

### 4.4.2 Fourier Analysis

Th following discrete Fourier transform (DFT) discussion is similar to that in.[106] The DFT formula

$$X(k) = \sum_{n=0}^{N-1} x(n) e^{-i2\pi kn/N} \,, \tag{4.7}$$

gives a complex frequency (amplitude and phase) description of a periodic signal $x$ with $N$ samples in a period. Fourier coefficients $X$ make up the frequency spectrum of the signal. Real-valued sample data are mapped to complex amplitudes in frequency bins $f_k = (f_s/N)k$, where $f_s$ is sample frequency, $k$ in $[0,\ N/2]$ and $f_0 = \mathrm{DC}$. Frequency values with $k$ greater than $N/2$ correspond to negative frequencies or, in other words, the second half of the periodic unit circle which contains no additional information. Both the discrete-time signal $x$ and its frequency spectrum contain complete information about the system,[107] so one can be obtained from the other. Similarly, the frequency response $H$ from a system with impulse response $h$ is given by

$$H(k) = \sum_{n=0}^{N-1} h(n) e^{-i2\pi kn/N} \,, \tag{4.8}$$

which can be inverted by multiplying both sides by $\exp(i2\pi km/N)$ (with $m$ running from 0 to $N-1$) and summing over $k$ to get the inverse DFT

$$h(m) = \frac{1}{N} \sum_{k=0}^{N-1} H(k) e^{i2\pi km/N} \,. \tag{4.9}$$

A simplification on the right hand side of Equation 4.8 is possible after multiplying by the exponential and summing because of the relation

$$\sum_{k=0}^{N-1} e^{-i2\pi k(n-m)/N} = \begin{cases} N & n-m = 0, \pm N, \pm 2N \ldots \\ 0 & \text{otherwise} \end{cases} . \tag{4.10}$$

For $n \neq m$, the sum is over equidistant (in angle) unit vectors on the imaginary plane whose total length is zero. Equation 4.9 is the primary relation used to convert a known or desired frequency response into an impulse response, after which convolution with unfiltered samples $x$ (Equation 4.6) produces a signal $y$ with frequency response defined by the system $H$.

### 4.4.3 Implementation

Simulation of RF frontends via FIR filtering first requires the desired frequency response $H$. This is measured then converted to an impulse response $h$ which can be convolved with unfiltered waveform samples to produce the filtered output. In practice, there are two important qualities of the DFT that specify the form of the designated frequency response—period and symmetry. Per the Nyquist requirement,[93] filter response is undefined for frequencies higher than half the sampling frequency $f_{\mathrm{s}}$, or 125 MHz for data sampled by the TARA DAQ. Because the DFT is periodic over a $2\pi$ range, we want to construct a desired response that is defined over 250 MHz bandwidth. Suppose the ideal frequency response is as shown in Figure 4.13 which is the measured RF frontend response (Figure 3.16) described in Section 3.5 but mirrored about zero. This fills the requirement that the desired frequency response is defined over $2\pi$ rad.

Furthermore, we want the impulse response to be real-valued both for ease of computation and because the input consists of real-valued frequency samples from a two-port VNA. A zero-phase filter is real-valued and preserves signal phase. It is a specific case of a linear (in frequency) filter that delays all frequency components equally, so there is no distortion. Simulation of receiver system response is not affected by the time delay because the location in time where filtered chirps are analyzed is arbitrary if the background is represented correctly.

If the desired frequency response is symmetric over $[0, 2\pi)$ and the imaginary component is zero, then the impulse will be real and have zero-phase because the

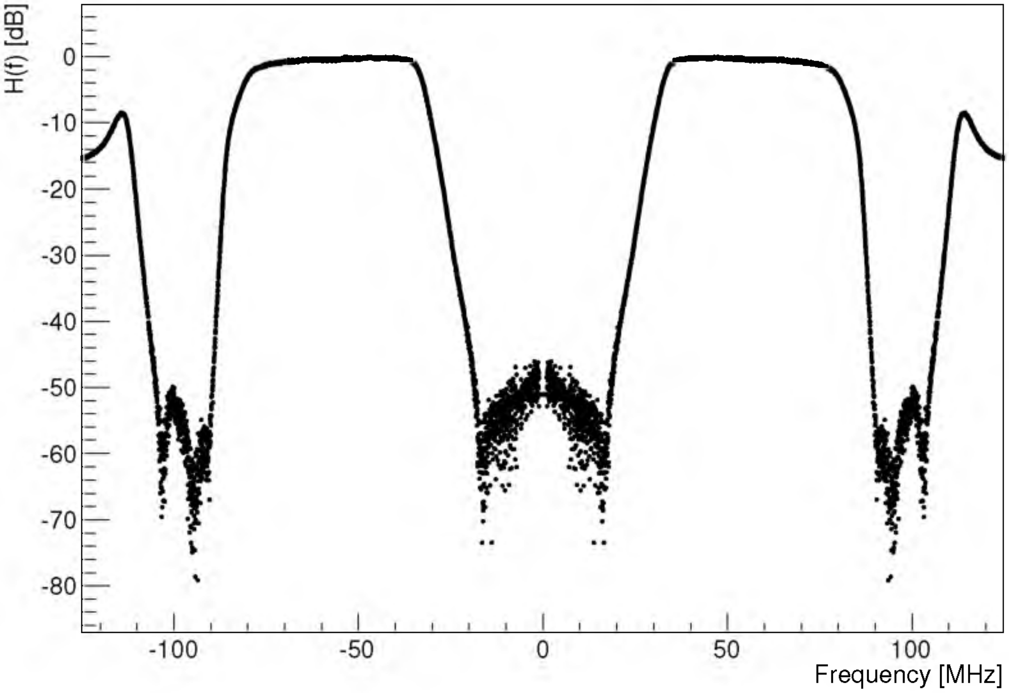

**Figure 4.13**: Frequency response $H$, which has been reflected about frequency 0 MHz, or DC. These data are the transmission coefficient $S_{21}$ data taken from filter bank 3 which we desire to emulate with a digital filter.

$iH(k)\sin(\phi_k)$ components will sum to zero. Extending the frequency response as described in the previous paragraph does satisfy this requirement, but *does not* reflect DFT output array mapping to frequency. Recall from the previous section that the lowest element in the DFT output array ($X(k=0)$) corresponds to DC, not $-f_s/2$ as in Figure 4.13. The origin is located at the zero-th element.

The points of $H$ in the range $[\pi, 2\pi)$ are filled by concatenating the original response with a reversed copy of itself and removing the new last element so all values are within $[0, N]$, where the origin is now at the beginning. This can be thought of as swapping the left and right halves of $H$. Figure 4.14 shows the result of making this change. This is the same as continuing the original *periodic* (from the perspective of the Fourier Transform) frequency response past $N/2$ up to $N$. In general, a zero-phase filter can be obtained by using a Hermitian symmetric frequency response $H(n) = H^*(N-n)$.

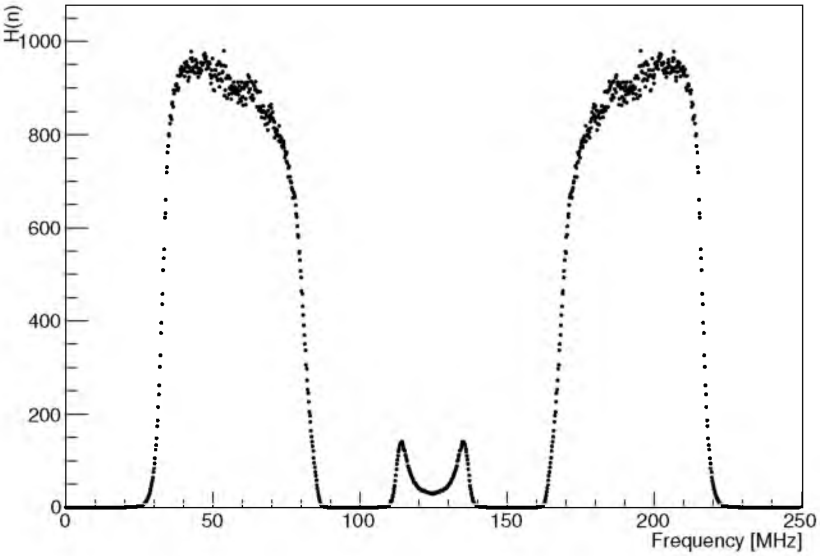

**Figure 4.14**: Frequency response $H$ has been extended to fill the range $[0, 2\pi)$, sampled (decimating by 6) and converted to linear values.

After performing an inverse DFT on $H$, time domain impulse response $h$ needs to be swapped to place the origin back at the center. In analogy to the frequency domain, the range of values is defined in $[-f_s/2, fs/2]$ and not $[0, f_s]$ where the origin is at the beginning. The correct form of the impulse response is $h' = h(\text{right half}) + h(\text{left half})$ is the array of values that will be convolved with time domain data. Figure 4.15 shows a spectrogram of a Gaussian noise background before and after the filter is applied. The desired frequency response features for $f = [0, f_s/2]$ in Figure 4.13 can be clearly seen in the second plot.

## 4.5 Matched Filter

Matched Filtering (MF) is a DSP technique used for detecting the presence of a known signal or template in a test waveform. The MF template is the ideal (no noise) signal that is being searched for in an unknown waveform. Scalar output from vector multiplication of the template with the test waveform is the MF response. Large MF response implies better match with the template. In practice, DSP software suites include convolution (Equation 4.6) functions, so MF response is generally described as the result of convolving the time-reversed template with the test waveform.

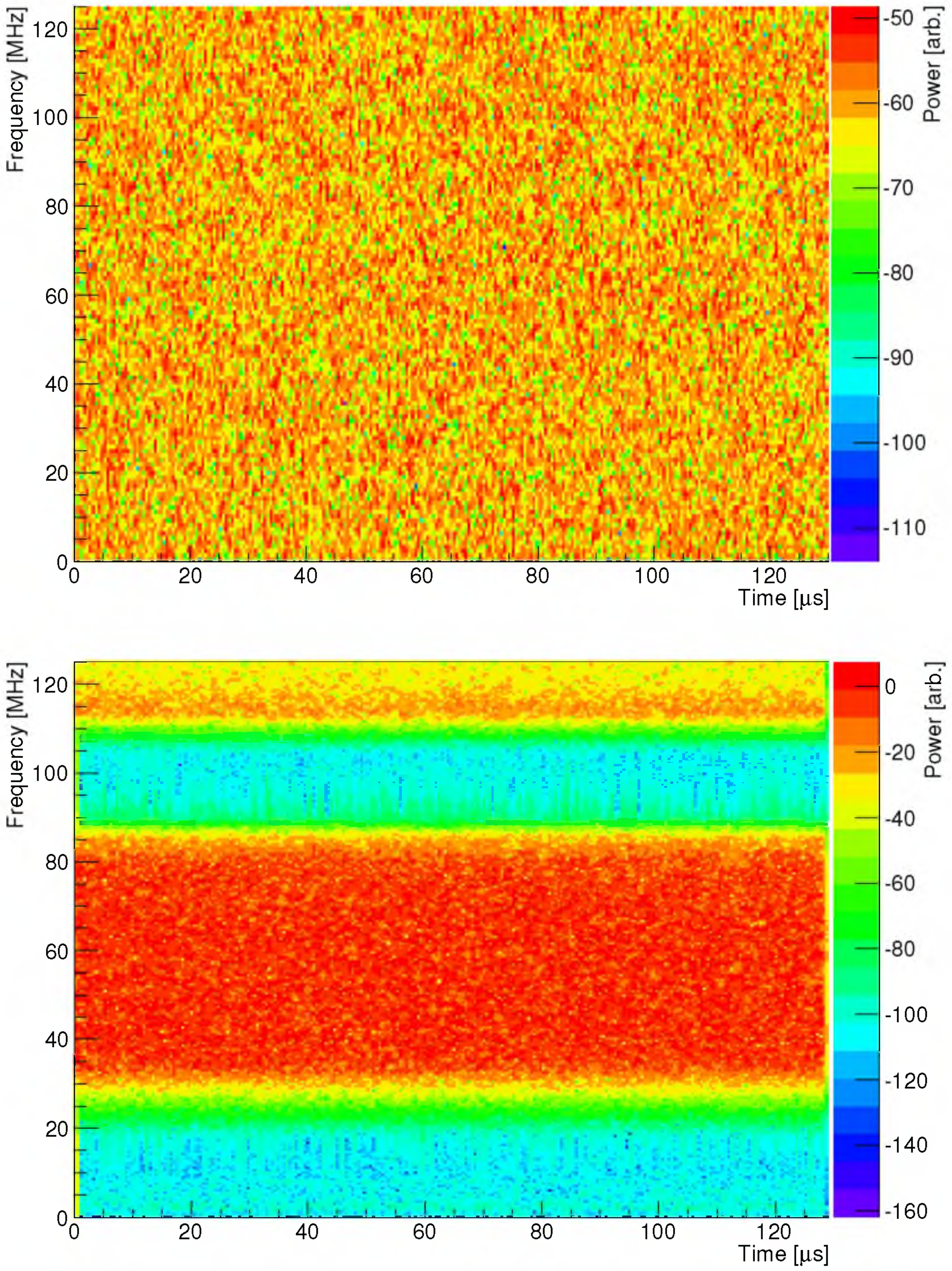

**Figure 4.15**: Spectrograms showing simulated Gaussian noise (top) and the same noise filtered with an FIR filter designed from the frequency response shown in Figure 4.13. Amplitude features can be directly compared between the spectrogram and the desired response.

Figure 4.16 shows three examples of a very basic test waveform and MF output. In each case a 10 $\mu$s duration sine wave is superimposed on Gaussian noise beginning at 20 $\mu$s (left plots). A template identical to the superimposed wave is used to calculate the absolute value of MF response as a function of the time where the vector product calculation begins (right plot). Peak MF response occurs at 20 $\mu$s where the template and the superimposed sine wave coincide in time and phase. The SNR of the three examples is 10, 0 and $-20$ dB SNR in power.

A template may be derived from a function or a simulated waveform that needs to be sampled or decimated before it can be used as a template. For FD-triggered data analysis, templates are constructed from the echo simulation output waveforms (described in Chapter 5) which are the ideal theoretical radar echo expectation. The simulation typically uses a time step that gives 500 MS/s sample rate waveforms. These are decimated by a factor of two to match the FlexRIO DAQ 250 MS/s sample rate and scaled such that the maximum voltage sample is 1.0 mV before being used as templates. Real-time applications like the FlexRIO DAQ self-trigger scheme often do not require MF output at each sample, in which case MF response is calculated periodically. To maximize sensitivity in the postprocessing analysis, MF response is calculated at each sample in the time range of interest. Also unlike the DAQ, there is no decimation of the native 250 MS/s sample stream by two before applying the MF.

In the DAQ performance section (Chapter 3, Section 3.6.4.2) I discuss a self-trigger mode performance test conducted in situ, where a simulated chirp is broadcast near the receiver antenna. Even with the disadvantage of real-time optimized match filtering (decimation, periodic application), detection is 100% at -7 dB ASNR.

Using the MF detection scheme described in Section 5.3 in which I calculate the MF *peak* response distribution mean and RMS to determine the threshold, 100% detection occurs further below noise at -11 dB ASNR. Figure 4.17 shows detection efficiency as a function of ASNR using the postprocessing MF technique. To generate this plot, 400 selected snapshots from the August, 2013 FD run are used to calculate the $3\sigma$ threshold. 200 snapshots superimposed with scaled echo waveforms are analyzed for each point on the plot.

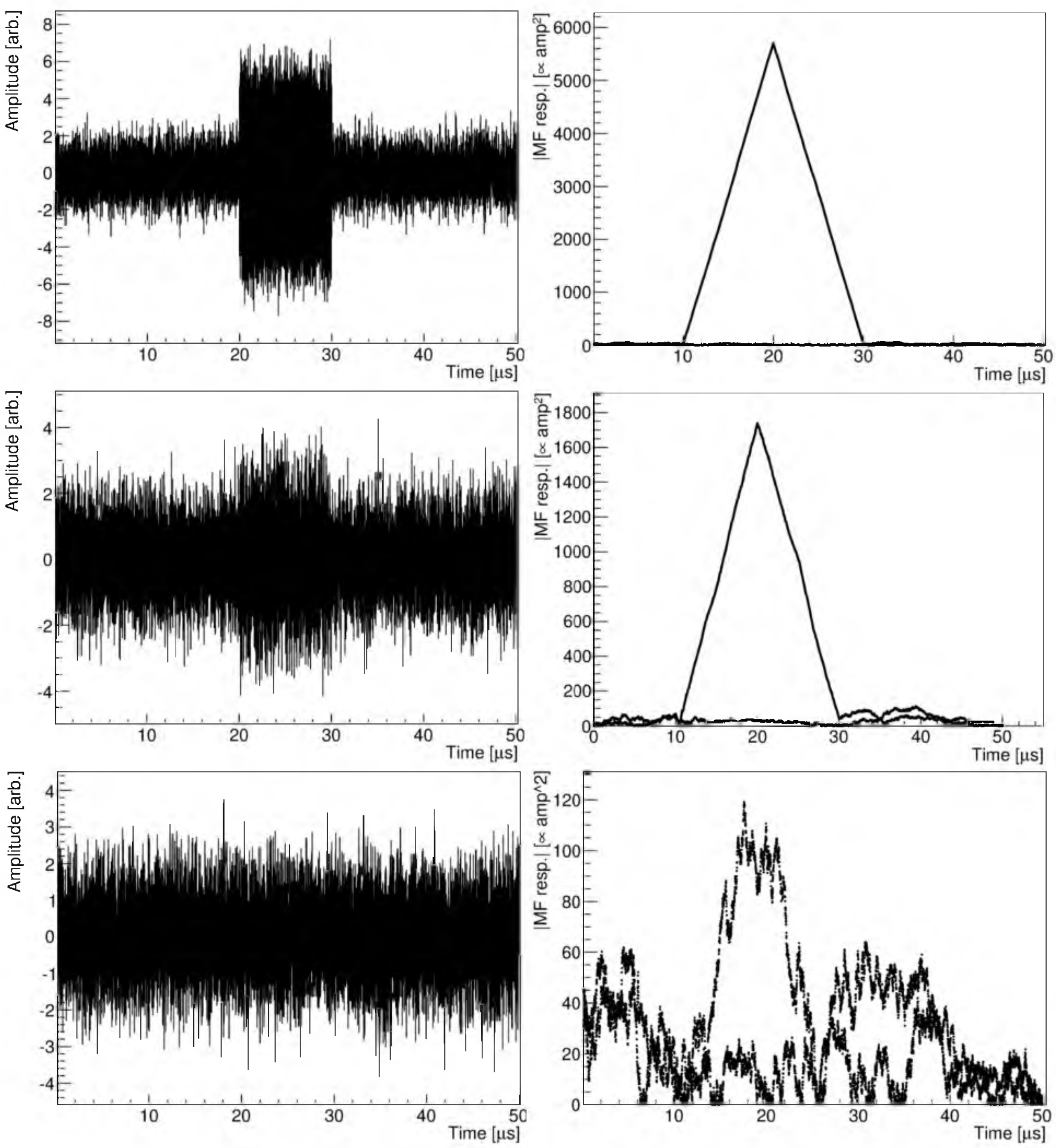

**Figure 4.16**: Three examples of test waveform (left plots) and their Matched Filter (MF) responses (right plots). In each case a 10 $\mu$s sine wave is superimposed on Gaussian noise. The absolute value of the MF response using a template identical to the superimposed sine wave is plotted versus the time where the MF is applied. Peak response occurs at 20 $\mu$s where the superimposed sine wave and the template are aligned. The top, middle and bottom plots show results from superimposing the sine wave at 10, 0 and $-20$ dB SNR in power.

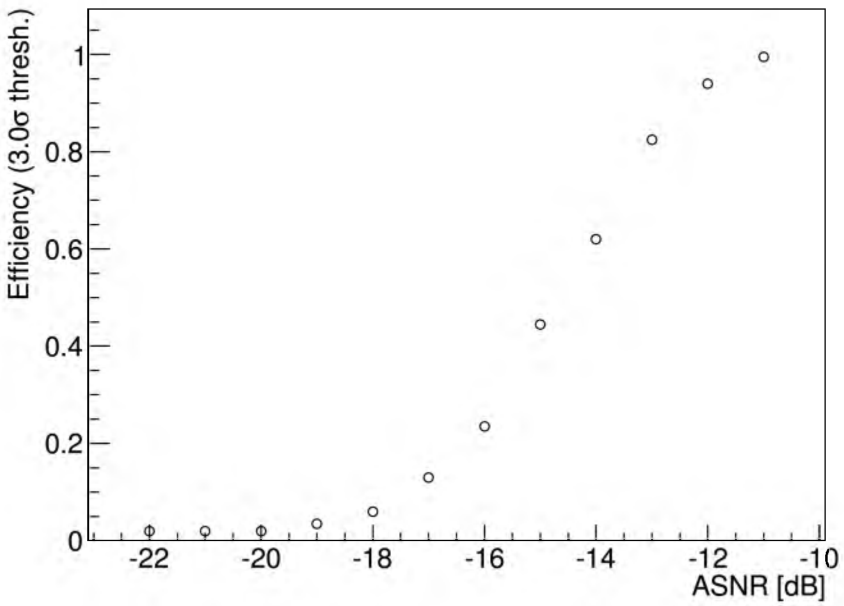

**Figure 4.17**: Matched filter detection efficiency as a function of ASNR using a canonical simulated radar echo. This detection scheme is described in Section 5.3. Selected snapshots from the August, 2013 FD run are used both to determine the $3\sigma$ response threshold and as backgrounds on which scaled echo waveforms are superimposed. In contrast with the FlexRIO self-triggering test conducted at the receiver site which resulted in a –7 dB ASNR 100% detection efficiency, this postprocessing scheme has 100% efficiency at –11 dB ASNR.

Also note that this postprocessing technique imposes higher thresholds for a given $\sigma$-level relative to the real-time DAQ scheme. The -7 dB measured ASNR result uses a $6\sigma$ threshold calculated from periodic (10 ms duration, decimated by two, 1 Hz) accumulation of MF statistics. The postprocessing technique compares only waveform *peak* MF responses. In the current comparison, the $3\sigma$ threshold is equivalent to $7.2\sigma$ in the real-time DAQ scheme. This further emphasizes the advantage of postprocessing.

# CHAPTER 5

# RCS CALCULATION

The self-triggered data stream comprises the largest portion of observed triggers by a factor of ten because the FD duty cycle is only about 10%. Even with much less exposure, FD-triggered data comprise the most hopeful data set because, by definition, a subset of those triggers occurred during actual CR events. Self-triggered data analysis will be discussed elsewhere.

A brief overview of the full analysis chain is as follows. The TARA DAQ (see Chapter 3) is operational 24 hours per day, during which the system is real-time self-triggering on RF input that has at least one of five MF responses that exceeds the $5\sigma$ level calculated from background measurements taken in the previous several seconds. Approximately two weeks out of the month, on clear nights when the moon is below the horizon the Long Ridge FD records data. Low level triggers from the FD force-trigger the DAQ in what is called the FD-trigger. Snapshot triggers are collected once per minute. The transmitter is also on 24 hours per day. A transmitter log entry is recorded every five minutes that includes the total transmitter forward power.

In the postprocessing stage, DAQ data including a combination of all three trigger types are parsed into ROOT files. Transmitter logs are also parsed into a format useful for finding transmitter operational periods. A list of well-reconstructed FD events, those that are left after applying cuts (see Table 4.1), are obtained from TA. TARA FD trigger timestamps are compared to those from reconstructed events to remove all triggers that are not matched in time to TA events within 200 $\mu$s.

Matched events are separated from all other triggers and set aside for the calculation described in detail in this chapter. The remaining larger set of self-triggers are saved for future analysis. Parameters from matched TA events are used to simulate the expected radar echo. Each matched TARA FD-trigger has a unique, simulated echo which is used to create a MF template. The radar echo simulation produces theoretical received signals according to transmitter power, detector and shower geometry, antenna gain and shower parameters. FD-matched TARA triggers have associated CR energy, geometry, $X_{\text{max}}$ and core location from the reconstructed FD event to which they are matched. These data are used in the radar echo simulation.

A set of snapshots is selected from the complete set of snapshots that occurred during the FD run. Both matched FD-triggers and snapshots sets are reduced slightly by a set of quality cuts applied to both types of triggers. Section 5.1.3 describes the cuts and snapshots selection process in detail.

A peak MF response distribution is created for each matched FD-triggered event using the set of selected snapshots. The distribution is used to calculate an MF threshold, which is a parameter in the final calculation of the scale factor $\Gamma$. I assign a per-event peak matched filter (MF) response threshold based on the $3\sigma$ (three standard deviations) level from the snapshot peak MF response distribution. Recall that $\Gamma$ is assumed to be proportional to the true RCS $\sigma_{\text{EAS}}$.

The unique MF template created from simulation is applied to the matched FD-trigger. If the matched event MF response exceeds its threshold it is counted as positive detection, otherwise it is counted as nondetection. Some events will exceed their thresholds because of background fluctuations. If the number of positive detections is statistically significant, I calculate the scale factor $\Gamma$ required to produce the event MF response and report $\sigma_{\text{EAS}}$, where $\sigma_{\text{EAS}} = \Gamma\,\sigma_{\text{TW}}$.

In outline, the calculation is carried out by superimposing simulated echo waveforms on snapshots to estimate MF response relative to background. For events counted as positive detection I calculate the scale factor $\Gamma_{\text{obs}}$ necessary to produce the observed event MF response on average in the MF response distribution of snapshots superimposed with simulated echoes. In the case of negative detection, I calculate scale factor $\Gamma_{90}$ required to produce the desired threshold MF response in 90% of the snapshots that have been superimposed with the echo waveform. Section 5.4 describes this process in detail. $\Gamma_{\text{obs}}\,\sigma_{\text{TW}}$ is considered the detected RCS (positive detection). $\Gamma_{90}\,\sigma_{\text{TW}}$ is the RCS *upper limit* (negative detection) at the 90% confidence level.

The analysis data set initially includes all FlexRIO triggers that occur on FD run days starting on the first FD run day of August, 2013 and ending on the last FD run day in April, 2014. During this period the DAQ collected FD-triggers, among self-triggers and snapshots, from the majority of six FD runs. Transmitter power is typically 25 kW (See Figure 5.1). Very few transmitter-on triggers were collected during the January and February, 2014 FD runs because of transmitter problems that occurred at that time.

The following sections describe the RCS calculation in detail:

- Section 5.1 Data Preparation: parse, time-match, transmitter logs, snapshots selection, snapshot/matched event RMS calculation
- Section 5.2 Simulation: simulate each FD-matched event, create MF template
- Section 5.3 Event Matched Filter Response: MF threshold, detection categorization
- Section 5.4 Calculate Γ

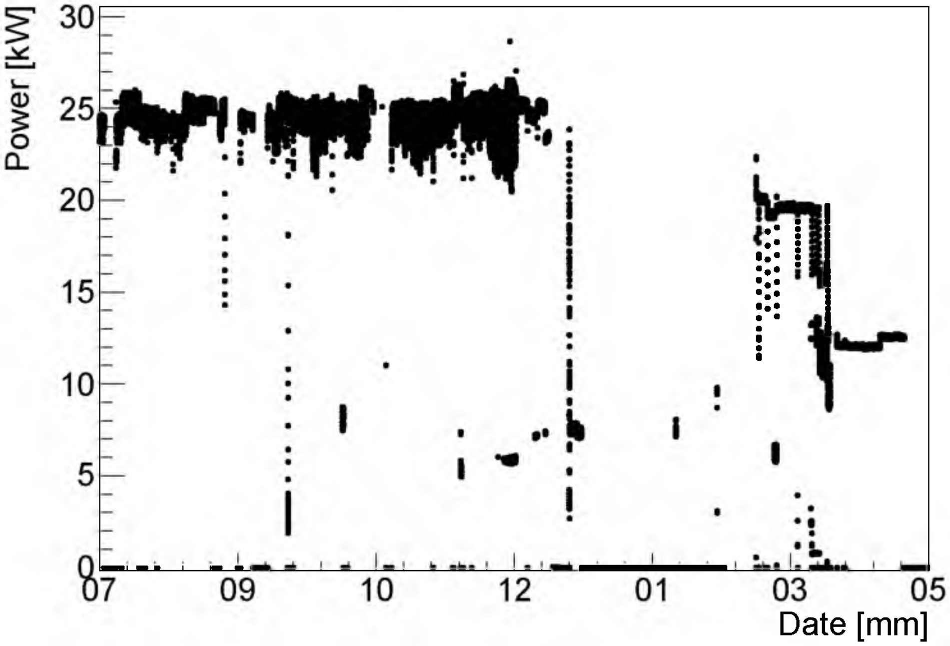

**Figure 5.1**: Transmitter forward power during the months in 2013/2014 when the analysis data set were recorded. The transmitter was turned off in January and February, 2014 due to power supply overheating and a failing power splitter. Power was reduced in March and April to avoid damaging the KTVN transmitter, which needed upgraded power amplifiers.

## 5.1 Data Preparation

In Chapter 4 I discuss raw data parsing from binary in to ROOT files and time-matching with TA Long Ridge FD reconstructed events. Monthly FD runs present a natural way to compile data parts, so I create a file for each FD run that initially includes all DAQ triggers taken during that period. Each FD run is processed separately. This remains true for all future analysis steps. Some files contain data that span fewer days than the actual FD data acquisition period because of known transmitter or receiver issues. January and February, 2014 FD run data are ignored because the transmitter was being repaired. FD run names and range of dates included in the analysis are shown in Table 5.1.

Each FD run data set is separately time-matched with reconstructed Long Ridge FD events. This step is the first to narrow the aggregate FD run file. Figure 5.2 shows the trigger delay of the FlexRIO DAQ relative to the FD for all FD triggers in the August, 2013 through April, 2014 data set.

It is important to remind the reader that four 32744 sample waveforms are included for each trigger, whether self-trigger, FD-trigger or snapshot. Channel three, horizontal polarization data are used in the self-triggering detection algorithm. The same channel will be used throughout the RCS calculation analysis procedure that follows.

**Table 5.1**: FD run names and dates included in the present analysis. January and February 2014 are omitted due to transmitter problems.

| FD Run Name | Dates (mmdd) |
|---|---|
| August 2013 | 0801–0816 |
| September | 0828–0914 |
| October | 0926–1014 |
| November | 1024–1112 |
| December | 1122–1212 |
| March 2014 | 0220–0309 |
| April | 0321–0407 |

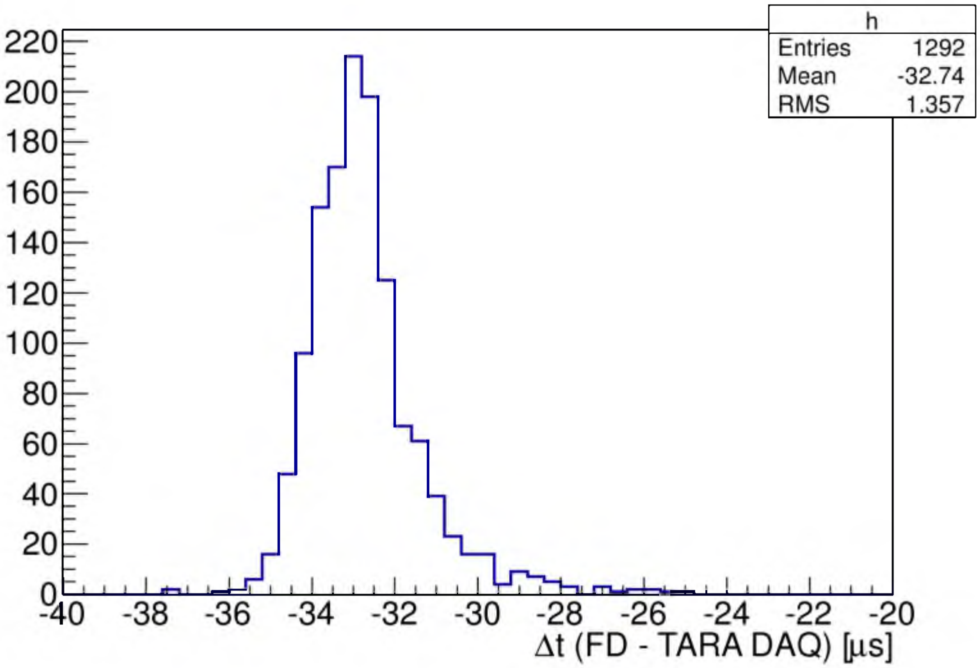

**Figure 5.2**: Time difference between FD reconstructed events and the TARA FD-triggered events to which they are matched for the entire data set (see Table 5.1). The 33 $\mu$s delay is caused by FD DAQ trigger formation, cable delay and TARA DAQ delay in signaling an event to the GPSY[18] GPS event logger.

### 5.1.1 Trigger Time Range

Spurious noise can interfere with the analysis. Waveforms with phase shifts or very high amplitude impulses will have large MF response which can mimic a positive detection or artificially elevate the background expectation. Waveforms with these features are eliminated from the data. To reduce the number of snapshots or matched FD-triggers that are discarded, all subsequent analysis steps are performed in a specific range of samples in the waveforms considered relevant (in time) to detection of possible echoes. Any waveform features outside of this range aren't considered in *any* step in the analysis.

The FlexRIO trigger time occurs at 96 $\mu$s from the beginning of the waveform. UV light produced by the shower leaves the column the same time as any scattered radar waves. FD trigger time is determined by the beginning of the 51.2 $\mu$s FADC readout where the actual trigger criterion is met between 12.8 and 38.4 $\mu$s into the window. To allow for some jitter, the beginning of the waveform time range is fixed at $96-33-15 = 48$ $\mu$s (at sample 48 $\mu$s $\cdot$ 250 MS/s = 12,000). Thirty-three $\mu$s are subtracted to account for delay in trigger formation and an additional 15 $\mu$s is subtracted in case the trigger criterion, which could be the peak response, is met at 12.8 $\mu$s into the window to ensure that the beginning of the signal is included. Candidate events are allowed to occur up to $96 - 33 + 38.4 \simeq 53$ $\mu$s past the adjusted trigger start time (at sample 25,250). Trigger criterion is often met when the signal is approaching its maximum, near $X_{\mathrm{max}}$, shortly after which the shower quickly dissipates or reaches the ground. The total range is [48,101] $\mu$s from the beginning of the trigger.

When the matched event peak MF response is calculated, the trigger range is actually altered such that the peak of the hypothetical radar signal is in the trigger range. For example, if the template has its voltage peak at sample 1000, the MF response will be calculated beginning on sample $12,000-1,000 = 11,000$. Subsequent MF responses will be calculated beginning on successive samples, up to sample $25,250 - 1,000 = 24,250$. In this way, if some hypothetical signal were to occur anywhere in the time range, the MF template would at some point match up perfectly with it. An adjustment to the trigger range is not necessary when analyzing snapshots superimposed with simulated echoes because the simulated waveform is always placed at 85 $\mu$s, well removed from the trigger range boundary.

Figure 5.3 shows the time domain of a notch-filtered snapshot with the DAQ trigger time marked by a solid red line and two red dashed lines marking the beginning and end of the adjusted trigger time range. Both a phase shift at 22 $\mu$s and high VRMS noise at 87 $\mu$s are present. In this case where the phase shift occurs outside the trigger range, the snapshot would not be removed from the set used for analysis (see Section 5.1.3 for a discussion of snapshots selection). Noise near the end of the trigger range would likely place this snapshot in the tails of the MF response distribution.

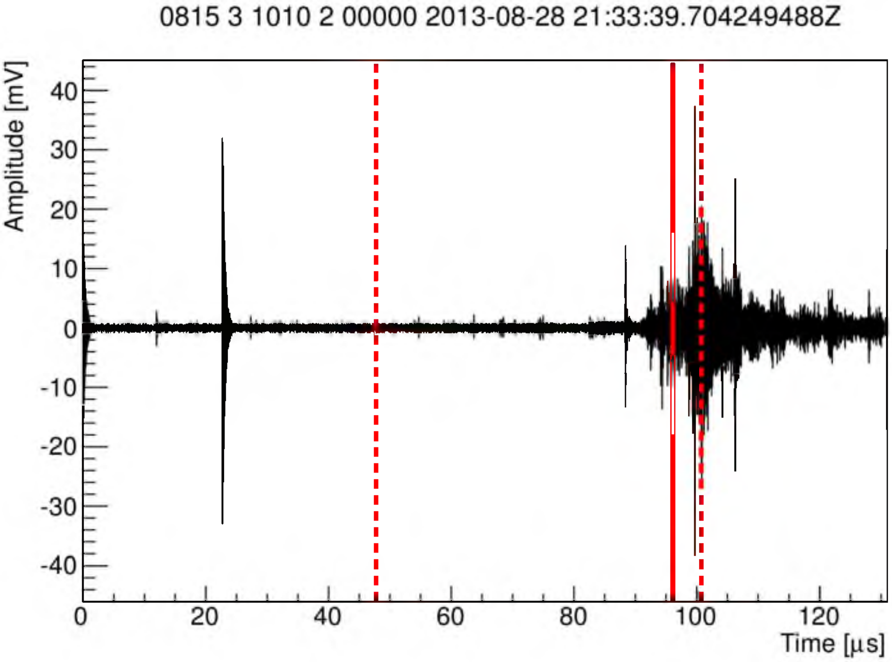

**Figure 5.3**: Time domain of notch-filtered snapshot taken in August, 2013 showing DAQ trigger time (96 $\mu$s, solid red line) and adjusted trigger range (48 $\mu$s and 101 $\mu$s, dashed red lines). This snapshot has both a phase shift at 22 $\mu$s and high VRMS noise at 87 $\mu$s. The phase shift occurs outside the trigger range under consideration, and therefore would not be excluded from the set of snapshots used in the analysis (discussed in Section 5.1.3). High VRMS noise near the end of the trigger range will cause large MF response, placing this snapshot in the tails of the MF response distribution.

### 5.1.2 Transmitter Logs

Transmitter monitoring and control software updates a text log file once per five minutes. Total forward and reflected power (see Figure 3.7), individual transmitter forward and reflected power, ambient temperature and any warning or error messages are recorded at each interval. Only total transmitter forward power is needed for RCS calculation.

Transmitter data are compiled in a root tree which is used to build a lookup table that contains start/stop times and transmitter forward power during that time, accurate to five minutes. The lookup table is queried for transmitter power before running the radar echo simulation.

The set of matched FD-triggered events is reduced by removing all triggers that occurred when the transmitter was off. After reducing the set of FD triggers by time matching with TA events and transmitter status, a typical FD run matched-event set has only a few hundred triggers or less. These are written to a separate file that's associated with a specific FD run.

### 5.1.3 Snapshots Selection

An important step in the analysis chain is estimating the MF response of a theoretical radar echo. Echo waveforms are superimposed on snapshots, which represent the background RF environment and shouldn't have any UHECR radar echo because of their extremely low flux. For each FD run data file, snapshots are first selected by requiring the transmitter to be on at the time they are acquired and choosing all snapshots that occur in five-minute bins in which the average FD-trigger rate is at least 1 Hz. Below this threshold the FD is not considered to be operating.

Selected snapshots are narrowed further by applying a phase shift and dead channel cut. Extremely rare dead channels are caused by malfunctioning RF chain amplifiers or amplifier DC power supply. Evidence of a dead channel is an non-filtered RMS value less than 1 mV. A functioning channel is dominated by the radar carrier and has RMS greater than 10 mV.

All snapshots in the time-limited set with phase shift or dead channel *in the predetermined trigger time range* are removed from all subsequent analysis steps. Similarly, any triggers in the matched-events set made in an earlier step are removed if they have phase shifts or dead channels. A separate file containing only selected snapshots is written to disk and will be used exclusively for analyzing data in the FD run for which they were selected.

Notch and 30 MHz high pass filtered snapshot waveform RMS values (calculated in the trigger time range) are used many times in the analysis procedure. To save processing time, the selected snapshots 54.1 MHz notch- and 30 MHz HP-filtered RMS values are written to a text file. A text file is also produced with RMS values of all the matched FD-triggers. Figure 4.6 shows a comparison of notched, HP filtered RMS values from selected snapshots and matched events recorded during the August, 2013 FD run.

## 5.2 Matched Event Simulation

The radar echo simulation is discussed in detail in Chapter 2. It takes as input event geometry (core location, zenith, azimuth), energy, $X_{\mathrm{max}}$ and transmitter power. Detector geometry, shower evolution parameters (beside $X_{\mathrm{max}}$), TX and RX polarization and full three dimensional radiation patterns (via lookup tables generated using NEC[16]) are included in the simulation. Together with transmitter power information the Long Ridge FD matched event provides all input parameters.

Starting at this point in the analysis procedure, all steps that proceed to and include $\Gamma$ calculation are conducted on a per-event basis. Each matched event is simulated and the output waveform is written to disk. In the August, 2013 set of simulated waveforms, maximum voltage spans five orders of magnitude [8.6e-7, 0.2] mV. Duration ranges from 5 $\mu$s to 100 $\mu$s. Frequency at maximum amplitude is as low as 30 MHz and as high as 160 MHz, but typically near 60 MHz.

MF response is maximized by creating the template from the specific simulation waveform. The output waveform is decimated to match the DAQ 250 MS/s sample rate and filtered according to the RF frontend FIR filter created with the measured transmission coefficient $S_{21}$ (see Section 4.4). An unmodified example radar echo and its spectrogram are shown in Figure 5.4. Figure 5.5 shows the result of frontend filtering the same waveform.

After filtering and decimation the waveform is truncated by removing samples at the beginning and end of the waveform that are below 5% of the peak value. For

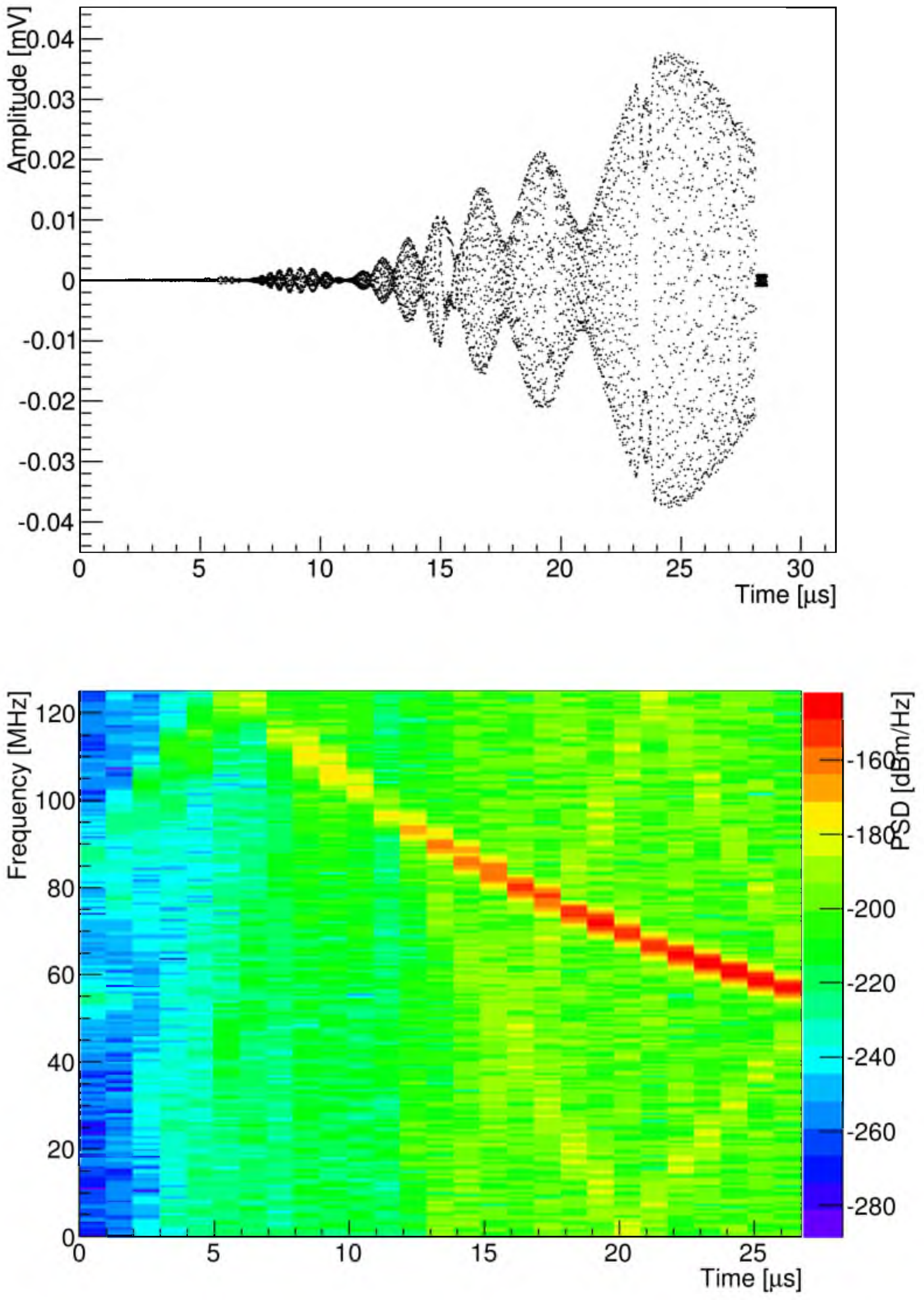

**Figure 5.4**: Simulated radar echo from a cosmic ray air shower located midway between the transmitter and receiver, inclined 30° out of the TX/RX plane. Top: Time domain waveform. Bottom: Spectrogram.

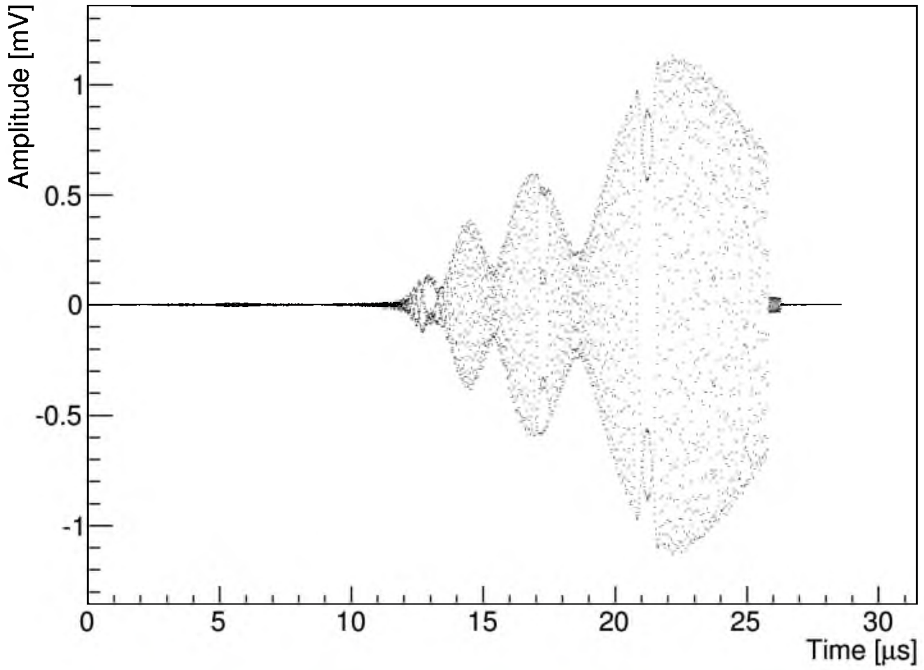

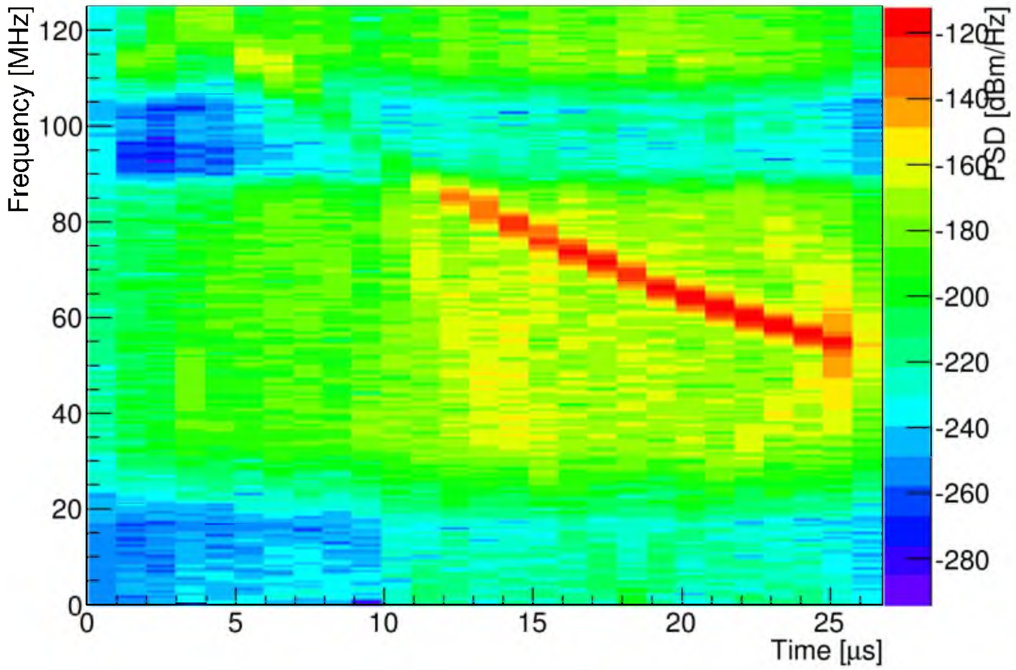

**Figure 5.5**: Simulated radar echo that has been filtered according to the RF frontend transmission coefficients $S_{21}$. Top: Time domain waveform. Bottom: Spectrogram.

example, the radar echo in Figure 5.5 loses approximately 10 $\mu$s from the beginning and several $\mu$s from the end without compromising detection efficiency. Processing time is reduced by removing low power tails. Finally, all chirp templates are scaled by their peak value to 1.0 mV before being written to disk. The template is ready for use directly after being read from disk.

## 5.3 Matched Event MF Response and Threshold

Each FD-triggered matched event will have a unique MF response distribution. Reconstructed shower parameters from the TA event are used to simulate the radar echo and make a fixed template as described in Section 5.2. The template is used to calculate the peak MF response $\beta$ for each of 400 snapshots. Before matched filtering, each snapshot is first notch and 30 MHz high pass filtered. An example distribution of peak MF responses is shown in Figure 5.6. Distribution mean ($\bar{x}$) and RMS are used to calculate the MF threshold $\gamma$ for the event under consideration. For this distribution, a 3 RMS threshold $\gamma_{\text{3RMS}} = \bar{x} + 3\,\text{RMS} = 32.6 + 3 \cdot 6.4 = 51.8$.

Following threshold calculation the FD-triggered event waveform is match filtered using the same radar echo template. Recall that matched events and snapshots are subject to the same quality cuts. All triggers with phase shifts in the trigger time range or those that have dead channels are removed. Before MF calculation, the waveforms are notch and HP filtered in the same way that snapshots are filtered.

Peak MF response $\beta_{\text{event}}$ is compared to the threshold $\gamma_{\text{3RMS}}$ specific to the event. If the threshold is exceeded, the event is tagged as a candidate positive detection and the algorithm proceeds to the calculation of the scale factor $\Gamma_{\text{obs}}$ necessary to produce the matched event response $\beta_{\text{event}}$ on average from the distribution of MF responses of 400 snapshots superimposed with the event-specific simulated echo. A response that's below threshold is tagged as a nondetection and $\Gamma_{90}$ is determined for the MF distribution threshold $\gamma_{\text{3RMS}}$. Recall that $\Gamma_{90}$ is the value of the scale factor $\Gamma$ that produces a peak MF response greater or equal to $\gamma_{\text{3RMS}}$ in 90% of 400 snapshots tested.

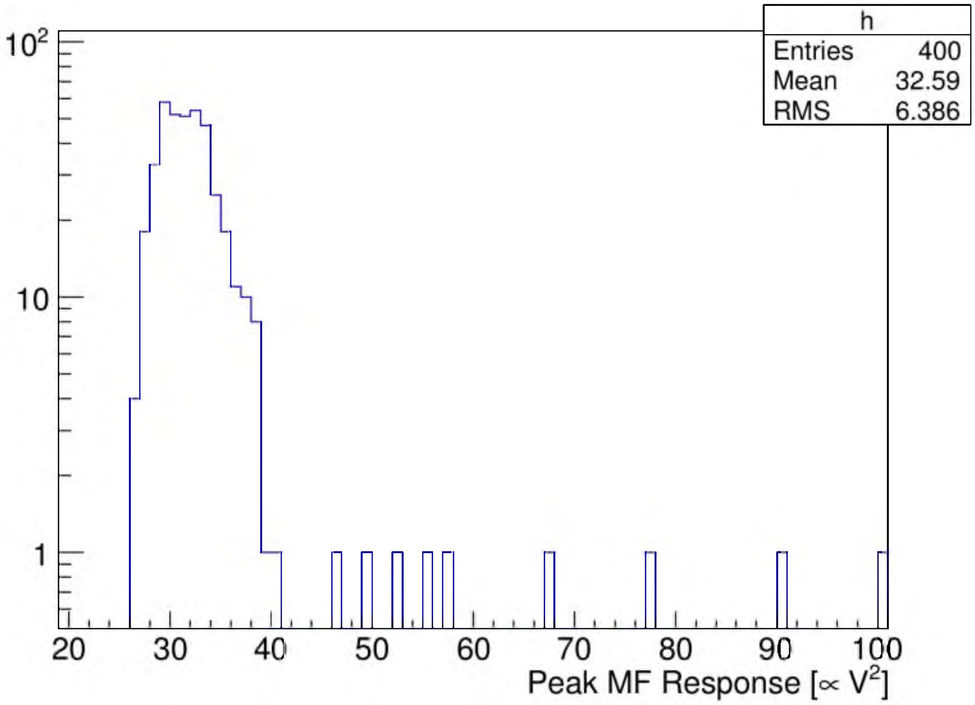

**Figure 5.6**: Peak MF response distribution for an August, 2013 FD-triggered matched event using 400 snapshots with a simulated radar echo MF template. The 3 RMS threshold is $32.6 + 3 \cdot 6.4 = 51.8$.

## 5.4 Scale Factor Γ

Γ calculation is similar for events tagged as either positive or nondetection. The only qualitative difference is the origin of the MF threshold $\gamma$ and the logic that's applied to the distribution of 400 snapshot + simulated echo peak MF responses. Each matched event has a unique template and threshold. Positive and nondetection events use the matched event peak MF response $\beta_{\text{event}}$ and snapshot peak MF response distribution threshold $\gamma_{\text{3RMS}}$, respectively, as the threshold used to calculate $\Gamma_{\text{obs}}/\Gamma_{90}$. Equation 5.1 shows the logic for determining $\gamma$.

$$\gamma = \begin{cases} \beta_{\text{event}} & \text{if } \beta_{\text{event}} > \gamma_{\text{3RMS}} \\ \gamma_{\text{3RMS}} & \text{if } \beta_{\text{event}} < \gamma_{\text{3RMS}} \end{cases} \tag{5.1}$$

For each matched event, Γ is calculated in the following steps with Λ being the value by which simulated echo voltage samples are scaled before being superimposed on the 400 test snapshots:

1. Load event-specific MF template. Use exclusively in remaining steps.

2. Load unmodified, simulated radar echo waveform
    (a) Downsample waveform to 250 MS/s DAQ sample rate
    (b) Filter simulated waveform according to RF frontend ($S_{21}$). Result: $x[\,]$[a].
    (c) Find maximum voltage value $V_{\text{max}}$ at index $i$
3. Calculate initial guess for $\Lambda$
    (a) Calculate first snapshot VRMS
    (b) $\Lambda = \text{VRMS}/(10 \cdot V_{\text{max}})$
4. Enter primary loop (exit when desired $\Lambda$ efficiency and precision is achieved)
    (a) Scale simulated echo waveform: $x'[\,] = x[\,] \cdot \Lambda$
    (b) Superimpose scaled waveform on 400 snapshots
        i. Superimpose $x'[\,]$ on snapshot waveform $j$ such that the peak at $i$ falls at 85 $\mu$s
        ii. Apply 54.1 MHz notch filter
        iii. Apply 30 MHz high pass filter
        iv. Get peak MF response $\beta_j$ in time range of interest
    (c) Apply positive-/negative-detection logic
        i. Positive detection: Test $\langle \beta_j \rangle = \gamma$
        ii. Negative detection: Test $N_{\text{exc}}/400 > 90\%$, where $N_{\text{exc}}$ is total number of $\beta_j$ that exceed $\gamma$
    (d) Increment/decrement $\Lambda$ and repeat until test is true and desired precision is found
5. Return scale factor $\Gamma = \Lambda^2$ because $V^2 \propto$ power $\propto \sigma_{\text{TW}}$ and $\Lambda$ scales waveform voltage samples.

---

[a] Empty brackets ($[\,]$) denote an array of discrete-time sampled data.

In the primary loop, $\Lambda$ is increased if $\langle \beta_j \rangle < \gamma$ (positive detection) or $N_{\mathrm{exc}}/400 < 90\%$ (negative detection) or decreased in the opposite case until the tests are true and the desired precision is achieved. The method for choosing subsequent $\Lambda$ values has been optimized by initially taking large steps in $\Lambda$ then decreasing $\Lambda$ each time the logic condition is passed from either below or above. There are other minor details which reduce calculation time, but give results which are exact compared to the brute force algorithm described here. It is sufficient to say that all $\Lambda$ values are calculated with precision shown in Equation 5.2.

$$\delta\,\Lambda = \begin{cases} 10^{\alpha} \text{ where } \alpha \equiv \mathrm{floor}\left(\log_{10}\left(\Lambda\right)\right) - 1 & \text{if } \Lambda > 1 \\ 0.0001 & \text{if } \Lambda < 1 \end{cases} \tag{5.2}$$

Only small scale factors ($\Gamma < 1$) contribute significantly to the result. The error for $\Gamma < 1$ is $\delta\,\Gamma = 0.000141\,\sqrt{\Gamma}$.

# CHAPTER 6

# RESULTS

Consider the meaning of scale factor $\Gamma$. The radar echo simulation uses the thin-wire approximation, a model for the RCS of an EAS segment. It predicts an absolute received power based on the model assumption and other known parameters such as antenna radiation patterns, detector geometry, transmitter power and shower geometry and energy. Only received power is model dependent (see Figures 2.8 and 2.9 and surrounding text in Chapter 2).

I have also shown in Chapter 2 that the thin-wire approximation is a likely representative of the scattering *geometry* of the true RCS and almost certainly an over-estimation of the scattering power because collisional damping and skin depth have not been taken into account. Therefore we don't expect to detect signals at the same power level predicted by the simulation. We do expect signals to have the same frequency vs. time graph.

The simulation over-estimates signal power, otherwise our data stream would have many positive SNR signals. Section 6.1 concludes that is not the case. Figure 6.1 shows a histogram in which PSD for all 1,292 simulated echoes (red) produced during the analysis and 1292 snapshot PSD values (black) are included for comparison. The simulated echo PSD is the maximum in the DAQ [40,80] MHz passband and snapshot PSD is calculated at 65 MHz without using any filters so snapshots can be compared with the noise floor (Figure 3.18), where PSD at 65 MHz is roughly -163 dBm/Hz (blue line). One observes that many simulated radar echoes exceed the background level, some by as much as 30 dB. Very low PSD echoes are those with geometry that avoided the radar radiation pattern main lobe. Also recall that the MF technique used in this analysis can detect theoretical signals at least 10 dB below the noise.

If we record significant positive detections (likely with $\Gamma_{\text{obs}} \ll 1$), we quote $\sigma_{\text{EAS}} = \Gamma_{\text{obs}} \cdot \sigma_{\text{TW}}$ using the event peak MF response $\beta_{\text{event}}$ as the threshold used to calculate

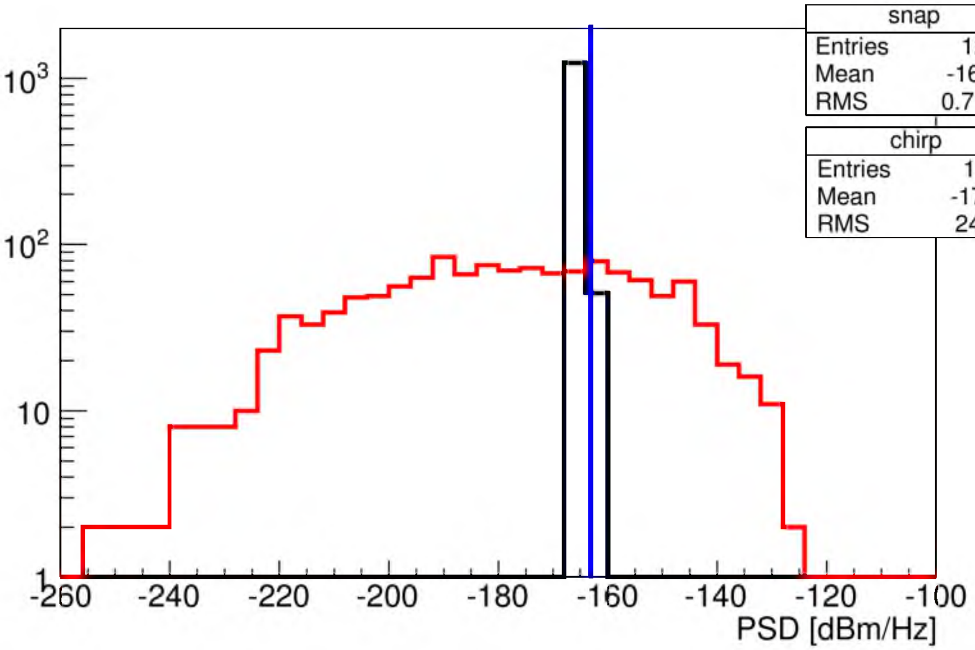

**Figure 6.1**: Power spectral density (PSD) of 1292 radar echoes (red) simulated from matched event parameters and 1292 snapshots (black) selected for analysis from the August, 2013 FD run using a 512 sample window size. Radar echo PSD is the maximum value in the [40, 80] MHz passband. Snapshot PSD is the un-filtered value at 65 MHz for comparison with the noise floor in Figure 3.18. The blue line is approximate noise floor level at 65 MHz. The simulation includes full TX/RX antenna radiation patterns, transmitter power at detection time and air shower geometry and energy reconstructed by Telescope Array. The thin-wire approximation (Equation 2.26) is used to calculate the RCS.

$\Gamma_{\text{obs}}$. $\Gamma_{\text{obs}}$ is the scale factor which produces an average matched filter response distribution equal to $\beta_{\text{event}}$. Otherwise the true RCS is below our detector capability so the snapshot distribution threshold $\gamma_{3\text{RMS}}$ is used in calculating $\Gamma_{90}$ in which case we report the RCS *upper limit* as $\sigma_{\text{EAS}} = \Gamma_{90} \cdot \sigma_{\text{TW}}$. Each FD-triggered matched event is analyzed to produce a scale factor, either $\Gamma_{\text{obs}}$ or $\Gamma_{90}$. Output from the analysis procedure described in Chapter 5 is discussed in detail in this chapter.

In the following sections I first present events tagged as positive detections and calculate the significance of that result compared to backgrounds. This is followed by plots showing the much larger set of events tagged as negative detections. The effect of systematic error is quantized in Section 6.3 and RCS upper limits are presented in Section 6.4.

## 6.1 Positive Detection Events

From all 1,292 events processed in the data set (taken from FD runs shown in Table 5.1), 17 events have MF response greater than $\gamma_{3\mathrm{RMS}}$. These are considered as possible positive detection of scattered radar waves from EAS. To properly gauge the significance of this value, I calculate the expected value of false positives for comparison.

A distribution of 400 peak MF responses is produced for each event, from which the threshold is calculated. MF response distributions have high side tails caused by anthropogenic sources. Tails are minimized, but not completely removed, by restricting the bandwidth (hardware RF frontend filters) and applying post-processing notch and HP filters. In nearly all distributions there are several snapshots that exceed the threshold. Figure 5.6 shows the MF response distribution for an event from August, 2013. The threshold is $\bar{x} + 3\mathrm{RMS} = 51.8$. Seven snapshots out of 400 exceed exceed the threshold.

The number of snapshots that exceed the threshold $N_{\mathrm{snap,exc}}$, per matched event, is a parameter saved in the analysis output. Figure 6.2 shows the distribution of $N_{\mathrm{snap,exc}}$ for all events included in the analysis that weren't rejected due to dead channels or phase shifts. The total number of expected false positives is the weighted expected value for all 1292 events, or the mean probability multiplied by the total number of events: $(5.50/400) \cdot 1292 = 17.77$. The chance probability of observing 17 positive detections, given an expected value of 17.77, is 60.4%. This means that there is no reason to believe positive detections are anything other than false positives caused by common backgrounds, so we turn our focus to negative detection events in Section 6.2.

## 6.2 Individual Event Scale Factor

Figure 6.3 shows the core location and $\Gamma_{90}$ value (color scale) for all events tagged as negative detections, those with peak MF response less than the threshold determined from the snapshot MF response distribution. The same data are presented in a one-dimensional histogram to better show $\Gamma_{90}$ distribution in Figure 6.4. Because these are negative detection events, scale factors are calculated using the threshold

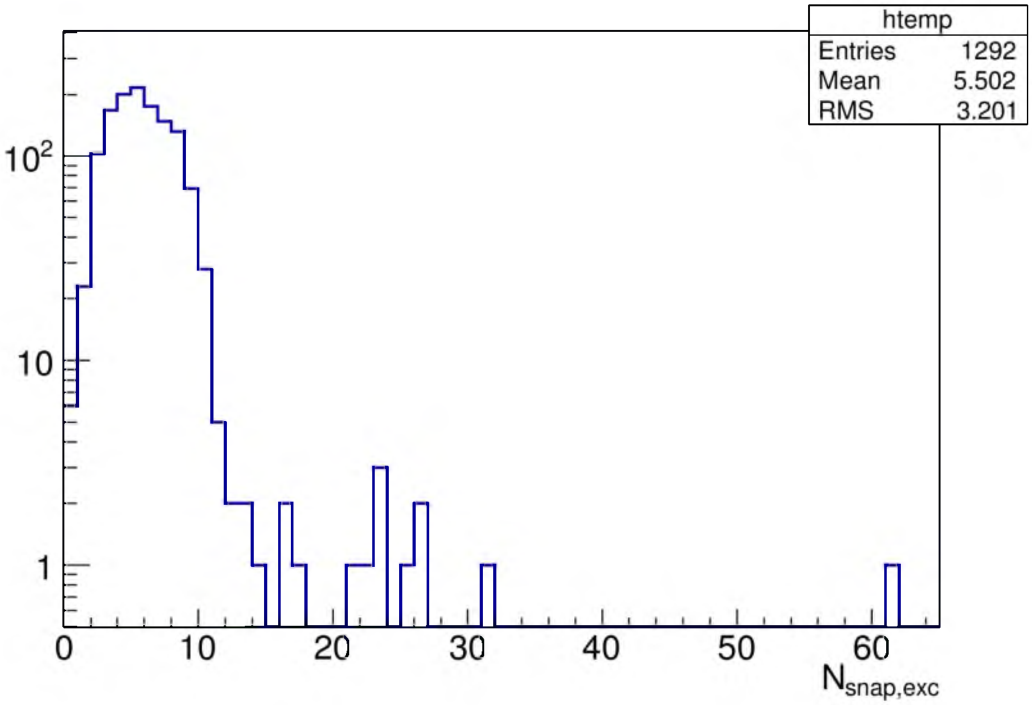

**Figure 6.2**: Distribution of $N_{\text{snap,exc}}$, number of snapshots whose peak MF response exceeds threshold. One entry per matched FD-triggered event.

$\gamma_{3\text{RMS}}$ that also determines detection status.

A similar plot including only events with $\Gamma_{90} < 0.1$ is shown in Figure 6.5. Events are clustered near the main lobe. Only very few events will have zenith angles near zero and good scale factor events must be those that pass through the main lobe. Therefore there will be few events along the center of the beam.

To show the effect of transmitter antenna main lobe, a scale factor plot is shown in Figure 6.6 that restricts the set of events to those with azimuth greater than 90° and less than 180°. All events in the plot point back to the source toward the second quadrant (upper left). Events above the beam can't interact with the main lobe, so their scale factors are very high. The lowest scale factor events are those that produce high echo voltages because of geometry and interaction with the main lobe. Reversing the general pointing direction of events, by limiting azimuth to greater than 270° and less than 360°, produces a similar plot, but with the high $\Gamma_{90}$ events below the main lobe and low $\Gamma_{90}$ above the main lobe.

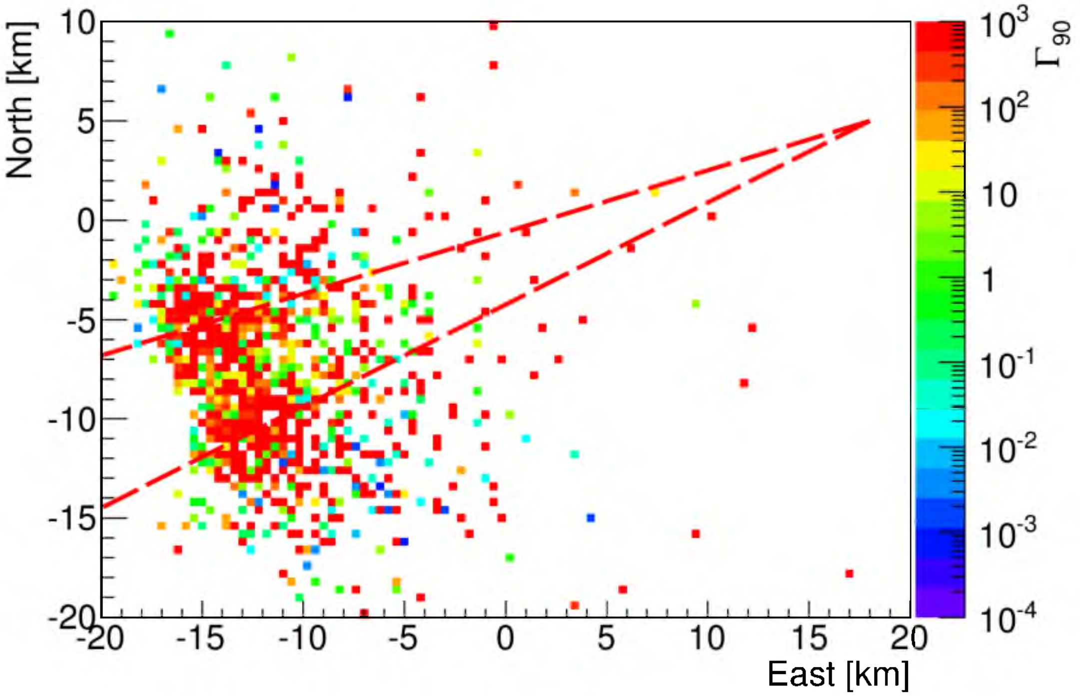

**Figure 6.3**: $\Gamma_{90}$ (color scale) for all negative detection (FD-triggered waveform peak MF response did not exceed threshold) events shown at reconstructed core locations in Telescope Array CLF (referenced to Central Laser Facility) coordinates. Red dashed lines mark the primary beam -3 dB beamwidth. This histogram format can be misleading because events with similar core locations can fall into the same bin.

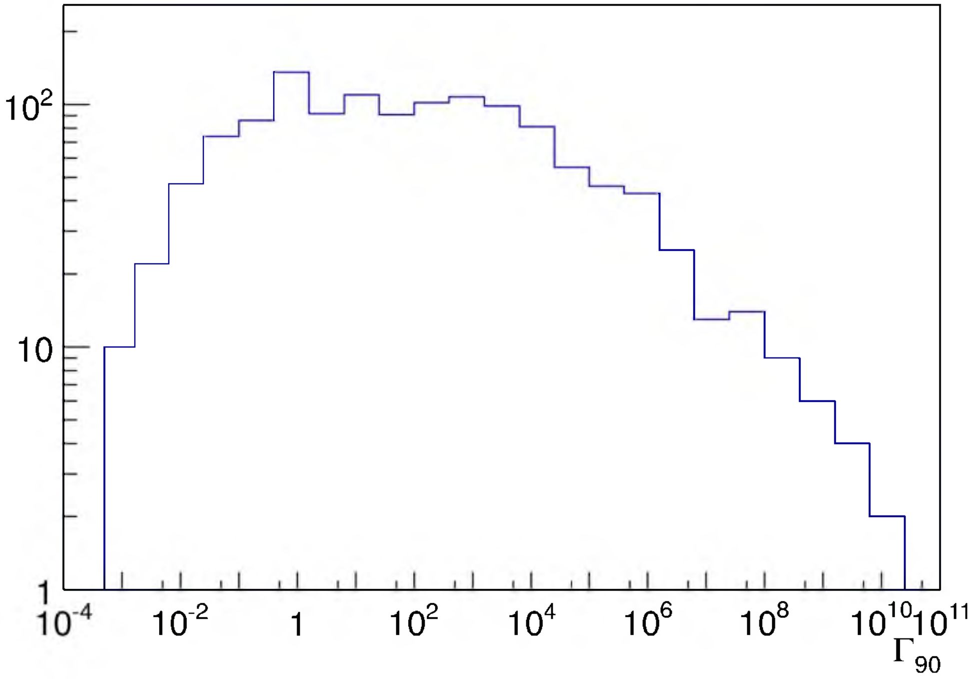

**Figure 6.4**: $\Gamma_{90}$ distribution of all negative detection events. Large $\Gamma_{90}$ occurs when matched-event geometry specifies an EAS that occurs outside the antenna main lobe.

## 6.3 Systematic Error

The bi-static radar equation,

$$P_R = \frac{P_T G_T}{4\pi R_T^2}\,\sigma\,\frac{G_R}{4\pi R_R^2}\frac{\lambda^2}{4\pi}, \tag{6.1}$$

copied from Equation 2.1 for convenience, is composed of factors which can introduce error to the radar echo simulation which directly influences the scale factor at the 90% confidence level $\Gamma_{90}$. Transmitter power $P_T$ is logged every five minutes. The maximum time difference allowed between a log entry and matched FD event is 10 minutes. In the remaining portion of this section I quantify the largest contributions to systematic error and apply it to the lowest five $\Gamma_{90}$ events. For these specific events, maximum time difference between FD event and transmitter log entry is 80 s. Two events differ by only 10 s. Interpolating by eye, the maximum error in $P_T$ is less than 100 W. Figure 3.6 shows stabilized transmitter forward power. Fluctuation in a single sample period is less than 100 W. Also, calibration error on values in transmitter logs has been observed to be approximately 200–300 W, or about 1%

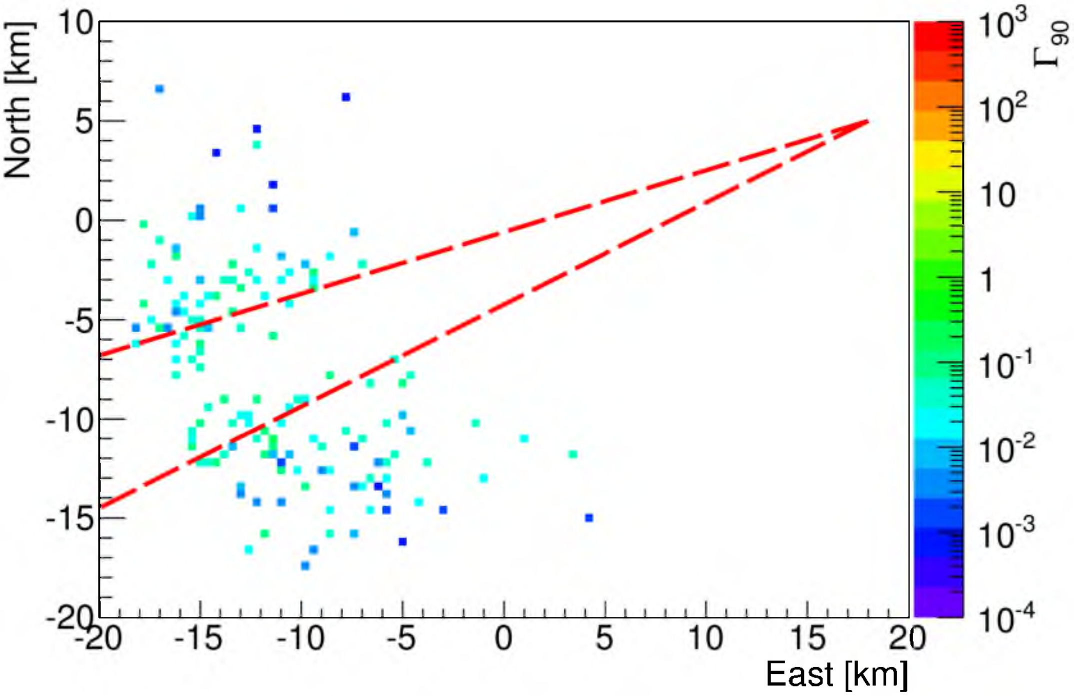

**Figure 6.5**: $\Gamma_{90}$ (color scale) for negative detection events with $\Gamma_{90} < 0.1$ shown at reconstructed core locations in Telescope Array CLF coordinates. Red dashed lines mark the primary beam -3 dB beamwidth.

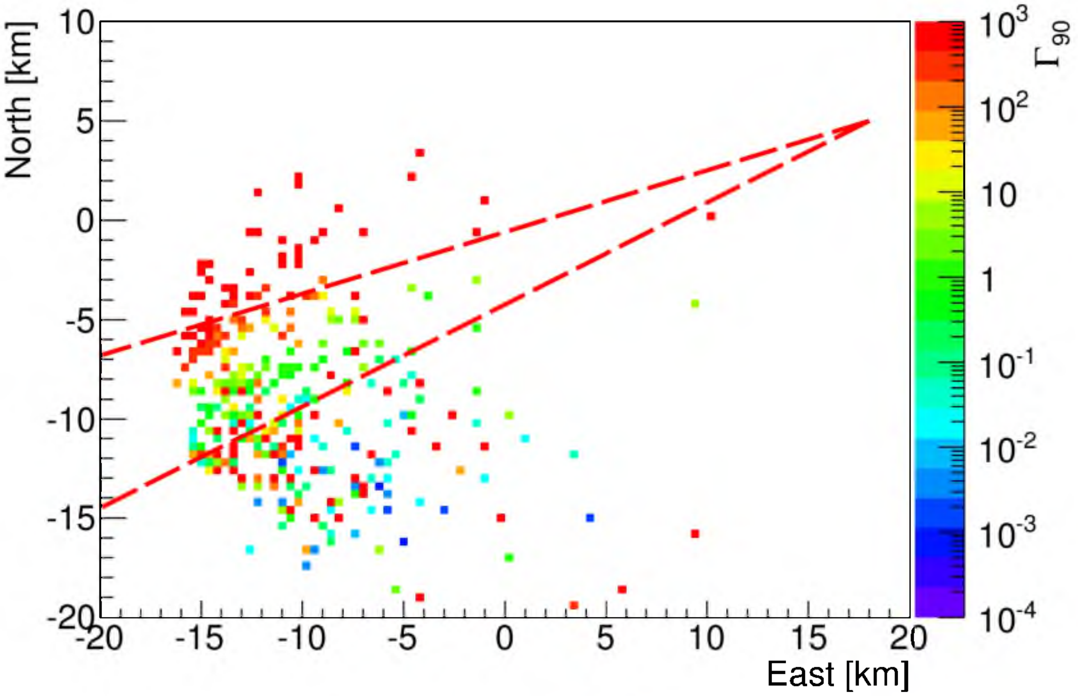

**Figure 6.6**: $\Gamma_{90}$ (color scale) negative detection events restricted to those with $90° <$ azimuth $< 180°$ shown at reconstructed core locations in Telescope Array CLF coordinates. Red dashed lines mark the primary beam -3 dB beamwidth.

of 25 kW power output during which the five events were recorded. The effect of uncertainty in transmitter power is neglected.

Transmitter and receiver antenna gains ($G_T$, $G_R$) are from simulations that have been shown to be accurate (see Section 3.3.2). Distances from transmitter to shower $R_T$ and shower to receiver $R_R$ are determined from core location (discussed in Section 6.3.1) and transmitter and receiver positions, which have been determined from GPS coordinates. Therefore, we consider error introduced from the bi-static radar equation to be minor compared to other sources.

$\Gamma_{90}$ is calculated for each FD-triggered waveform that has been time-matched to reconstructed FD events. Reconstruction parameters have associated uncertainty which affect the RCS upper limit expressed through $\Gamma_{90}$. Reconstructed parameters used in the radar echo simulation include $E_0$, core location, zenith and azimuth angle, and $X_{\max}$. $E_0$ primarily affects the radius of the collision-less overdense region of the EAS. The thin-wire approximation for the RCS of EAS (see Equation 2.26) is dependent on radius only logarithmically, so we ignore the effect of error in $E_0$. An expanded description of the reconstructed parameter problem and a method for estimating its effect is given in Section 6.3.1.

In the echo simulation, three-dimensional models are used to calculate transmitter and receiver antenna gain. Both models assume that 54.1 MHz waves are transmitted/received. This assumption is correct for the transmitter antenna which only transmits the single tone. Electrons in the receiver antenna oscillate at the frequency of the total electric field. Recall from Section 2.5 that a chirp signal is expected because of superposition of waves scattered at different points along the shower track that arrive at the receiver with the same fundamental frequency, but different phase. The total electric field frequency changes rapidly with time. Ideally, the simulation would calculate the real-time received frequency and use a receiver antenna model specific to that frequency. The error introduced from using a fixed 54.1 MHz model will be estimated in Section 6.3.2.

### 6.3.1 Effect of Uncertainty in Reconstructed Shower Parameters

The TARA DAQ is triggered by the monocular mode FD, so uncertainty in reconstructed parameters is greatest for events that rely on estimation of distance in the radial direction from the detector. This affects core location and shower geometry. Events with azimuth aligned with radial direction have the greatest error in geometry.

Two common geometry variables $R_p$ and $\Psi$ are calculated in FD event reconstruction and compared with Monte Carlo events to calculate their error. Both are values in the shower/detector plane (SDP). $R_p$ is the impact parameter. It is the shortest distance between shower track and detector. $\Psi$ is the angle between shower axis and ground plane in the SDP.

The RMS resolutions of monocular reconstruction are 1.4 km in $R_p$, 7.7° in $\Psi$, 17% on $E_0$ and 72 g/cm$^2$ on $X_{\max}$.[108] To test the effect of error in $\Psi$ we transform shower geometry into a coordinate system in which the $z$ and $x$ axes are in SDP. The new zenith angle is modified to reflect an increase in $\Psi$ of 7.7°. Then its coordinates are transformed back to the original system. $\Psi$ and $R_p$ are strongly correlated, so only the effect of $\Psi$ on $\Gamma_{90}$ is considered. The final reconstructed parameter test estimates the effect of error in $X_{\max}$ on $\Gamma_{90}$ using a pessimistic shift decrease of 100 g/cm$^2$.

The estimation procedure assumes that the primary contribution to the width of a distribution of MF responses $\beta$ at a fixed scale factor $\Gamma$ is a result of Gaussian noise. Voltage distribution of a notch and high pass filtered FD trigger waveform is show in Figure 6.7. A Gaussian curve has a very good fit with the distribution. Snapshot voltage samples are also Gaussian distributed.

MF distribution mean $\bar{\beta}_{90}$ using $\Gamma_{90}$ scale factor for one of the fives lowest $\Gamma_{90}$ events from the August, 2013 data set is show in Figure 6.8. Each $\beta$ in the histogram is the peak MF response of a radar echo superimposed on a snapshot (background) waveform using the scale factor $\Gamma_{90}$. The template for the MF is created from the same simulated echo that is superimposed. By definition the $\Gamma_{90}$ scale factor produces a distribution of MF responses of which 90% exceed the predetermined detection threshold $\gamma$ (see Section 5.3).

A comparison distribution (Figure 6.9) is generated using the same template and snapshots but superimposing a new radar echo simulated with $\Psi$ angle increased 7.7°. All other parameters are held constant. Comparing the two distributions, one observes that the mean changes by about 23 standard deviations while $\sigma$ changes by only six standard deviations. An error Gaussian is constructed with the mean of

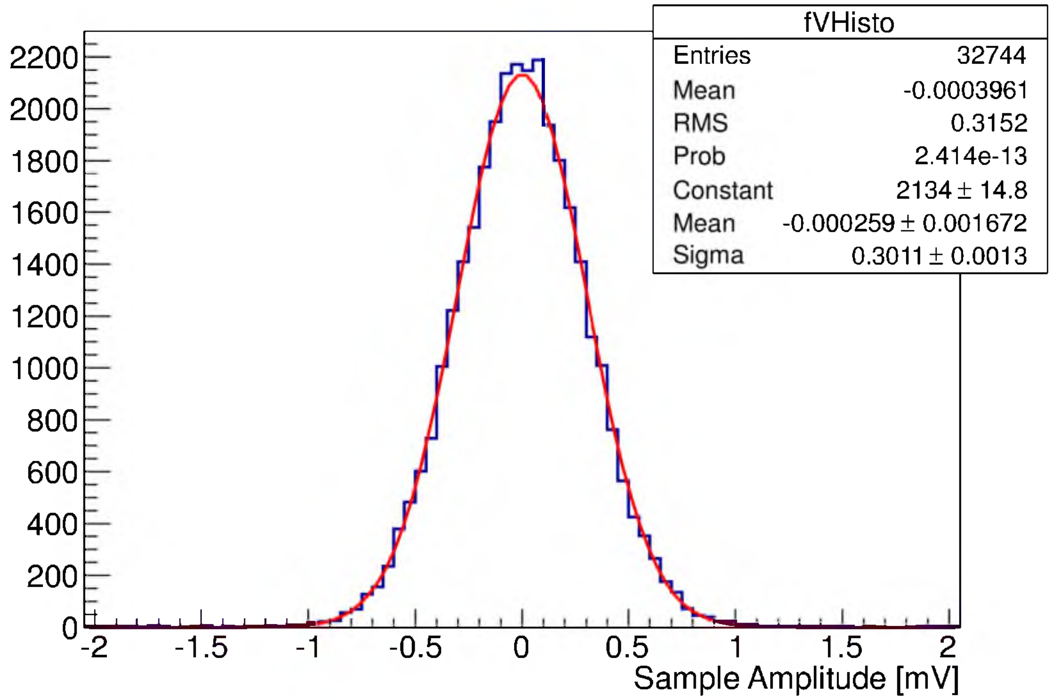

**Figure 6.7**: 54.1 MHz notch and 30 MHz high pass filtered FD trigger waveform sample histogram. Red line is a Gaussian fit.

the unmodified distribution $\mu_{\text{orig}}$ and RMS $\sigma_{\text{err}}$ equal to the difference in the mean between the original and modified distribution. For this example the error Gaussian has $\mu = \mu_{\text{orig}} = 76.35$ and $\sigma = \sigma_{\text{err}} = 76.35 - 61.98 = 14.37$.

Error in $\Psi$ (transformed to zenith and azimuth) has the effect of increasing the RMS of the original $\beta$ distribution. A new distribution of MF responses is created by convolving the original distribution with the error distribution. By applying the convolution theorem (see the section in[106] regarding properties of the Fourier transform for discrete-time signals), one can derive the convolution of two Gaussian distributions with parameters ($\mu_1$, $\sigma_1$) and ($\mu_2$, $\sigma_2$), which is a new Gaussian distribution with $\mu = \mu_1 + \mu_2$ and $\sigma = \sqrt{\sigma_1^2 + \sigma_2^2}$.[109] We consider just the RMS increase, so the new distribution has parameters ($\mu_{\text{orig}}$, $\sqrt{\sigma_{\text{orig}}^2 + \sigma_{\text{err}}^2}$).

The new distribution has less than 90% of its MF values above the threshold $\gamma$ because it has become wider. Therefore, I calculate the change in $\bar{\beta}_{90}$ (denoted $\Delta\bar{\beta}_{90}$) necessary such that 90% of MF values exceed $\gamma$. Here, $\gamma$ is the position on the original histogram where an integration of the *fitted* curve from $-\infty$ to $\gamma$ equals 10%.

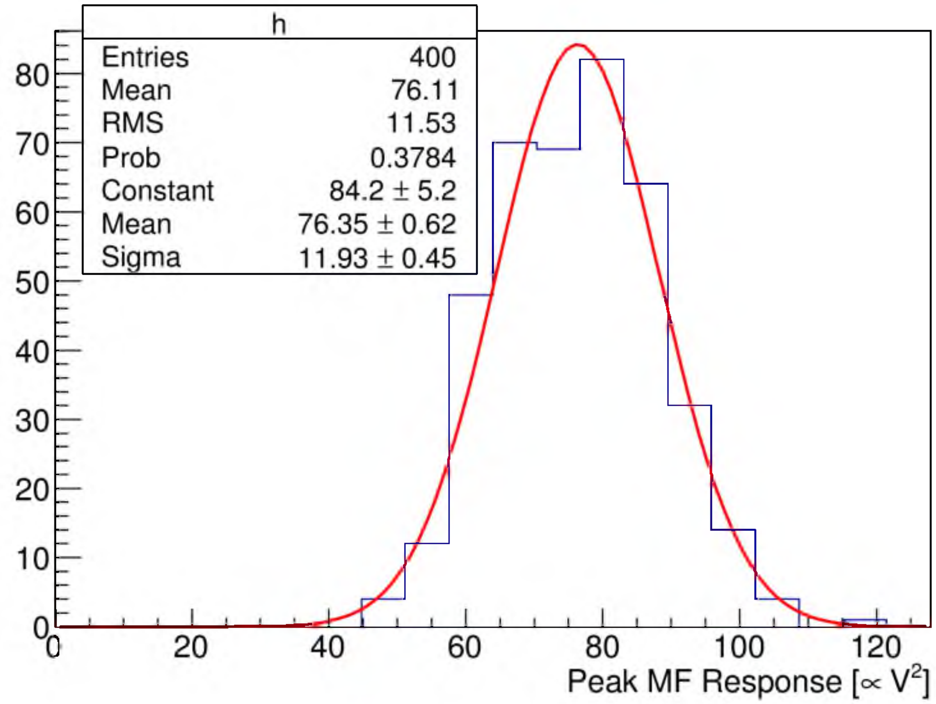

**Figure 6.8**: Distribution of peak matched filter responses from 400 snapshots superimposed with a simulated radar echo using scale factor $\Gamma_{90}$. The simulated radar echo is from a low $\Gamma_{90}$ August, 2013 event. A Gaussian is fitted to the data.

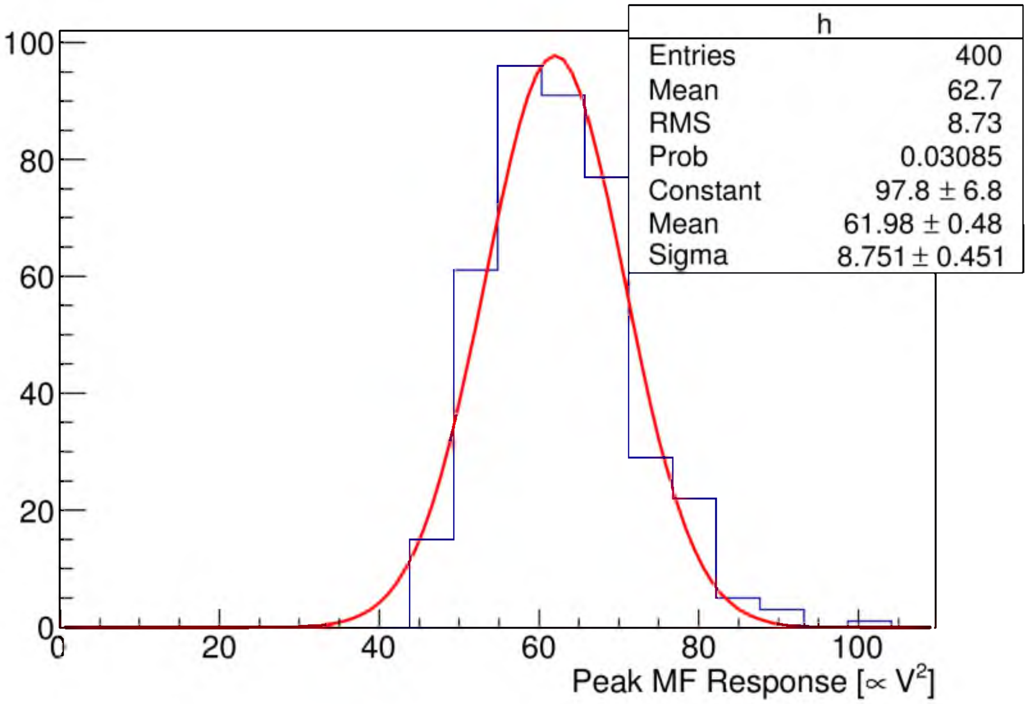

**Figure 6.9**: Distribution of peak matched filter responses from 400 snapshots superimposed with a simulated radar echo using scale factor $\Gamma_{90}$. The simulated radar echo is from a low $\Gamma_{90}$ August, 2013 event that has been modified by increasing the $\Psi$ angle 7.7°. A Gaussian is fitted to the data.

$\gamma$ calculated from snapshot peak MF response distribution is slightly different due to the error in the fit. Using it to compare fitted curves would give erroneous results.

Scale factor $\Gamma$ and mean MF response $\bar{\beta}$ are proportional. Superimposed echoes have voltage units that are scaled by $\sqrt{\Gamma}$ ($\Lambda$ in Section 5.4) before being superimposed on snapshot waveforms that share the same units. The MF process is a dot product between a template, also in voltage units, and the superimposed waveform. The result has units proportional to $V^2$, which is proportional to power, which is also true of $\Gamma$. Figure 6.10 shows two plots, both functions of $\Gamma$, near $\Gamma_{90}$. $\Gamma_{90}$ can be read from the top plot at the point where detection probability is 0.9 or $\Gamma_{90} = 0.00088$.

Mean MF response is linear near $\Gamma_{90}$. The slope must be known in order to project the change in mean MF response $\Delta\,\bar{\beta}_{90}$ to the change in $\Gamma_{90}$, $\Delta\,\Gamma_{90}$. This is accomplished by also calculating the mean MF response $\bar{\beta}_{50}$ of the distribution for which 50% of responses exceed $\gamma$. Scale factors $\Gamma_{90}$ and $\Gamma_{50}$ together with mean MF responses $\bar{\beta}_{90}$ and $\bar{\beta}_{50}$ are used to calculate the slope $m$ in the bottom plot of Figure 6.10. The change in $\Gamma_{90}$ is $\Delta\,\Gamma_{90} = \Delta\,\bar{\beta}_{90}/m$. For this event $\Gamma_{90}$, the scale factor that yields an event with amplitude sufficient to trigger the detector 90% of the time, sees an increase of 23%.

The procedure described above was repeated on the five lowest $\Gamma_{90}$ events, which are listed in Table 6.1. Two events occurred during the August, 2013 run, (the second of which was used as the example) and one event each comes from October, November, and December FD runs. Percent difference in $\Gamma_{90}$ for these events due to 7.7° increase in $\Psi$ is also shown. Error introduced to each event from 100 g/cm$^2$ decrease in depth of $X_{\text{max}}$ is much less than 1% for all events, and therefore not shown. Figure 6.11 is similar to the plot in Figure 6.5, but includes green arrows that begin at the core location of the five lowest $\Gamma_{90}$ events and point in the direction of the azimuth. Arrow length is proportional to the zenith angle. One observes that the five lowest events are highly inclined in order to match transmitter and receiver polarization and have azimuth values which allow them to interact with the main lobe.

Of the two perturbations made to simulation output only one has meaningful effect. $\Psi$ increases the five lowest $\Gamma_{90}$ events at most about 60%. $\Gamma_{90}$ is calculated with uncertainty $\delta\,\Gamma_{90} = 0.000141\,\sqrt{\Gamma_{90}}$, which has an effect of at most about 1%.

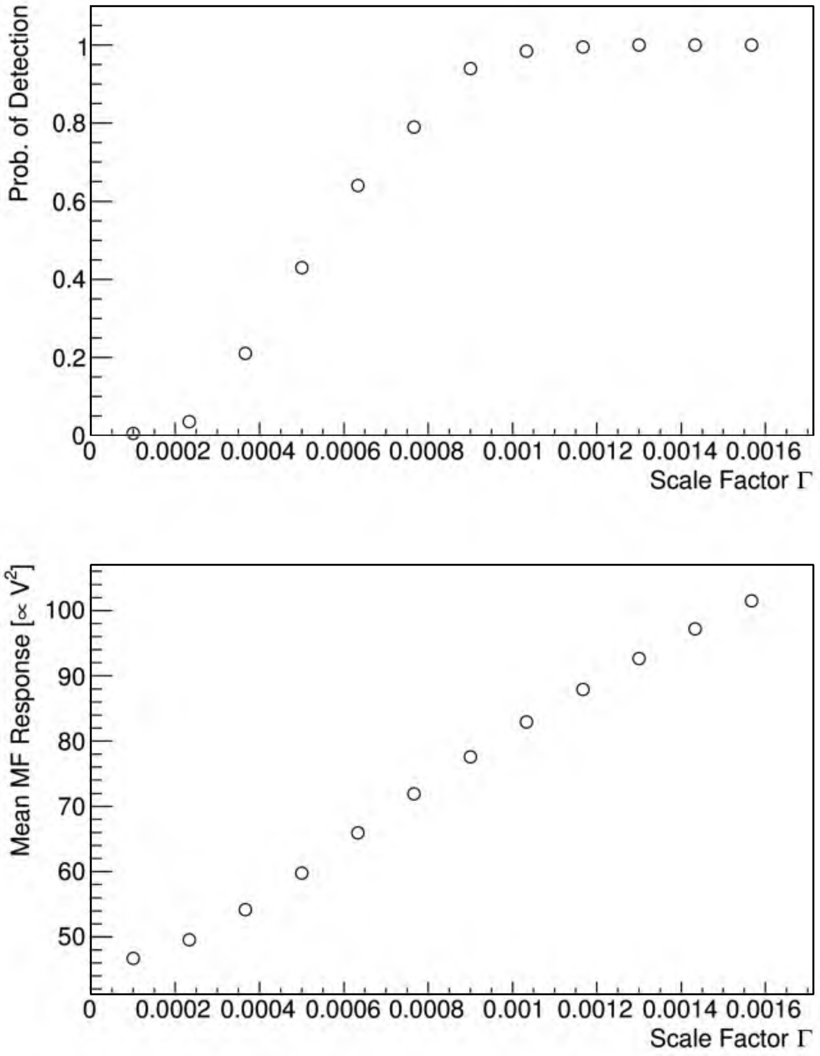

**Figure 6.10**: Behavior of detection probability and mean peak MF response $\bar{\beta}$ as a function of scale factor Γ. Γ range is chosen such that it includes $\Gamma_{90}$, which is 0.00088.

### 6.3.2 Effect of Fixed Frequency Receiver Antenna Model in Echo Simulation

Error introduced in $\Gamma_{90}$ values from using a static 54.1 MHz receiver antenna radiation pattern is mitigated by the frequency range of the lowest five $\Gamma_{90}$ events. The top plot in Figure 6.12 shows a spectrogram of one of the lowest five $\Gamma_{90}$ events recorded in August, 2013. It is also the first entry in Table 6.1. $F_{\text{max}}$ , the frequency at maximum power, is 57.6 MHz. All five $F_{\text{max}}$ of the lowest $\Gamma_{90}$ events occupy either the 55.7 MHz or 57.6 MHz frequency bin. $F_{\text{max}}$ corresponds to the highest amplitude

**Table 6.1**: Summary of five lowest $\Gamma_{90}$ events and the corresponding increase in $\Gamma_{90}$ due to systematic uncertainty multiplied by a factor of $10^4$. Error in $\Gamma_{90}$ is $\delta\,\Gamma_{90} = 0.000141\,\sqrt{\Gamma_{90}}$, at most about 1%. Reconstructed FD-matched event parameters are also given in the following units: energy in EeV, core location in (x,y) pairs in km relative to TA's central laser facility (CLF), zenith and azimuth angles in degrees, and $X_{\text{max}}$ in g/cm$^2$.

| Date | $\Gamma_{90} \times 10^4$ | Energy | Core Loc. | Zen. | Azi. | $X_{\text{max}}$ |
|---|---|---|---|---|---|---|
| 20130809 | $8.4 + 5.0$ | 1.22 | (-11.5,1.9) | 65.7 | 301.6 | 772 |
| 20130816 | $8.8 + 2.0$ | 1.43 | (-7.9,6.2) | 68.6 | 280.5 | 755 |
| 20130926 | $9.7 + 2.8$ | 1.38 | (-14.3,3.2) | 54.9 | 299.5 | 837 |
| 20131105 | $9.2 + 3.9$ | 1.83 | (-4.8,-16.0 | 59.6 | 121.4 | 805 |
| 20131202 | $5.2 + 2.5$ | 11.04 | (-6.4,-13.6) | 62.7 | 114.6 | 859 |

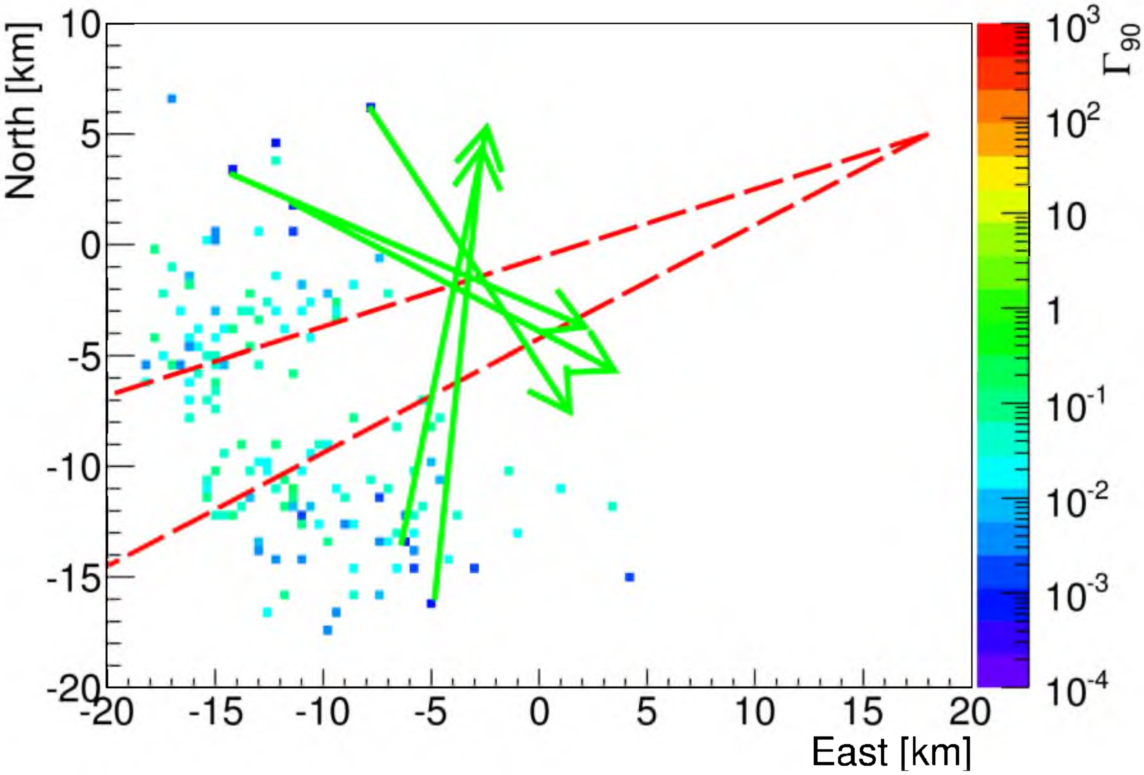

**Figure 6.11**: $\Gamma_{90}$ (color scale) for negative detection events with $\Gamma_{90} < 0.1$, similar to Figure 6.5. Additionally, green arrows begin at the core location of the five lowest $\Gamma_{90}$ events and point in the direction of each event's azimuth. Arrow length is proportional to zenith angle.

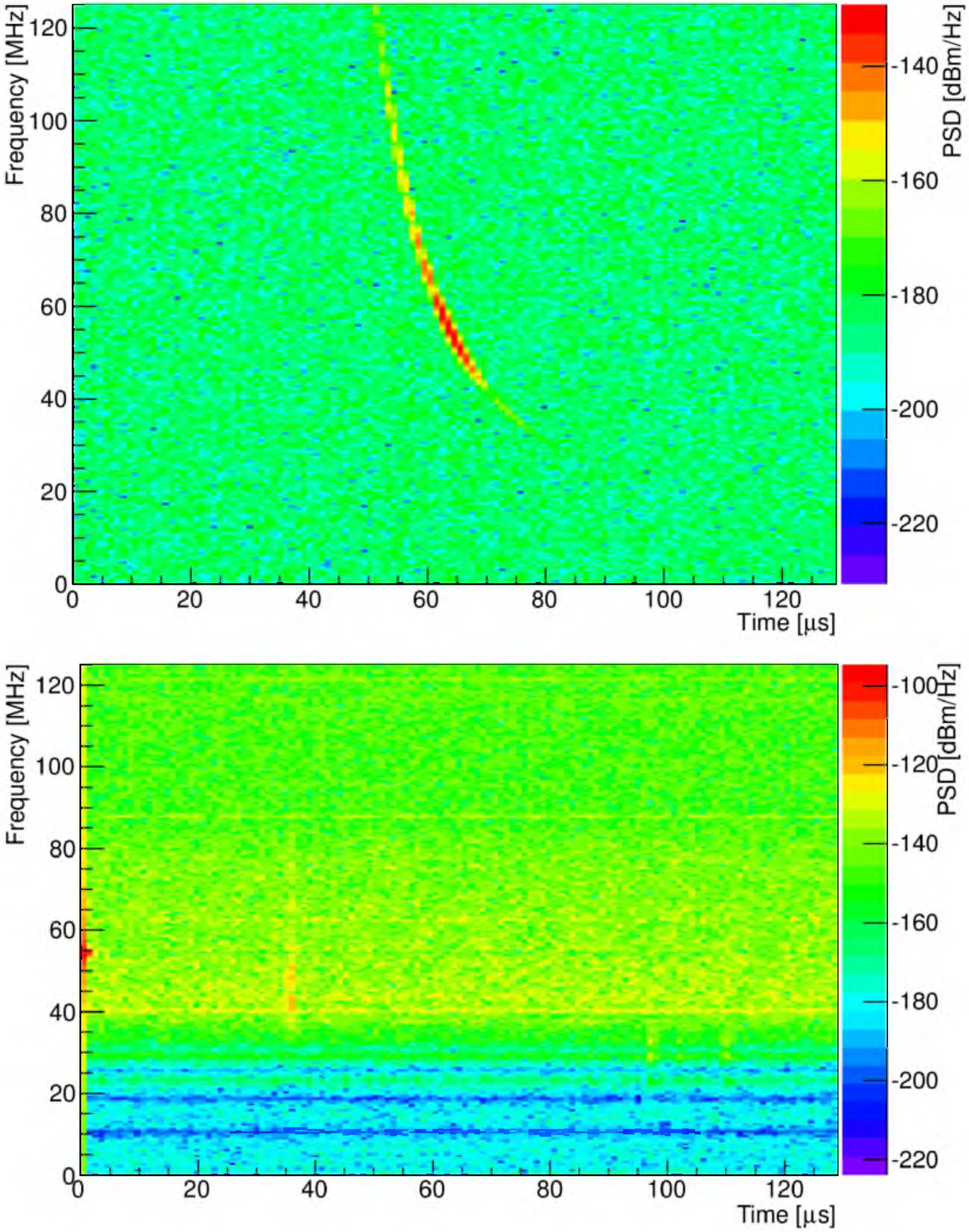

**Figure 6.12**: Spectra of the first entry in Table 6.1 corresponding to on of the five lowest $\Gamma_{90}$ events detected in the present analysis. Top: Spectrogram of simulated radar echo created using FD event reconstructed parameters with $\sigma_{\mathrm{TW}}$ RCS. Gaussian noise has been added to emphasize only the primary expected received signal. Frequency at maximum power $F_{\mathrm{max}}$ is 57.6 MHz, very close to the assumed 54.1 MHz receiver radiation pattern used in the simulation. Bottom: Spectrogram of matched radar waveform which has been 54.1 MHz notch-filtered and 30 MHz high pass-filtered.

frequency bin of the expected echo and therefore is most influential on $\Gamma_{90}$.

For comparison the FD-triggered DAQ spectrogram is shown in the bottom plot of Figure 6.12. The two spectra can't be compared by power directly because the detected waveform is recorded after passing through a series of RF filters and 30 dB amplifier (Section 3.5). Echoes are simulated using matched event energy, geometry, TARA detector geometry and $\sigma_{\mathrm{TW}}$ RCS exactly as those produced for analysis except they are not filtered according to the RF frontend FIR filter. The simulated echo has been superimposed on the same time scale as the FD-triggered spectrogram such that $F_{\max}$ occurs at the trigger time $96 - 33 = 63$ $\mu$s and decimated to the DAQ 250 MS/s sample rate. Recall that the time range in which matched events are analyzed is [48,101] $\mu$s (Section 5.1.1). The remaining four lowest $\Gamma_{90}$ events (the second of which is the event used as an example in Section 6.3.1) are shown in the same format and in the order given in Table 6.1 in Figures 6.12 to 6.16.

Unmodified $\beta_{90}$ distributions for all five events were compared with distributions modified by using a 65.0 MHz receiver antenna radiation pattern in simulation. The procedure for determining the effect on $\Gamma_{90}$ is the same as that described in Section 6.3.1. Of five events analyzed, the highest percent difference in $\Gamma_{90}$ is 16%. $F_{\max}$ differs at most by 3.5 MHz from 54.1 MHz, much less than 65.0 MHz, so we ignore any error introduced by the 54.1 MHz fixed-frequency approximation.

## 6.4 RCS Upper Limits

An optimistic guess at the minimum RCS detectable with the self-triggered DAQ scheme was given in the conclusion section (Section 3.7) of Chapter 3. In that calculation we assumed transmitter and receiver maximum gain, ground level detection, ability to trigger on echoes 7 dB below the noise and constant amplitude radar echo that occurs in the DAQ 5 MHz passband. The smallest self-triggered RCS is 50 cm$^2$ for an event with core location in the transmitter/receiver plane. FD-triggered data analyzed as described in Chapter 5 have for the lowest value $\Gamma_{90} = 0.00052$, shown in Table 6.1. To correct for uncertainty in shower parameters this scale factor must be scaled up by 48% to 0.00077.

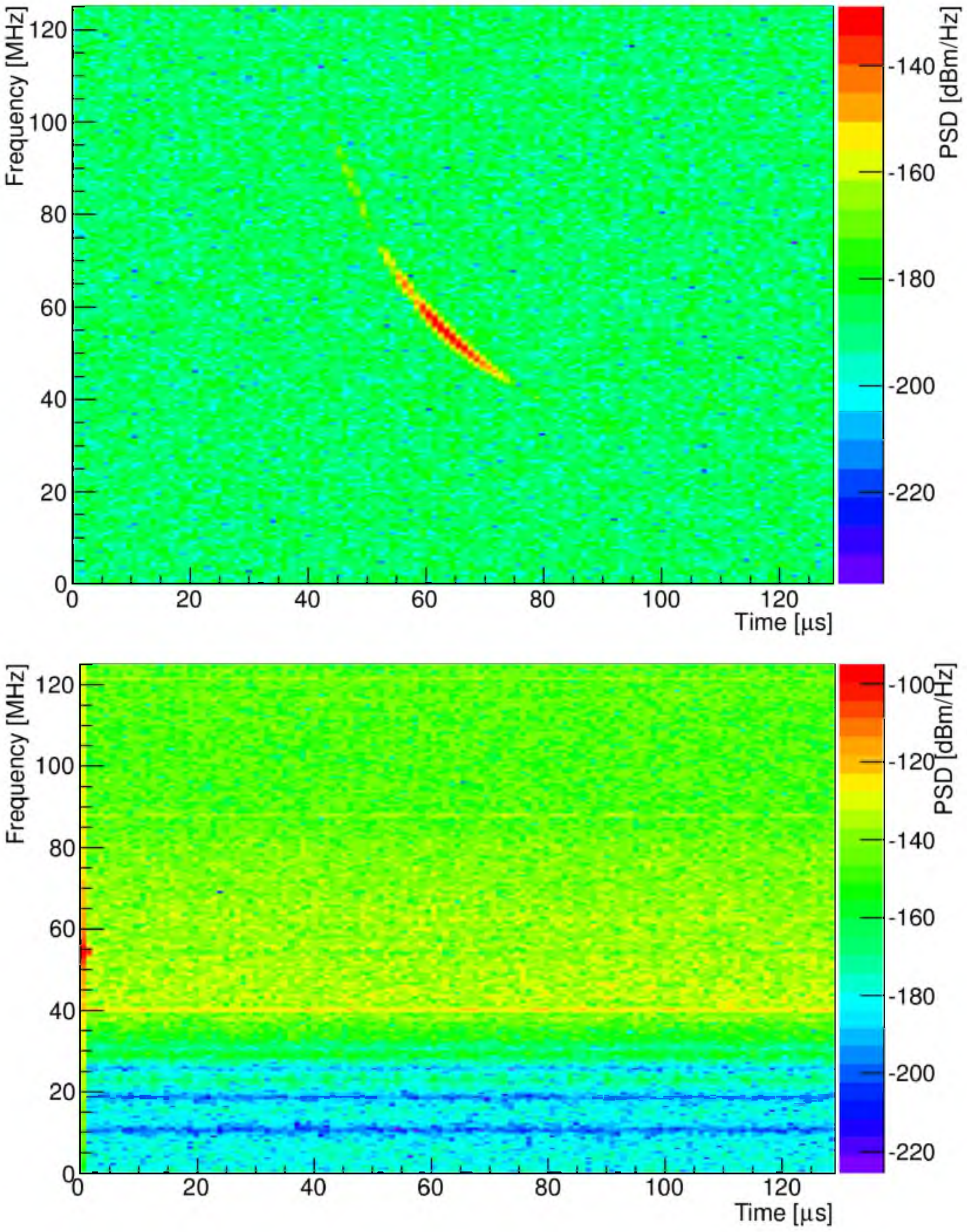

**Figure 6.13**: Spectra of the second entry in Table 6.1 corresponding to one of the five lowest $\Gamma_{90}$ events detected in the present analysis. Top: Spectrogram of simulated radar echo created using FD event reconstructed parameters. Gaussian noise has been added to emphasize only the primary expected received signal. $F_{\mathrm{max}}$ is 55.7 MHz. Bottom: Spectrogram of matched radar waveform which has been 54.1 MHz notch-filtered and 30 MHz high pass-filtered.

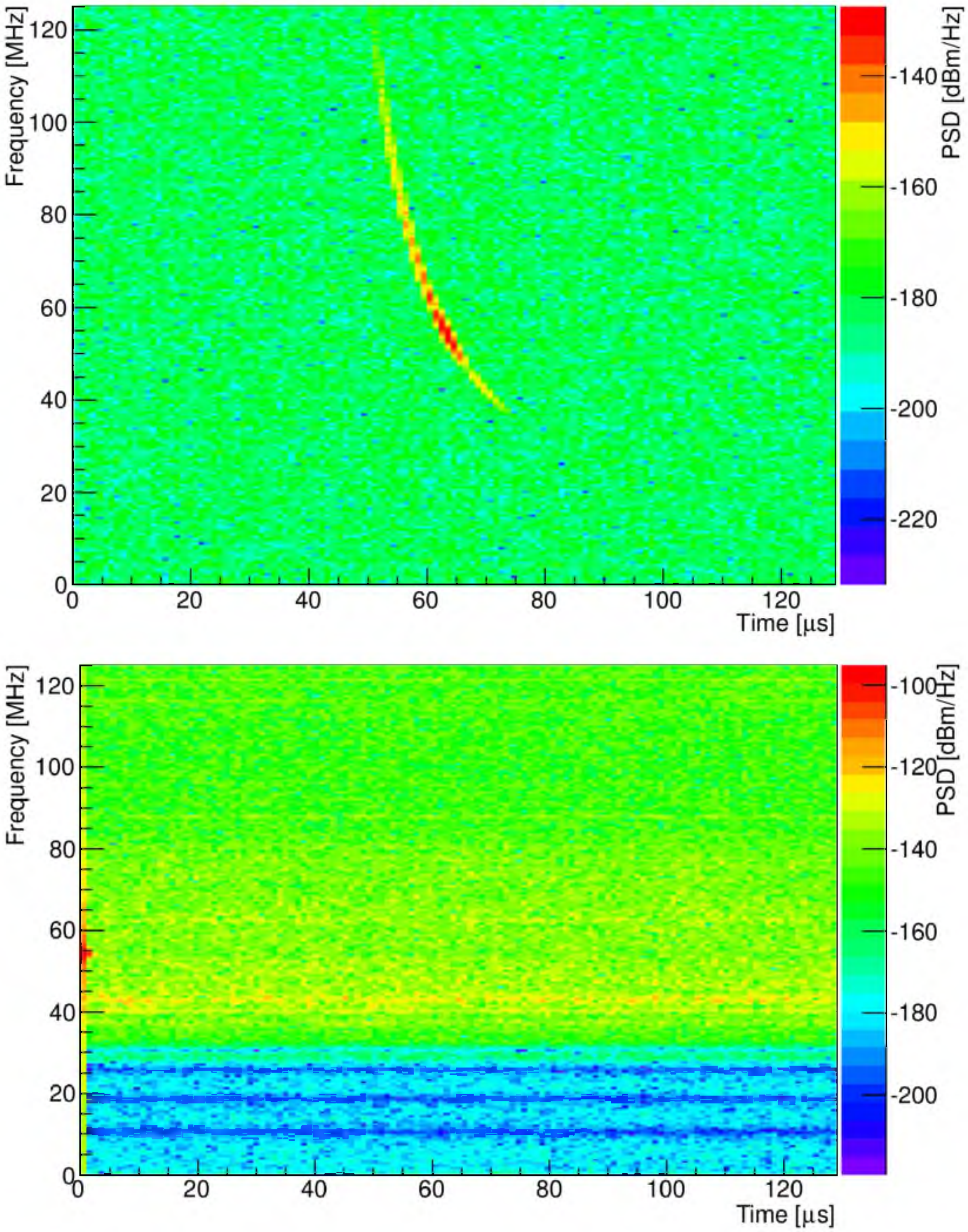

**Figure 6.14**: Spectra of the third entry in Table 6.1 corresponding to one of the five lowest $\Gamma_{90}$ events detected in the present analysis. Top: Spectrogram of simulated radar echo created using FD event reconstructed parameters. Gaussian noise has been added to emphasize only the primary expected received signal. $F_{\max}$ is 55.7 MHz. Bottom: Spectrogram of matched radar waveform which has been 54.1 MHz notch-filtered and 30 MHz high pass-filtered.

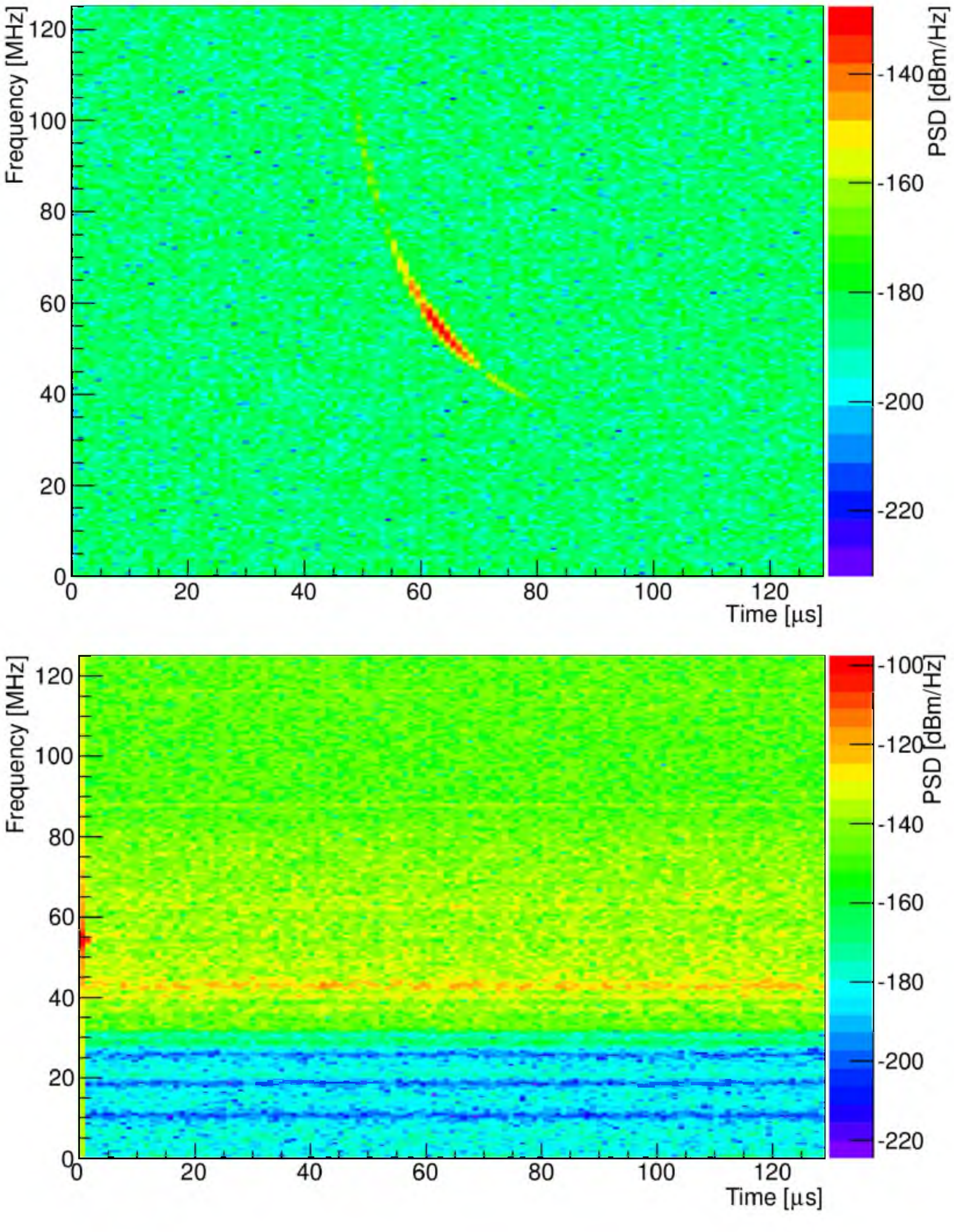

**Figure 6.15**: Spectra of the fourth entry in Table 6.1 corresponding to one of the five lowest $\Gamma_{90}$ events detected in the present analysis. Top: Spectrogram of simulated radar echo created using FD event reconstructed parameters. Gaussian noise has been added to emphasize only the primary expected received signal. $F_{\max}$ is 55.7 MHz. Bottom: Spectrogram of matched radar waveform which has been 54.1 MHz notch-filtered and 30 MHz high pass-filtered.

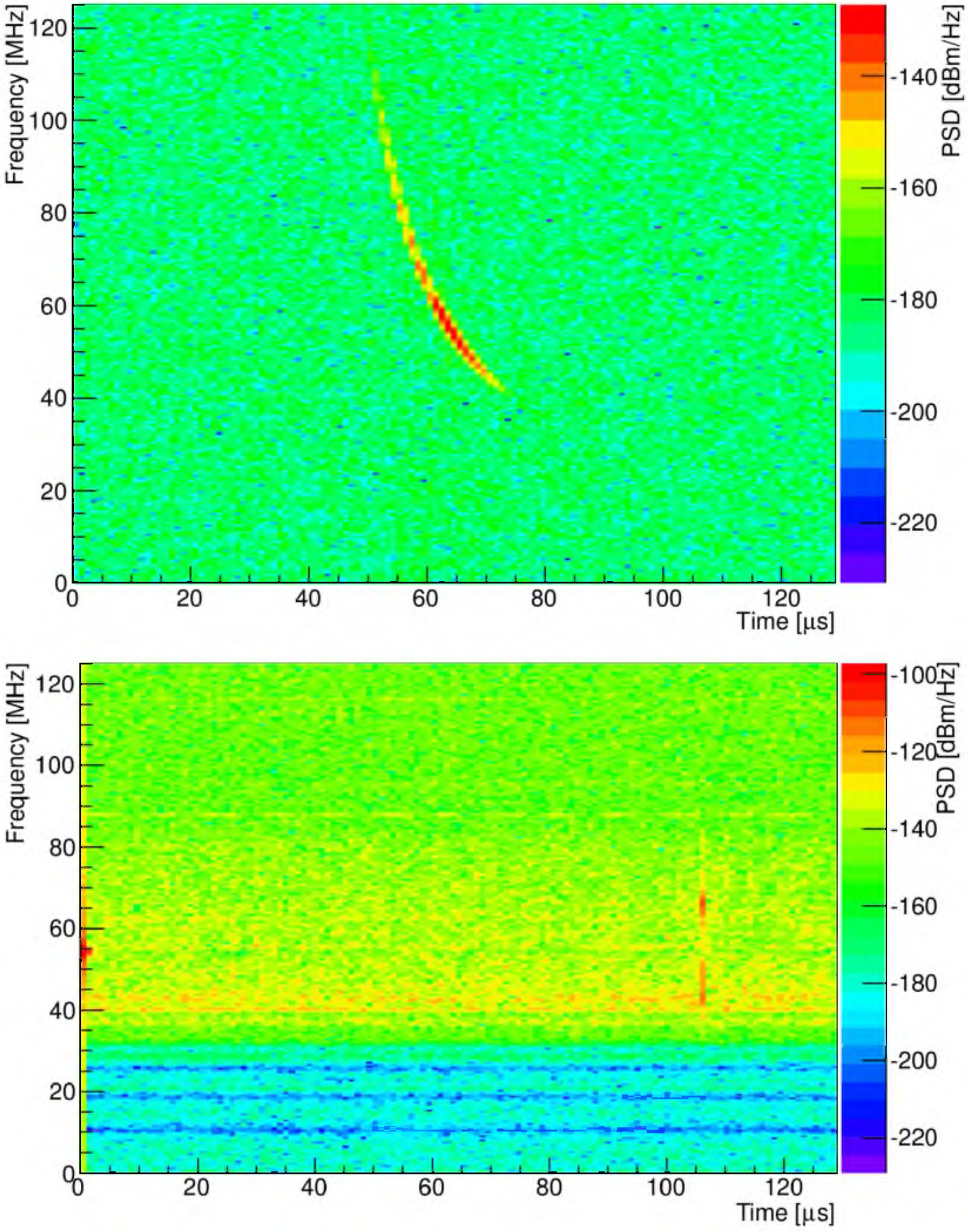

**Figure 6.16**: Spectra of the fifth entry in Table 6.1 corresponding to one of the five lowest $\Gamma_{90}$ events detected in the present analysis. Top: Spectrogram of simulated radar echo created using FD event reconstructed parameters. Gaussian noise has been added to emphasize only the primary expected received signal. $F_{\mathrm{max}}$ is 57.6 MHz. Bottom: Spectrogram of matched radar waveform which has been 54.1 MHz notch-filtered and 30 MHz high pass-filtered.

By definition the RCS $\sigma_{\mathrm{EAS}}$ upper limit is model dependent: $\sigma_{\mathrm{EAS}} = \Gamma_{90}\,\sigma_{\mathrm{TW}} = 0.00077\,\sigma_{\mathrm{TW}}$. This relationship does not offer an immediate interpretation. Figure 6.17 shows the total integrated thin-wire RCS as a function of time during shower evolution and propagation toward the ground for the specific event with $\Gamma_{90} = 0.00052$. Not only is RCS integrated over every longitudinal segment of the shower with plasma age less than 5 $\tau$ at each 2 ns time step, phase factors attributed to differing path length are included in each term in the sum.

At its peak, this particular shower has a total RCS of 5.5 $\mathrm{m}^2$ assuming the thin-wire approximation *without* collisional damping effects. After including detector sensitivity, nonobservation of signal and effect of systematic uncertainty the effective RCS upper limit can be expressed through the scale factor $\Gamma_{90} = 0.00077$, which gives $\sigma_{\mathrm{EAS,\,peak}} = 0.00077 \cdot 5.5\,\mathrm{m}^2 = 42\ \mathrm{cm}^2$ at the 90% confidence level. This is slightly smaller than the area of a Post-it® note.

Figure 6.18 shows simulated received power vs. time for the event with $\Gamma_{90} = 0.00077$. The top (black), middle (blue), and bottom (green) curves are the unmodified simulated received power, the top curve power multiplied by the scale factor $\Gamma_{90}$, and the top curve power multiplied by the damping factor $10^{-6}$ calculated in Section 2.3.2, respectively. The red line is integrated TARA passband noise power, which is received after 30 dB of amplification. Simulated received power has also been increased by 30 dB to account for front end amplifiers. This plot was also shown in Chapter 2, but without the curve multiplied by $\Gamma_{90}$. This plot shows that damping is large and the analysis technique has the ability to detect signal below the noise floor.

Future TARA analysis will push the upper limit down further. The entire self-triggered data stream is yet to be compared with Telescope Array SD data which exceeds FD data volume by 10:1. Transmitter antenna polarization was changed to vertical in November, 2014. Vertically polarized transmitter and receiver channels better align with the majority of air showers detected by the SD array and will allow shower geometries which maximize TARA sensitivity.

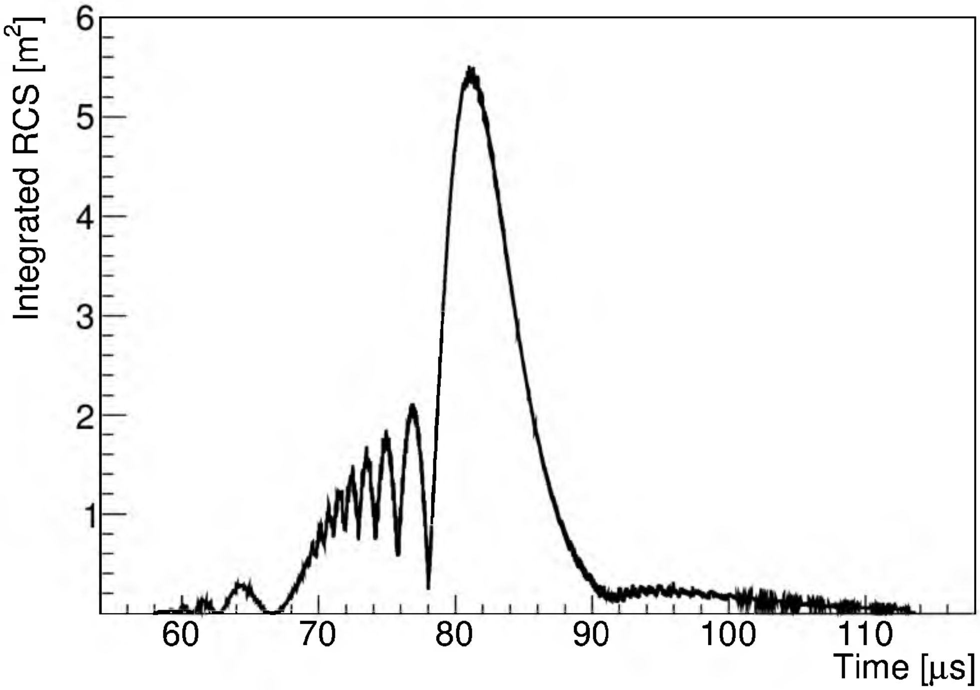

**Figure 6.17**: Integrated thin-wire approximation to RCS for a simulated radar echo according to reconstructed shower parameters. Phase factors are included in the sum of the total RCS to properly account for each longitudinal shower segment.

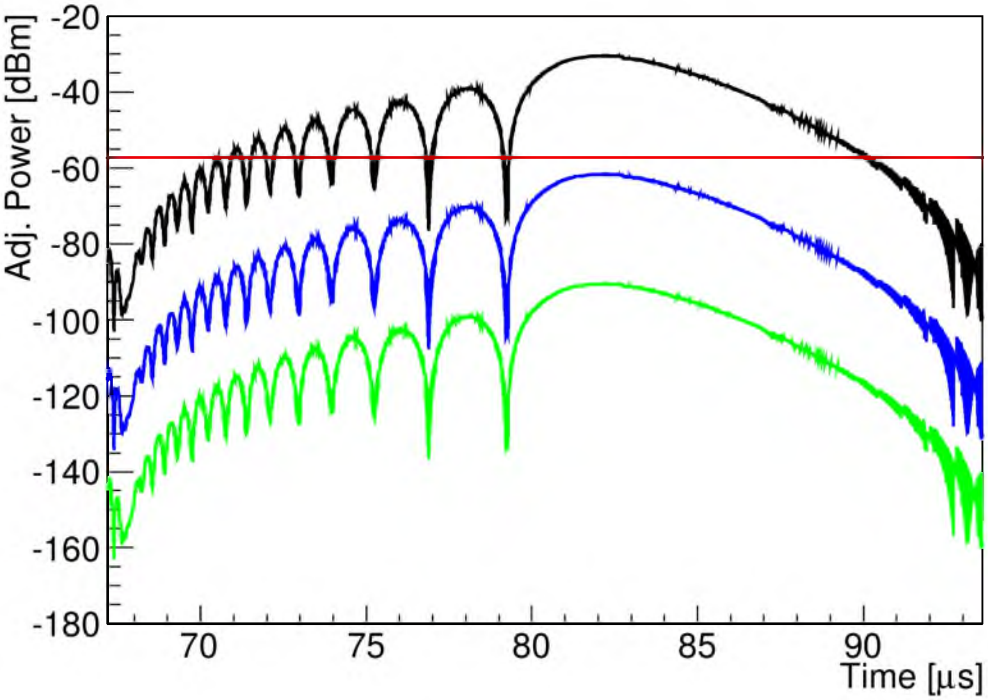

**Figure 6.18**: Received power vs. time for the event with $\Gamma_{90} = 0.00077$ (black). The same received power curve is shown multiplied by $\Gamma_{90}$ (blue) and the damping factor $10^{-6}$ (green) calculated in Section 2.3.2 to account for collisional damping. Note that the damping factor is calculated assuming a collision frequency of $10^{11}$ Hz, which is likely overestimated due to the assumption of near-thermal ionization electron energies (see Section 2.3.2). The red line is integrated background noise power in the TARA passband (see Chapters 3 and 4). Simulated received power has been adjusted by +30 dB to account for front end amplifiers, through which background noise has passed.

# CHAPTER 7

# CONCLUSION

In this dissertation I have presented a complete picture of physics experimentation including hardware, data collection and analysis with TARA. Motivation for the technique is offered in Chapter 1. Chapter 2 has a discussion about a simple approach to EAS scattering and characteristics of the received signal. The distilled message from that chapter is radar echoes are broadband, short in duration (few $\mu$s) and exhibit rapidly changing frequency. Collisional damping, or "molecular quenching" in some literature, is caused by high rate collisions with neutral atmospheric particles and decreases scattering power by orders of magnitude. This fact was not mentioned substantively in literature until late 2014 (see[14]) and not by any peer-reviewed articles at the time of this writing in the first quarter of 2015.

The TARA detector is described in detail in Chapter 3. Data collected with this detector and analysis techniques follow in Chapter 4. Chapter 5 elaborates on an analysis technique hinted at in Chapter 2 in which model dependent radar echo simulation waveforms are used in combination with unbiased snapshot waveforms as a metric for estimating detection thresholds. The number of events recorded with the FD-triggered data stream starting in August, 2013 and ending in May, 2014 that exceed the threshold is not statistically significant. For events that don't exceed the threshold, expected echoes are also used to estimate a scale factor $\Gamma$ by which the echo can be scaled to produce a snapshot + simulated echo MF response that exceeds the threshold. The scale factor that produces a positive-detection response in 90% of test cases is labeled $\Gamma_{90}$ and represents the extensive air shower RCS upper limit $\sigma_{\mathrm{EAS}}$ at the 90% confidence level when multiplied by the thin-wire RCS used in simulation: $\sigma_{\mathrm{EAS}} = \Gamma_{90}\, \sigma_{\mathrm{TW}}$.

Chapter 6 gives results of this analysis in two different parts. First, general results from the majority of $\Gamma_{90}$ values are presented. In the second part, uncertainty in $\Gamma_{90}$

is discussed in the context of the five lowest $\Gamma_{90}$ events. In the present chapter I compare TARA with other recent cosmic ray radar experiments, the expected response predicted in Chapter 2 and recent theoretical papers on the subject.

## 7.1 Comparison with Other Experiments

### 7.1.1 Atmospheric Radars

Jicamarca Radio Observatory (JRO) is an atmospheric radar array located in Lima, Peru. Thousands of dipole elements tuned to 50 MHz project 2 MW maximum pulses every 200 $\mu$s and cover 85,000 m$^2$. Dipole elements in this mono-static configuration both transmit and receive in the vertical direction.

An algorithm is presented[63] to search for vertical EAS in data recorded during a meteor detection run. Horizontal EAS, those perpendicular to the direction of the radar beam at JRO are acknowledged as having the geometry most often considered (see, e.g.,[65]). However, the authors realize the eventual necessity of confirming candidate events with conventional methods. In the case of a horizontal search, "[i]t would therefore not be possible to perform the simultaneous detection of particles which could provide conclusive evidence of the cosmic ray origin of the signal." This is a fundamental concern, one which TARA addresses by projecting its radar beam over an area instrumented by Telescope Array SDs and in the field of view of FDs.

The search obtained results that didn't match other known events detected at JRO. Some events had echo signatures indicating speeds near that of light and scattered in close proximity. The rate of selected events (0.1 s$^{-1}$) is relatively high for UHECR. The authors posit that echoes are occurring from horizontal showers high in the atmosphere, $\sim$ 25 km MSL, where detection aperture is large. High altitude events are unlikely scatterers because of low atmospheric density and thus low ionization density.

MU radar in Shigaraki, Japan is also an atmospheric radar that attempted a search for CR radar echoes.[64] The radar system is similar in several ways to JRO: 46.5 MHz radar frequency, 1 MW peak power, meteor detection. Differences include a much smaller array (8,330 m$^2$), larger beamwidth for detection below 50° zenith angle and 4 ms pulse period. An algorithm to remove known echoes and anomalous events with SNR less than 10 dB is prescribed.

Results were limited to one candidate event recorded in 2009 at a zenith angle of 12°, range 24±4.8 km and contained within one 2 $\mu$s interval. The researchers also acknowledge the need to confirm candidate events with conventional means. Again, radar detection of such a high altitude event seems unlikely. Further, pulsed radars are a poor choice for detecting extremely rare, randomly occurring events.

### 7.1.2 MARIACHI

MARIACHI[66,67] (Mixed Apparatus for Radar Investigation of Atmospheric Cosmic-rays of High Ionization) was an outreach program based on Long Island, NY, that combined passive bi-static radar with conventional particle detectors. Nearly a dozen high schools involved in the outreach program hosted scintillator detectors, from which data were later compared in time with radar receiver data. Carrier signals from existing analog high power television transmitters, of which there were several in surrounding $\sim$ 100 km, were assumed to be adequate radar sources which could be scattered from EAS ionization columns toward receiver antennas.

The search for radar echoes is a time-matching of radar and scintillator events. Several large SNR radar pulses were found coincident in time with scintillator events. Unfortunately, MARIACHI was operational in radar and SD mode for only a few weeks. Peer-reviewed papers were never published.

MARIACHI was the inspiration for combining CR radar detection with a conventional detector at Telescope Array which eventually led to the creation of TARA. TARA improves upon MARIACHI in a number of ways, some of which will be quantified shortly. One major improvement is the use of a dedicated continuous wave transmitter controlled by the experimentalists and high gain antenna. This resolves ambiguity in scattering calculations introduced by unknown transmitter location, power or antenna gain.

Given that MARIACHI recorded several large SNR radar pulses correlated with SD triggers during a short observation period and TARA have not positively detected any features in excess of backgrounds even with the ability to see well below the noise, we are led to believe that MARIACHI's events were only due to RF noise. To compare TARA and MARIACHI detectors, I introduce a figure of merit FOM, a factor proportional to power in the bi-static radar equation (Equation 2.1) with some additional parameters to quantify detector performance:

$$\text{FOM} = \left(\frac{P_T G_T}{R^4}\right) \cdot \left(\frac{B}{ND}\right) . \qquad (7.1)$$

The factor in parentheses on the left is from the bi-static radar equation and the right side factor captures other detector performance attributes that influence detection ability. $P_T$, $G_T$ and $R$ represent the standard bi-static radar equation parameters transmitter power, transmitter gain and distance from transmitter to EAS. Here we assume the distance from EAS to receiver is very small and the same for TARA and MARIACHI. $B$ is the band parameter. It allows a comparison of the signal bandwidth detectable by a specific receiver. Large band signals have structure which can be detected well below the noise using, for example, the MF technique described in Chapter 4. Very narrow band receivers are less likely to inhabit frequency space that is occupied by a given radar echo. Band size is proportional to the probability of detection. $N$ represents background noise which influences the minimum detectable power level. $D$ quantifies detection threshold, which specifies the power necessary to trigger the receiver or to be observable in some postprocessing analysis.

One likely, ideal transmitter candidate for MARIACHI is an analog channel four TV station located 130 km from the receiver location.[110] Its power output was 100 kW, although only a fraction of that power is in the carrier. If we assume a cosmic ray EAS arrives very close to the receiver in both MARIACHI and TARA geometries, the ratio in FOM parameter $R$ for TARA and MARIACHI is $(130\,\text{km}/40\,\text{km})^2 \simeq 10$. TARA transmitter/receiver separation is roughly 40 km.

Typical television transmitter antennas are low gain, emphasizing 360° coverage to surrounding areas. Dipole antennas are uniform in azimuth with a toroidal pattern and have approximately 2 dBi gain. We assume an optimistic 6 dBi gain for the 100 kW transmitter that may have been the source of MARIACHI signal and neglect the fact that only a fraction of 100 kW is at the carrier frequency. TARA transmitter antenna gain is 22.6 dBi and the majority of data used in this dissertation were recorded while transmitter output was 25 kW (Section 3.3.3). The FOM ratio for the product $P_T G_T$, transmitter power with gain converted to linear units, is $(10^{2.26} \cdot 25\,\text{kW})/(10^{0.6} \cdot 100\,\text{kW}) \simeq 10$.

Another consideration is the extremely narrow-band MARIACHI DAQ (2.8 kS/s complex sample rate, 2.8 kHz band) compared with the broadband TARA DAQ (250 MS/s sample rate, 125 MHz band). A smaller band is advantageous because the noise floor is lower, but can be a disadvantage when only a small part of the broadband radar echo can be detected. Starting with the disadvantage, we can assume the power spectrum of all radar echoes is within 10 dB of the peak for a duration of 10 $\mu$s and have $-1$ MHz/$\mu$s chirp rate. This gives a 10 MHz band echo, of which only $2.8\,\text{kHz}/10\,\text{MHz} \simeq 0.0003$ can be detected in a 2.8 kHz bandwidth. If the echo is in the [0, 125] MHz range, the complete radar echo will be detected by the TARA DAQ. The FOM ratio in $B$ is $1/0.0003 \simeq 3000$.

The advantage of a small band can be seen in the formula for the noise power $P_n = kTb$, where $k$ is Boltzmann's constant, $T$ is noise temperature in Kelvin and $b$ is bandwidth in Hz. The FOM ratio for $N$ is $2.8\,\text{kHz}/125\,\text{MHz} \simeq 0.00002$. $N$ is in the denominator because lower $P_n$ is better. It is almost certain that RF noise pollution in the densely populated area around Long Island will have a large effect on the noise floor, in which case the noise temperature is much higher than galactic noise, the limiting source in the radio quiet desert near Delta, UT (see Section 3.5). Again, we view MARIACHI optimistically and assume the galactic noise temperature for Long Island antennas.

I have analyzed several MARIACHI candidate radar echo waveforms, one of which has 36 dB ASNR. Figure 7.1 shows the time and frequency domain representation of that event. Other candidates have lower SNR ratios that also substantially exceed 0 dB. The TARA DAQ can theoretically detect echoes 20 dB below the noise floor (Section 4.5). To be consistent with an optimistic view of MARIACHI, we use the measured SNR of a detection test conducted in situ with the self-triggered scheme, -7 dB ASNR (see Section 3.6.4.2). In linear units the FOM ratio for $D$ is $21.5\,\text{dB} - (-7\,\text{dB}) = 28.5\,\text{dB} = 700$. With this parameter, I quantify the observation that MARIACHI may have detected large SNR EAS echoes, while TARA has no evidence of echoes even with the ability to detect chirp signals below the noise floor and an observation period greatly exceeding that of MARIACHI.

All FOM ratios are collected in Table 7.1. Their product gives an estimate of

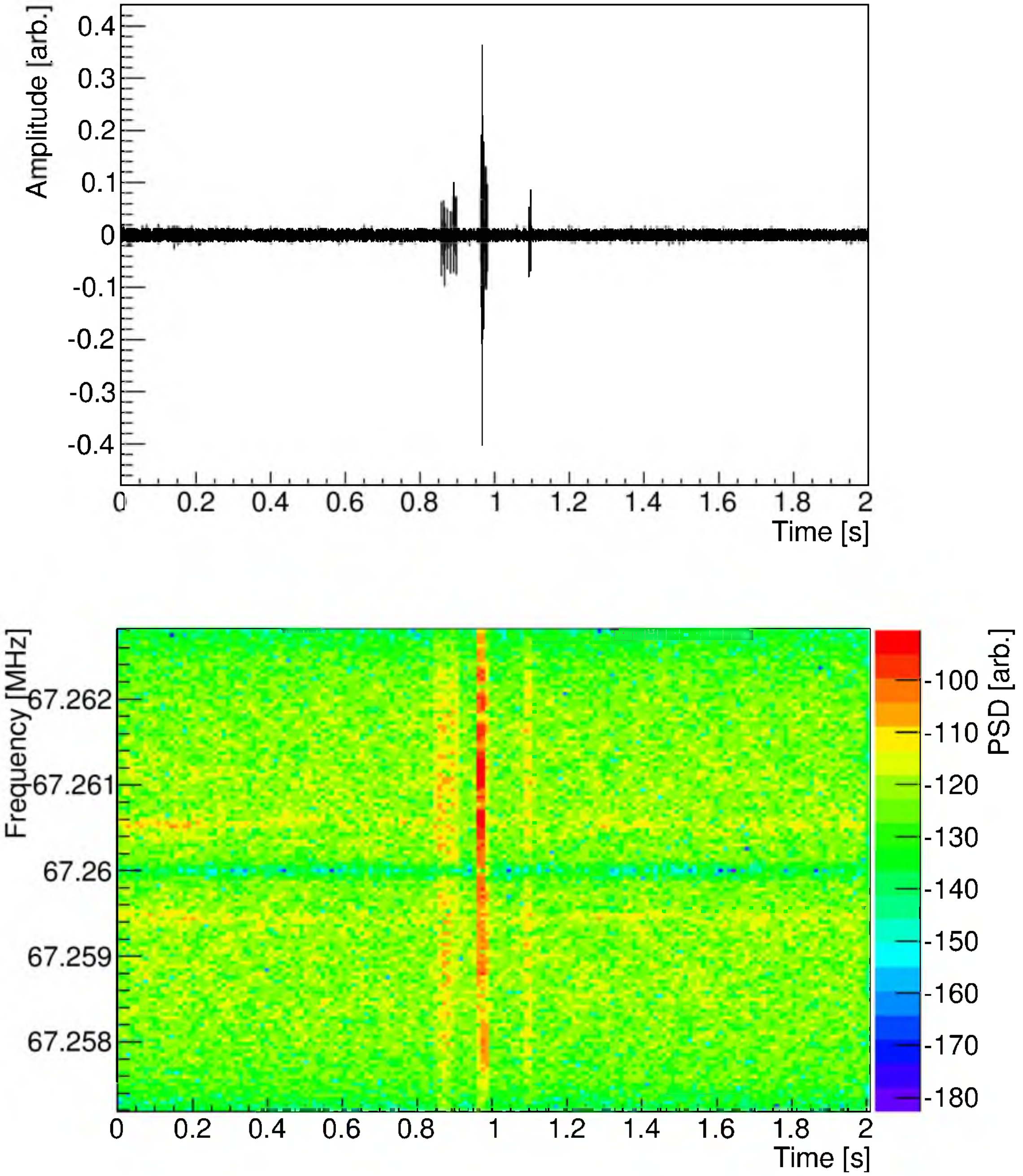

**Figure 7.1**: Event display of a 36 dB ASNR MARIACHI radar echo candidate that was time-matched to a scintillator detector event. The passband DAQ was tuned to 67.26 MHz and used 2.8 kHz sample rate.

**Table 7.1**: Ratios of figure of merit (FOM, Equation 7.1) parameters comparing TARA with MARIACHI. Ratios greater than unity indicate TARA advantages. The product of ratios is roughly 1000. It represents an effective advantage of TARA over MARIACHI.

| Parameter | Description | FOM(TARA)/FOM(MARIACHI) |
|---|---|---|
| $R$ | Transmitter Distance | 10 |
| $P_T$ | Transmitter Power | 10 |
| $B$ | Receiver Bandwidth | 3000 |
| $N$ | Noise Floor | 0.00002 |
| $D$ | Detection Level | 700 |
| FOM | | $\sim 1000$ |

the TARA advantage relative to MARIACHI, which is $\sim 1000$. In summary, TARA has a detector advantage of approximately three orders of magnitude even when using optimistic assumptions about MARIACHI. Transmitter selection is ideal; other transmitters in the area are hundreds of kilometers distant and have lower output power. Transmitter gain is likely closer to unity. The MARIACHI DAQ noise floor in this calculation assumes zero anthropogenic noise, etc.

Further, data used in this dissertation were triggered by Telescope Array's well publicized, state-of-the-art fluorescence detector—it is a statement of fact that TARA FD-triggered events were recorded when the transmitter was operational and a cosmic ray EAS was present in the field of view of the FD with which TARA receivers are co-located. It seems unlikely that large amplitude pulses in MARIACHI's data stream are passive bi-static radar detections of EAS when TARA have not seen any waveform features that cannot be explained by background noise.

Nevertheless, MARIACHI triggers are unique because both surface scintillator and radar receiver activity is required. The large spatial distribution of SD and radar receivers ($\sim 150\,\mathrm{km}^2$) also rules out trivial noise sources. There has been some speculation that high-altitude lightning discharge or short-duration utility power transients[111] could be the cause of this phenomenon.

## 7.2 Comparison with Other Theoretical Results

TARA RCS upper limits can be compared with Gorham[65] and Stasielak,[14] which were presented in Section 2.3.2. Using Gorham's assumptions, the EAS radar cross section for normal incidence on a 100 EeV shower using 10 m radar wavelength is $\sigma_{\text{EAS}} = 10^4$ m$^2$. Given this RCS we wish to compute SNR using the measured noise floor and TARA detector parameters. TARA bi-static radar equation parameters are similar to those used in Section 3.7: $P_T = 25$ kW, $G_T = 22.6\,\text{dBi} = 182$, $G_R = 12.6\,\text{dBi} = 18.2$, $R_T = R_R = 20$ km, $\lambda = 5.5$ m and $\sigma_{\text{EAS}} = 10^4$ m$^2$. The majority of spectra shown in this dissertation use 512 sample Fourier transform window size, which is quite small when attempting to maximize SNR, but suitable for this calculation. Received power using these parameters is -41 dBm.

Converting to power spectral density reduces this value by $10\log_{10}((250\,\text{MHz})/512) = 57\,\text{dB}$. Figure 3.18 shows that noise PSD across the TARA band is roughly $-160$ dBm/Hz. The SNR expected from a shower with $\sigma_{\text{EAS}} = 10^4$ m$^2$ is $(-41-57)\,\text{dBm/Hz}-(-160\,\text{dBm/Hz}) = 62\,\text{dB}$. Granted this value is very optimistic because of the assumption that the shower has very high energy and is illuminated by the maximum gain portion of the radiation pattern, six orders of magnitude SNR would certainly have been detected by TARA. Recall the self-triggered scheme can detect emulated echoes in situ 7 dB below the noise (Section 3.6.4.2), or about -167 dBm/Hz. There were 19 events above 10 EeV, up to 58 EeV, that occurred during TARA detector operation and 496 events greater than 1 EeV. The only reasonable explanation of nondetection is the RCS is greatly overestimated.

Stasielak's RCS for a 1 EeV shower, also at normal incidence, is $\sigma_{\text{EAS}} = 4 \times 10^{-10}$ cm$^2$ at maximum. The difference between Stasielak's and Gorham's RCS is –174 dB, 112 dB below the noise floor. Stasielak's RCS and results presented in Chapter 6 are consistent because our measurement is an *upper* limit to the RCS using an analysis technique sensitive to 11 dB below noise (postprocessing analysis technique, Section 4.5), finding no convincing detection candidates. If Stasielak's values are correct, positive detections are not expected below an increase in total detector performance of 105 dB considering the ability of the DAQ to detect echoes 7 dB below noise in self-triggered mode (Section 3.6.4.2), or $\sim$ 100 dB according to the theoretical postprocessing sensitivity (Section 4.5).

A more realistic comparison discards the simple, optimistic received power using the bi-static radar equation and uses our lowest upper limit result, 42 $\mathrm{cm}^2$ at peak (Section 6.4). The ratio of our lowest measured RCS upper limit to the maximum Stasielak RCS is $42/4 \times 10^{-10} \simeq 110$ dB. Increasing transmitter/receiver performance by 110 dB is extraordinarily impractical.

## 7.3 CR Radar Viability

The TARA detector is designed with a high gain antenna, high power transmitter, short baseline and sensitive detection algorithms that have pushed the RCS upper limit down by nearly three orders of magnitude compared to simulated echoes that do not include damping. Over-estimated received power is expected based on the simple analysis in Chapter 2. We suspect that an upgraded experiment using better detection algorithms, higher gain antenna, shorter baseline and more powerful transmitter will push the upper limit down further, but not yield positive detection unless properties represented in the bi-static radar equation can by modified to increase detector performance by several orders of magnitude, perhaps as much as 90 or 110 dB, per the conclusions in Section 7.2.

Consider a comparison between a hypothetical radar detector with sensitivity in the area covered by the transmitter main lobe and equivalent TA SD array that occupies the same area. There is a 40 km baseline between transmitter and receiver, 10° transmitter main lobe azimuthal beamwidth and 8° vertical beamwidth. Receiver antenna patterns are nearly uniform in the narrow transmitter beamwidth so its effect can be ignored. In 140 $\mathrm{km}^2$ main lobe coverage approximately 80 Telescope Array SDs are located on a 1.2 km grid. Unlike the TA SD array, our hypothetical detector can only detect cosmic rays with $E_0 > 10$ EeV, zenith angle $\theta$ greater than 60° because two lowest $\Gamma_{90}$ have $\theta > 60°$ in the horizontal polarization configuration and azimuth angles that orient air showers roughly perpendicular to the transmitter/receiver plane (let us assume $\pm\,30°$ from perpendicular).

Total detector solid angle is $\pi/6$ str and aperture is $140 \cdot \pi/6 = 70$ $\mathrm{km}^2$ str. Similar to the SD array, duty cycle is 100%. The SD array covers 700 $\mathrm{km}^2$, and has an aperture of 1100 km$^2$ str and 100% efficiency for $E_0 > 10$ EeV.[97] Scaling by 140 km$^2$ coverage, the comparable SD array has 220 km$^2$ str aperture.

Per unit surface detector costs are \$15,000, which gives a hypothetical 80 SD array cost of \$1.2 million. Repair and upkeep costs for the TA SD array over its 15-year lifetime is \$150,000. TARA transmitter site infrastructure including used television transmitters, high gain antenna and building materials and construction are estimated at \$550,000. Monthly utility costs (assuming grid connectivity) for 25 kW power output from two 20 kW analog TV transmitters is \$6,000. Receiver site structures, solar panel power (assuming the transmitter broadcasts toward a remote location that does not have grid connectivity), antennas and receiver electronics is estimated at \$60,000.

Ignoring transmitter upkeep, which has been costly and time consuming, the 15-year lifetime cost of radar detection is \$1.7 million. In summary, SD technology is 75% the cost of radar detection assuming the TARA RCS upper limit is the detection level for UHECR with $E_0 > 10$ EeV. We have also ignored the important fact that the TA SD is nearly 100% efficient above 10 EeV, but detects many UHECRs below that level where flux is much higher.

In the current study, CR radar is not a viable detection technique. Our experiment is designed to maximize the probability of detection rather than detect cosmic rays en masse, yet there is no evidence of detection. Even assuming that the measured RCS upper limit $\Gamma_{90}\,\sigma_{\mathrm{TW}}$ (42 cm$^2$ peak in our lowest limit) is the actual RCS $\sigma_{\mathrm{EAS}}$, CR radar is not a viable detection technique compared to conventional methods. We conclude that other methods should be pursued that can efficiently and economically survey large detection apertures in preparation for the next generation of cosmic ray discoveries.

# REFERENCES

[1] E. Barcikowski, *The Composition of Ultra High Energy Cosmic Rays Through Hybrid Analsysis at Telescope Array*, PhD thesis, University of Utah, 2011.

[2] T. Abu-zayyad et al., Astrophys. J. Lett. **768**, L1 (2013).

[3] A. Hillas, Annu. Rev. Astron. Astr. **22**, 425 (1984).

[4] R. Abbasi et al., Astrophys. J. Lett. **790**, L21 (2014).

[5] R. Abbasi et al., Phys. Rev. Lett. **104**, 161101 (2010).

[6] D. Heck et al., Wissenschaftliche Berichte FZKA **6019** (1998).

[7] J. Abraham et al., Phys. Rev. Lett. **104**, 091101 (2010).

[8] R. Abbasi et al., Astrophys. J. **622**, 910 (2005).

[9] R. Abbasi et al., Astropart. Phys. **64**, 49 (2015).

[10] R. Vidmar, IEEE T. Plasma Sci. **18**, 733 (1990).

[11] Y. Itikawa, Planet. Space Sci. **19**, 993 (1971).

[12] Sir Bernard Lovell, F.R.S., Notes Rec. R. Soc. Lond. **47**, 119 (1993).

[13] K. Suga, Methods for Observing Extremely Large Extensive Air Showers, in *Proc. Fifth Interamerican Sem. on Cosmic Rays*, volume XLIX, 1962.

[14] J. Stasielak et al., ArXiv e-prints (2014).

[15] R. King and T. Wu, *The Scattering and Diffraction of Waves*, Harvard University Press, Cambridge, Massachusetts, 1959.

[16] G. Burke et al., NEC - Numerical Electromagnetics Code for Antennas and Scattering, in *Antennas and Propagation Society International Symposium*, volume 17, 1979.

[17] H. Cane, Mon. Not. R. Astron. Soc. **189**, 465 (1979).

[18] J. Smith et al., GPSY2: A Programmable Hardware Module for Precise Absolute Time Event Generation and Measurement, in *Proceedings of the 30th ICRC*, volume 5, pages 997–1000, 2008.

[19] V. Hess, Phys. Zeitschr. **13**, 1084 (1912).

[20] V. Hess, *The Electrical Conductivity of the Atmosphere and its Causes*, Constable & Co., London, 1928.

[21] P. Auger et al., Rev. Mod. Phys. **11**, 288 (1939).

[22] C. Anderson, Phys. Rev. **43**, 491 (1933).

[23] S.Neddermeyer and C. Anderson, Phys. Rev. **51**, 884 (1937).

[24] C. Lattes et al., Nature **160**, 453 (1947).

[25] CERN Communications Group, CERN FAQ, `http://cds.cern.ch/record/1165534/files/CERN-Brochure-2009-003-Eng.pdf`, Retrieved 2015-04-06.

[26] G. Askaryan, Sov. J. Exp. Theor. Phys. **14**, 441 (1962).

[27] P. Gorham et al., Phys.Rev. **D78**, 032007 (2008).

[28] H. Falcke and others, Nature **435**, 313 (2005).

[29] P. Blackett et al., Proc. Roy. Soc. A **177**, 183 (1941).

[30] D. Ivanov, *Energy Spectrum Measured by the Telescope Array Surface Detector*, PhD thesis, Rutgers, The State University of New Jersey, 2012.

[31] G. Zatsepin and V. Kuz'min, Soviet Journal of Experimental and Theoretical Physics Letters **4**, 78 (1966).

[32] J. Blümer et al., Prog. Part. Nucl. Phys. **63**, 293 (2009).

[33] A. Kusenko, Nuclear Physics B - Proceedings Supplements **212**, 194 (2011).

[34] A. Letessier-Selvon and T. Stanev, Rev. Mod. Phys. **83**, 907 (2011).

[35] T. Antoni et al., Astropart. Phys. **24**, 1 (2005).

[36] T. Stanev et al., Astron. Astrophys. **274**, 902 (1993).

[37] L. Sveshnikova et al., Astron. Astrophys. **409**, 799 (2003).

[38] E. Fermi, Phys. Rev. Lett. **75**, 1169 (1949).

[39] P. Lagage and C. Cesarsky, Astron. Astroph. **125**, 249 (1983).

[40] S. Swordy, Expectations for Cosmic Ray Composition Changes in the Region $10^{14}$ to $10^{16}$ eV, in *Proceedings of the 24th ICRC*, 1995.

[41] A. Lagutin et al., Nucl. Phys. B - Proc. Sup. **97**, 267 (2001).

[42] V. Ptuskin et al., Astron. Astrophys. **268**, 726 (1993).

[43] S. Karakula and W.Tkaczyk, Astropart. Phys. **1**, 229 (1993).

[44] R. Wigmans, Astropart. Phys. **19**, 379 (2003).

[45] D. Allard et al., Astropart. Phys. **27**, 61 (2007).

[46] E. Waxman, Phys. Rev. Lett. **75**, 386 (1995).

[47] P. Bhattacharjee and G. Sigl, Phys. Rep. **327**, 109 (2000).

[48] A. Vilenkin and E. Shellard, *Cosmic Strings and Other Topological Defects*, Cambridge University Press, Cambridge, UK, 1995.

[49] K. Shinozaki and M. Teshima, Nucl. Phys. Proc. Suppl. **136**, 18 (2004).

[50] K. Greisen, Physical Review Letters **16**, 748 (1966).

[51] R. Abbasi et al., Phys. Rev. Lett. **100**, 101101 (2008).

[52] J. Horandel, Mod. Phys. Lett. A **22**, 1533 (2007).

[53] R. Abbasi et al., (2015), Working group report given at UHECR 2014 (Springdale, UT, USA).

[54] T. Abu-Zayyad et al., Astropart. Phys. **61**, 93 (2015).

[55] D. McKinley, *Meteor Science and Engineering*, McGraw-Hill Book Company, New York, NY, First edition, 1961.

[56] T. Abu-Zayyad et al., Astropart. Phys. **39–40**, 109 (2012).

[57] D. Saltzberg et al., Phys.Rev.Lett. **86**, 2802 (2001).

[58] G. Askaryan, Soviet Physics JETP **14**, 441 (1962).

[59] D. Bergman and J. Krizmanic, AIP Conf.Proc. **1516**, 282 (2012).

[60] R. Smida et al., Phys. Rev. Lett. **113**, 221101 (2014).

[61] T.L. Eckersley, J. Instn Elect. Engrs **67**, 99 (1929).

[62] A. Iyono et al., Radar Echo Detection System of EAS Ionization Columns as Part of a LAAS Detector Array, in *Proceedings of the 28th ICRC*, pages 217–220, 2003.

[63] D. Wahl et al., The Search for Vertical Extended Air Shower Signals at the Jicamarca Radio Observatory, in *Proceedings of the 30th ICRC*, volume 5, pages 957–960, 2008.

[64] T. Terasawa et al., Search for Radio Echoes from EAS with the MU Radar, Shigaraki, Japan, in *Proceedings of the 31st ICRC*, 2009.

[65] P. Gorham, Astropart. Phys. **15**, 177 (2001).

[66] M. Bugallo et al., MARIACHI: A Multidisciplinary Effort to Bring Science and Engineering to the Classroom, in *IEEE Internation Conference on Acoust., Speech, Signal Process.*, pages 2661–2664, 2008.

[67] M. Bugallo et al., Hands-on Engineering and Science: Discovering Cosmic Rays Using Radar-based Techniques and Mobile Technology, in *IEEE Internation Conference on Acoust., Speech, Signal Process.*, pages 2321–2324, 2009.

[68] M. A. B. Othman et al., Radar Detection of UHECR Air Showers at the Telescope Array, in *Proceedings of the 32nd ICRC*, 2011.

[69] H. Takai et al., Forward Scattering Radar for Ultra High Energy Cosmic Rays, in *Proceedings of the 32nd ICRC*, 2011.

[70] W. Heitler, *The Quantum Theory of Radiation*, Dover Publications, Inc., Mineola, New York, Third edition, 1984.

[71] P. Sokolsky, *Introduction to Ultrahigh Energy Cosmic Ray Physics*, Westview Press, Boulder, Colorado, 2004.

[72] J. Beringer et al., Phys. Rev. D **86**, 010001 (2012).

[73] T. Gaisser and A. Hillas, Reliability of the Method of Constant Intensity Cuts for Reconstructing the Average Development of Vertical Showers, in *Proceedings of the 15th ICRC*, volume 8, page 353, 1977.

[74] K. Greisen, Ann. Rev. Nucl. Sci. **10**, 63 (1960).

[75] G. Moliere, Z.Naturforsch. **A2**, 133 (1947).

[76] K. Kamata and J. Nishimura, Prog. Theor. Phys. Supp. **6**, 93 (1958).

[77] B. Rossi, *High Energy Particles*, Prentice-Hall, Inc., Englewood Cliffs, NF, 1952.

[78] F. Nerling and others, Astropart. Phys. **24**, 421 (2006).

[79] S. Ostapchenko, Nucl. Phys. B-Proc. Suppl. **151**, 143 (2006).

[80] J. Jackson, *Classical Electrodynamics*, John Wiley & Sons, Inc., Third edition, 1999.

[81] P. Bernardini et al., Study of the Shower Front Structure at Few Meters from the Core with ARGO-YBJ, in *Proceedings of the 33rd ICRC*, 2013.

[82] M. Abramowitz, *Handbook of Mathematical Functions with Formulas, Graphs, and Mathematical Tables*, Dover Publications, Inc., Mineola, NY, 1965.

[83] K. Davies, *Ionospheric Radio Waves*, Blaisdell Publishing Company, Waltham, Massachusetts, 1969.

[84] I. Shkarofsky, Planet. Space Sci. **6**, 24 (1961).

[85] Y. Itikawa et al., J. Phys. Chem. Ref. Data **15**, 985 (1986).

[86] A. Dogariu et al., Appl. Phs. Lett. **103**, 224102 (2013).

[87] S. Nijdam et al., J. Phys. D: Appl. Phys. **44**, 145204 (2011).

[88] D. Underwood, Large Doppler Shift in RADAR Detection of Ultra-high Energy Eosmic Rays, in *Radar Conference, RADAR '08. IEEE*, pages 1–5, 2008.

[89] A. Zech, *A Measurement of the Ultra-High Energy Cosmic Ray Flux with the HIRES FADC Detector*, PhD thesis, Rutgers University, 2004.

[90] NASA, U.S. Standard Atmosphere, Technical report, U.S. Government Printing Office, 1976.

[91] K. S. Gage and others, Radio Sci. **16**, 1447 (1981).

[92] J. Crispin and A. Maffett, P. IEEE **53**, 833 (1965).

[93] B. Farhang-Boroujeny, *Signal Processing Techniques for Software Radios*, self-published, Second edition, 2010.

[94] R. Abbasi et al., Nucl. Instrum. Meth. A **767**, 322 (2014).

[95] M. Bakunov et al., Astropart. Phys. **33**, 335 (2010).

[96] N. Willis, *Bistatic Radar*, Scitech Publishing, Raleigh, NC, 1995.

[97] T. Abu-Zayyad et al., Nucl. Instrum. Meth. A **689**, 87 (2012).

[98] T. Abu-Zayyad et al., Astropart. Phys. (2014), submitted.

[99] M. Teshima et al., J. Phys. G **12**, 1097 (1986).

[100] M. Takeda et al., Astropart. Phys. **19**, 447 (2003).

[101] T. Abu-Zayyad et al., Astropart. Phys. **48**, 16 (2013).

[102] J. Kraus and R. Marhefka, *Antennas For All Applications*, McGraw-Hill, New York, NY, Third edition, 2003.

[103] G. Dulk et al., Astron. Astrophys. **365**, 294 (2001).

[104] M. Othman et al., On Radar Detection of Chirp Signals with Nondeterministic Parameters in Challenging Noise Background, in *Radar Conference (RADAR), 2013 IEEE*, pages 1–6, 2013.

[105] R. Brun and F. Rademakers, Nucl. Instrum. Meth. A **389**, 81 (1997).

[106] J. Proakis and D. Manolakis, *Digital Signal Processing*, Prentice Hall, Upper Saddle River, NJ, Third edition, 1995.

[107] W. Smith, *The Scientist and Engineer's Guide to Digital Signal Processing*, California Technical Publishing, Poway, CA, 1997.

[108] T. Fujii, Mass Composition of Ultra-High Energy Cosmic Rays Measured with the Telescope Array Fluorescence Detector Using a Monocular Analysis, private communication, 2015.

[109] E. Weisstein, Convolution, `http://mathworld.wolfram.com/Convolution.html`, Retrieved 2015-02-24.

[110] H. Takai, private communication, 2015.

[111] L. Blackburn et al., Classical Quant. Grav. **25**, 184004 (2008).